NASA Technical Memorandum 4663

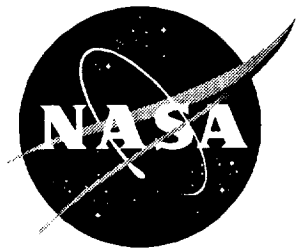

Water Tunnel Flow Visualization Study Through Poststall of 12 Novel Planform Shapes

Gregory M. Gatlin and Dan H. Neuhart

March 1996

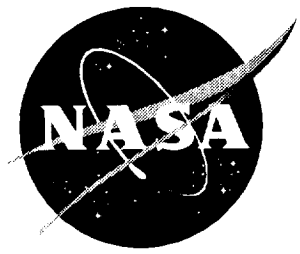

NASA Technical Memorandum 4663

Water Tunnel Flow Visualization Study Through Poststall of 12 Novel Planform Shapes

Gregory M. Gatlin
Langley Research Center • Hampton, Virginia

Dan H. Neuhart
Lockheed Engineering & Sciences Company • Hampton, Virginia

National Aeronautics and Space Administration
Langley Research Center • Hampton, Virginia 23681-0001

March 1996

Available electronically at the following URL address: http://techreports.larc.nasa.gov/ltrs/ltrs.html

Printed copies available from the following:

NASA Center for AeroSpace Information
800 Elkridge Landing Road
Linthicum Heights, MD 21090-2934
(301) 621-0390

National Technical Information Service (NTIS)
5285 Port Royal Road
Springfield, VA 22161-2171
(703) 487-4650

Summary

To determine the flow field characteristics of 12 planform geometries, a flow visualization investigation was conducted in the Langley 16- by 24-Inch Water Tunnel. Concepts studied included flat-plate representations of diamond wings, twin bodies, double wings, cutout-wing configurations, and serrated forebodies. The planform models tested were 0.25-in-thick flat plates with beveled edges on the lower surface to ensure uniform flow separation at angle of attack. A removable, simulated balance housing also was tested to determine the potential effects on the flow field characteristics. The off-surface flow patterns were identified by injecting colored dyes from the model surface into the free-stream flow. These dyes generally were injected so that localized vortical flow patterns were visualized. Photographs were obtained for angles of attack ranging from 10° to 50°, and all investigations were conducted at a test section speed of 0.25 ft per sec.

Results from the investigation indicate that the formation of strong vortices on highly swept forebodies can improve poststall lift characteristics; however, the asymmetric bursting of these vortices could produce substantial control problems. The simulated balance housing affected the vortex structure on some configurations, but these effects were noted only at angles of attack of 20° and below. The vortices that formed on the additional forebody and the wings of the twin-body and double-wing configurations probably account for the lift increases noted when these configurations are compared with the single-body and wing configuration. A wing cutout will significantly alter the position of the forebody vortex on the wing by shifting the vortex inboard. The diamond-shaped cutout produced a vortex over the aft inboard portion of the wing; however, this did not happen with a triangular-shaped cutout. Serrated forebodies effectively generated multiple vortices over the configuration. Vortices from the 65° swept forebody serrations tended to roll together, while vortices from the 40° swept serrations were more effective in generating additional lift caused by their more independent nature.

This report states that color photographs are presented. Most copies of this document were printed in black and white; however, a limited number of color copies are available from the author. The color images are also available in the electronic version at URL http://techreports.larc.nasa.gov/ltrs/ltrs.html.

Introduction

As the demands to develop increased maneuverability are continually being pursued for fighter aircraft (ref. 1), novel control concepts are receiving more attention. Multiple concepts, such as deployable strakes (refs. 2 through 5), blowing and suction systems (refs. 5 through 10), and porous surfaces (refs. 11 through 13), have been developed for a variety of applications. These novel means of control could be incorporated into a newly developed vehicle design, thus resulting in a configuration with substantial levels of maneuverability.

To develop such a vehicle, the appropriate initial studies would include an investigation of various promising planform shapes. This type of investigation has been conducted with 21 planform models that incorporate twin-body, double-wing, cutout-wing, and serrated-forebody concepts. The investigation was conducted in the Langley Subsonic Basic Research Tunnel over an angle-of-attack range from 0° to 70° at a free-stream dynamic pressure of 30 psf. The results of this wind tunnel investigation, which include longitudinal force and moment data and minituft surface-flow visualization, are presented in reference 14.

The concepts investigated were chosen based on the expectations that these particular planform shapes would effectively generate high lift across the angle-of-attack range. Double-wing and cutout-wing configurations were expected to derive benefits from a forward and aft lifting surface that would act independently at moderate to high angles of attack. These lift improvements were expected because previous research findings on close-coupled wing-canard configurations (refs. 15 through 17) have shown favorable improvements in maximum lift coefficient when a close-coupled canard was added to the basic wing planform. The intent of including the twin-body and serrated-forebody configurations was to investigate the effects of multiple forebody vortices on the high-angle-of-attack characteristics. The serrated-forebody concept was specifically designed so that a vortex would form on each forebody serration, and thus the multiple vortices that would extend over the length of the configuration would enhance the lift-generating capability at moderate to high angles of attack.

As a follow-on study to the wind tunnel test, an off-surface flow visualization investigation was conducted in the Langley 16- by 24-Inch Water Tunnel. The results of this investigation are presented in this report. The goal of the investigation was to develop a more thorough understanding of the flow fields associated with the planform concepts under consideration. A water tunnel that operates at low speed is capable of providing high-quality, detailed flow visualization of complex flows, which include vortex generation, interactions between multiple vortices and aerodynamic surfaces, and vortex burst. For thin, sharp-edged configurations, the results obtained in a water tunnel at low Reynolds number can be related in a qualitative manner to high Reynolds number flow in air.

These issues are fully discussed and supported in reference 18.

Although 21 planform models were tested in the wind tunnel investigation, only 12 planforms were examined further in the water tunnel investigation. Generally, the configurations that showed the most promise in the wind tunnel were also examined in the water tunnel. Furthermore, insight from the wind tunnel investigation indicated that several of the 21 planforms tested had very similar off-surface flow field characteristics, and thus further examination in the water tunnel was not necessary.

The off-surface flow patterns for 12 planform models were identified in the present investigation by injecting colored dyes from the model surface into the free-stream flow. The colored dyes were generally injected in a manner so that localized vortical flow patterns would be visualized. Specifically, colored dyes were injected at the forebody apex, the wing/body junction, and any other location where a vortex would be expected to exist. The planform models were 0.25-in-thick flat plates with a beveled lower surface on the leading edges to ensure a uniform flow separation at angle of attack. Both top- and side-view photographs were obtained for angles of attack ranging from 10° to 50°. All investigations were conducted at a test section flow speed of 0.25 ft per sec, which corresponds to a Reynolds number of 25000 per ft.

This report states that color photographs are presented. Most copies of this document were printed in black and white; however, a limited number of color copies are available from the author. The color images are also available in the electronic version at URL http://techreports.larc.nasa.gov/ltrs/ltrs.html.

Symbols

All measurements are presented in U.S. Customary Units. All data have been reduced to standard coefficient form, and lift coefficient data are presented in the stability axis system.

b	reference span, in.
C_L	lift coefficient, $\frac{\text{Lift}}{q_\infty S}$
$C_{L_{max}}$	maximum lift coefficient
c	reference length of planform, in.
q_∞	free-stream dynamic pressure $\frac{1}{2}\rho V_\infty^2$, psf
S	planform reference area, ft^2
V_∞	free-stream velocity, ft/sec
α	angle of attack, deg
ρ	density, $slug/ft^3$

Model Description

This investigation was conducted in the Langley 16- by 24-Inch Water Tunnel, as illustrated in figure 1. All models were held in the test section by the offset model support system that is shown in figure 2. Twelve planform configurations were tested. The first seven planforms were models that were specifically designed and built according to predetermined specifications. The remaining five planforms were generated by modifying several of the original planforms.

Sketches of the original seven planform models are presented in figures 3 through 6. These models include 55° and 65° delta wings, 30° and 40° diamond wings, a twin-body configuration, and two double-wing configurations. The figures show a side and bottom view of each model, as it was tested. As illustrated, the 0.50-in-diameter sting was attached to the bottom surface of each model and was inclined 5°. In addition, a simulated balance housing was mounted on the top of each configuration. This housing was added so that the upper surface of each model would be identical to that of the configurations tested in the wind tunnel investigation (ref. 14). The simulated balance housing was cylindrical with a 0.50-in. radius and a hemispherical front end. This housing was also removable so that testing could be conducted to determine if it produced any substantial effects. Each planform model was 0.25-in. thick and had a flat upper surface. To ensure a uniform flow separation at angle of attack, the leading edges were sharpened by beveling the lower surface. The trailing edges also were beveled on the lower surface for all configurations except the two delta-wing planforms.

Five modified planforms also were tested in the investigation, and they are identified in figures 7 and 8. Each of these modified planforms was generated by attaching 0.0625-in. flat plate pieces to the top of an existing model to produce the desired planform. In all cases, the edges of the flat plate pieces were taped to minimize the effects of any forward and rearward facing steps.

The first set of modified planforms presented (fig. 7) are referred to as cutout-wing concepts. The 30° diamond cutout wing, as presented in figure 7(a), was not tested in its original configuration in this investigation; however, the side- and bottom-view sketches are presented to provide a complete description of the modified cutout configurations. The two 30° diamond cutout-wing planforms that were investigated include one with a triangular-shaped cutout (fig. 7(b)) and one with a diamond-shaped cutout (fig. 7(c)). Both planforms were generated by modifying the original planform, which was referred to as the 30° diamond cutout wing (fig. 7(a)). Because all the geometric details of the original unmodified

30° diamond cutout wing are presented in figure 7(a), only the overall planform shapes are presented in figures 7(b) and 7(c) for the modified planforms. The cutout area on the 30° diamond with triangular cutout configuration was set equal to the cutout area on the 30° diamond with diamond cutout configuration so that the effects of the cutout shape alone could be examined.

The final set of modified planforms, presented in figure 8, was designed to examine the effects of serrated forebodies. The first planform is referred to as the 65° delta with delta sawteeth, and it was generated by adding a delta sawtooth-shaped forebody to the original 65° delta-wing model. Another sawtooth-shaped forebody concept also was tested, as illustrated in figure 8(b), and it was generated by adding 3 diamond-shaped sawteeth that were swept 40° to the forebody of the original 40° diamond wing model. The final serrated-forebody configuration (fig. 8(c)) was produced by adding a nose tip to the 40° diamond with 3 diamond sawteeth configuration.

All the original and modified configurations were painted white to provide maximum contrast with the colored dye. The complete planform area, length, and span for each of the original and modified configurations tested are presented in table I.

Test Conditions and Techniques

Water Tunnel Description

The investigation was conducted in the Langley 16- by 24-Inch Water Tunnel, as described in reference 19. This facility is a closed-return water tunnel that is capable of test section velocities from 0 to 0.75 ft per sec with flow through in a downward (vertical) direction (fig. 1) through the 16- by 24-inch test section. The velocity normally used for testing, which was used for the present investigation, is 0.25 ft per sec. This velocity produces the most uniform flow. The flow rate is also slow enough to easily observe the flow phenomena, such as vortex flow, with the unaided eye. The model support system can be operated in the pitch and yaw planes of rotation through ±33° and ±15°, respectively. An offset sting, as illustrated in figure 2, can be used to shift the available pitch range to 62°.

To visualize the model flow field, red, green, and blue vegetable dyes or fluorescent dyes can be injected into the free-stream flow through a remotely controlled probe that is mounted above the test section. These same dyes can also be remotely injected into the flow through orifices located on the model surfaces. The clear acrylic test section walls and the location of the model in the test section at approximately eye level above the floor produce an environment that is well suited for generating photographic records of the flow patterns around the model.

Test Conditions

All 12 planforms were tested at a flow velocity of 0.25 ft per sec with the model on the tunnel centerline. This condition corresponds to a Reynolds number of 25000 per ft. Flow visualization photographs generally were obtained at 10°, 20°, 30° and/or 35°, and 50°. In some limited cases, additional angles of attack were investigated. All testing was conducted at a sideslip angle of 0°.

Test Techniques

Because the goal of the investigation was to gain a better understanding of the off-surface flow field characteristics associated with each planform concept, the investigation focused on flow visualization. Specifically, when conducting flow visualization studies with colored dyes in the Langley 16- by 24-Inch Water Tunnel, the best flow visualization occurs when the dye gets wrapped in a vortex. Because this was the desired condition, the technique of injecting dye directly from the model into the flow was chosen as the most appropriate method. When this technique is used, dye generally can be injected into the flow at just the right location so that it clearly identifies a vortex in the flow field.

Therefore, dye injection tubes had to be attached before each planform model was mounted on the support system in the water tunnel. These tubes, which were 0.04 in. in diameter, were attached to the undersurface of each configuration with the tube opening located such that the dye would be distributed into the flow at just the right location. The appropriate location for dye injection generally was at the forebody apex, at the junction of the wing leading edge and the body, and at any other position on the configuration where vortex flow would be expected. These additional positions include wing cutout and serrated-forebody locations. Because the end of the dye tube would probably be very close to a significant flow region, it had a steep bevel angle of approximately 20° to minimize any possible interference effects. A sketch that illustrates a typical dye tube installation is presented in figure 2.

The final data obtained in this investigation and presented in this report are color photographs. Top-view photographs are presented for each test condition, and side-view photographs are presented for selected cases. Note that when side-view photographs are presented, they were not taken simultaneously with the top-view photographs.

Discussion

To further understand and interpret the flow visualization photographs, lift coefficient versus angle-of-attack data are presented for each configuration. These data are taken directly from reference 14, and they were obtained on the same planform models that were tested in the water tunnel. These aerodynamic data were obtained in the Langley Subsonic Basic Research Tunnel at a free-stream dynamic pressure of 30 psf. Since these data are analyzed in reference 14 and are presented in this report solely to support the interpretation of the flow visualization, they will not be analyzed in detail in this paper.

To address the flow characteristics of the planforms in a meaningful fashion, the discussion of the test results has been divided into four sections. These sections are delta and diamond wings, twin bodies and double wings, cutout wings, and serrated forebodies. In each section, the lift coefficient versus angle-of-attack data are presented first, and the flow visualization photographs for each configuration are presented second. All color photographs that illustrate the flow visualization patterns obtained and the graphical representations of the aerodynamic data are presented in the figures, as listed in table II.

Delta and Diamond Wings

To establish a baseline set of flow visualization photographs on a simple planform concept, initial testing was conducted on 55° and 65° delta-wing configurations. It was anticipated that first obtaining flow visualization on some simple, well-known planforms would help interpret and understand the flow patterns later visualized on the more complex configurations. In addition to the delta planforms, simple 30° and 40° diamond wing planforms were included in the initial investigations. Lift coefficient versus angle-of-attack data are presented in figure 9 for these four configurations. The corresponding flow visualization photographs are presented in figures 10 through 13. Examination of the aerodynamic data indicates that for the 55° delta wing, maximum lift is generated at approximately an angle of attack of 25°. For the 65° delta wing, $C_{L_{max}}$ occurs at approximately 30°, and for both diamond wings, $C_{L_{max}}$ occurs at approximately 35°. This information will help interpret the flow visualization photographs.

The first set of photographs, presented in figure 10, is for the 55° delta wing at angles of attack of 10°, 20°, 25°, 35°, and 50°. Both top- and side-view photographs are presented for each of these angles of attack. The first photographs (in which $\alpha = 10°$) clearly show the location of the core of the primary vortices that are formed at the apex. Although the exact location of vortex bursting is not necessarily clear in these photographs, it is evident that vortex flow will have a significant effect on the majority of the configuration at this angle of attack. Also note that a colored dye shadow is present directly on the surface of the model. This shadow is easily seen on the mid to aft region of the model, and the phenomenon occurred on each configuration throughout the investigation. At an angle of attack of 20° (fig. 10(c)), vortex bursting occurs at a location that is approximately 20 percent of the reference length back from the apex. The side-view photograph indicates that the vortices are now slightly farther above the model surface than at an angle of attack of 10°, as would be expected. At an angle of attack of 25° (fig. 10(e)), the vortices appear to burst just after they are formed at the apex. This result supports the fact that the aerodynamic data indicate stall in the vicinity of an angle of attack of 25°. At angles of attack of 35° and 50° (figs. 10(g) through 10(j)), the flow visualization photographs indicate separated flow over the configuration. The dye present in these figures flows more directly aft in the streamwise direction and farther above the model surface than at an angle of attack of 25°, thus indicating a separated flow condition. This condition is expected because the aerodynamic data indicate that angles of attack of 35° and 50° are well beyond stall.

Flow visualization photographs for the 65° delta wing are presented in figure 11. Photographs were obtained at angles of attack of 10°, 20°, 30°, 35°, and 50°. In addition, photographs were obtained with the simulated balance housing removed to determine if the housing had any effect on the location of the primary vortices. In general, the photographs presented indicate that the vortices formed on the 65° delta wing extend farther aft before bursting than those formed on the 55° delta wing at all angles of attack. When the 65° delta wing is at an angle of attack of 10° (figs. 11(a) and 11(b)), vortex bursting does not occur until aft of the trailing edge. Vortex flow is present on the 65° delta wing at the angles of attack tested up to 35°. At this point, vortex bursting occurs relatively close to the apex, thus indicating a flow condition near stall. At an angle of attack of 50°, the flow visualization photographs indicate separated flow over the configuration. When comparing the photographs with and without the simulated balance housing, no identifiable effects were observed in terms of vortex location or vortex bursting. This observation holds true for all angles of attack tested. If an effect had occurred, it probably would have been seen at angles of attack of 10° or 20°, because the vortices are much closer to the simulated balance housing at those angles of attack than at the higher angles of attack.

Flow visualization photographs for the 30° diamond wing were obtained at angles of attack of 10°, 20°, 30°, 35°, and 50°, and they are presented in figure 12. For this configuration, colored dye was injected into the flow at

the apex of the forebody and at the junction of the forebody and the wing leading edge. At an angle of attack of 10° (fig. 12(a)), the forebody vortices extend completely down the forebody and onto the main wing. The vortices that are formed at the wing/body junction, which will be referred to as wing vortices, also extend over the majority of the wing, but they do not interact with the forebody vortices. The side-view photograph (fig. 12(c)) shows that the wing vortices lie farther above the model surface than the forebody vortices. This orientation is why the wing vortex wraps over and around the forebody vortex when the vortices interact at an angle of attack of 20° (fig. 12(d)). Although the wing vortex appears to be pulled around the forebody vortex at an angle of attack of 20°, the forebody vortex is pulled outboard because of the influence of the wing vortex. Thus, both vortices affect each other. At an angle of attack of 30° (fig. 12(g)), the bursting of the forebody vortices has moved upstream far enough so that the wing vortices can no longer interact with them. At an angle of attack of 35° (fig. 12(j)), which is approximately $C_{L_{max}}$, the forebody vortices burst at the end of the forebody. Not only does this prohibit any interaction with the wing vortices but also it may hinder their formation. Although the flow patterns indicated by the colored dyes at angles of attack of 30° and 35° could suggest the presence of wing vortices, note that the definite existence of these vortices is inconclusive. This statement generally holds true for all configurations that will be presented with a wing leading-edge sweep of 30°. At an angle of attack of 50° (fig. 12(m)), no wing vortices are present; however, the forebody vortices still extend halfway down the forebody before bursting occurs. The existence of the forebody vortices at this angle of attack causes a more gradual dropoff in lift beyond stall than existed for the delta-wing configurations. This forebody effect will generally be found on all configurations presented with a forebody of this type.

Flow visualization photographs were also obtained on the 30° diamond wing without the simulated balance housing. When the photographs with and without the simulated balance housing are compared at an angle of attack of 10° (figs. 12(a) and 12(b)), a difference in the flow patterns is noted. The simulated balance housing appears to delay vortex bursting for both the forebody and the wing vortices; however, its presence generally does not cause the spanwise location of the vortices to change. At an angle of attack of 20°, the configuration with the simulated balance housing appears to be producing a smoother, more uniform vortical flow pattern. It is uncertain why the simulated balance housing has this effect, but it could be related to the accelerated streamwise flow around the housing. Accelerated axial flow is known to stabilize the vortices and move downstream the vortex breakdown. Note that more dye was being injected into the forebody and wing vortices in figure 12(e) than in figure 12(d). The greater dye intensity on the configuration with the simulated balance housing removed (fig. 12(e)) could account for the vortical flow patterns not appearing to be as smooth and uniform as they are on the configuration with the simulated balance housing. Since it is difficult to set the dye injection rate at exactly the same value for each configuration, it is important that the flow fields not be misinterpreted because of variations in the amounts of dye injection. At an angle of attack of 30° and beyond, the simulated balance housing appears to have no effect on the vortical flows.

Flow visualization photographs for the 40° diamond wing are presented in figure 13. The photographs that indicate the flow conditions at an angle of attack of 10° show the forebody vortices rolling around the wing vortices. This effect is very different from the flow conditions noted on the 30° diamond wing. When the 30° diamond wing was at an angle of attack of 10° (fig. 12(a)), there was no interaction of the wing and forebody vortices. The higher wing sweep on the 40° diamond wing produces a wing vortex that is swept farther aft than on the 30° diamond wing. This wing sweep positions the wing and forebody vortices closer together, and therefore they interact. At an angle of attack of 20°, the flow pattern on the 40° diamond wing is very similar to that on the 30° diamond wing. At this angle of attack, the wing vortices wrap around the forebody vortices on both diamond wing configurations. The side-view photograph for the 40° diamond wing (fig. 13(e)) shows how the wing vortex goes up and around the forebody vortex. At an angle of attack of 30°, the forebody vortices on the 40° diamond wing burst in the vicinity of the junction of the forebody and the wing leading edge, which generally eliminates any interaction of the wing vortices with the forebody vortices.

Additional observations were made at an angle of attack of 30°, and as a result, additional photographs of these observations are presented. Although the model was held fixed at an angle of attack of 30° and a sideslip angle of 0°, the forebody vortices did not always burst in a symmetric fashion. This effect is clearly illustrated in figures 13(g) and 13(h). One vortex would burst at the wing/body junction, while the other vortex would burst downstream over the wing. The bursting locations would then move toward, pass one another, and end up in the longitudinal location where the other had been. Ultimately this process continues, and the fore and aft forebody vortex bursting locations proceed to swap back and forth. This phenomenon has been observed by other researchers, and it is described in detail in reference 20. The effect was also observed at an angle of attack of 35°,

even though only a slightly asymmetric pattern is shown in the photograph. Note further that the wing vortices are also present in an asymmetric fashion (figs. 13(g), 13(h), and 13(j)). This effect is most evident in figure 13(g) where the vortex on the right wing is more coherent than the vortex on the left wing. The asymmetric bursting of the forebody vortices is probably directly producing the asymmetries present in the wing vortices. At an angle of attack of 50° (fig. 13(k)), the forebody vortices are still present, and the bursting is still occurring in an asymmetric fashion.

The effects of the simulated balance housing were also investigated on the 40° diamond wing, and photographs are presented with the housing removed for angles of attack of 10°, 20°, and 30° (figs. 13(b), 13(d), and 13(i)). These photographs indicate that the simulated balance housing had little influence on the wing or forebody vortices.

The overall results of the delta-wing and diamond wing investigations indicate that the flow fields are dominated by strong vortical flows. Strong vortices that form off the forebody can interact with wing vortices, depending on angle of attack and wing leading-edge sweep. Asymmetric forebody vortex bursting occurred on both diamond wing configurations even though photographs of this effect were only presented for the 40° diamond wing configuration. These asymmetric vortical flows could produce control problems; therefore, their location and behavior are significant. The forebody vortices exist for angles of attack up to at least 50° on the diamond wing configurations, and thus they explain the reduced poststall lift loss for these configurations compared with the delta planforms. The simulated balance housing generally did not affect the vortical flows on any of the configurations except the 30° diamond wing. On this configuration, the shape of the vortices as well as the vortex burst location were influenced by the simulated balance housing only for angles of attack up to 20°.

Twin Bodies and Double Wings

Because twin bodies and double wings produced additional vortices in the flow fields, these configurations were of significant interest in this investigation. Two additional 30° diamond wing configurations were tested; one had twin bodies and one had twin wings. An additional double-wing configuration, referred to as the 60° double arrow, was also tested. Lift coefficient versus angle-of-attack data are presented in figure 14 for these configurations, and flow visualization photographs are presented in figures 15 to 17. The wind tunnel data indicate improvements in lift caused by the twin bodies and double wings when compared with the original 30° diamond wing configuration.

The flow visualization photographs for the 30° diamond wing with twin-body configuration indicate vortical flows on each forebody and wing at an angle of attack of 10° (fig. 15(a)). The wing vortex wraps up and around the outboard forebody vortex. This effect is unlike that of the 30° diamond wing where the wing and forebody vortices stay independent at an angle of attack of 10° (fig. 12(a)). Evidence is also present (figs. 15(a) and 15(b)) which indicates that the inboard vortices from each forebody flow directly into the simulated balance housing. This is evident in both the top- and side-view photographs. No testing was conducted with the simulated balance housing removed; therefore, no direct comparisons can be made. At an angle of attack of 20°, the vortical flows are still similar to the case in which the angle of attack equals 10°; however, now the outboard forebody vortices are bursting near the wing trailing edge. In addition, the side-view photograph (fig. 15(d)) indicates that the inboard forebody vortices are now much higher above the model surface than the outboard forebody vortices. This may be due to the simulated balance housing.

When angle of attack is increased to 35°, the forebody vortices burst either on the forebody or near the back of the forebody, and no wing vortices appear to be present. Asymmetric forebody bursting is now seen on each forebody, and the vortices are observed to burst anywhere from halfway down the forebody to just in front of the simulated balance housing. Typically the outboard vortices tend to burst farther upstream than the inboard vortices; however, longitudinal movement of all forebody vortex bursting does take place over time.

Two flow visualization photographs are presented at an angle of attack of 35° to identify the presence of the two classic types of vortex bursting. These two types of vortex bursting, as defined and described in reference 21, are referred to as bubble-type and spiral-type bursting. The first photograph presented for the twin-body configuration at an angle of attack of 35° (fig. 15(e)) has bubble-type vortex bursting on the outboard vortices of each forebody. In the following photograph (fig. 15(f)), a classic example of spiral-type vortex bursting is noted on the outboard side of the left-hand forebody. The inboard forebody vortices (shown in both photographs) generally burst in a manner that is a combination of the two types. Throughout the investigation, forebody vortex bursting would slowly oscillate between these two types on every configuration with this 80° swept forebody.

At an angle of attack of 50°, forebody vortices are still present; however, now vortex bursting occurs when the vortices are approximately one-third of the way down the forebody. These vortices stay relatively close to the

forebody until bursting occurs, as noted in the side-view photograph (fig. 15(i)).

The presence of four forebody vortices on the twin-body configuration at angles of attack up to 50° will generate more lift than that generated by the single set of vortices on the 30° diamond wing with only one forebody. This would explain why the twin-body configuration generates a greater lift coefficient than the 30° diamond wing configuration at all angles of attack greater than 20°.

Flow visualization photographs for the 30° diamond twin wing are presented in figure 16. Dye injection tubes were again located at the forebody apex as well as at the inboard leading edge of both wings. In addition, dye injection tubes were also placed at the wing tips of the forward wing.

When examining the flow visualization photographs obtained at an angle of attack of 10° (fig. 16(a)), strong forebody vortices extend down the configuration, with bursting not taking place until aft of the trailing edge of the forward wing. The forward wing vortex wraps up and around the forebody vortices, while the aft wing vortex stays independent. The dye injection tube located at the inboard leading edge of the aft left wing was not placed in the appropriate location for the dye to get caught in the wing vortex; therefore, this dye does not show any significant flow characteristics at any of the angles of attack presented. At an angle of attack of 20° (fig. 16(b)), the flow patterns are similar to those noted at an angle of attack of 10°; however, now the forebody vortices are bursting at the trailing edge of the forward wing. At an angle of attack of 35° (fig. 16(c)), the forebody vortices are bursting just aft of the forward wing leading edge, thus hindering the formation of the vortices on the forward wing, or forward wing vortices may not be present at this angle of attack. The aft wing vortices, however, are still present, probably because of the reduced incidence as a result of the forward wing downwash. The presence of these vortices indicates that the aft wing is still producing considerable lift, and thus explains the greater $C_{L_{max}}$ produced by the 30° diamond twin wing compared with the 30° diamond wing. At an angle of attack of 50°, only the forebody vortices still exist, with bursting occurring approximately halfway down the forebody. The dye injected at the tips of the forward wing did not reveal any significant flow characteristics at any angle of attack.

A second double-wing configuration, referred to as the 60° double arrow, was tested, and flow visualization photographs for this configuration are presented in figure 17. Colored dye was injected in the usual forebody apex and forward wing inboard leading-edge locations. In addition, colored dye was injected at the wing tips and at the inboard trailing edge of the forward wing.

At angles of attack of 10° and 20°, strong forebody vortices extend over the length of the configuration. In both cases, the forward wing vortices roll over and around the forebody vortices, and this combined vortex pair flows over the aft, inboard portion of the space between the two wings. In addition, an upward flow exists in the space between the two wings. This upward flow is most easily noted in the side-view photograph presented for an angle of attack of 20° (fig. 17(f)). In this photograph, the forebody vortex cores move abruptly away from the upper surface of the model as they flow aft over the space between the two wings. At an angle of attack of 35° (fig. 17(g)), the forebody vortices burst at a location approximately halfway between the leading and trailing edges of the forward wing, thus hindering the formation of the wing vortices as the colored dye from this location rolls around the bursting forebody vortices. At an angle of attack of 50°, once again only the forebody vortices exist. The photographs that show the configuration with the simulated balance housing removed indicate that the housing had essentially no effect on the vortical flows across the angle-of-attack range presented.

The results of the twin-body and double-wing portion of the investigation indicate that the vortices that form on the twin forebodies and double wings would add additional lift when compared with the single component, 30° diamond wing configuration. The existence of wing vortices on the aft wing of the 30° diamond twin-wing configuration is probably enhanced because of the aft wing being in the downwash from the forward wing. This downwash effectively reduces the local angle of attack of the aft wing, thereby allowing it to maintain its lift-generating ability to a higher overall model angle of attack. The simulated balance housing interfered with the inboard forebody vortices on the 30° diamond wing with twin-body configuration for angles of attack up to 20°. No simulated balance housing effects were found, however, for the double-wing configurations.

Cutout Wings

The effects of wing cutouts were another area of interest in which flow visualization was expected to provide valuable insight into understanding the flow physics. Lift coefficient versus angle-of-attack data are presented in figure 18 for the original 30° diamond wing configuration as well as for two cutout-wing configurations. The cutout-wing configurations consist of a planform with a triangular cutout shape and one with a diamond cutout shape. Both these cutout shapes are equal in area so that the effects of cutout shape alone could be examined. The aerodynamic data presented

indicate that lift increases across the angle-of-attack range for both cutout configurations over the original 30° diamond wing; however, the diamond cutout shape is the most effective.

Flow visualization photographs have been obtained for the 30° diamond with triangular cutout configuration with and without the simulated balance housing, and they are presented in figure 19. Colored dye was injected at the usual forebody apex and inboard wing leading-edge locations in addition to the forward inboard corner and outboard corner of the cutout. At an angle of attack of 10°, forebody vortices extend the length of the configuration, while they always maintain a position inboard of the wing cutouts. The wing vortices extend across the forward portion of the wing; however, bursting occurs as they cross over the outboard portion of the cutout region. When compared with the 30° diamond wing at an angle of attack of 10° (fig. 12(a)), differences in the flow patterns caused by the wing cutout are noted. The cutout appears to cause the wing vortices to burst sooner, and it also causes the forebody vortices to sit farther inboard over the wing portion of the configuration.

At an angle of attack of 20° (fig. 19(c)), the wing and forebody vortices now progress farther outboard over the wing portion of the configuration, as compared with the conditions noted at an angle of attack of 10°. The wing vortices no longer flow into the cutout region; however, now the forebody vortices do flow over the aft inboard portion of the cutout region. This phenomenon is very different from how the wing and forebody vortices roll together on the original 30° diamond wing configuration (fig. 12(d)).

At an angle of attack of 30° (fig. 19(e)), the forebody vortices now burst in the region between the wing leading edge and the cutout, thus tending to disrupt the wing vortices similar to the effect that occurred on the noncutout configuration. At an angle of attack of 35°, the wing and forebody vortices behave similar to the way they behaved on the original 30° diamond wing. The forebody vortex bursting at the intersection of the forebody with the wing leading edge appears to drive the wing vortex outboard, and the two vortices have no further interaction. As mentioned previously for the 30° diamond wing, at angles of attack of 30° and 35°, wing vortices could be present, but their actual existence is inconclusive. At an angle of attack of 50°, the flow pattern is again similar to that on the original 30° diamond wing.

The photographs obtained with the simulated balance housing removed indicate that the housing may or may not interfere with the vortical flows, depending on angle of attack. When the angle of attack is 10° or 30°, no obvious effects caused by the balance housing are indicated. However, at an angle of attack of 20°, the simulated balance housing appears to affect the vortical flows (figs. 19(c) and 19(d)). When the simulated balance housing is on the configuration at this angle of attack, the wing vortices flow outboard and away from the forebody vortices. However, when the simulated balance housing is removed, the wing vortices flow aft and interact with the forebody vortices. This phenomenon also tends to draw the forebody vortices farther inboard.

The colored dye that was injected in the inboard and outboard regions of the cutout did not reveal any additional significant flow characteristics at any of the angles of attack presented.

Flow visualization photographs for the 30° diamond with diamond cutout configuration are presented in figure 20. Colored dye was injected in the same forebody and wing locations as before; however, in the cutout region, dye was injected at the most inboard and most aft locations.

The photograph that shows the flow conditions at an angle of attack of 10° (fig. 20(a)) indicates similar trends to those noted for the 30° diamond with triangular cutout. The forebody vortices extend the length of the configuration while they maintain a position inboard of the wing cutouts. The forebody vortices move progressively outboard as they flow downstream over the configuration; however, the cutout acts to redirect the vortices so that they stay inboard of the cutout region rather than flow over it. Once again the cutout region appears to cause the wing vortices to burst sooner than they did on the original 30° diamond wing.

At an angle of attack of 20° (fig. 20(b)), the wing vortices wrap over and around the forebody vortices similar to the way that was noted on the 30° diamond wing configuration. A new flow condition, however, is also noted. The dye that is injected at the inboard corner of the cutouts reveals the existence of a vortex that flows aft and outboard over the remainder of the wing.

At angles of attack of 30° and 35°, the forebody vortices burst near the junction of the wing leading edge and the forebody, thus hindering the development of the wing vortices and also preventing the wing vortices from rolling around the forebody vortices. As before, this condition assumes that wing vortices are present at these conditions. The vortices that form at the inboard corner of the wing cutouts are still present. These cutout vortices are probably the reason why the 30° diamond with diamond cutout configuration produces a greater $C_{L_{max}}$ than the triangular cutout-wing configuration. The cutout vortices produce a smoother, more well-behaved flow on the aft inboard portion of the wing than would be present without the vortices. Thus it appears that when the aft

edge of the cutout is swept in the same direction as the wing leading-edge, vortices from the cutout are formed.

Once again the forebody vortices are still present at an angle of attack of 50° (fig. 20(e)), and the bursting occurs approximately halfway down the forebody.

The results of the cutout-wing portion of the investigation indicate that wing cutouts can significantly alter the vortex structure over the configuration. Forebody vortices will tend to be shifted inboard because of the wing cutout, while wing vortices may burst prematurely when interacting with the cutout region. The diamond-shaped cutout will generate an additional vortex aft on the wing; this vortex is not generated by the triangular-shaped cutout. The additional vortex produces a more favorable flow condition on the aft, inboard portion of the 30° diamond with diamond cutout configuration, and thus explains why this configuration generates a greater $C_{L_{max}}$.

Serrated Forebodies

The final phase of the investigation was focused on illustrating the effects of serrated forebodies. Lift coefficient versus angle-of-attack data are presented for the serrated-forebody configurations in figure 21. Data for the original configurations, which were modified to produce the serrated-forebody configurations, are also presented for comparison purposes. Aerodynamic data, however, were not obtained for the 40° diamond with 3 diamond sawteeth and nose tip configuration.

The 65° delta with delta sawteeth configuration was generated by adding a 65° swept serrated forebody to the 65° delta wing. Dye was injected at the apex of the configuration and at the inboard corner of each of the three serrations. Flow visualization photographs, which are presented in figure 22, were obtained both with and without the simulated balance housing.

The first set of photographs presented are for the configuration at an angle of attack of 12°. Photographs were taken at this angle of attack, as opposed to 10°, because an angle of attack of 10° was not high enough for a vortex to form off each serration. This in turn resulted in poor flow visualization. At an angle of attack of 12°, however, a vortex does form at each serration, and as shown in the photograph, all the vortices on each side of the configuration tend to wrap around one another.

At an angle of attack of 20° (fig. 22(c)), the cores of the apex vortices are shown to extend the entire length of the configuration, and the vortices from the other serrations appear to roll right into the apex vortices. At an angle of attack of 30°, the same trend continues with all the vortices rolling into one; however, now vortex bursting begins to occur before the trailing edge of the configuration.

At an angle of attack of 50° (fig. 22(h)), vortices still appear to form at each serration. The apex vortices are clearly present; however, they now burst before they reach the end of the first serration. Vortex development is now more difficult to identify on the downstream serrations.

When the photographs with and without the simulated balance housing are compared, no evidence is indicated that the simulated balance housing affects the vortex structure or location at any of the angles of attack presented.

Photographs for the 40° diamond with 3 diamond sawteeth configuration are presented in figure 23. Dye was injected at the apex and the inboard corner of each of the three sawteeth, just as it was for the 65° delta with delta sawteeth configuration. The photographs, which illustrate the flow conditions at an angle of attack of 10°, indicate that vortices are beginning to form on the second and third sets of sawteeth and on the main wing. At this angle of attack, however, the vortices on the sawteeth are not well defined. Also at this angle of attack, the dye injected at the apex was flowing under but not over the configuration so that no flow over the first set of sawteeth was visualized.

At an angle of attack of 20° (fig. 23(b)), separated flow is indicated by the dye injected at the apex over the first set of sawteeth, while vortices are indicated on the second and third sets of sawteeth and on the main wing. Each of these vortices appears to stay independent as it flows downstream over the configuration.

The vortices on the second and third sets of sawteeth and on the main wing appear stronger and more well defined at angles of attack of 30° and 35° than they did at an angle of attack of 20°. Once again these vortices stay independent as they flow over the model. (See figs. 23(c) through 23(e).) This independence is clearly a different vortex flow behavior than the way all the vortices roll together on the 65° delta with delta sawteeth configuration. The independent nature of the vortices from the diamond sawtooth forebody appears to affect a significant region of the flow over the main wing, thus probably preventing flow separation on the aft part of the configuration and accounting for the significant lift increases noted in the data presented in figure 21. In addition, the wing vortices on the diamond sawtooth configuration are much more well defined than those on the 40° diamond wing configuration. (See figs. 13(f) through 13(j).) This better vortex definition may be caused by the absence of the forebody vortices bursting in close proximity to the wing vortices as is the case for the 40°

diamond wing configuration. It may also be due to a lower effective wing incidence caused by the downwash field from the upstream vortices generated by the sawteeth.

At an angle of attack of 35° (fig. 23(e)), note that the wing vortices are asymmetric. It appears that the vortex on the right wing has begun to lift off the surface, but the vortex on the left wing has not, which suggests that at an angle of attack of 35°, the wing vortex breakdown is beginning to occur.

At an angle of attack of 50° (fig. 23(f)), the flow is still separated over the first set of sawteeth; however, vortices do still exist over the second and third sets of sawteeth and the main wing. The presence of these vortices continues to produce lift improvements when compared with the 40° diamond wing configuration, as illustrated by the data of figure 21.

The 40° diamond with 3 diamond sawteeth configuration has effectively generated multiple vortices that have improved the lift characteristics by significantly increasing $C_{L_{max}}$. The first set of sawteeth, however, was not effective across the angle-of-attack range. Therefore, to improve the effectiveness, a nose tip was added to the 40° diamond with 3 diamond sawteeth configuration (as illustrated in fig. 8(c)), and a final set of flow visualization photographs was obtained. These photographs are presented in figure 24.

At an angle of attack of 10°, vortices are visible on the nose tip and the main wing; however, as before, the vortices on the sawteeth are not well defined. At an angle of attack of 20°, the vortices on the second and third sets of sawteeth become more defined, but the bursting of the nose tip vortices may affect the formation of the vortices on the second set of sawteeth.

At angles of attack of 30° and 35° (figs. 24(c) through 24(e)), all the vortices are well defined and exist independently. The nose tip vortices now burst before they can interfere with the formation of the vortices on the second set of sawteeth. The location of the nose tip vortices certainly suggests that they would improve the flow condition over the first set of sawteeth as compared with the configuration with no nose tip.

Although the nose tip vortices burst before they reach the second set of sawteeth at angles of attack of 30° and 35°, the nose tip vortices still affect the vortices on the second set of sawteeth. This effect is clear when the photographs with and without the nose tip are compared at these angles of attack. The vortices on the second set of sawteeth are located farther inboard on the configuration with the nose tip than they are on the configuration without the nose tip. The vortices on the third set of sawteeth are located in the same position on the configuration whether the nose tip is on or not.

Finally at an angle of attack of 50° (fig. 24(f)), all the vortices are still present and exist independently on the configuration with the nose tip. Since the nose tip vortices are still present, it is implied that this configuration would have better lift characteristics at this angle of attack than the configuration without the nose tip.

The results of the serrated-forebody portion of the investigation indicate that multiple vortices can be generated on a configuration by a serrated forebody. The vortices generated by the 65° delta sawtooth forebody tend to roll together as they flow over the configuration, whereas the vortices generated by the diamond sawtooth forebody tend to stay more independent. The more independent nature of the diamond sawtooth vortices is probably the cause for the significant lift improvement that is generated when the diamond sawtooth forebody is added to the 40° diamond wing configuration. The addition of a nose tip to the diamond sawtooth forebody eliminates the separated flow condition that would otherwise exist on the first set of diamond sawteeth and thus further improves the flow characteristics over the 40° diamond with 3 diamond sawteeth configuration.

Summary of Results

The results of a flow visualization investigation of 12 different planforms tested in the Langley 16- by 24-Inch Water Tunnel are summarized as follows:

1. As expected, the formation of strong vortices on highly swept forebodies will improve poststall lift characteristics. The asymmetric bursting of these vortices, however, could produce substantial control problems.

2. On the configurations where the effects of the balance housing were investigated, it was found that the simulated balance housing did affect the vortex structure on the 30° diamond wing, the 30° diamond wing with twin body, and the 30° diamond with triangular cutout. These effects, however, were only noted at angles of attack of 20° and below.

3. The vortices that form on the additional forebody and the wings of the twin-body and double-wing configurations would account for the lift increases noted when these configurations are compared with the single-component configuration.

4. For the cutout-wing configurations investigated, it was found that a wing cutout can significantly alter the vortex structure over a configuration. Specifically, forebody vortices are shifted inboard in the vicinity of a wing cutout. The formation of a vortex over the

inboard portion of the wing aft of a diamond-shaped cutout explains why this cutout shape generates a greater maximum lift than a triangular-shaped cutout.

5. Serrated forebodies will effectively generate multiple vortices over a configuration. Vortices from a 65° delta sawtooth forebody will roll together, while vortices from a 40° swept diamond sawtooth forebody will stay more independent. The addition of a highly swept nose tip to a 40° swept diamond sawtooth forebody will improve flow conditions by producing vortical flows over the first set of sawteeth, which would otherwise generate a separated flow.

NASA Langley Research Center
Hampton, VA 23681-0001
August 21, 1995

References

1. Chambers, Joseph R.: High-Angle-of-Attack Technology—Progress and Challenges. *High-Angle-of-Attack Technology,* Volume I, Joseph R. Chambers, William P. Gilbert, and Luat T. Nguyen, eds., NASA CP-3149, Part 1, 1992, pp. 1–22.

2. Murri, Daniel G.; Biedron, Robert T.; Erickson, Gary E.; Jordan, Frank L., Jr.; and Hoffler, Keith D.: Development of Actuated Forebody Strake Controls for the F-18 High Alpha Research Vehicle. *High-Angle-of-Attack Technology,* Volume I, Joseph R. Chambers, William P. Gilbert, and Luat T. Nguyen, eds., NASA CP-3149, Part 1, 1992, pp. 335–380.

3. Erickson, Gary E.; and Murri, Daniel G.: Forebody Strakes for High-Angle-of-Attack Vortex Flow Control: Mach Number and Strakes Planform Effects. *High-Angle-of-Attack Technology,* Volume I, Joseph R. Chambers, William P. Gilbert, and Luat T. Nguyen, eds., NASA CP-3149, Part 1, 1992, pp. 381–480.

4. Murri, Daniel G.; and Rao, Dhanvada M.: Exploratory Studies of Actuated Forebody Strakes for Yaw Control at High Angles of Attack. AIAA-87-2557, Aug. 1987.

5. Malcolm, Gerald N.; Ng, T. Terry; Lewis, Liane C.; and Murri, Daniel G.: Development of Non-Conventional Control Methods for High Angle of Attack Flight Using Vortex Manipulation. *Technical Papers—7th AIAA Applied Aerodynamics Conference,* 1989, pp. 249–267. (Available as AIAA-89-2192.)

6. Ng, T. Terry; and Malcolm, Gerald N.: Aerodynamic Control Using Forebody Vortex Control. *High-Angle-of-Attack Technology,* Volume I, Joseph R. Chambers, William P. Gilbert, and Luat T. Nguyen, eds., NASA CP-3149, Part 1, 1992, pp. 507–531.

7. Ng, T. Terry; and Malcolm, Gerald N.: Aerodynamic Control Using Forebody Blowing and Suction. AIAA-91-0619, Jan. 1991.

8. White, E. Richard: Effects of Suction on High-Angle-of-Attack Directional Control Characteristics of Isolated Forebodies. *High-Angle-of-Attack Technology,* Volume I, Joseph R. Chambers, William P. Gilbert, and Luat T. Nguyen, eds., NASA CP-3149, Part 1, 1992, pp. 533–556.

9. Schreiner, John A.; Erickson, Gary E.; and Guyton, Robert W.: Application of Tangential Sheet Blowing on the Forebody of an F-18-Like Configuration for High-Angle-of-Attack Maneuverability. *High-Angle-of-Attack Technology,* Volume II, Joseph R. Chambers, William P. Gilbert, and Luat T. Nguyen, eds., NASA CP-3150, 1992, pp. 1–25.

10. Roberts, Leonard; Tavella, Domingo A.; and Celik, Zeki: Controlled Vortex Flows Over Forebodies and Wings. *High-Angle-of-Attack Technology,* Volume I, Joseph R. Chambers, William P. Gilbert, and Luat T. Nguyen, eds., NASA CP-3149, Part 2, 1992, pp. 659–671.

11. Bauer, Steven X. S.; and Hemsch, Michael J.: Alleviation of Side Force on Tangent-Ogive Forebodies Using Passive Porosity. AIAA-92-2711, June 1992.

12. Wood, Richard M.; Banks, Daniel W.; and Bauer, Steven X. S.: Assessment of Passive Porosity With Free and Fixed Separation on a Tangent Ogive Forebody. AIAA-92-4494, Aug. 1992.

13. Modi, V. J.; and Stewart, A. C.: Approach to Side Force Alleviation Through Modification of the Pointed Forebody Geometry. *Technical Papers—AIAA Atmospheric Flight Mechanics Conference,* 1990, pp. 349–358. (Available as AIAA-90-2834.)

14. Gatlin, Gregory M.; and McGrath, Brian E.: *Low-Speed Longitudinal Aerodynamic Characteristics Through Poststall for Twenty-One Novel Planform Shapes.* NASA TP-3503, 1995.

15. Gloss, B. B.: *Effect of Wing Planform and Canard Location and Geometry on the Longitudinal Aerodynamic Characteristics of a Close-Coupled Canard Wing Model at Subsonic Speeds.* NASA TN D-7910, 1975.

16. Yip, L. P.; and Paulson, John W., Jr.: *Effects of Deflected Thrust on the Longitudinal Aerodynamic Characteristics of a Close-Coupled Wing-Canard Configuration.* NASA TP-1090, 1977.

17. Paulson, John W., Jr.; and Thomas, James L.: *Summary of Low-Speed Longitudinal Aerodynamics of Two Powered Close-Coupled Wing-Canard Fighter Configurations.* NASA TP-1535, 1979.

18. Erickson, G. E.: Vortex Flow Correlation. AFWAL-TR-80-3143, U.S. Air Force, Jan. 1981. (Available from DTIC as AD A108 725.)

19. Pendergraft, Odis C., Jr.; Neuhart, Dan H.; and Kariya, Timmy T.: *A User's Guide to the Langley 16- by 24-Inch Water Tunnel.* NASA TM-104200, 1992.

20. Ayoub, A.; and McLachlan, B. G.: Slender Delta Wing at High Angles of Attack—A Flow Visualization Study. AIAA-87-1230, June 1987.

21. Payne, F. M.; and Nelson, R. C.: An Experimental Investigation of Vortex Breakdown on a Delta Wing. *Vortex Flow Aerodynamics,* Volume 1, J. F. Campbell, R. F. Osborn, and J. T. Foughner, Jr., eds., NASA CP-2416, 1986, pp. 135–161.

Table I. Geometric Characteristics of Planform Models

	Planform description	Reference area S, ft^2	Reference length c, in.	Reference span b, in.
1	55° delta wing	0.3236	8.16	11.42
2	65° delta wing	0.3236	10.00	9.32
3	30° diamond wing	0.3140	11.90	11.80
4	40° diamond wing	0.3565	13.67	10.52
5	30° diamond wing with twin body	0.3421	11.33	11.80
6	30° diamond twin wing	0.2942	12.89	8.34
7	60° double arrow	0.3067	14.96	7.36
8	30° diamond with triangular cutout	0.2909	11.90	11.80
9	30° diamond with diamond cutout	0.2909	11.90	11.80
10	65° delta with delta sawteeth	0.3696	13.56	9.32
11	40° diamond with 3 diamond sawteeth	0.3998	13.67	10.52
12	40° diamond with 3 diamond sawteeth and nose tip	0.4012	14.67	10.52

Table II. Presentation of Results

	Planform description	Figure in which lift coefficient data are presented	Figure in which flow visualization is presented
1	55° delta wing	9	10
2	65° delta wing	9, 21	11
3	30° diamond wing	9, 14, 18	12
4	40° diamond wing	9, 21	13
5	30° diamond wing with twin body	14	15
6	30° diamond twin wing	14	16
7	60° double arrow	14	17
8	30° diamond with triangular cutout	18	19
9	30° diamond with diamond cutout	18	20
10	65° delta with delta sawteeth	21	22
11	40° diamond with 3 diamond sawteeth	21	23
12	40° diamond with 3 diamond sawteeth and nose tip	Not obtained	24

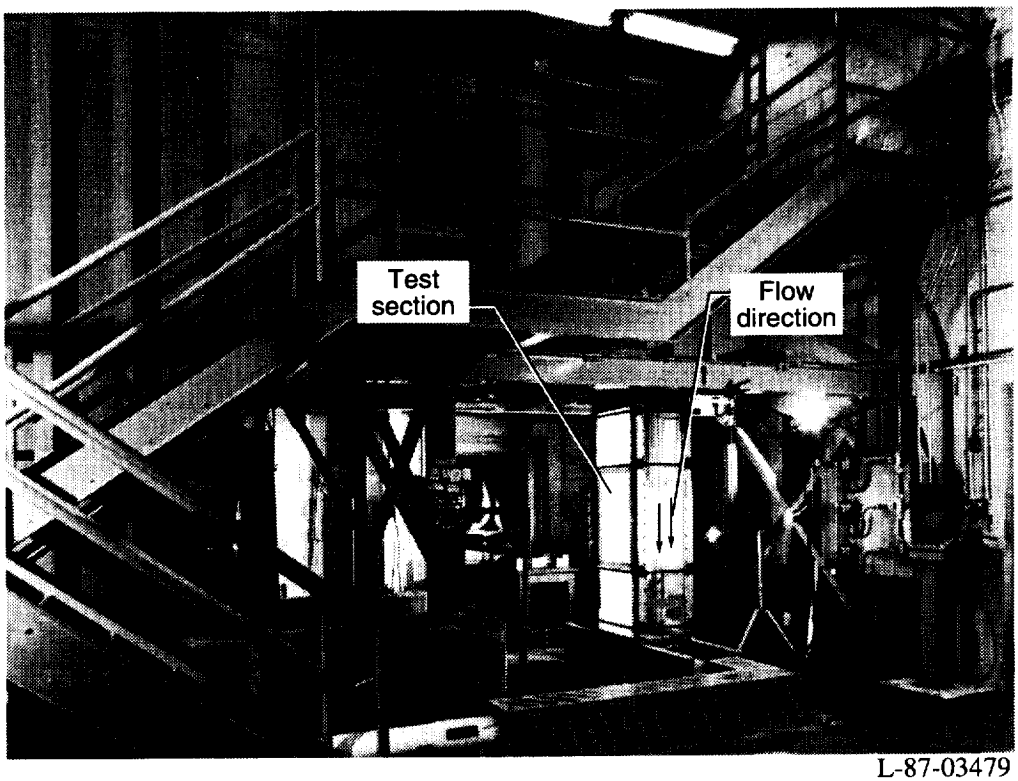

L-87-03479

Figure 1. Langley 16- by 24-Inch Water Tunnel.

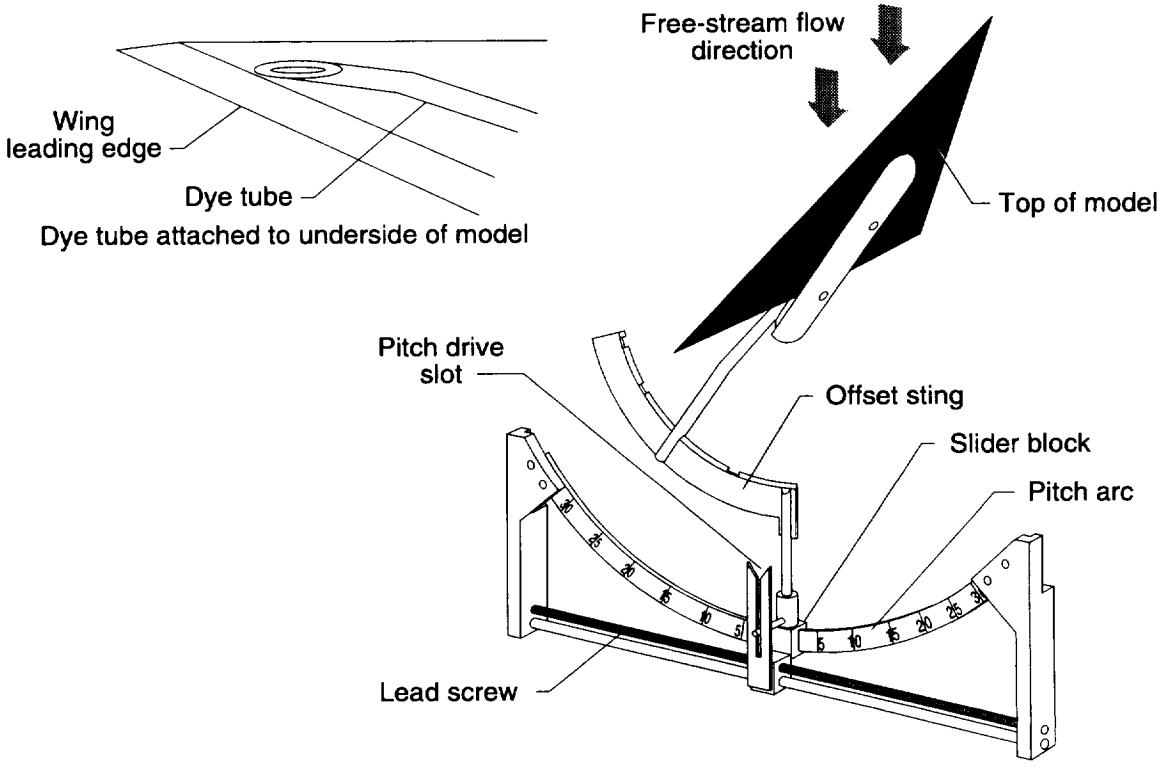

Figure 2. Offset model support system used in Langley 16- by 24-Inch Water Tunnel.

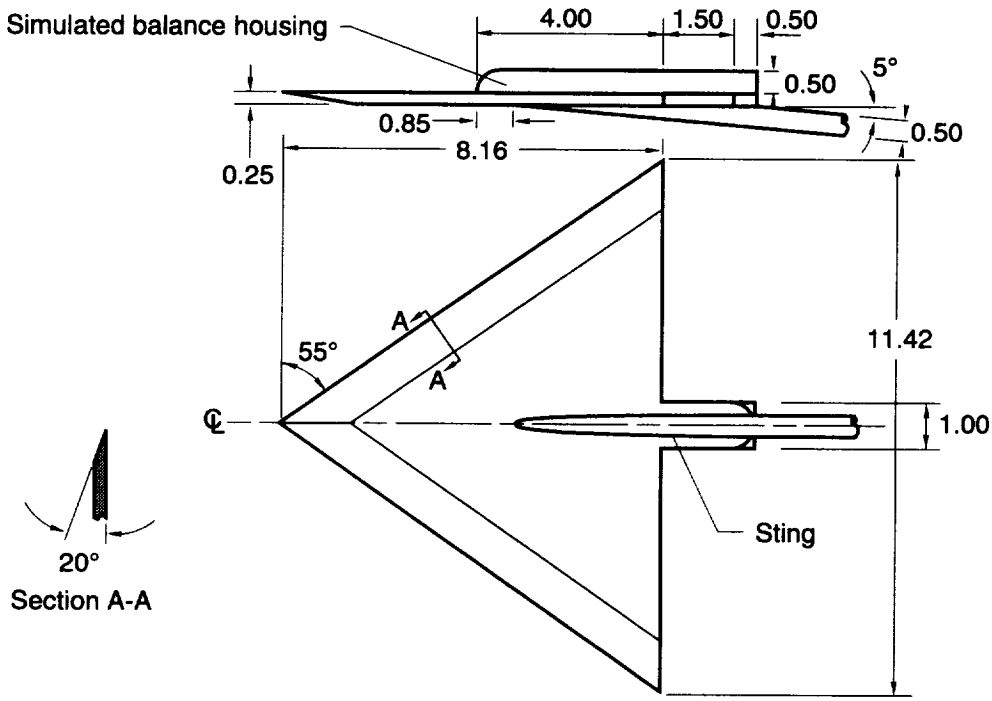

(a) 55° delta wing.

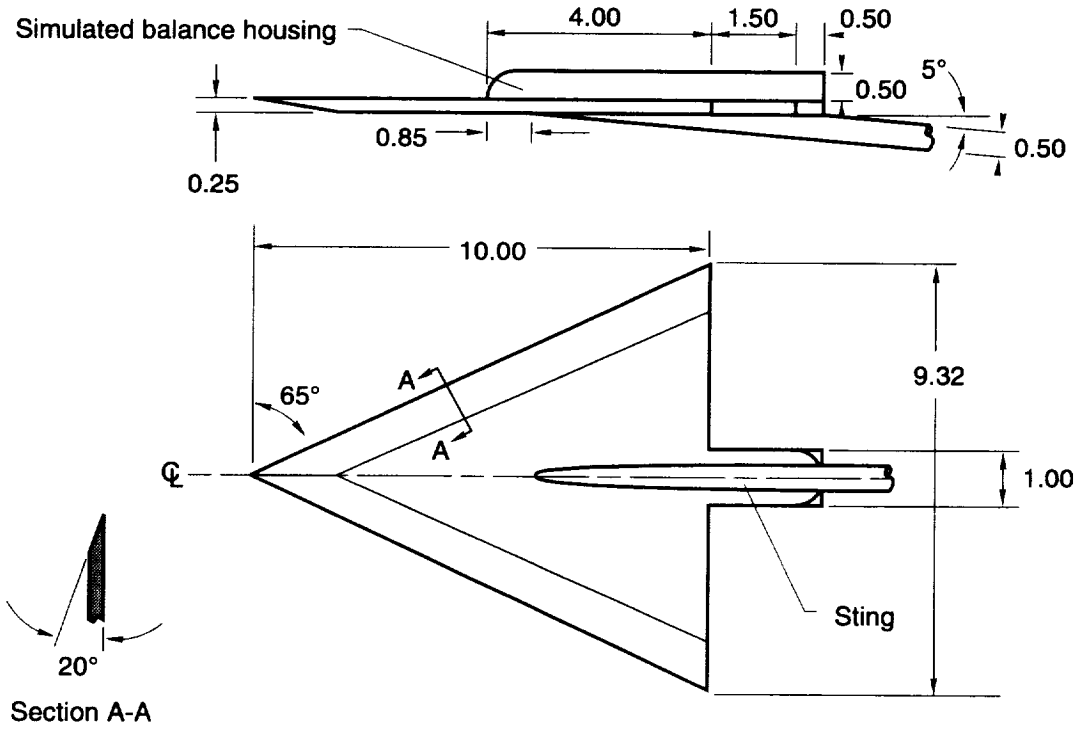

(b) 65° delta wing.

Figure 3. Side- and bottom-view sketches of delta-wing configurations. All linear dimensions are given in inches.

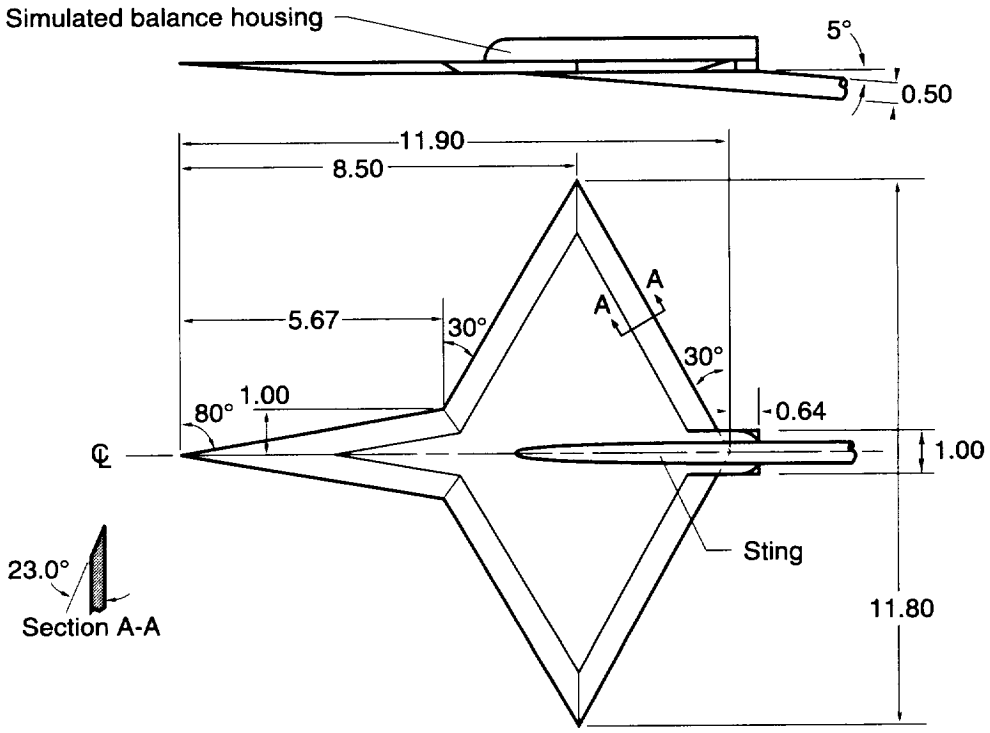

(a) 30° diamond wing.

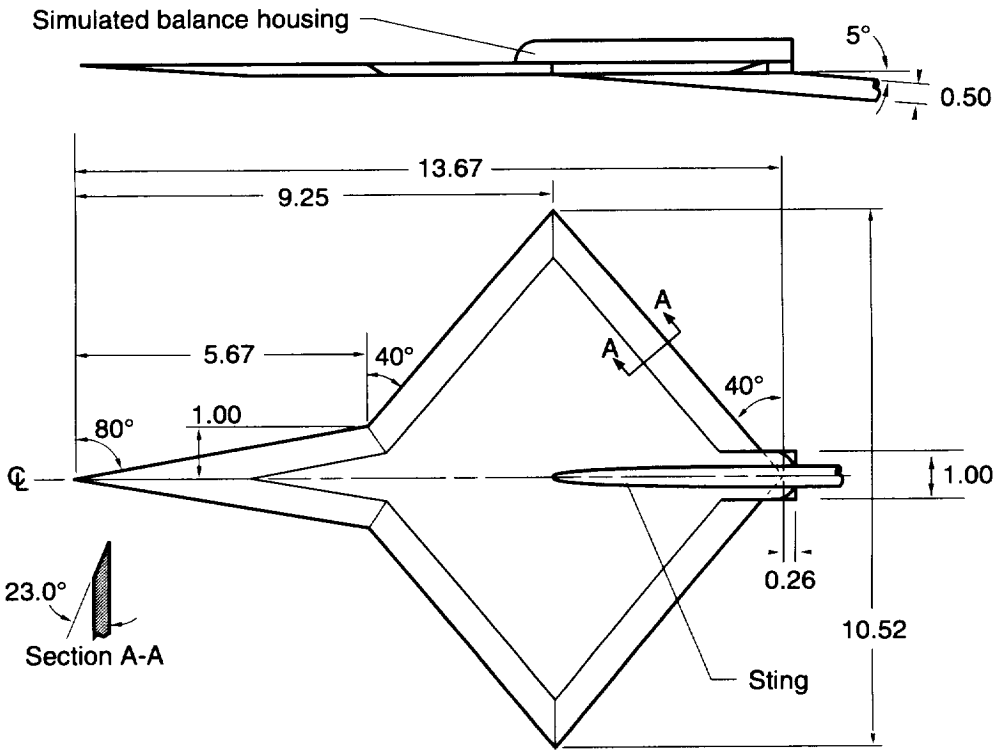

(b) 40° diamond wing.

Figure 4. Side- and bottom-view sketches of diamond-wing configurations. All linear dimensions are given in inches.

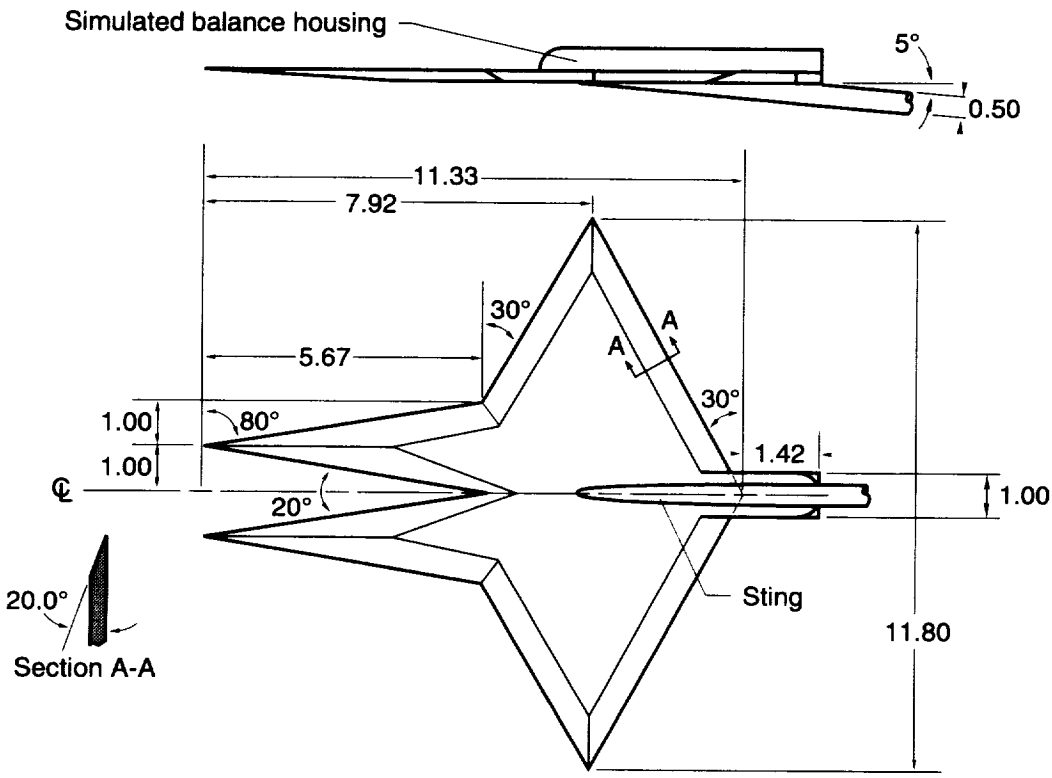

Figure 5. Side- and bottom-view sketches of 30° diamond wing with twin-body configuration. All linear dimensions are given in inches.

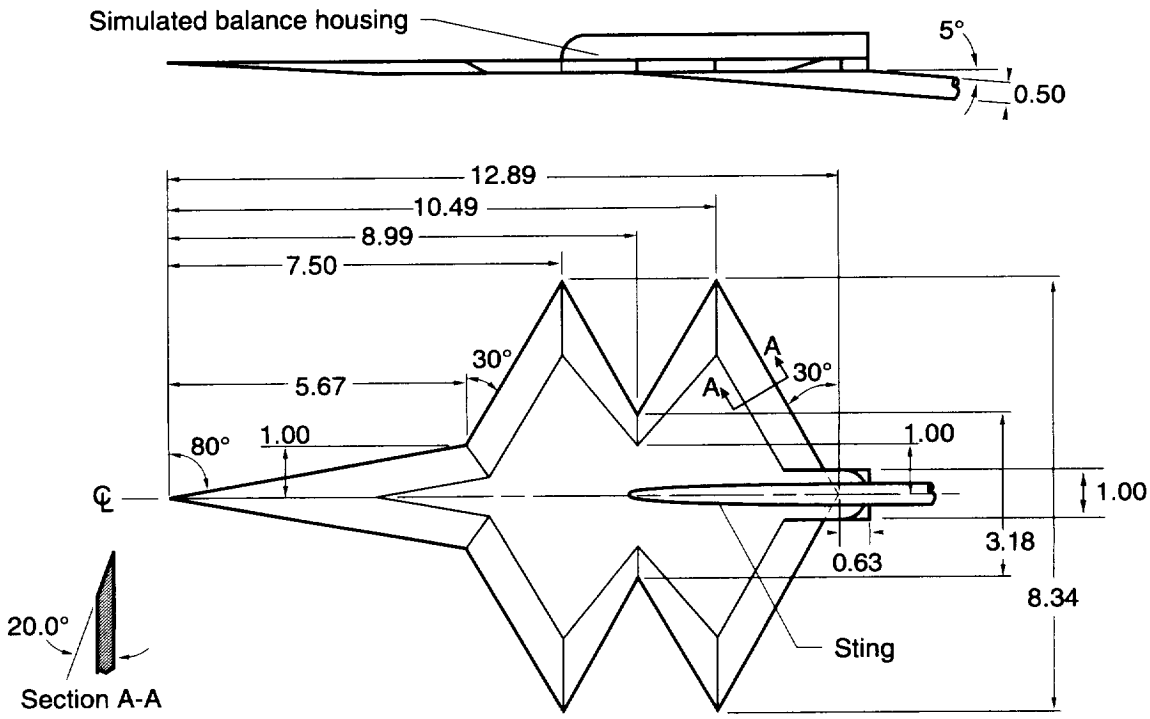

(a) 30° diamond twin wing.

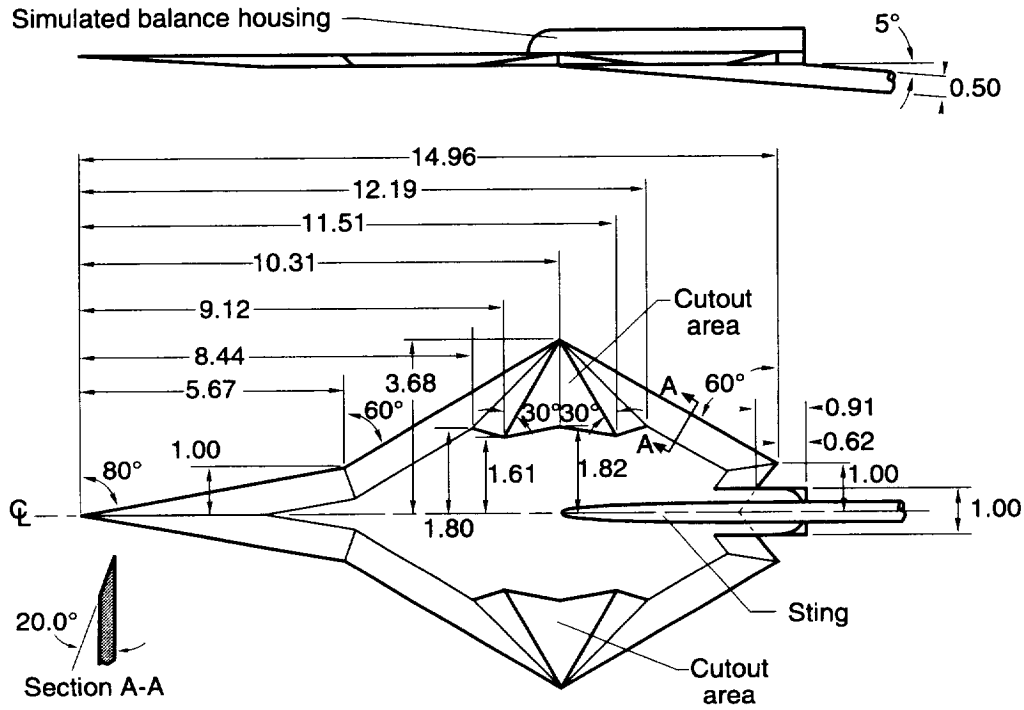

(b) 60° double arrow.

Figure 6. Side- and bottom-view sketches of double-wing configurations. All linear dimensions are given in inches.

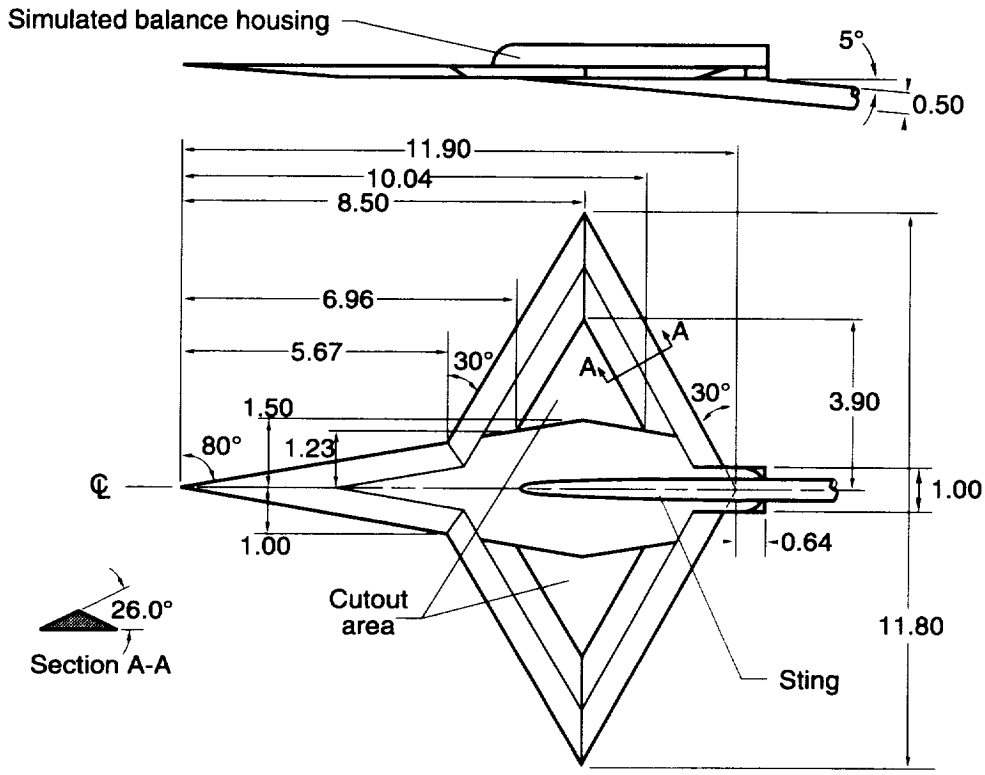

(a) Side and bottom view of original 30° diamond cutout wing.

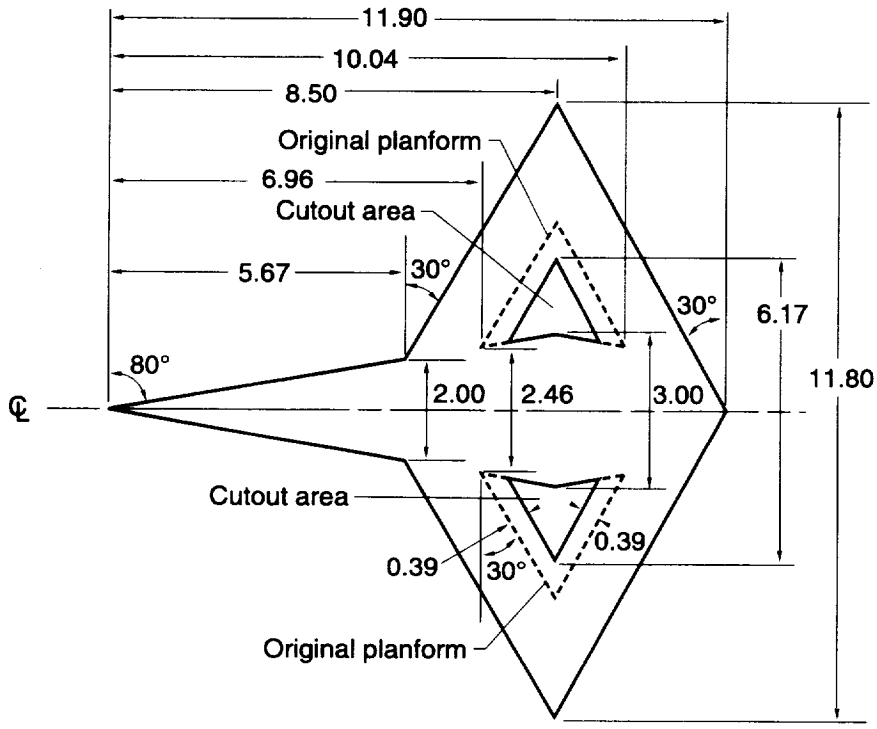

(b) Planform of 30° diamond with triangular cutout.

Figure 7. Sketches of 30° diamond cutout-wing configurations. All linear dimensions are given in inches.

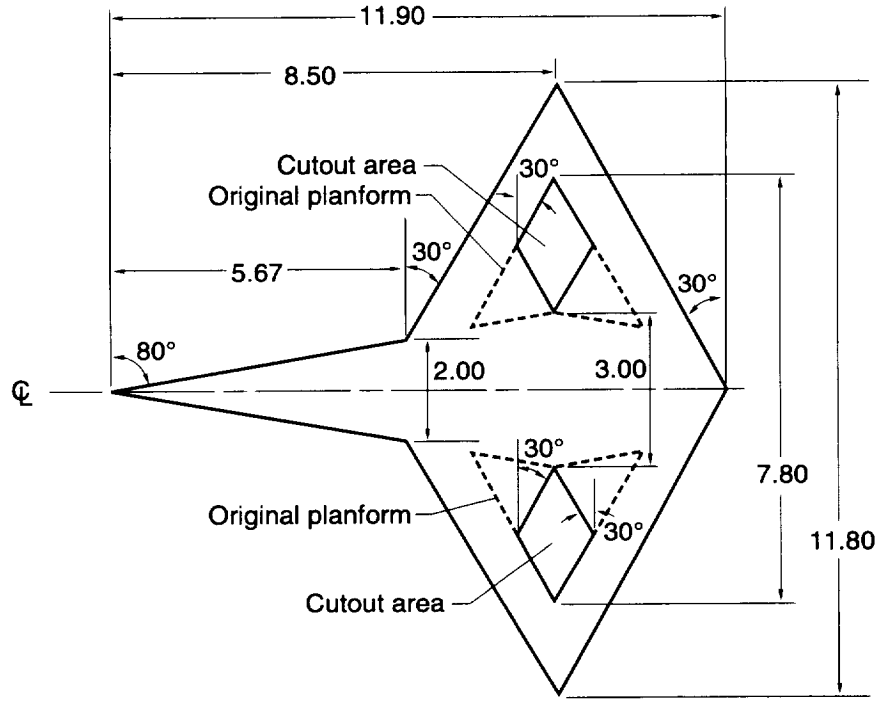

(c) Planform of 30° diamond with diamond cutout.

Figure 7. Concluded.

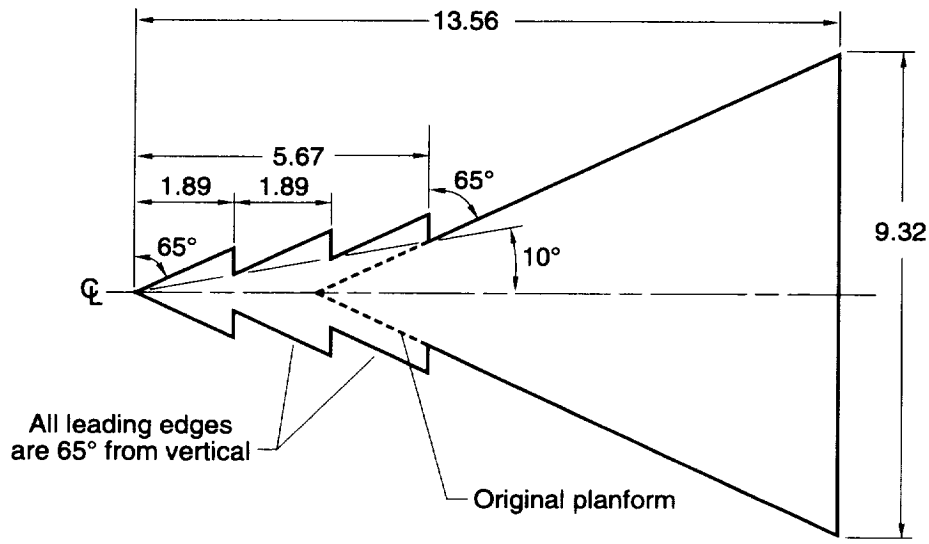

(a) 65° delta with delta sawteeth.

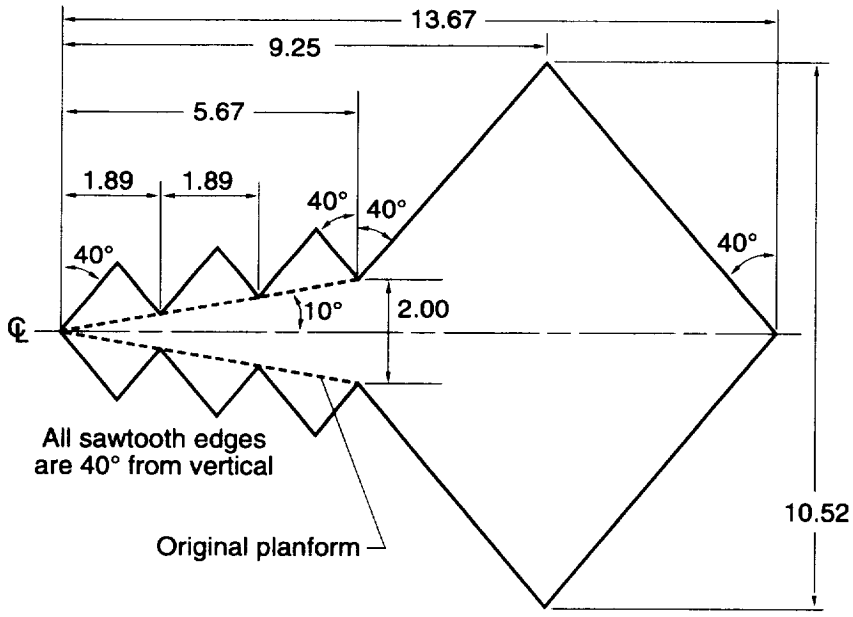

(b) 40° diamond with 3 diamond sawteeth.

Figure 8. Planform sketches of serrated-forebody configurations. All linear dimensions are given in inches.

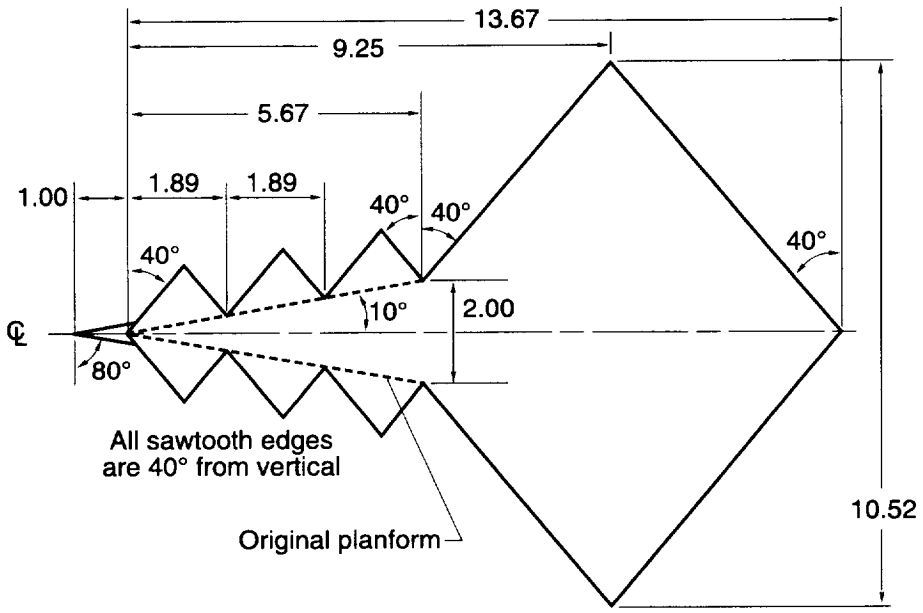

(c) 40° diamond with 3 diamond sawteeth and nose tip.

Figure 8. Concluded.

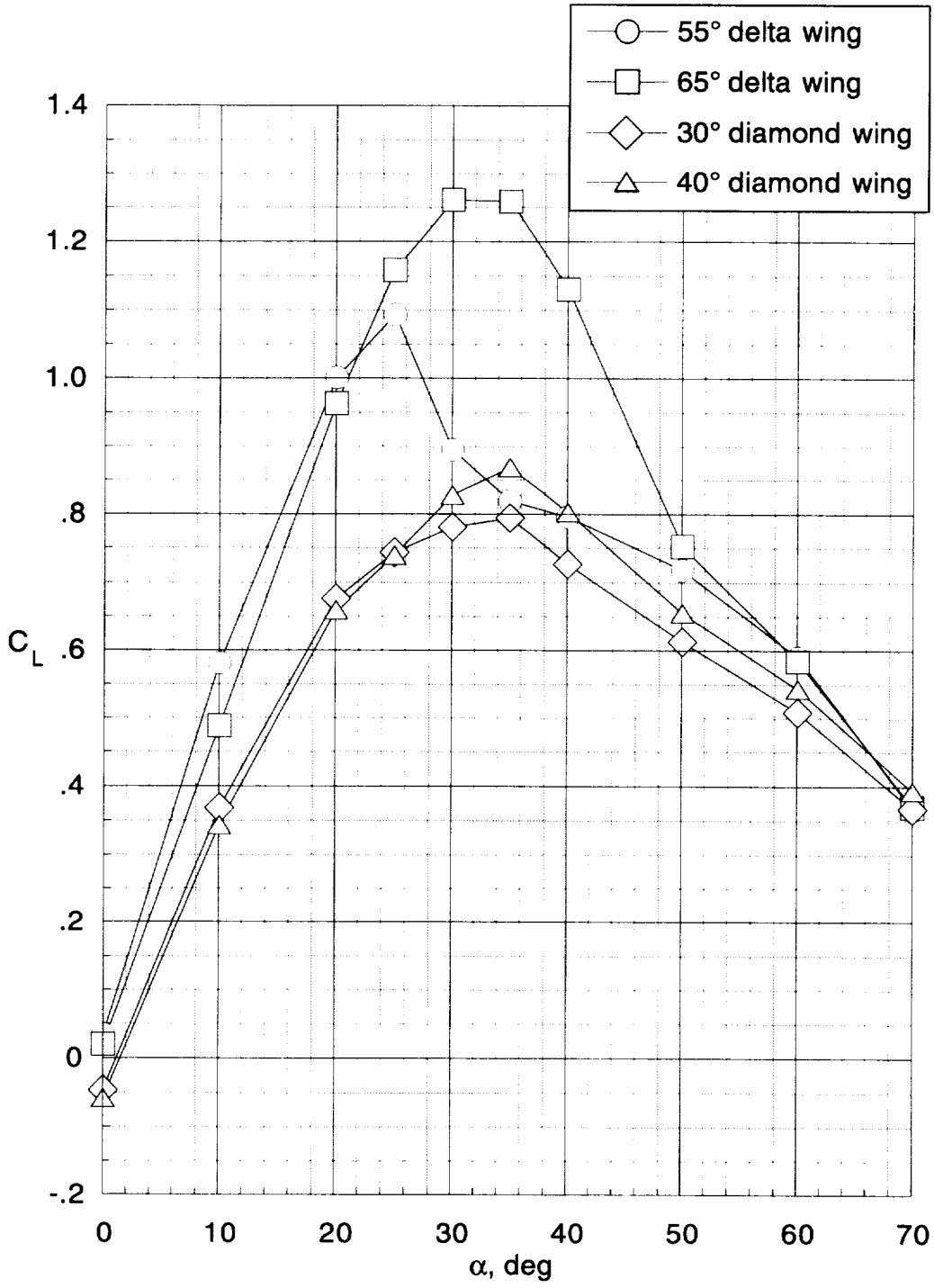

Figure 9. Lift coefficient versus angle of attack for delta and diamond wings (ref. 14).

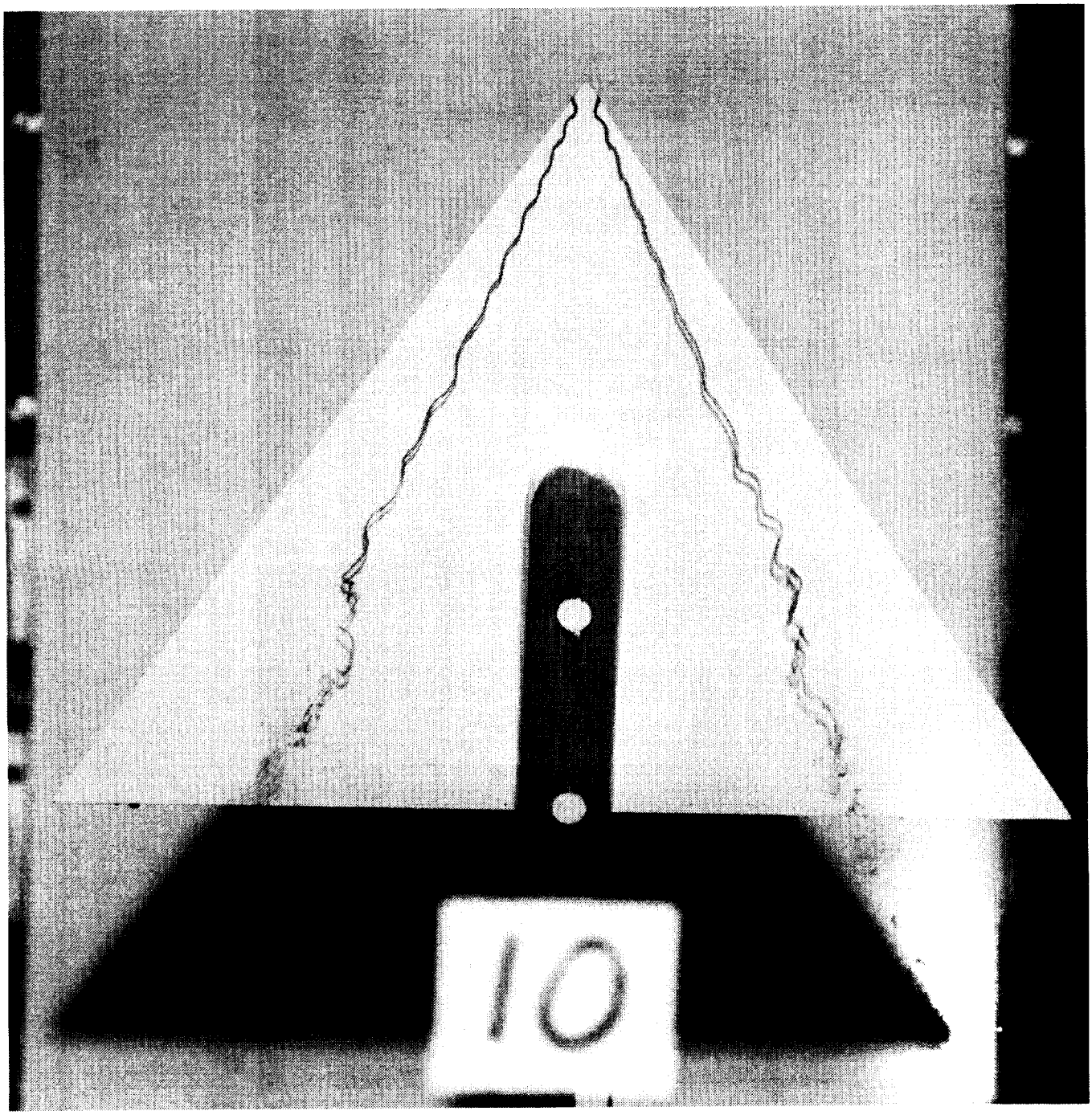

(a) Top view; $\alpha = 10°$.

Figure 10. Photographs of 55° delta wing.

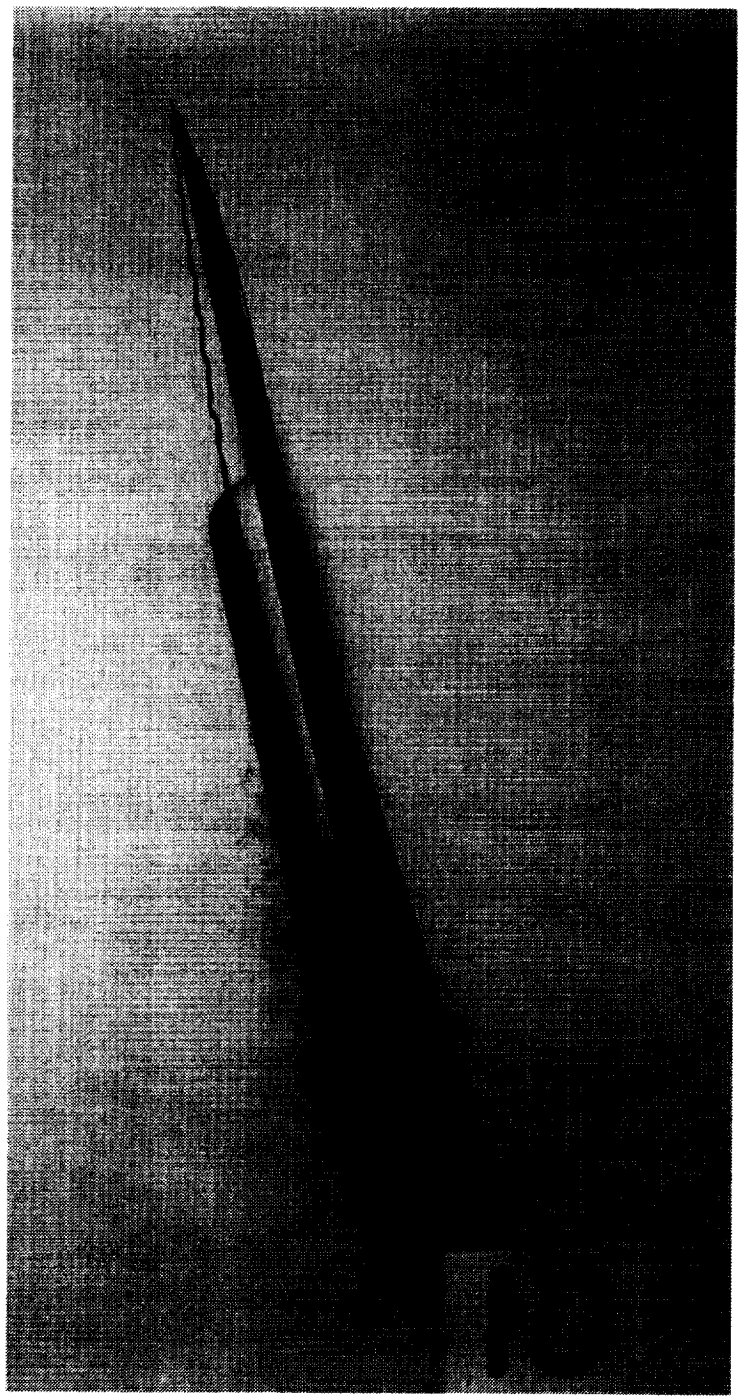

(b) Side view; $\alpha = 10°$.

Figure 10. Continued.

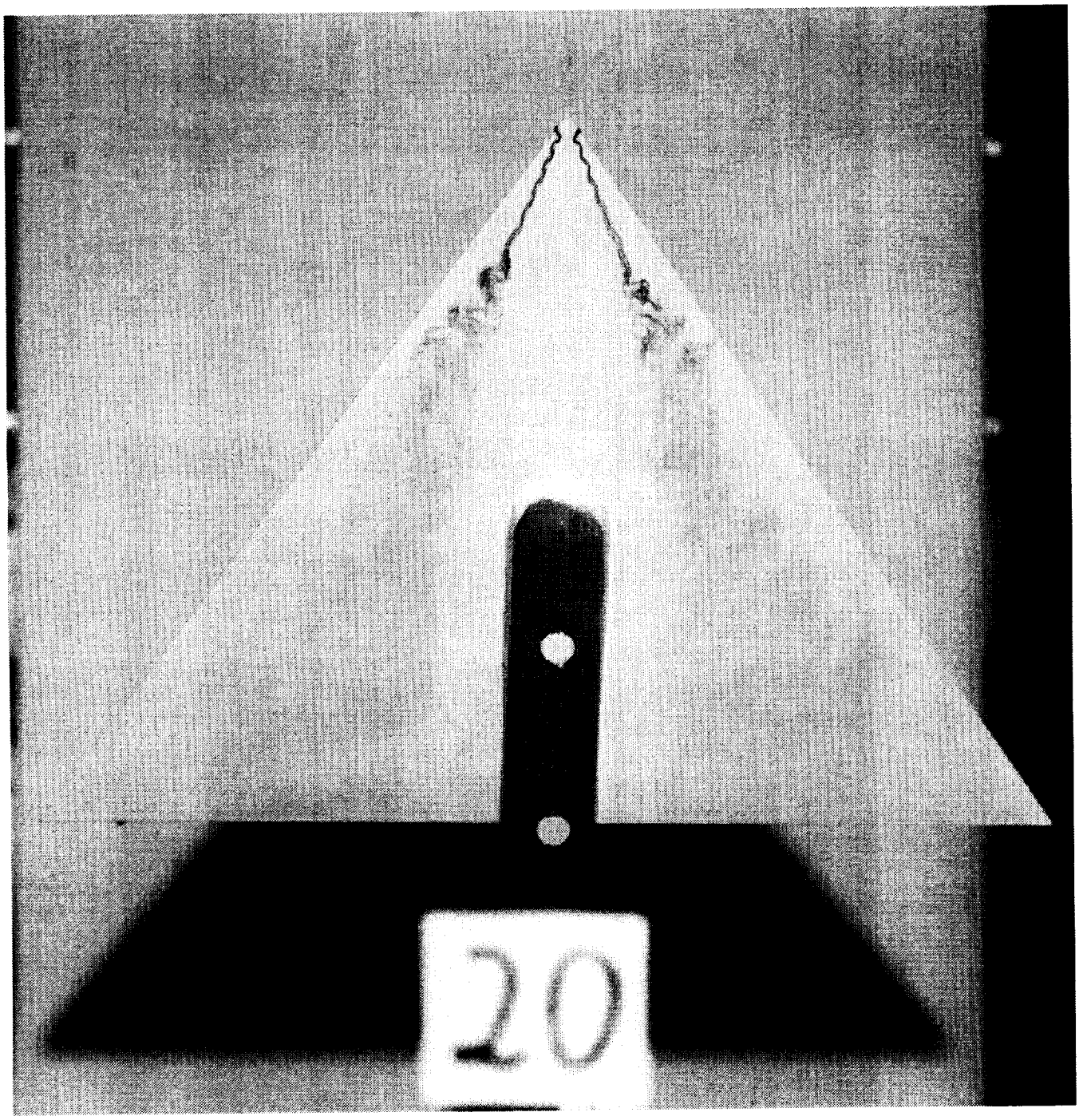

(c) Top view; $\alpha = 20°$.

Figure 10. Continued.

(d) Side view; $\alpha = 20°$.

Figure 10. Continued.

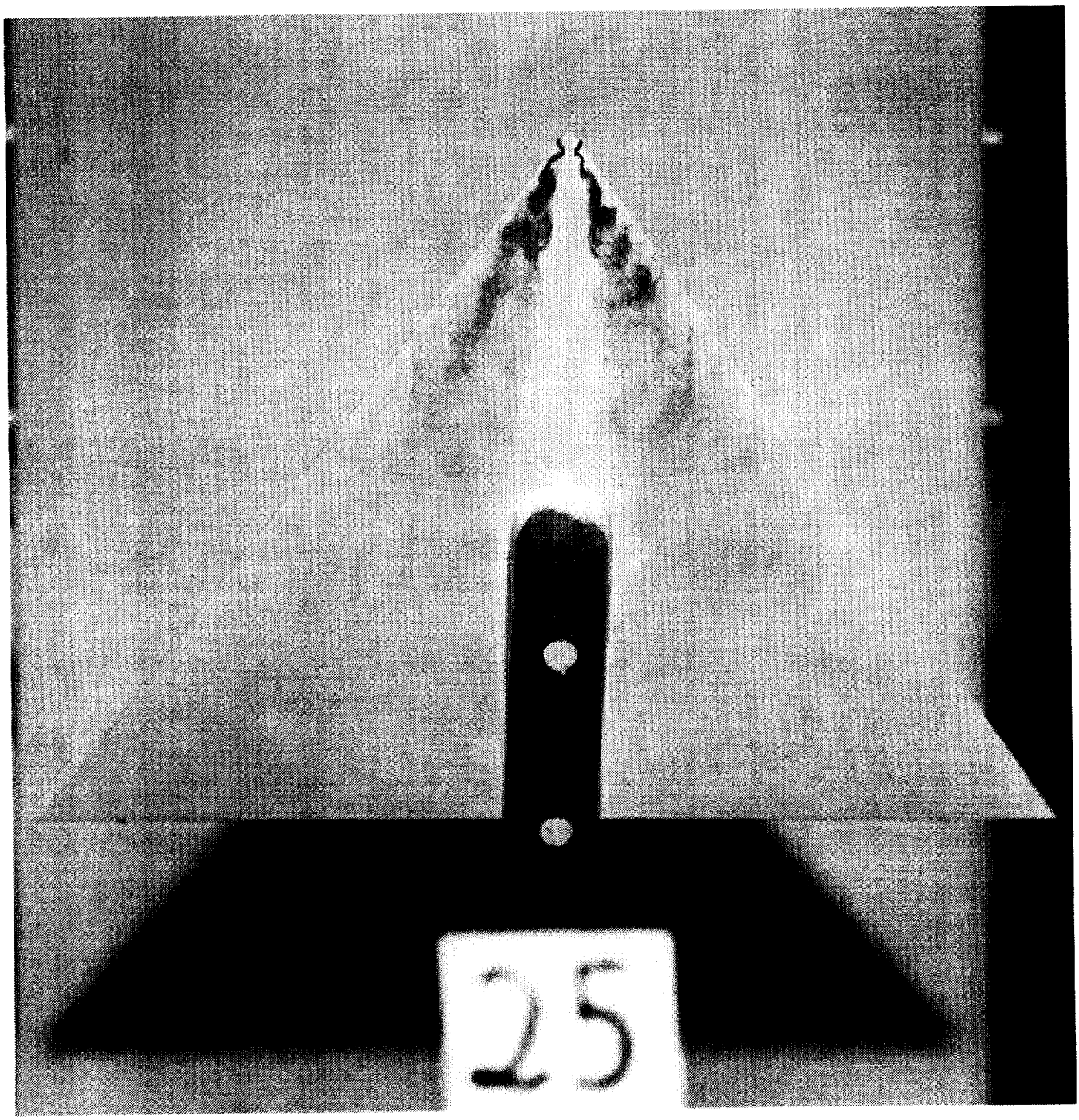

(e) Top view; $\alpha = 25°$.

Figure 10. Continued.

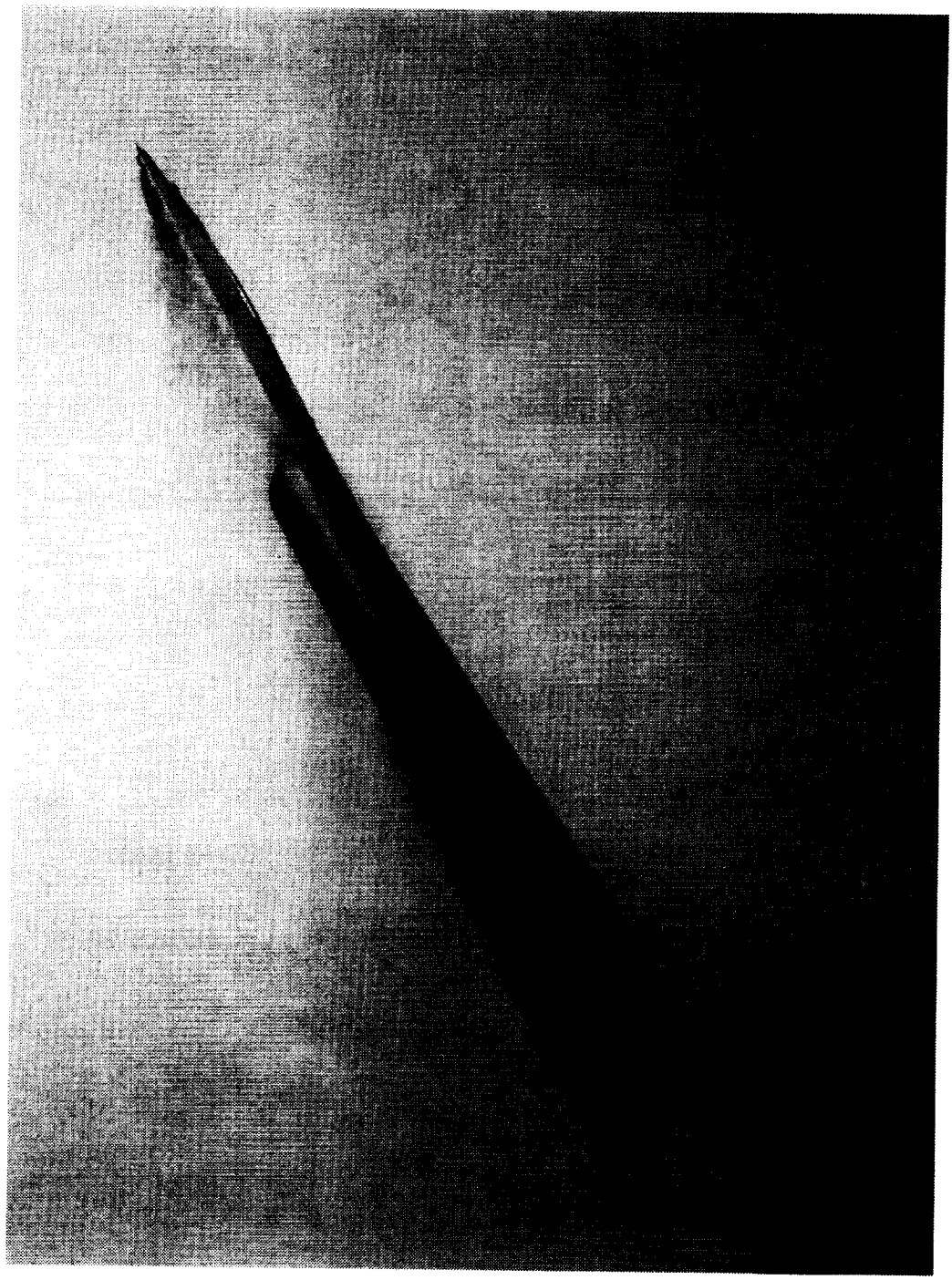

(f) Side view; $\alpha = 25°$.

Figure 10. Continued.

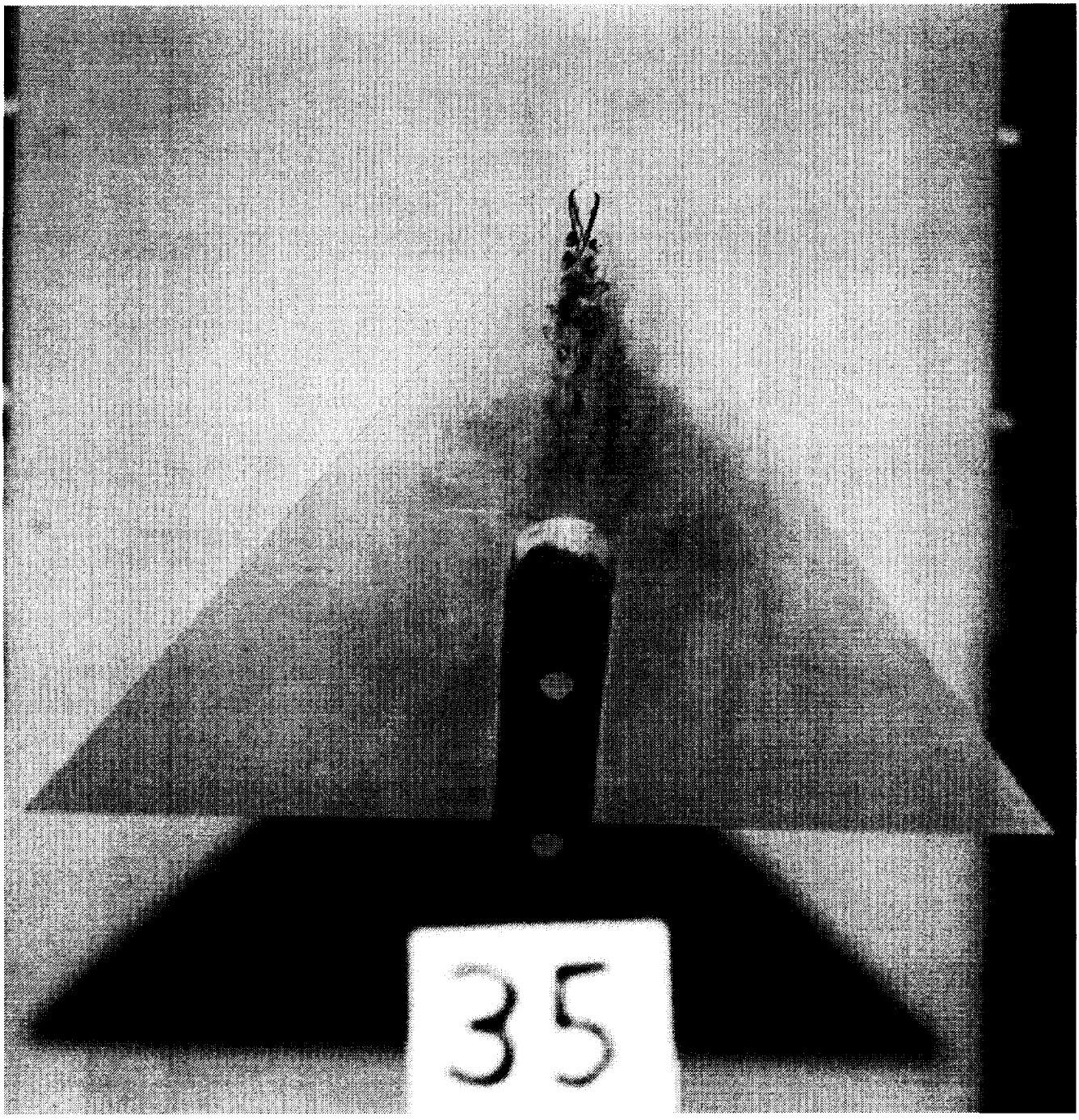

(g) Top view; $\alpha = 35°$.

Figure 10. Continued.

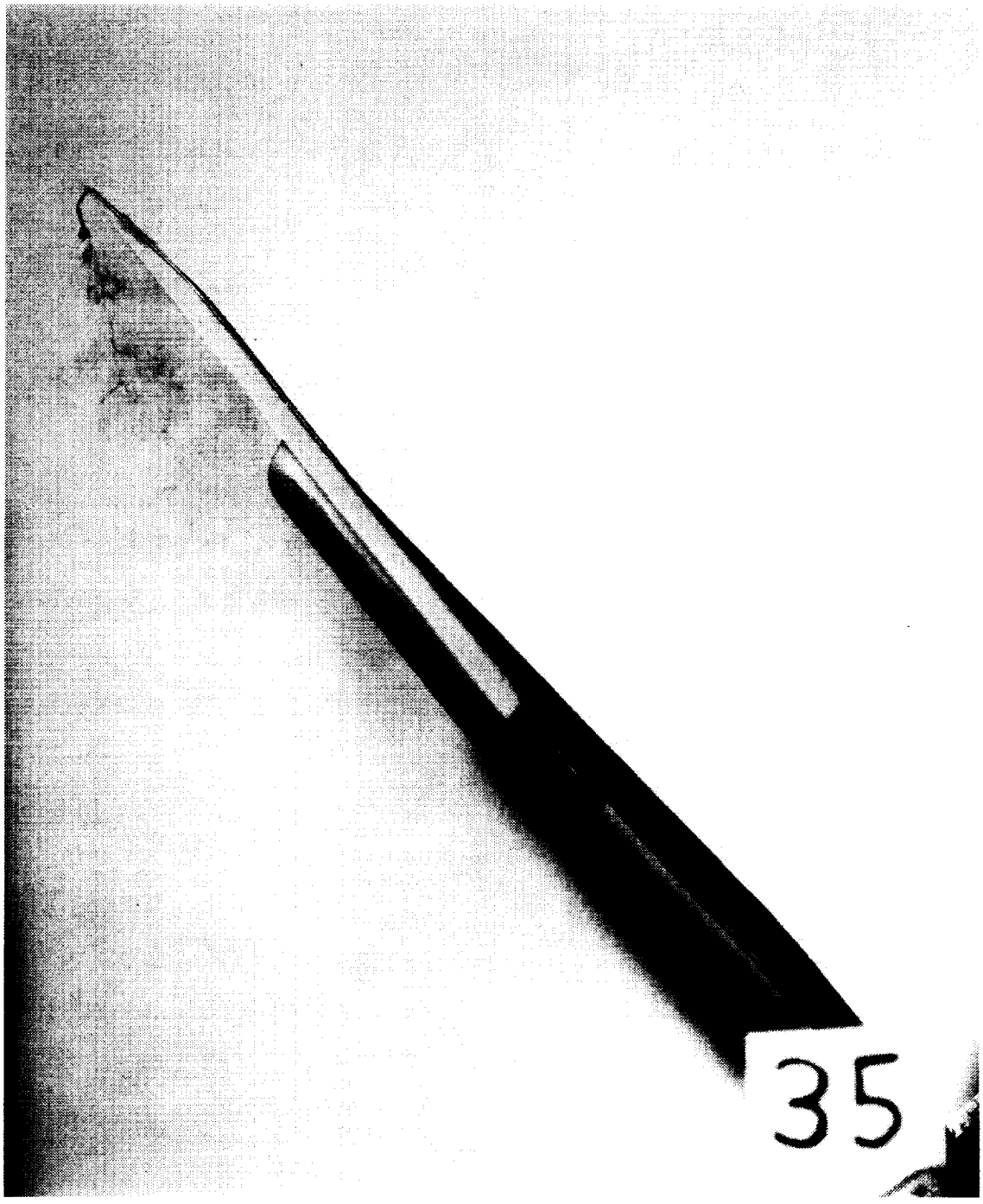

(h) Side view; $\alpha = 35°$.

Figure 10. Continued.

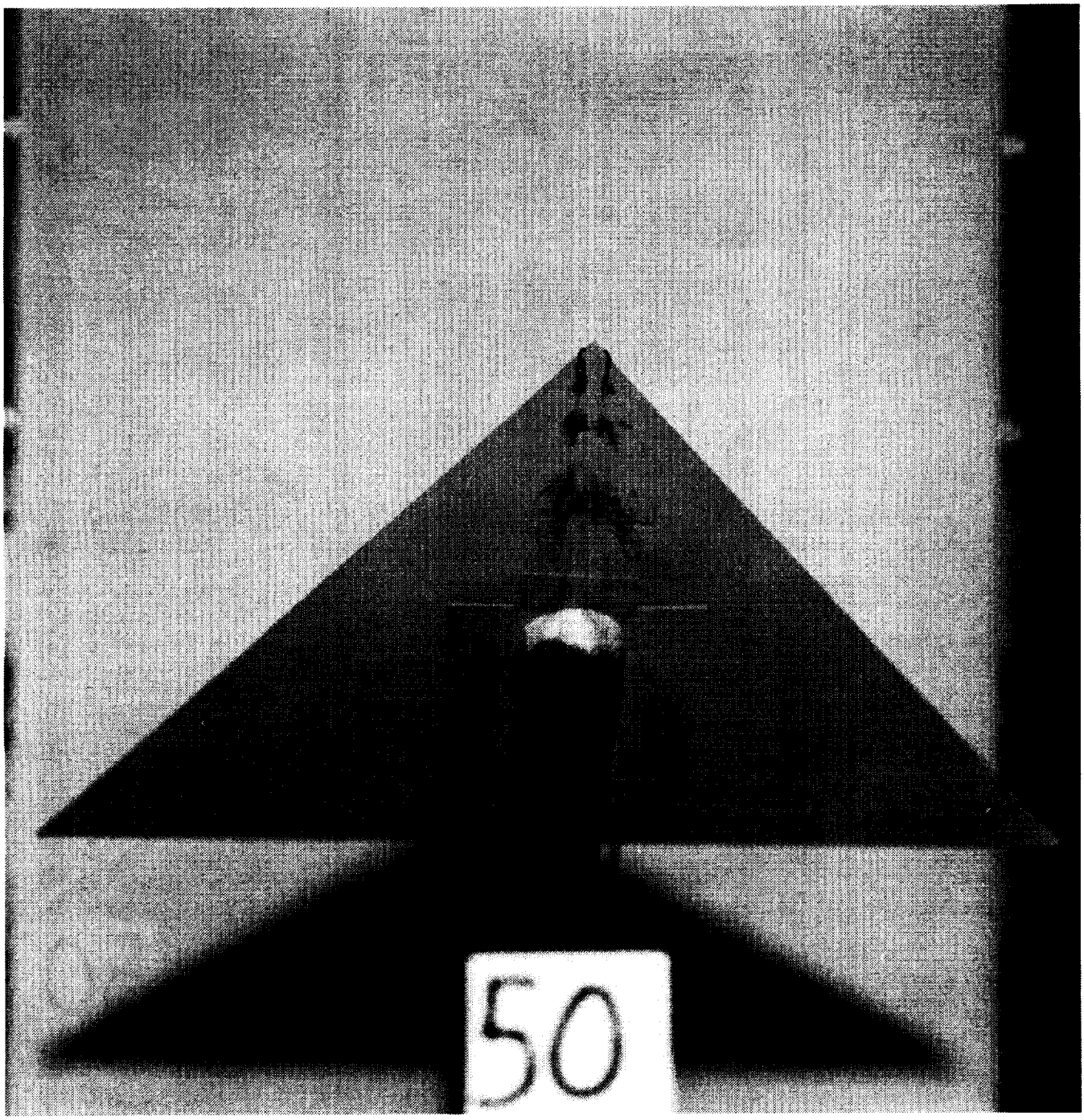

(i) Top view; $\alpha = 50°$.

Figure 10. Continued.

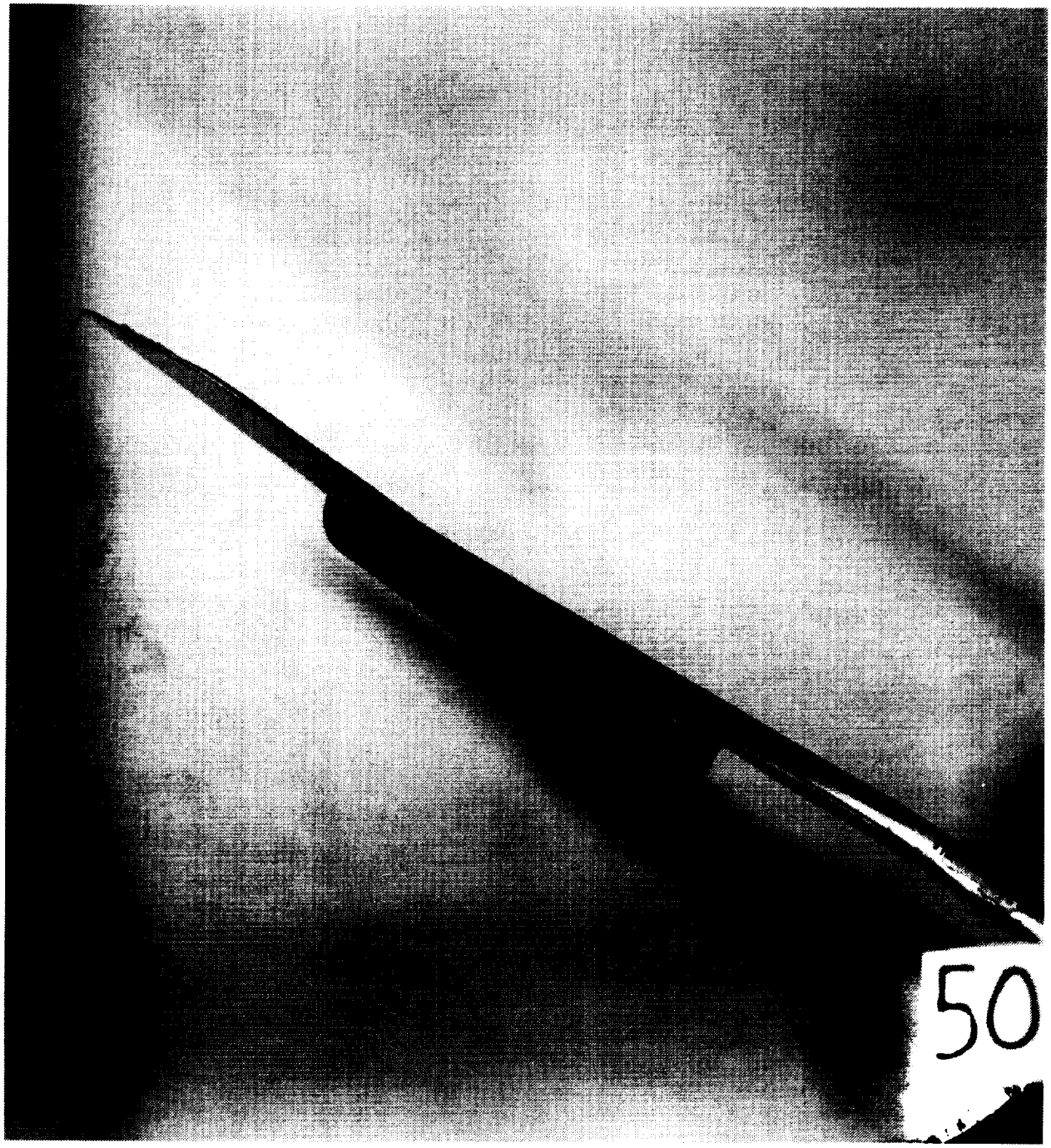

(j) Side view; $\alpha = 50°$.

Figure 10. Concluded.

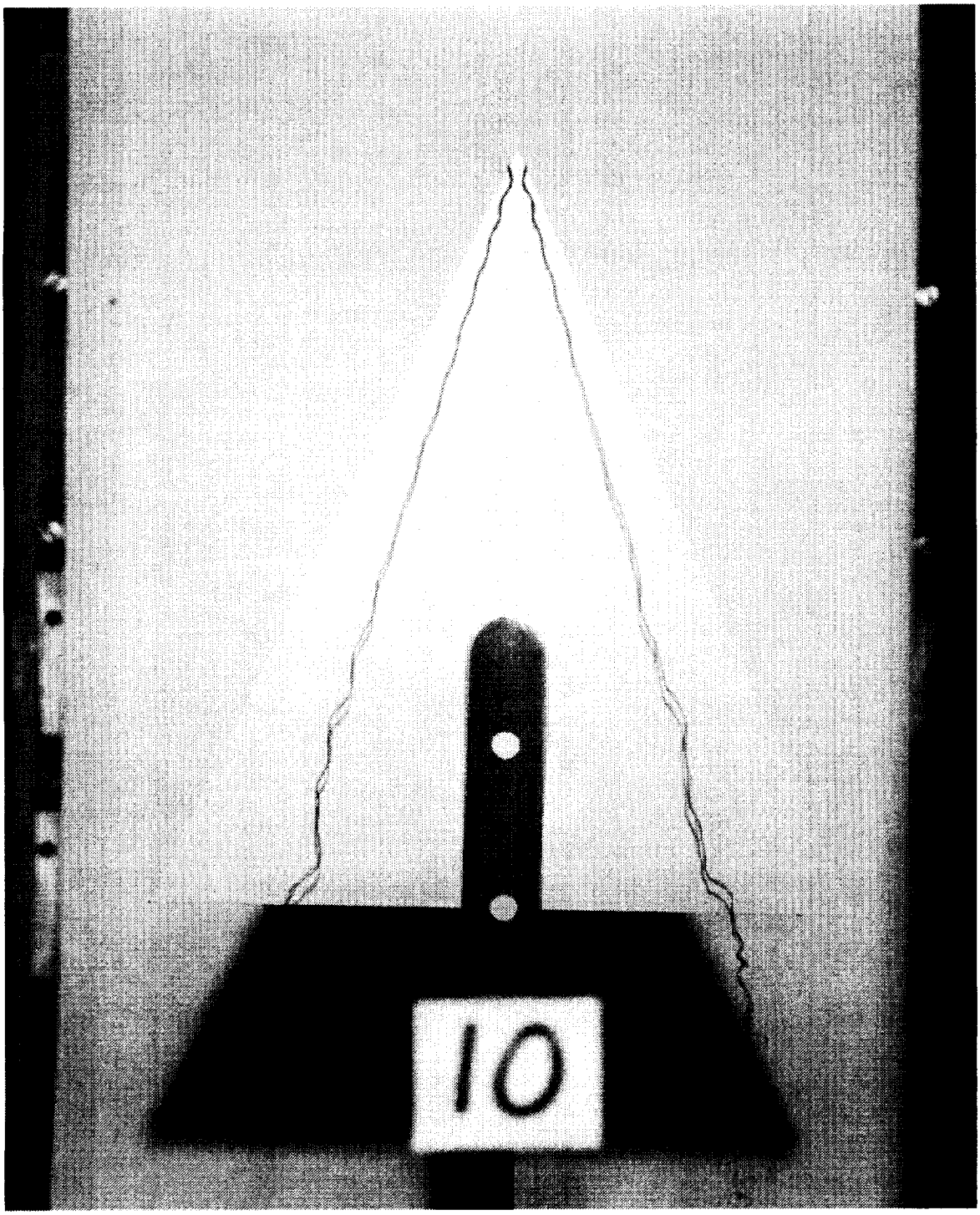

(a) $\alpha = 10°$.

Figure 11. Top-view photographs of 65° delta wing.

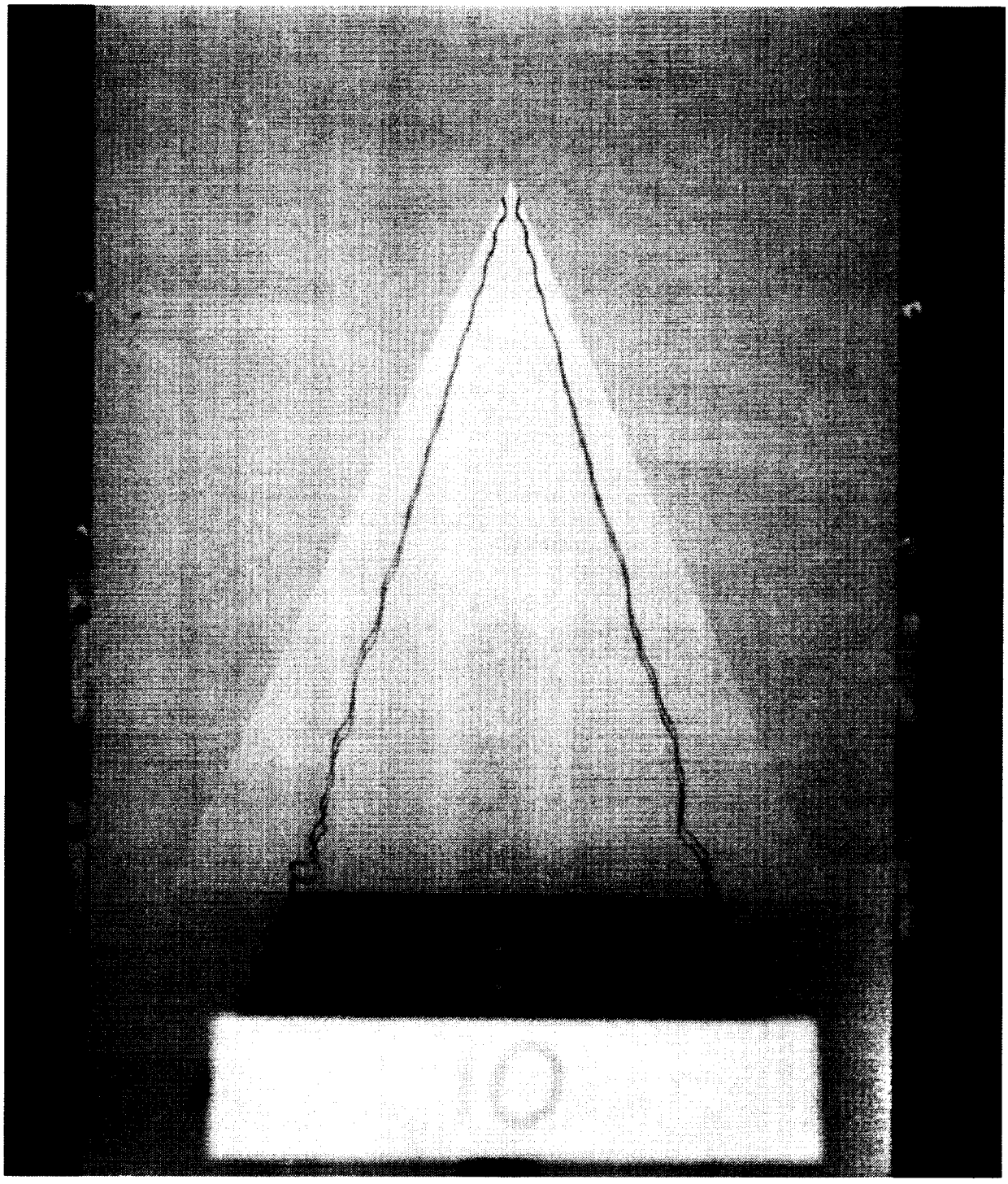

(b) Simulated balance housing removed; $\alpha = 10°$.

Figure 11. Continued.

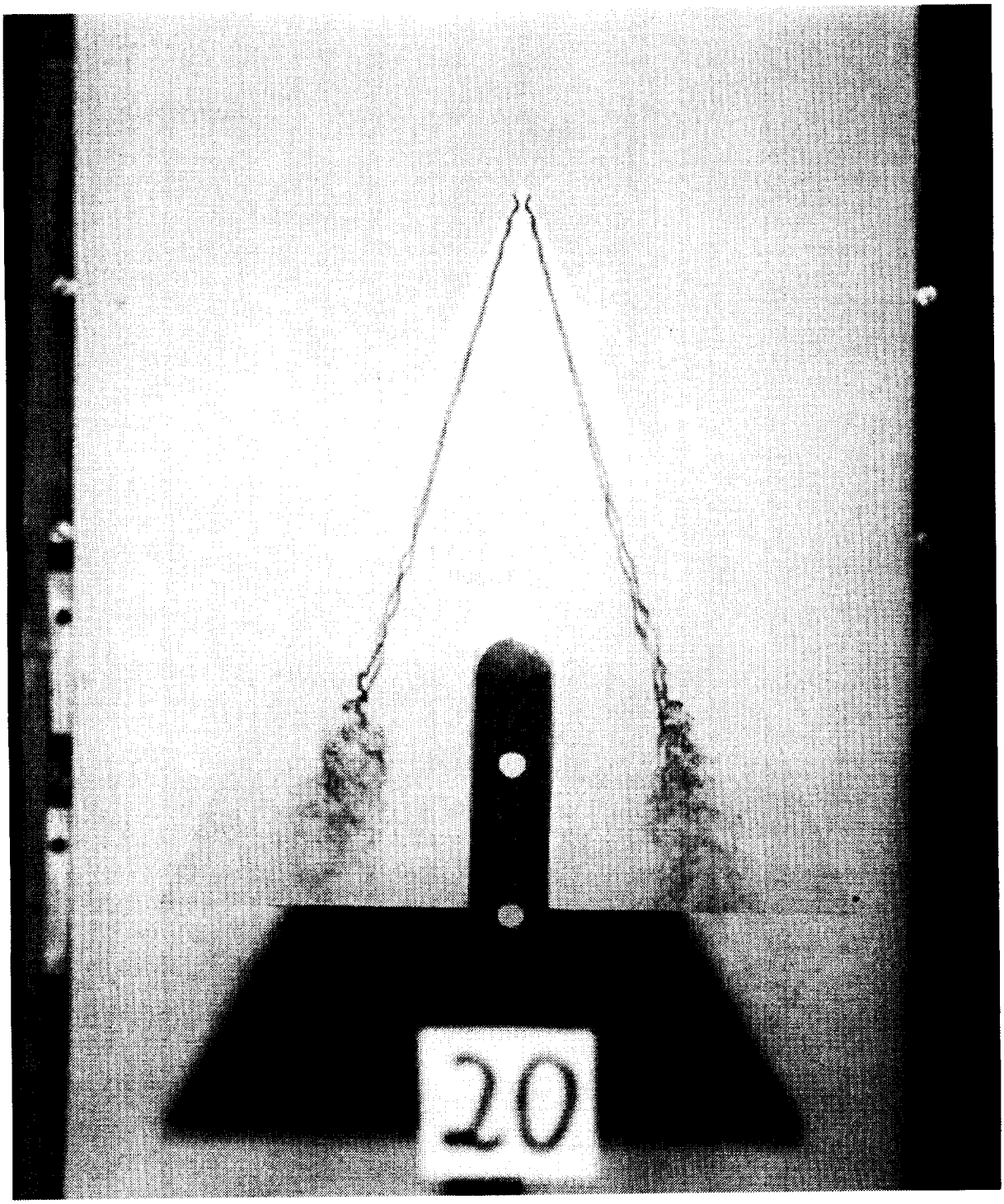

(c) $\alpha = 20°$.

Figure 11. Continued.

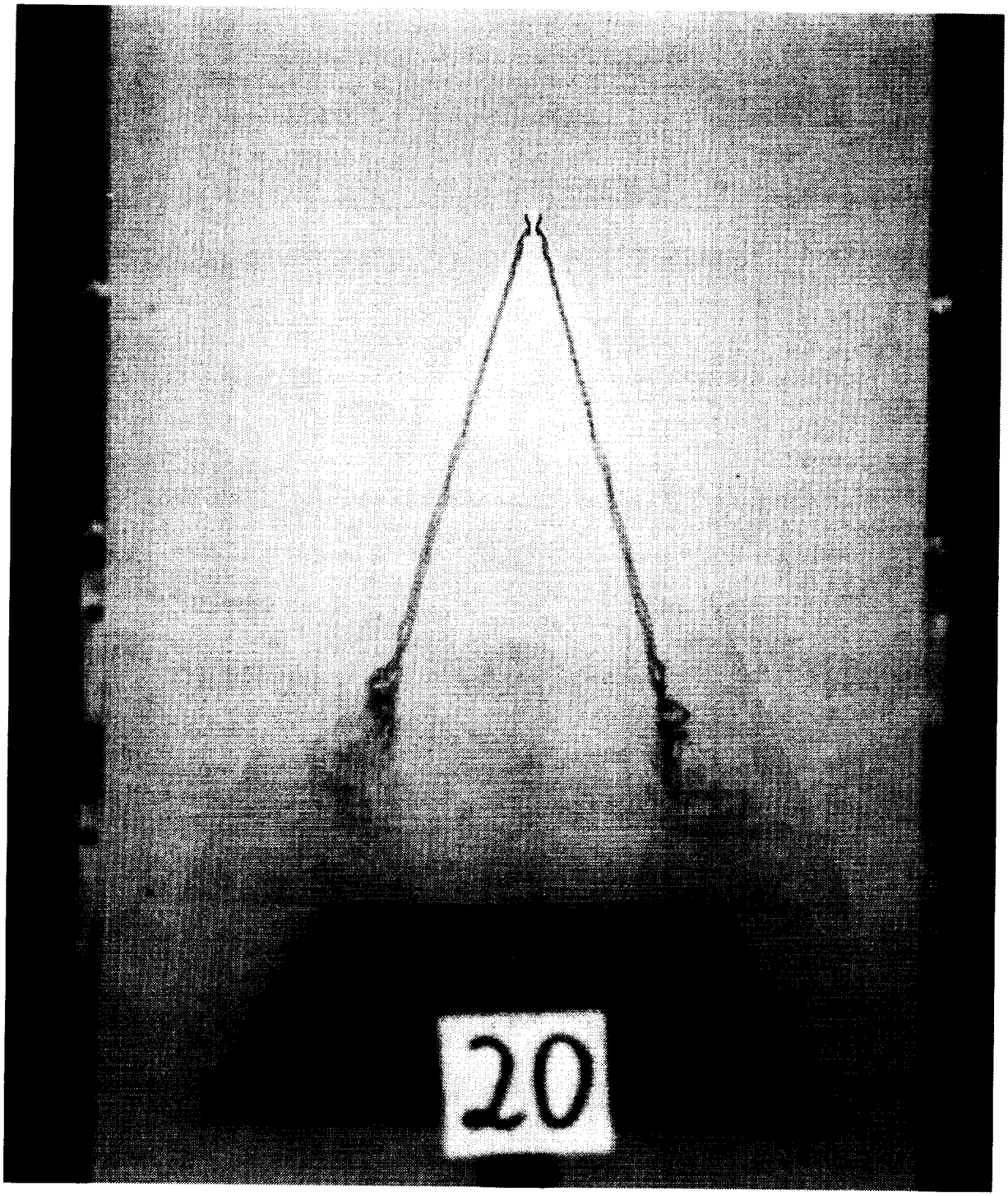

(d) Simulated balance housing removed; $\alpha = 20°$.

Figure 11. Continued.

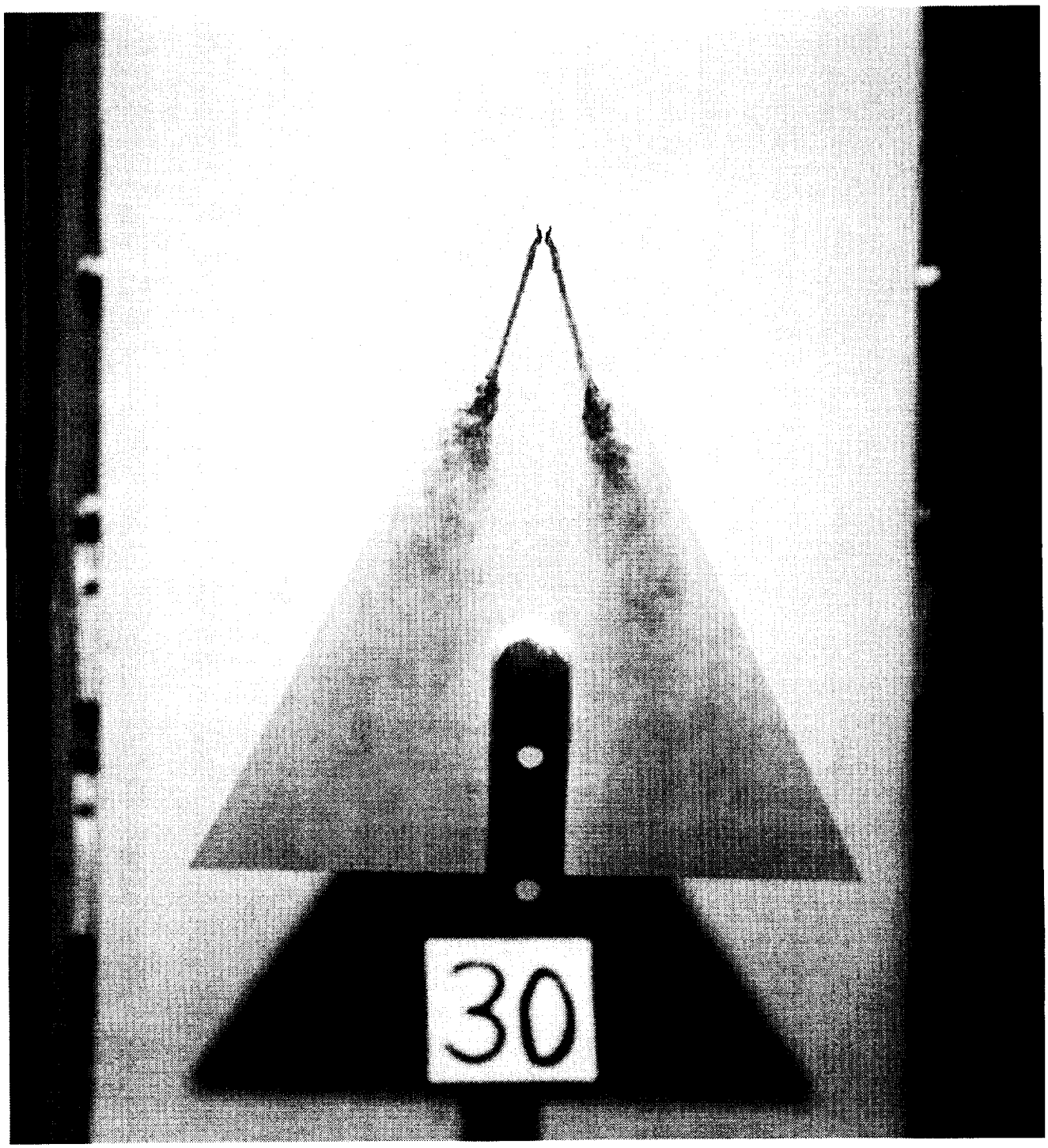

(e) $\alpha = 30°$.

Figure 11. Continued.

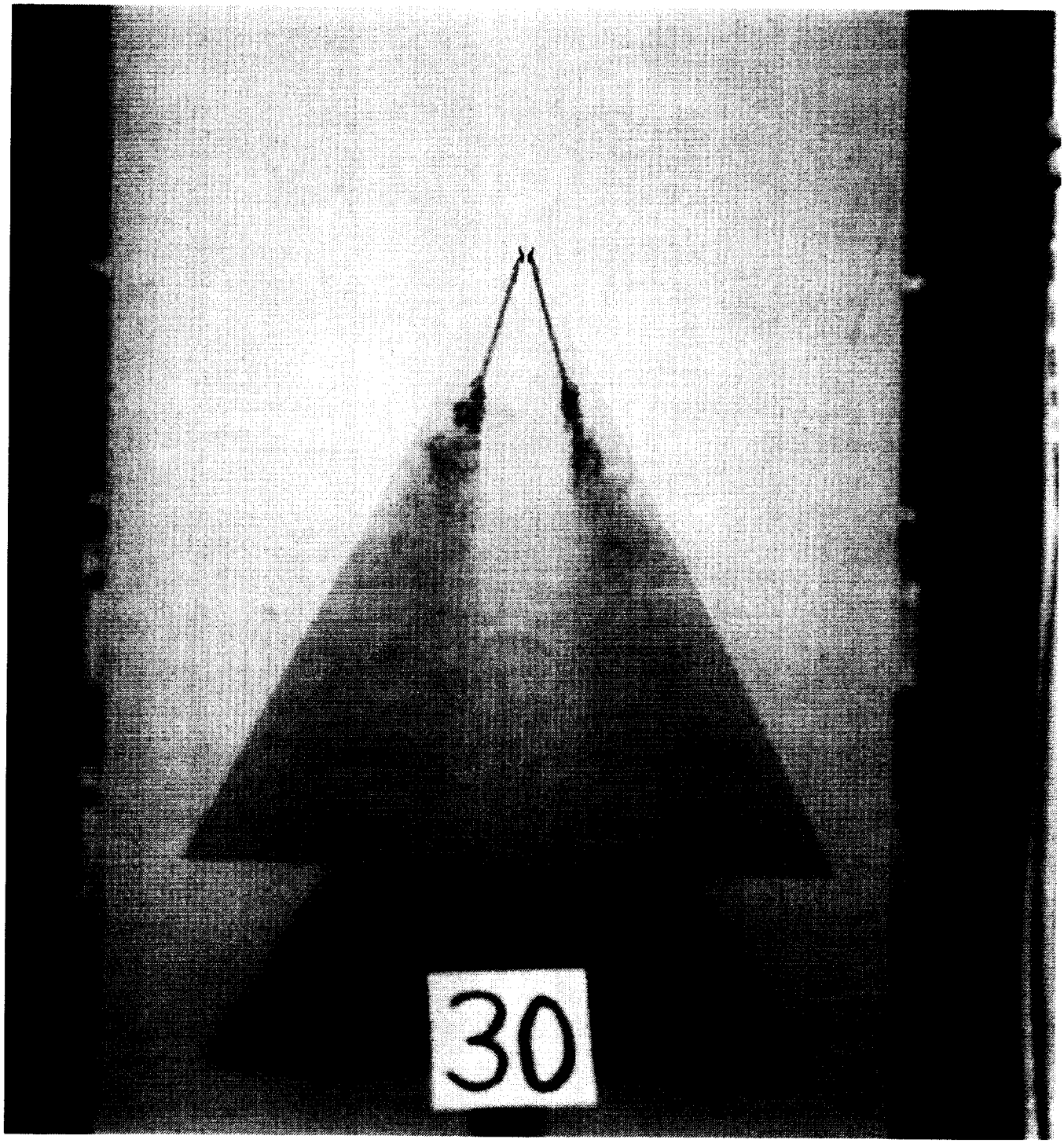

(f) Simulated balance housing removed; $\alpha = 30°$.

Figure 11. Continued.

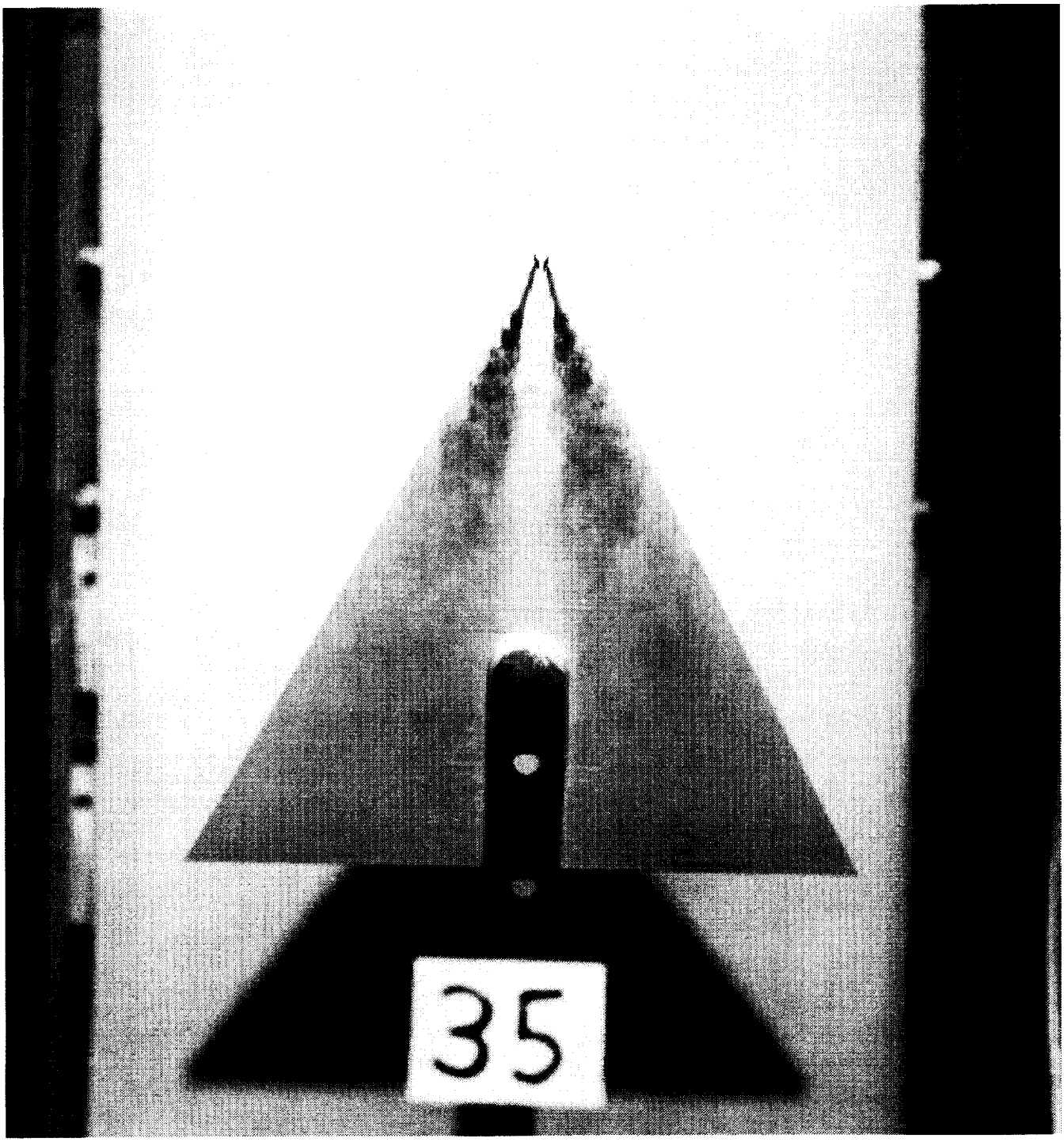

(g) $\alpha = 35°$.

Figure 11. Continued.

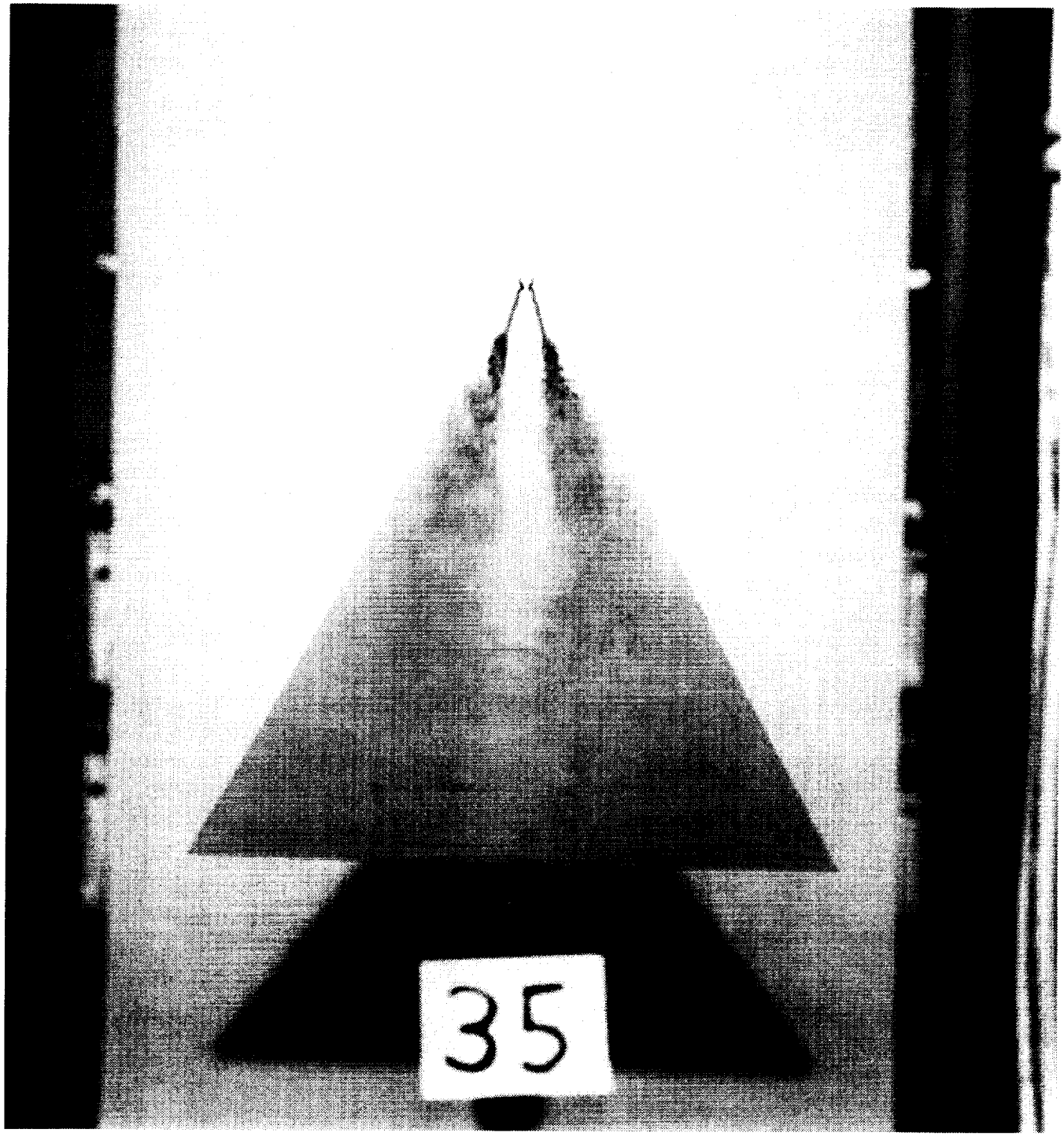

(h) Simulated balance housing removed; $\alpha = 35°$.

Figure 11. Continued.

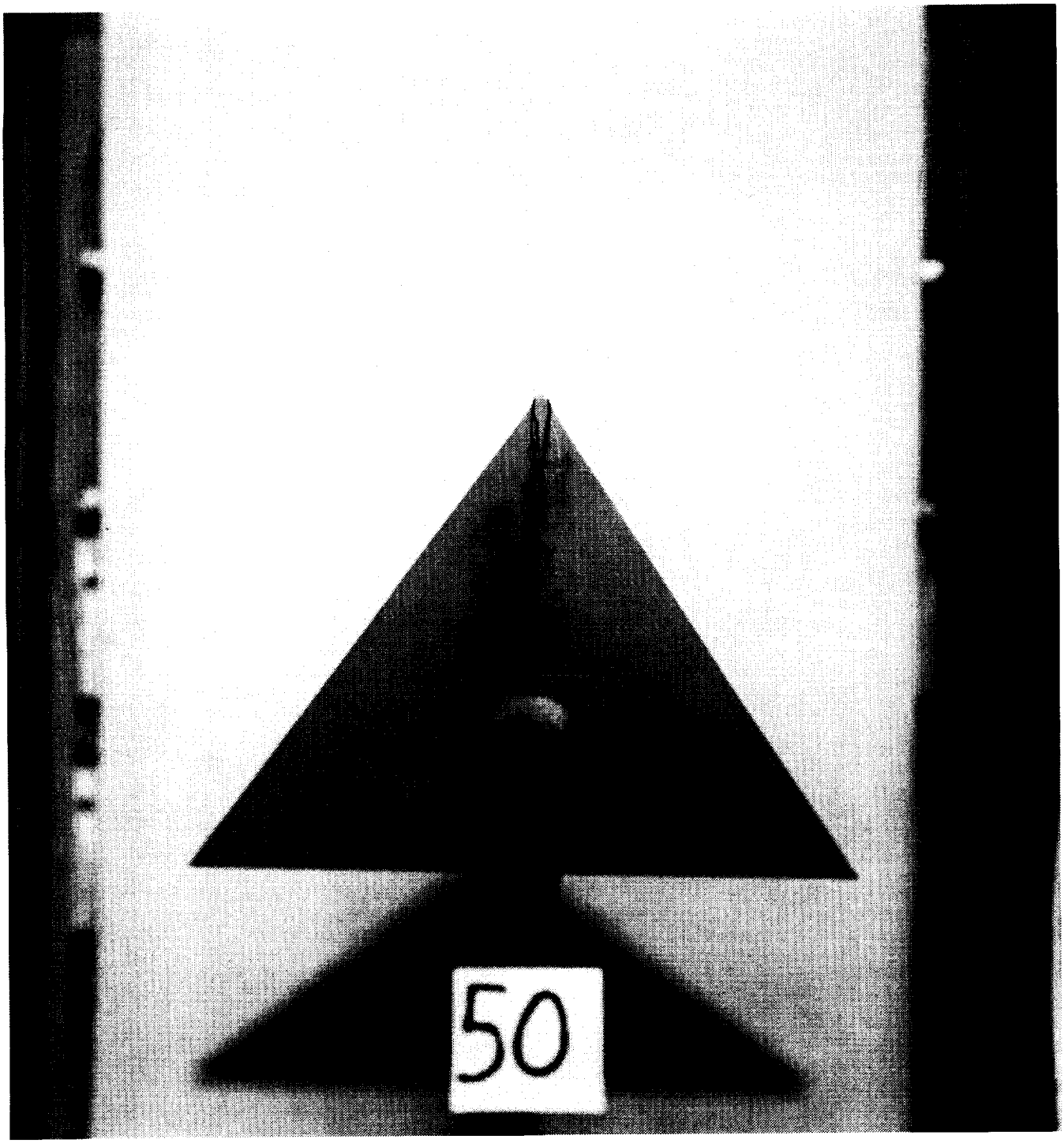

(i) $\alpha = 50°$.

Figure 11. Continued.

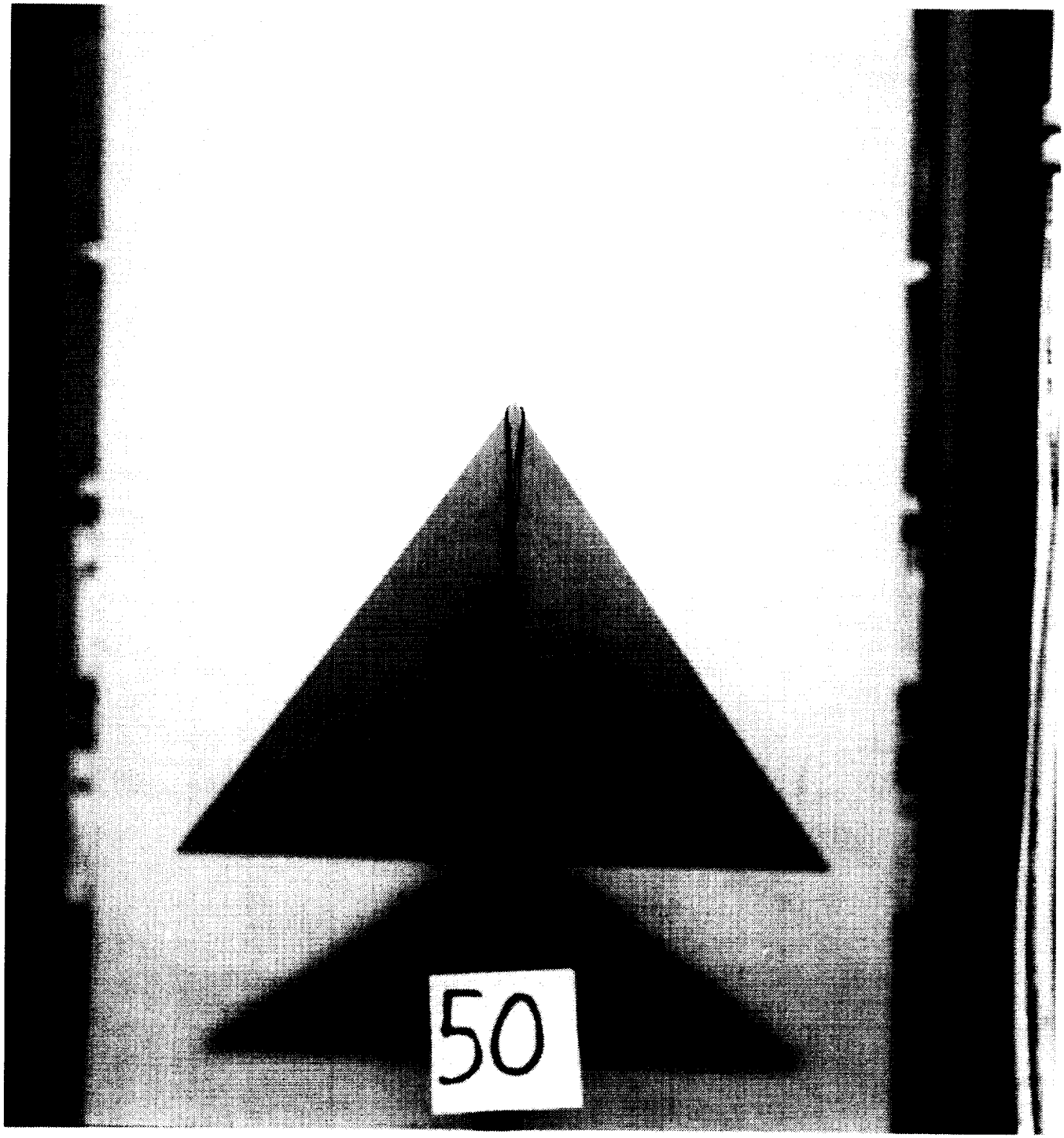

(j) Simulated balance housing removed; $\alpha = 50°$.

Figure 11. Concluded.

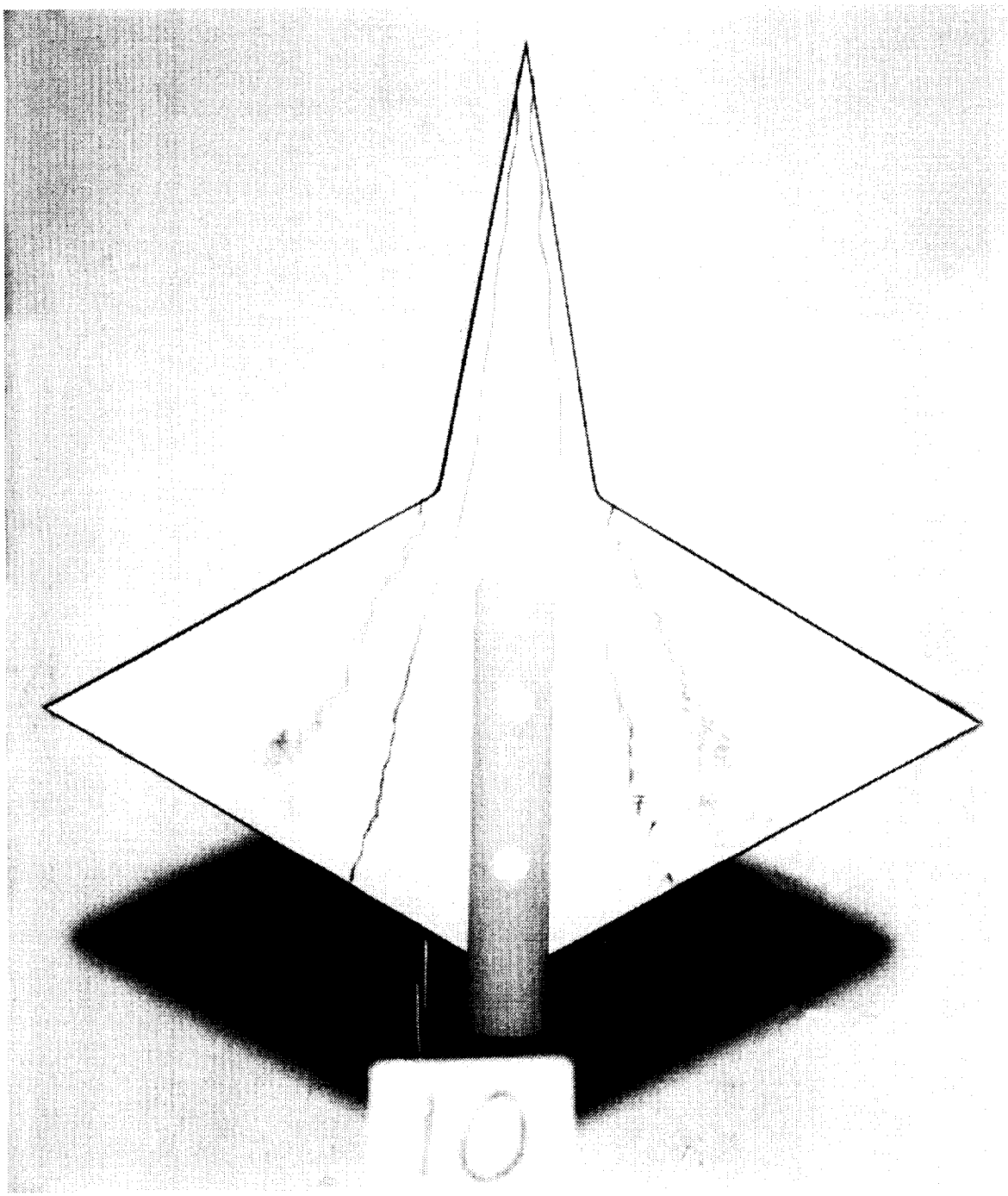

(a) Top view; $\alpha = 10°$.

Figure 12. Photographs of 30° diamond wing.

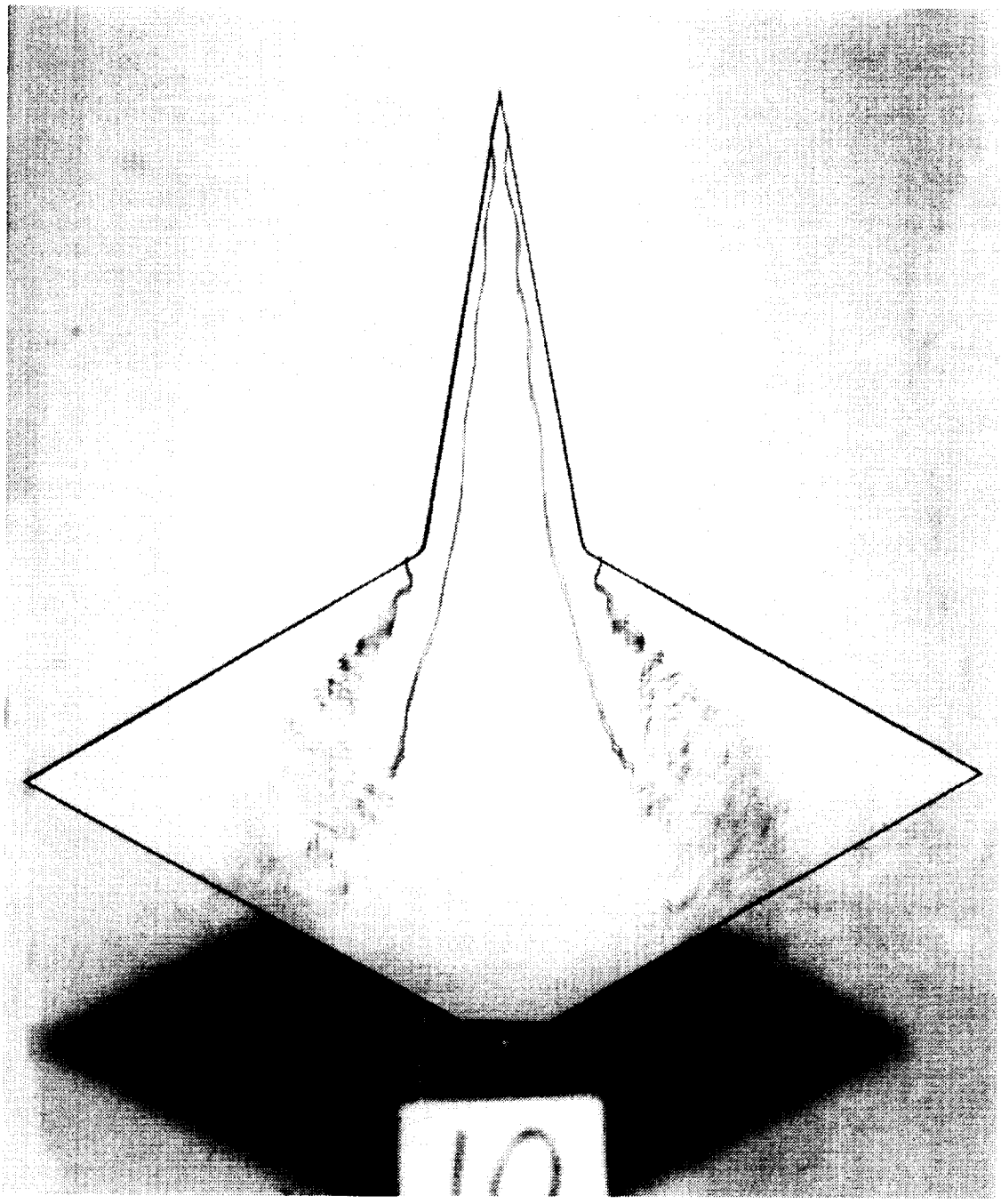

(b) Simulated balance housing removed; top view; $\alpha = 10°$.

Figure 12. Continued.

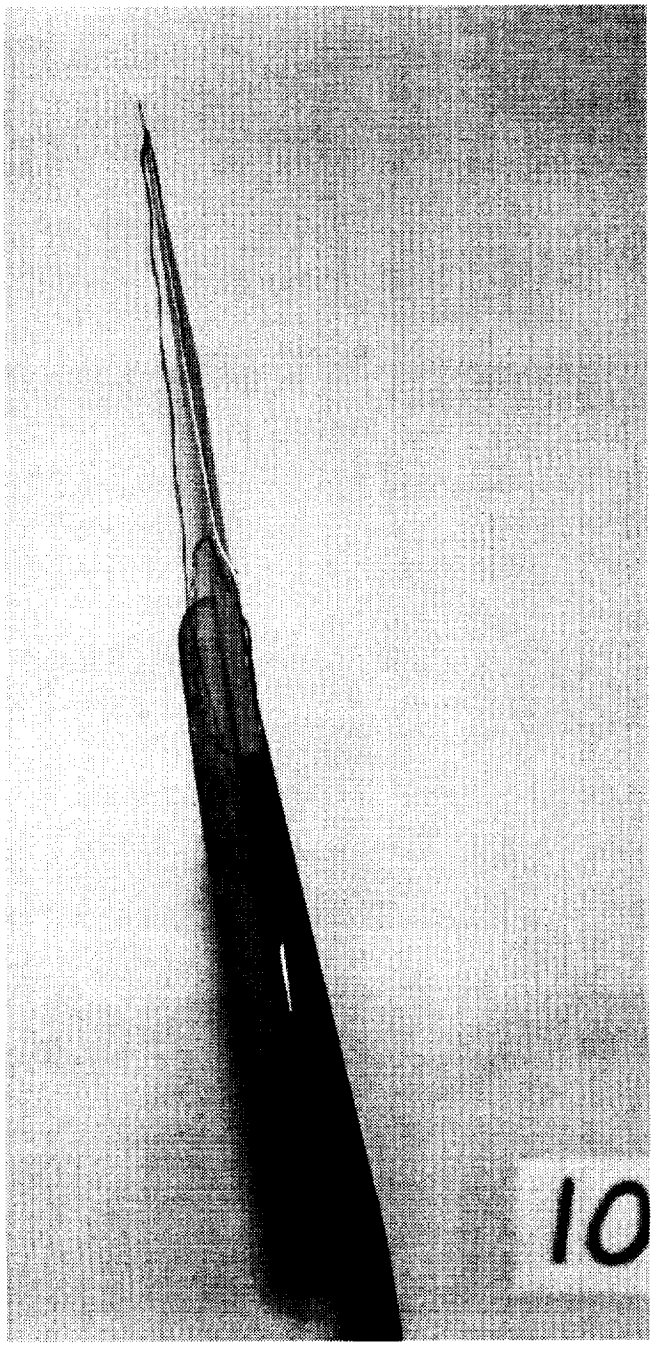

(c) Side view; $\alpha = 10°$.

Figure 12. Continued.

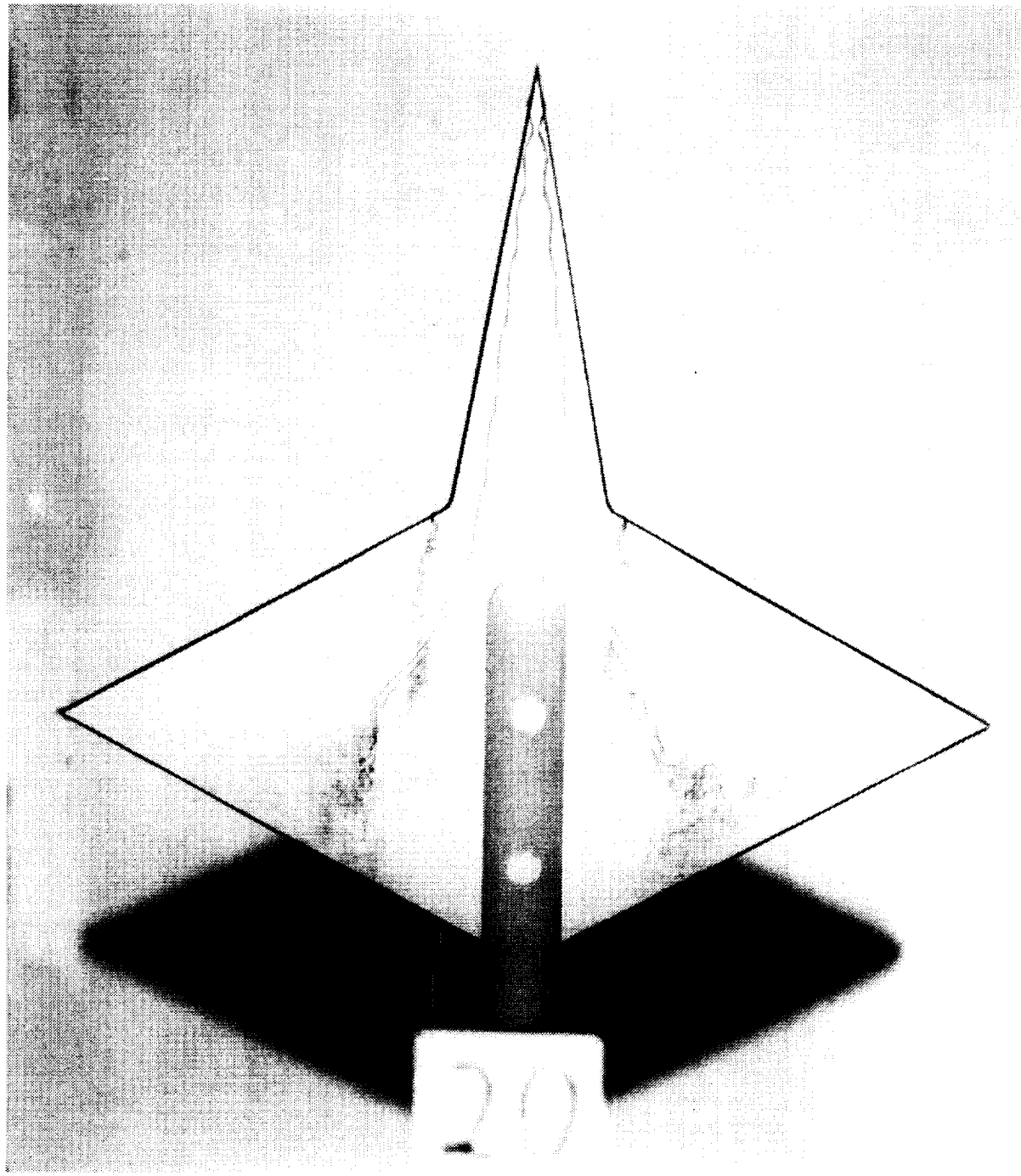

(d) Top view; $\alpha = 20°$.

Figure 12. Continued.

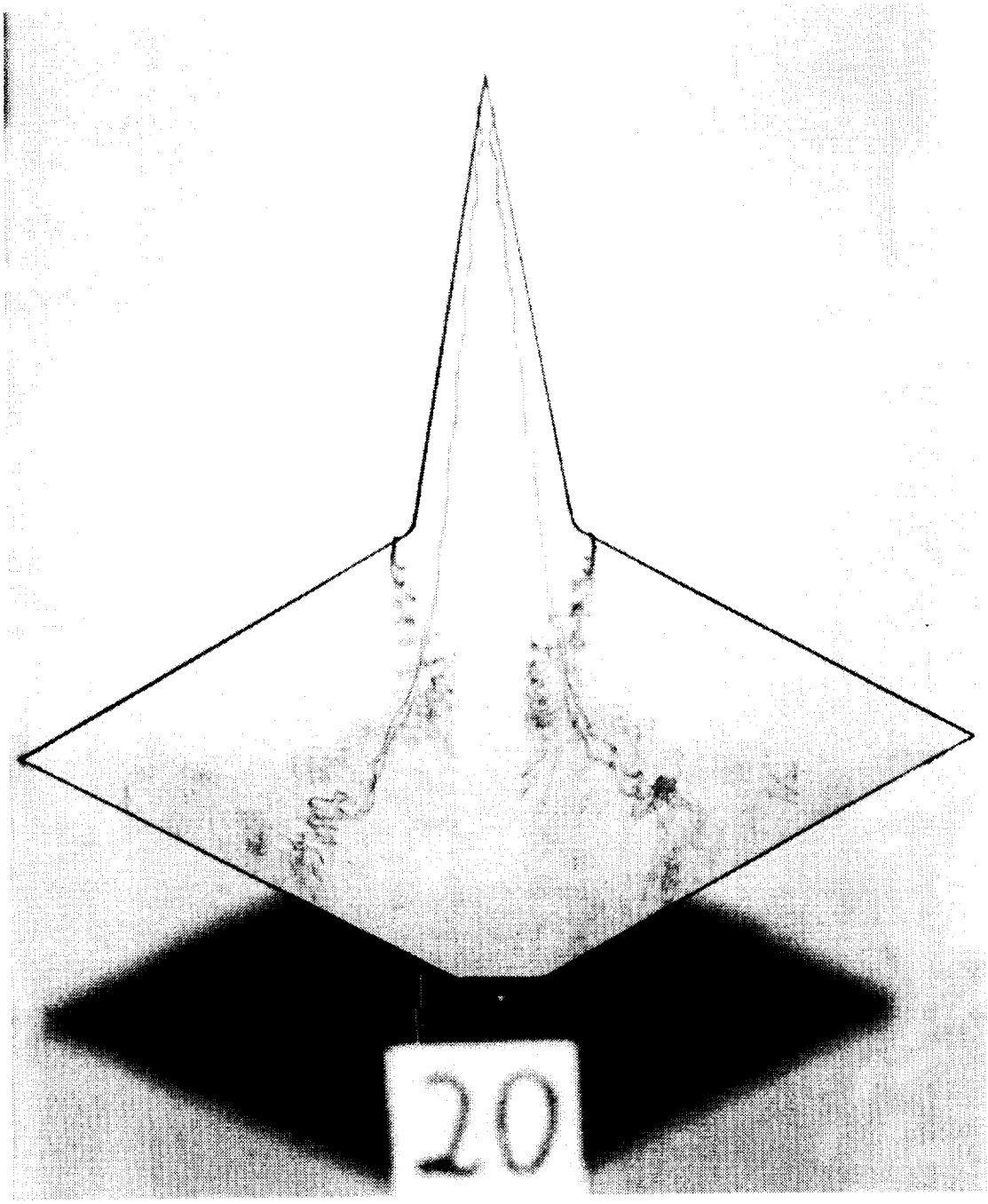

(e) Simulated balance housing removed; top view; $\alpha = 20°$.

Figure 12. Continued.

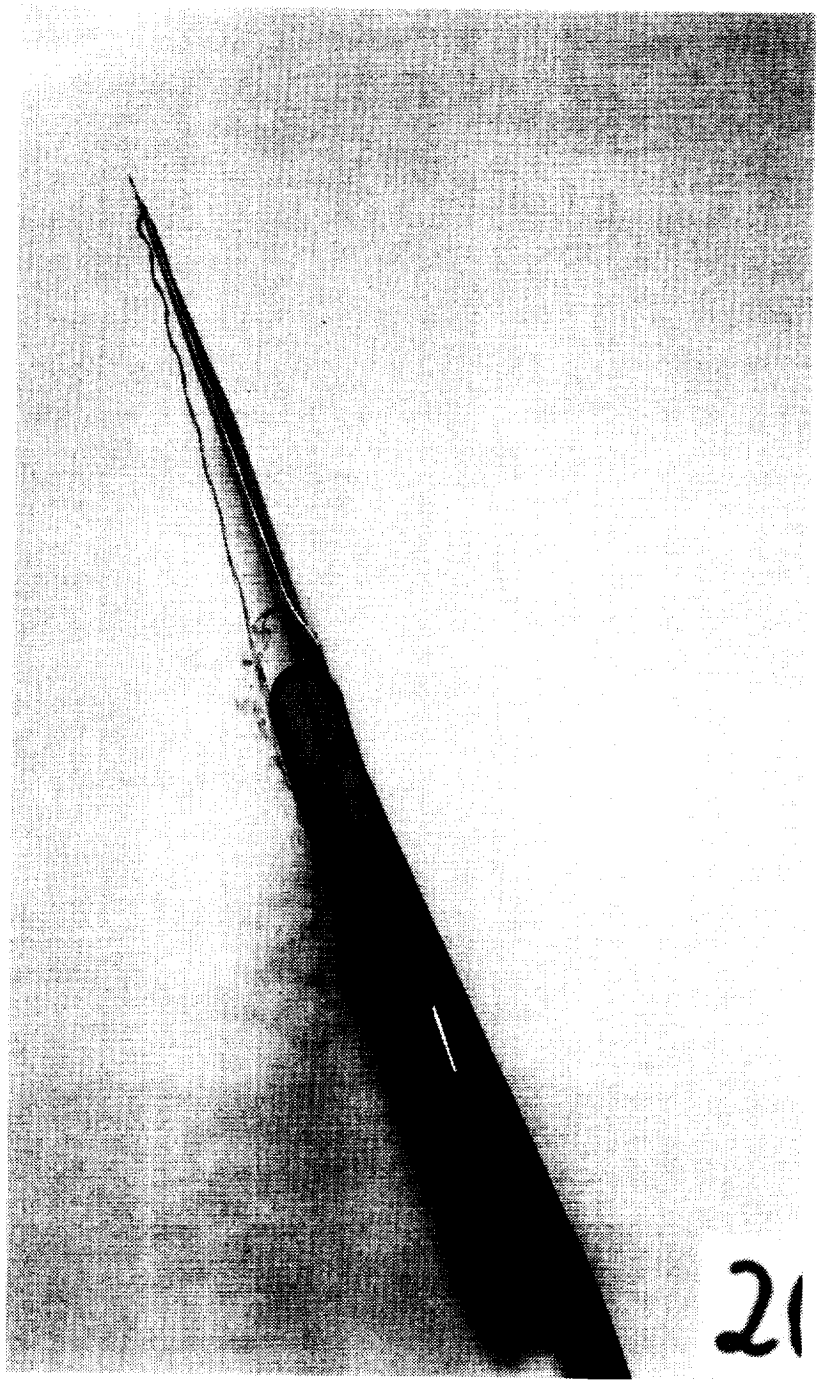

(f) Side view; $\alpha = 20°$.

Figure 12. Continued.

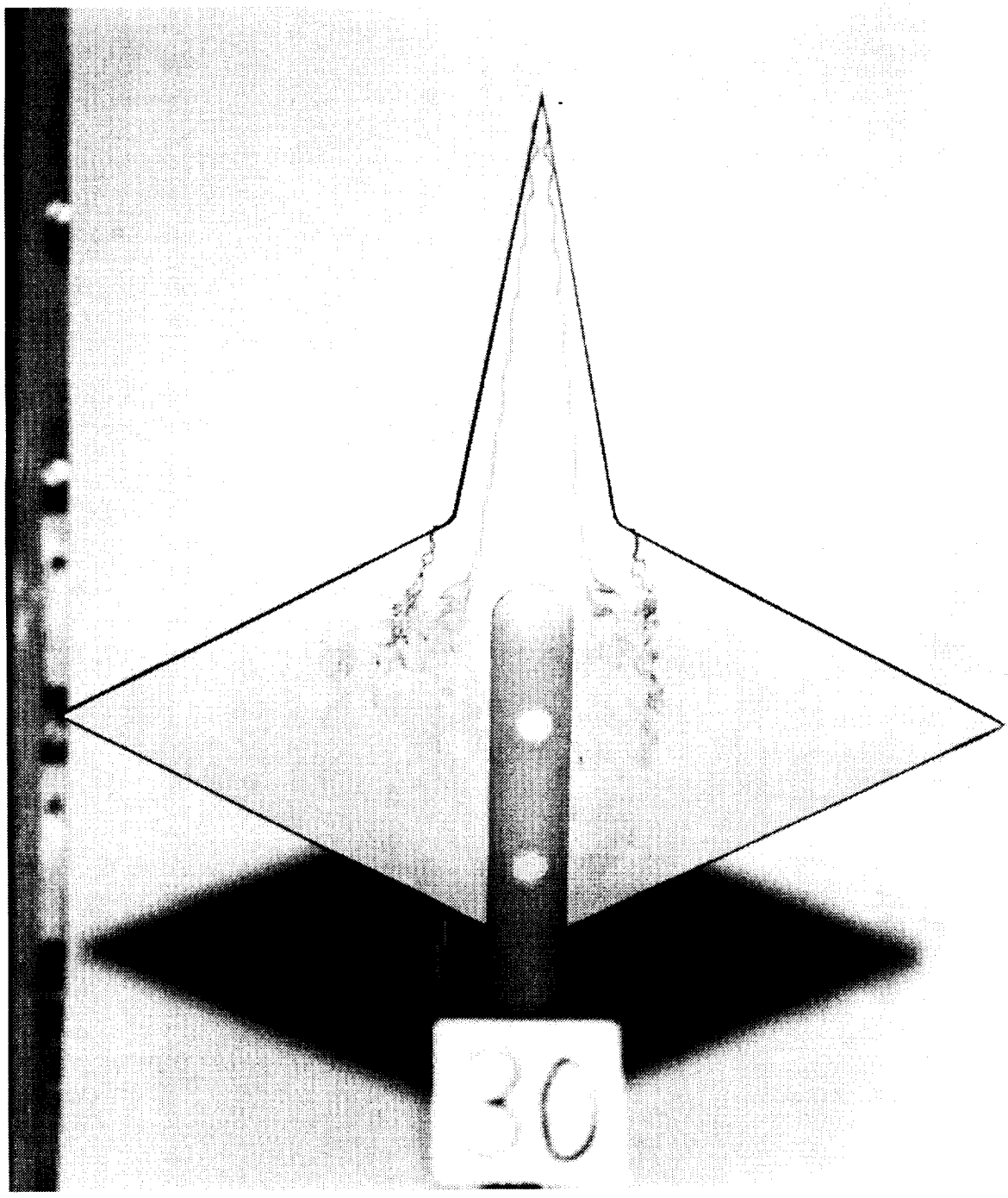

(g) Top view; $\alpha = 30°$.

Figure 12. Continued.

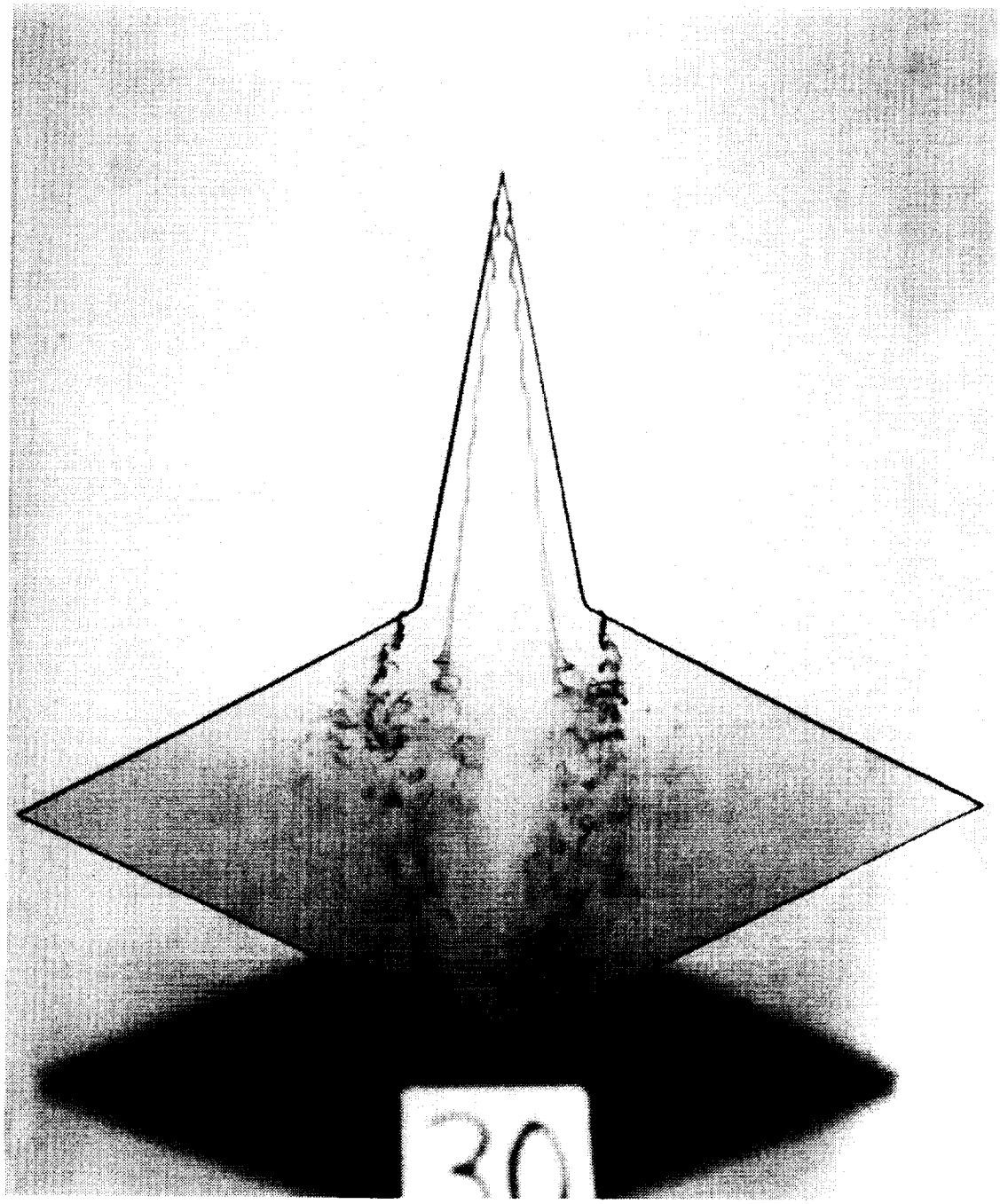

(h) Simulated balance housing removed; top view; $\alpha = 30°$.

Figure 12. Continued.

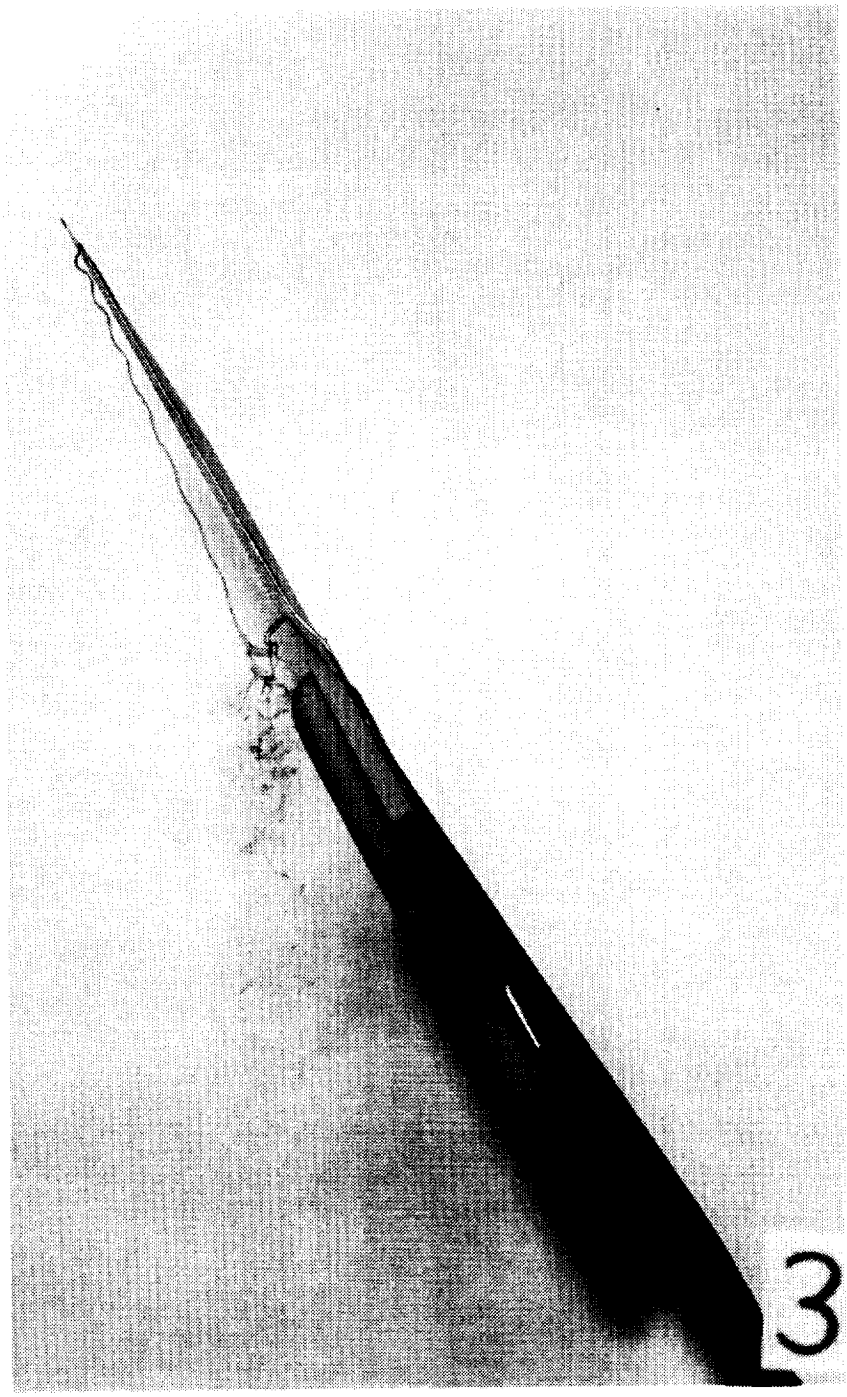

(i) Side view; $\alpha = 30°$.

Figure 12. Continued.

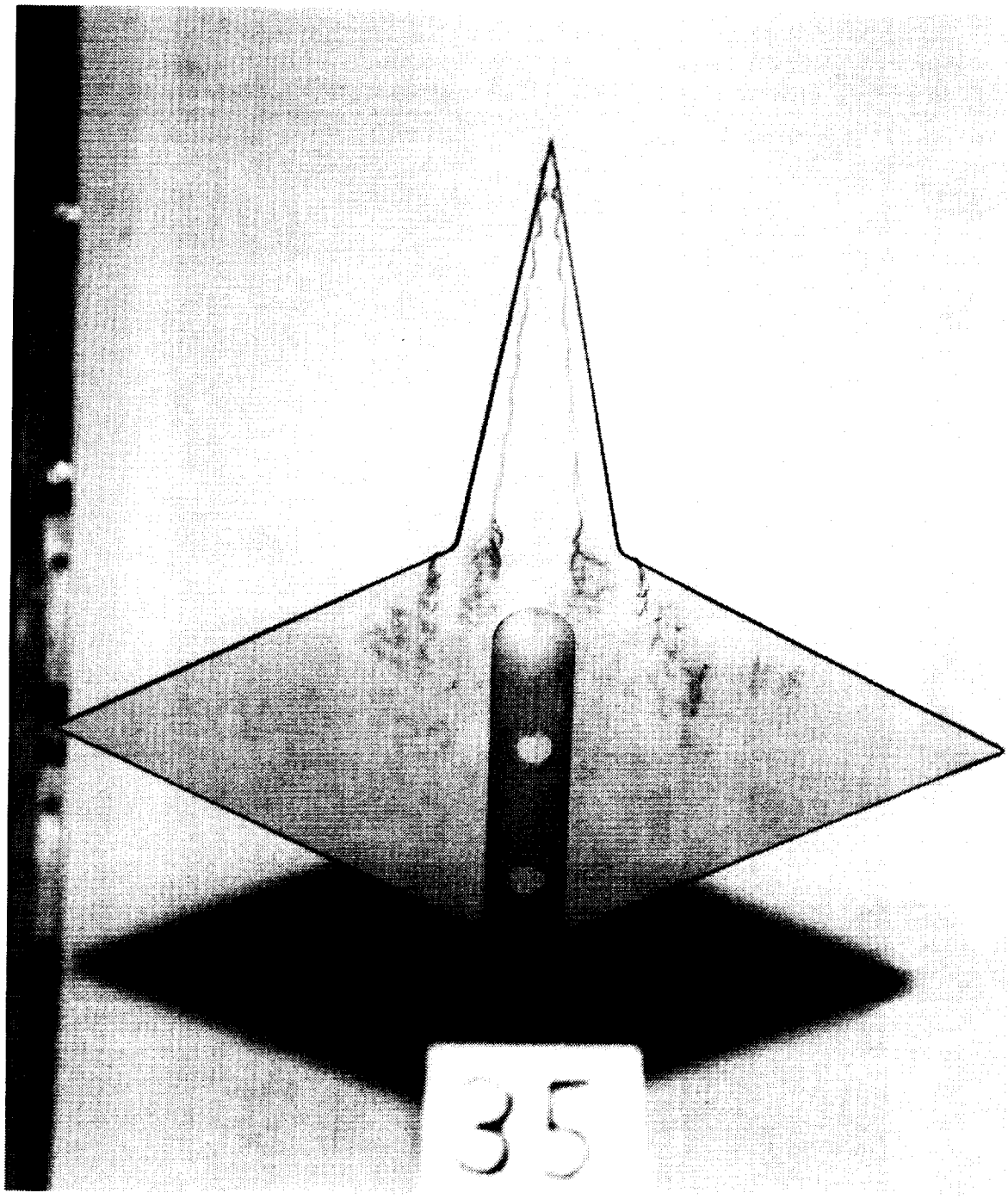

(j) Top view; $\alpha = 35°$.

Figure 12. Continued.

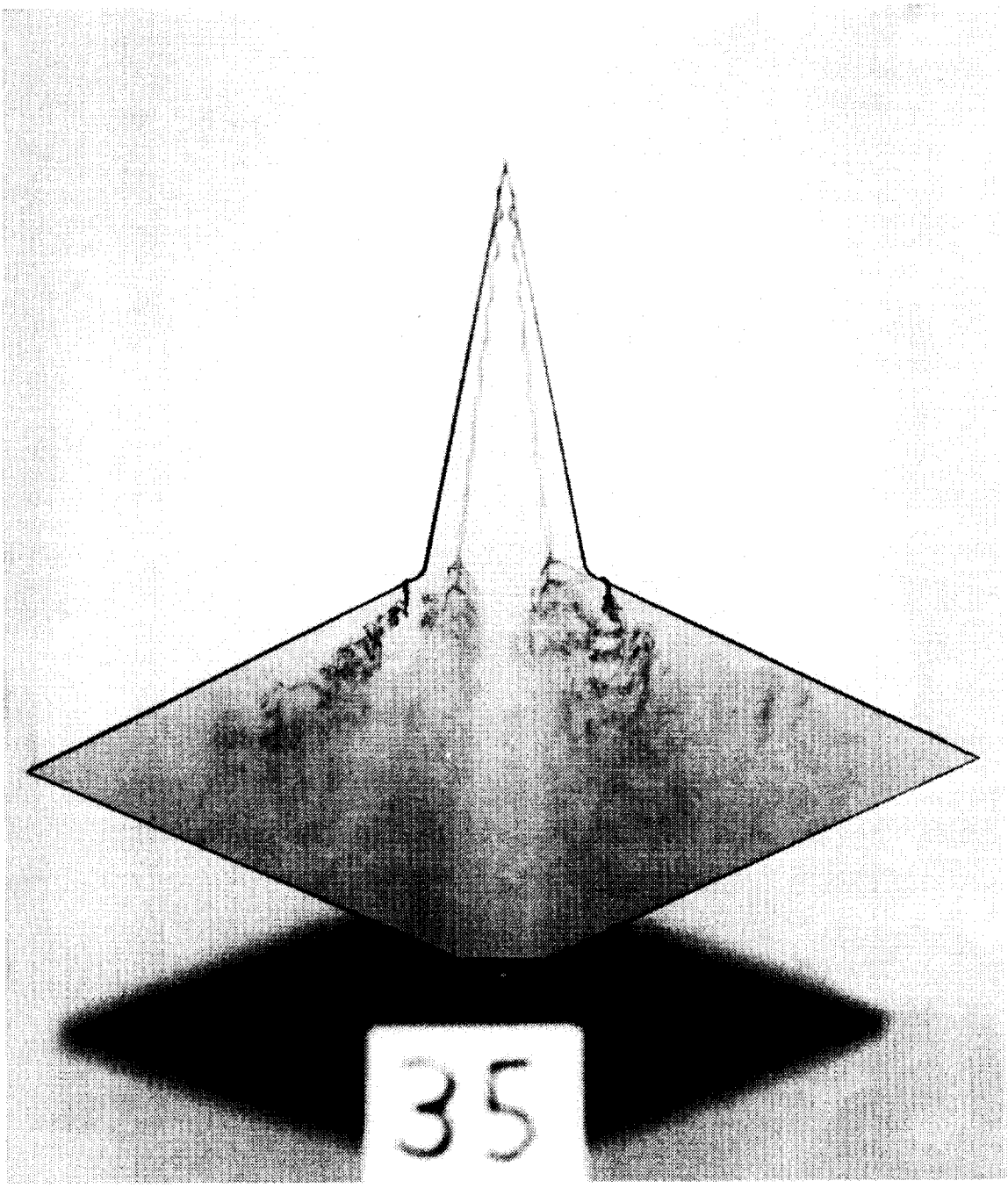

(k) Simulated balance housing removed; top view; $\alpha = 35°$.

Figure 12. Continued.

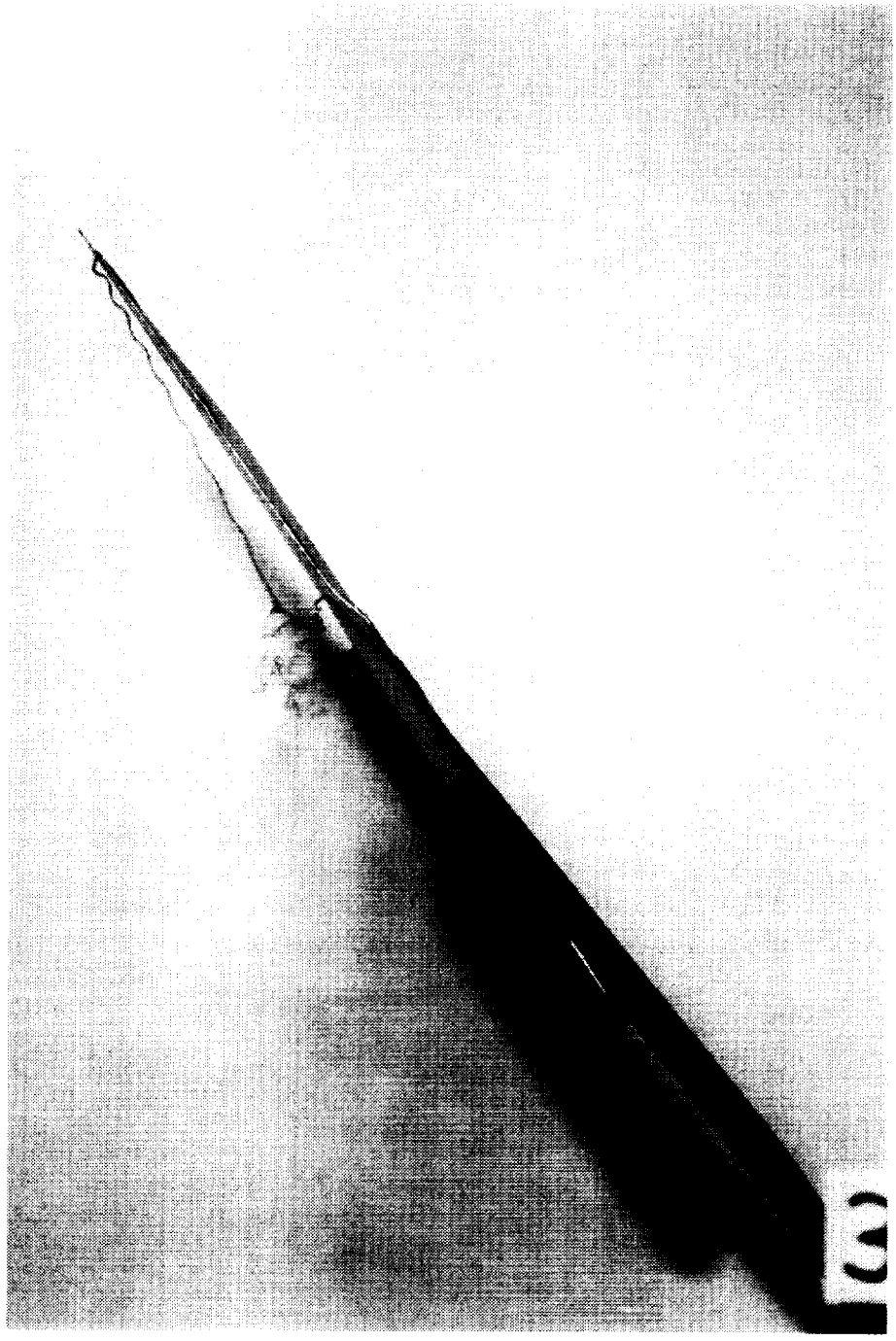

(l) Side view; $\alpha = 35°$.

Figure 12. Continued.

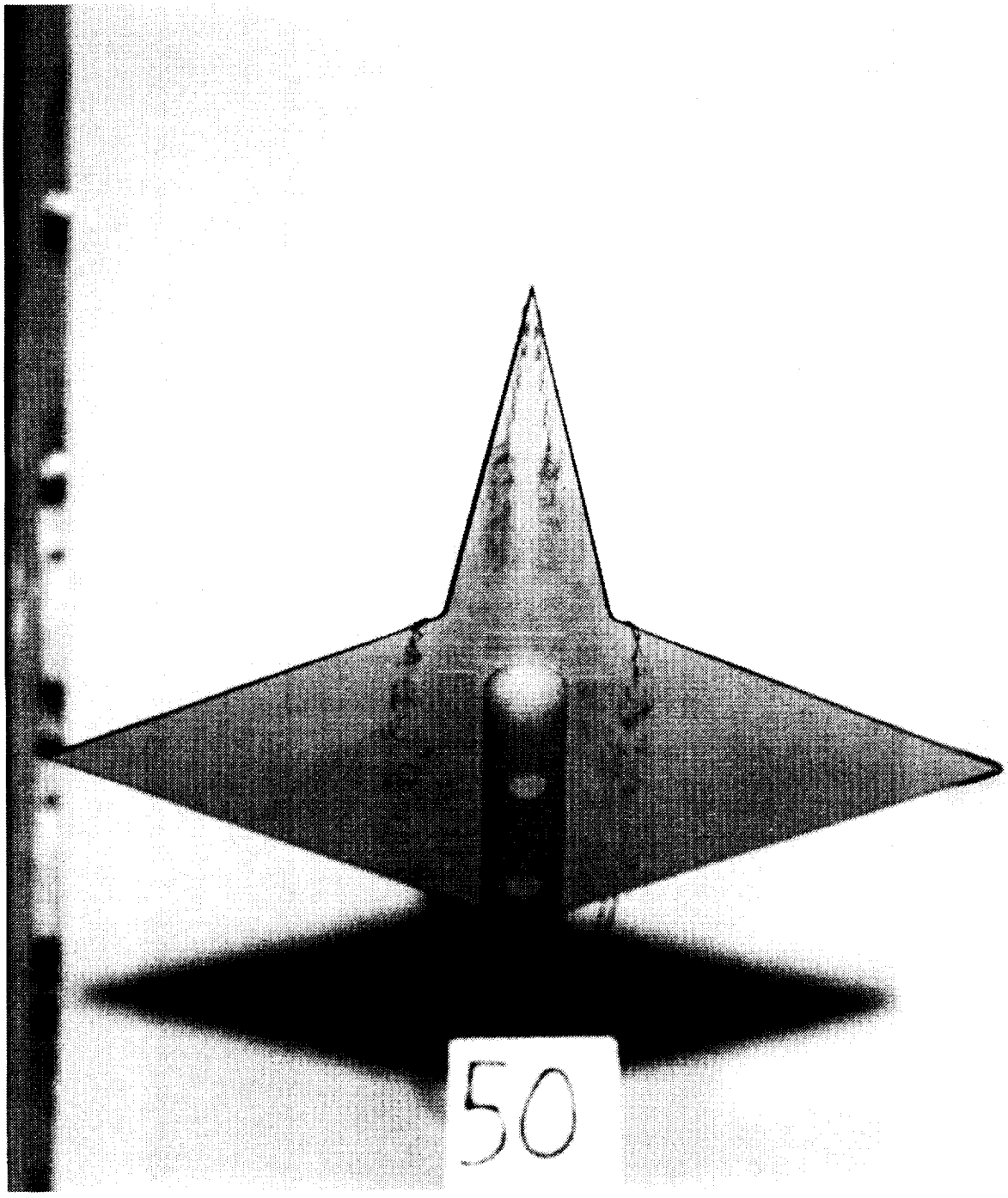

(m) Top view; $\alpha = 50°$.

Figure 12. Continued.

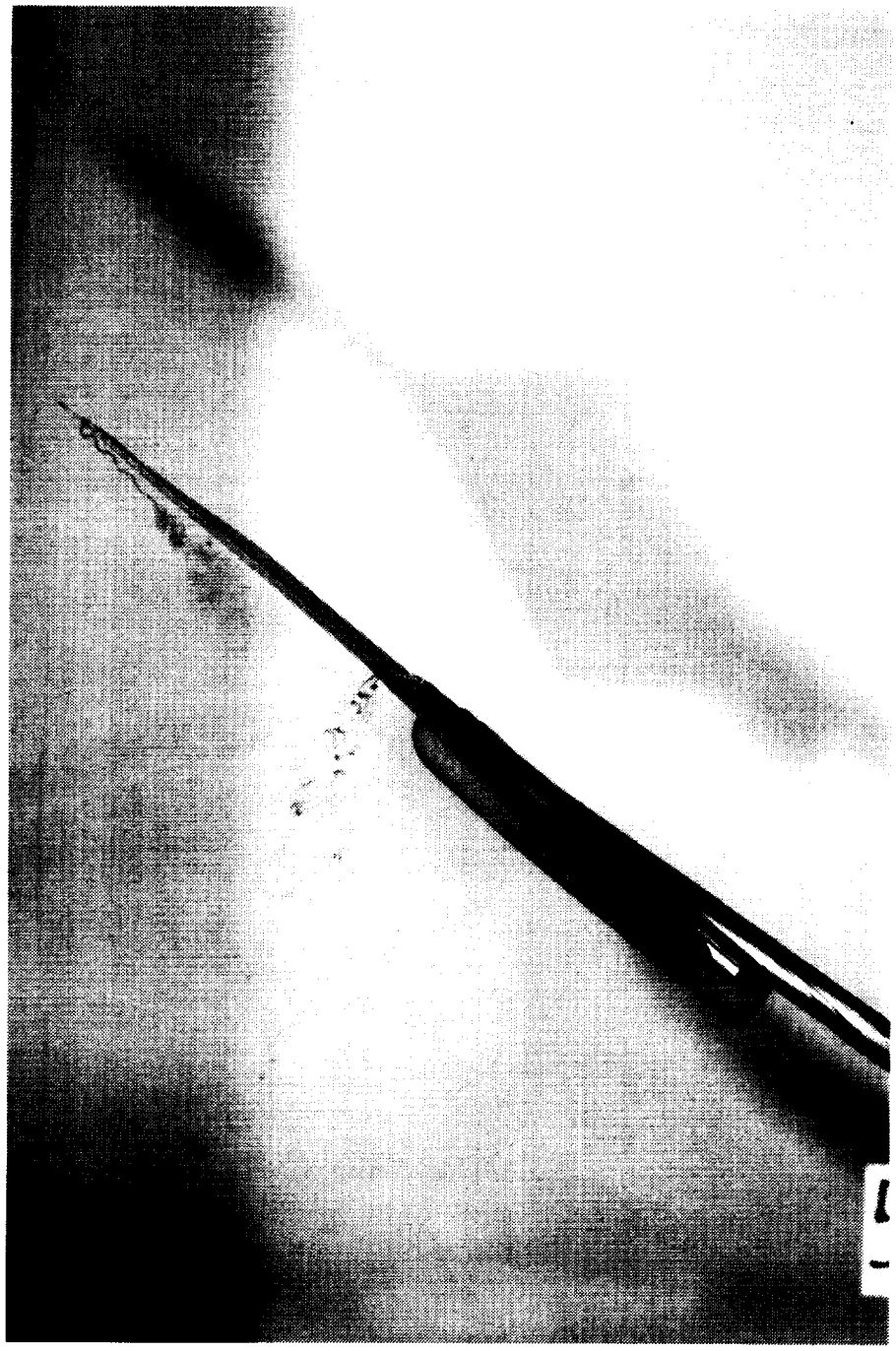

(n) Side view; $\alpha = 50°$.

Figure 12. Concluded.

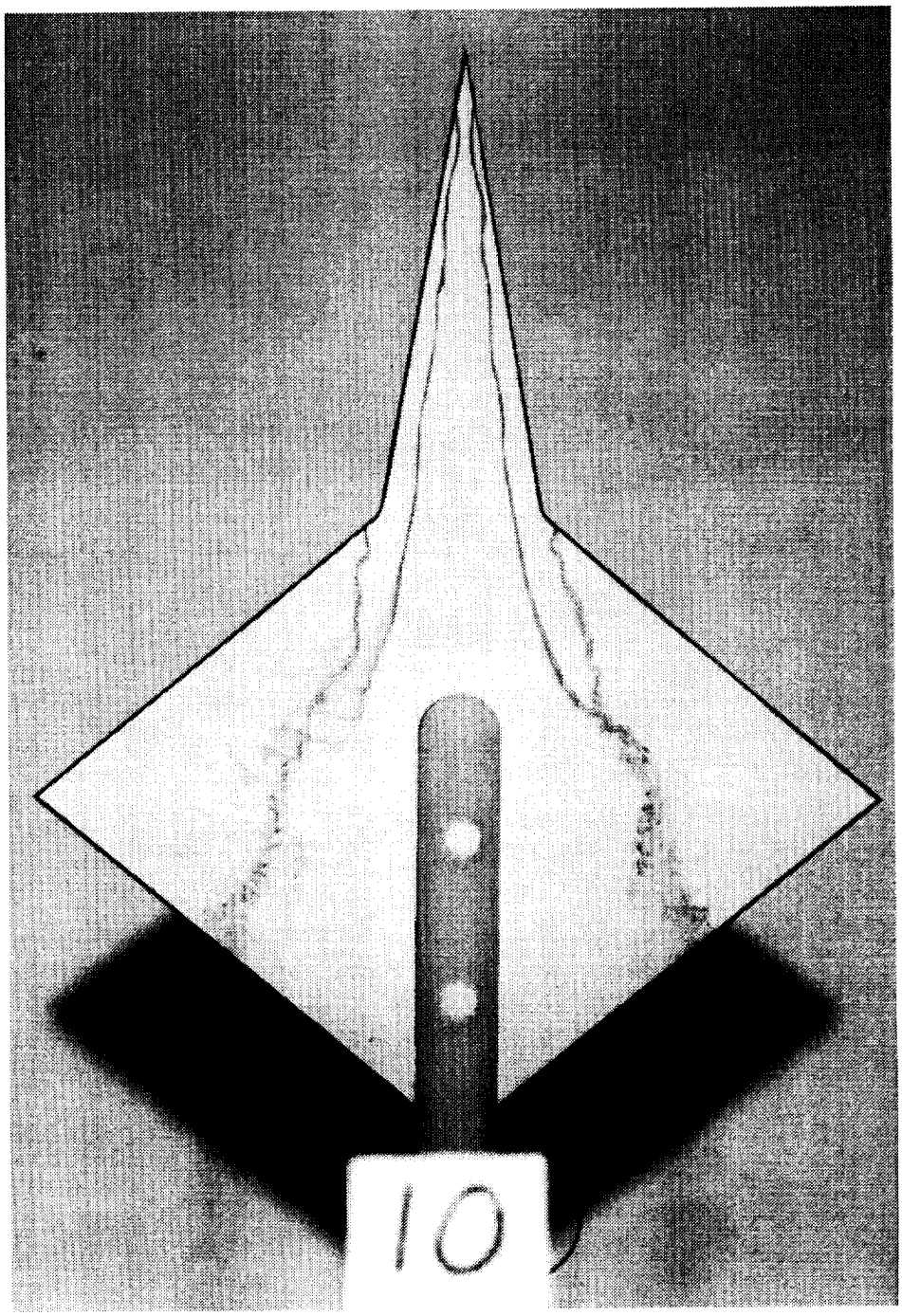

(a) Top view; $\alpha = 10°$.

Figure 13. Photographs of 40° diamond wing.

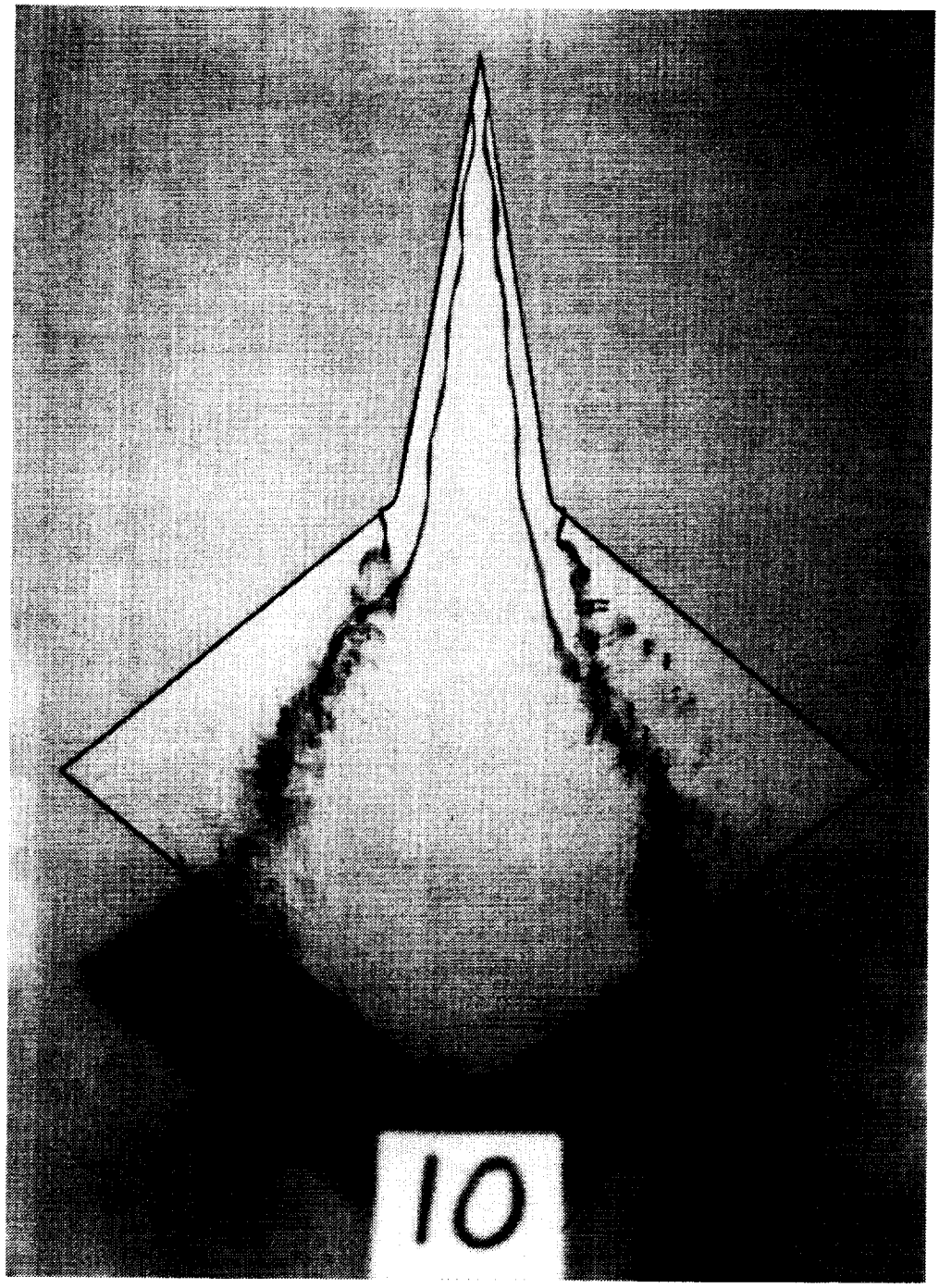

(b) Simulated balance housing removed; top view; $\alpha = 10°$.

Figure 13. Continued.

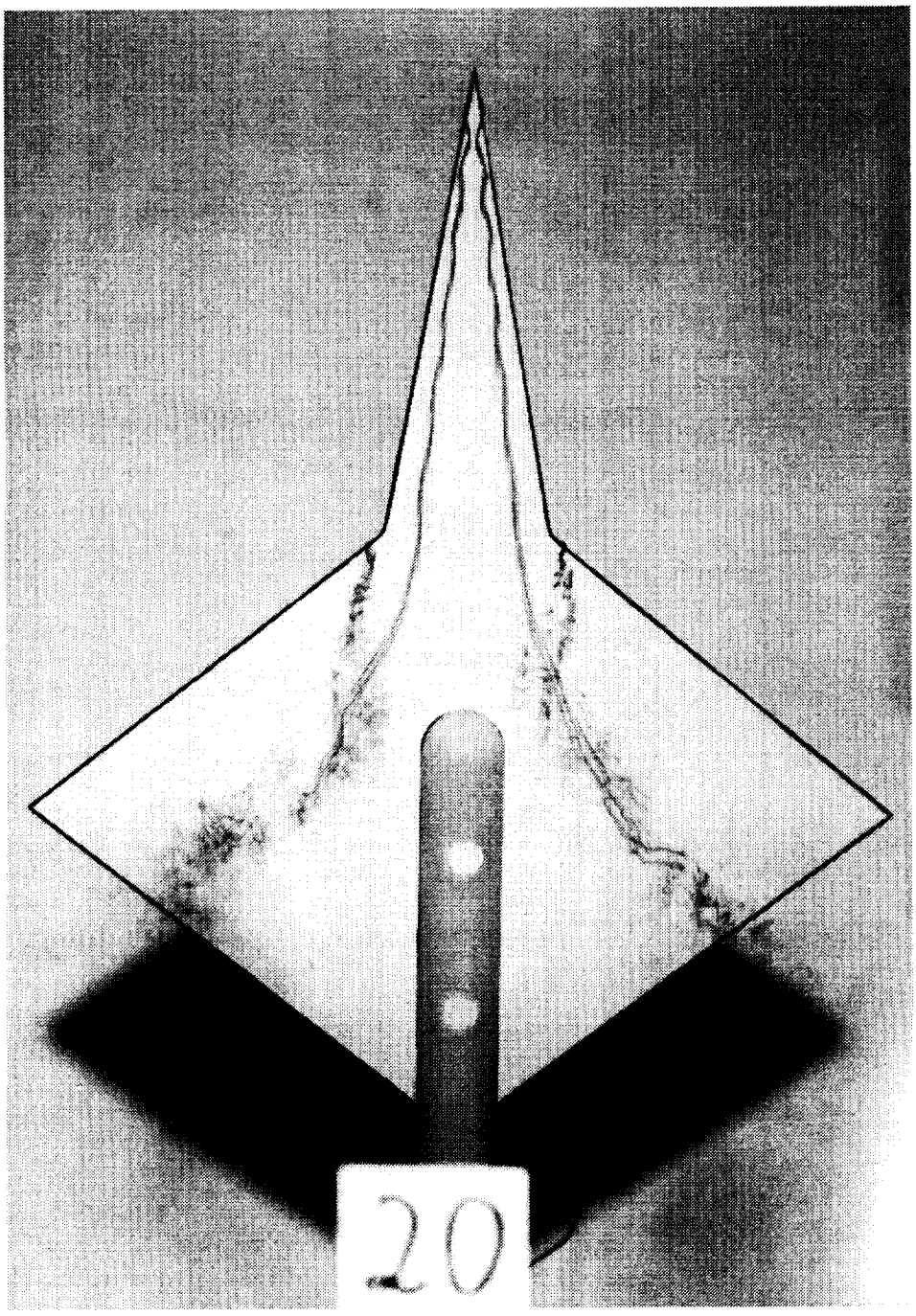

(c) Top view; $\alpha = 20°$.

Figure 13. Continued.

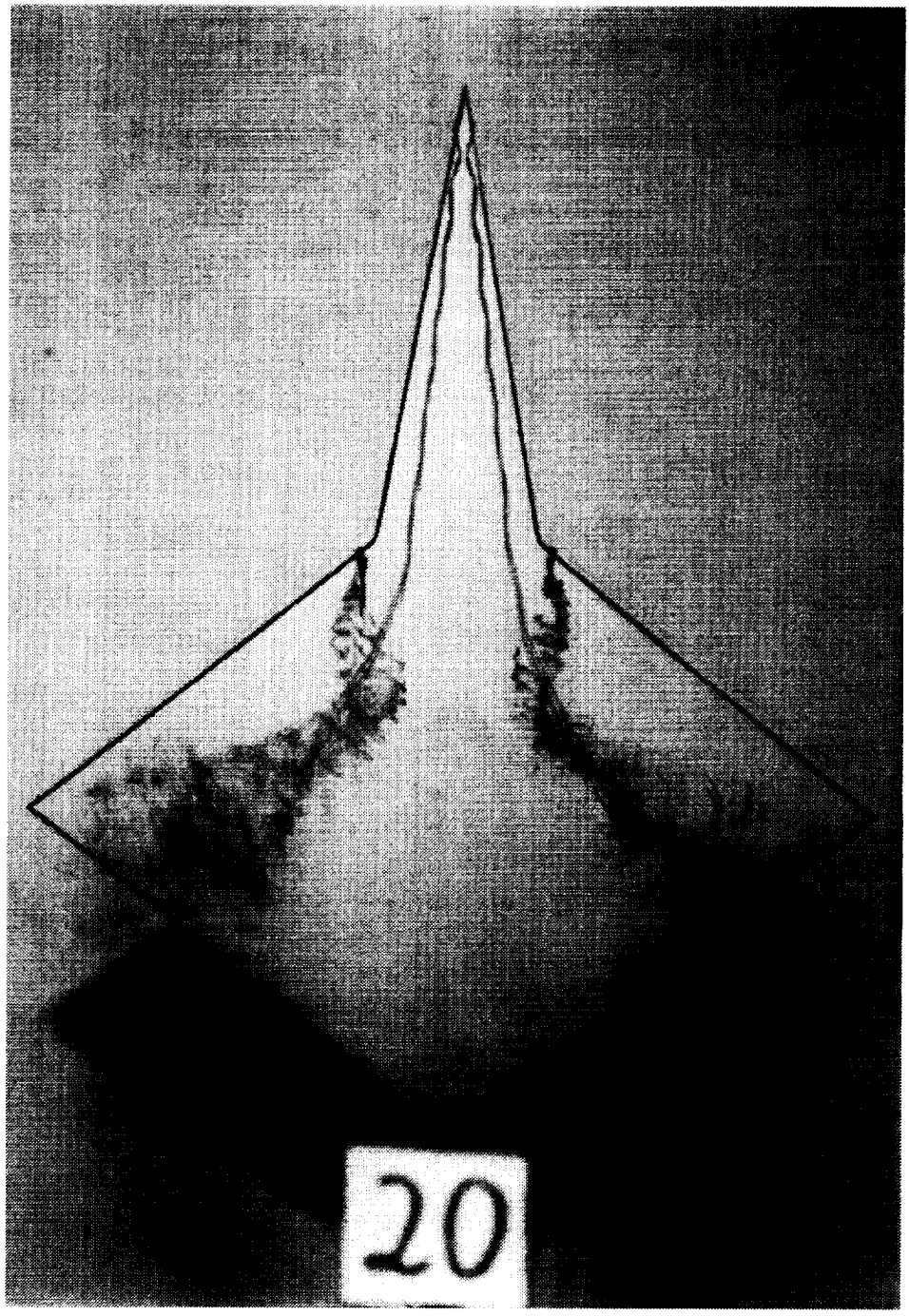

(d) Simulated balance housing removed; top view; $\alpha = 20°$.

Figure 13. Continued.

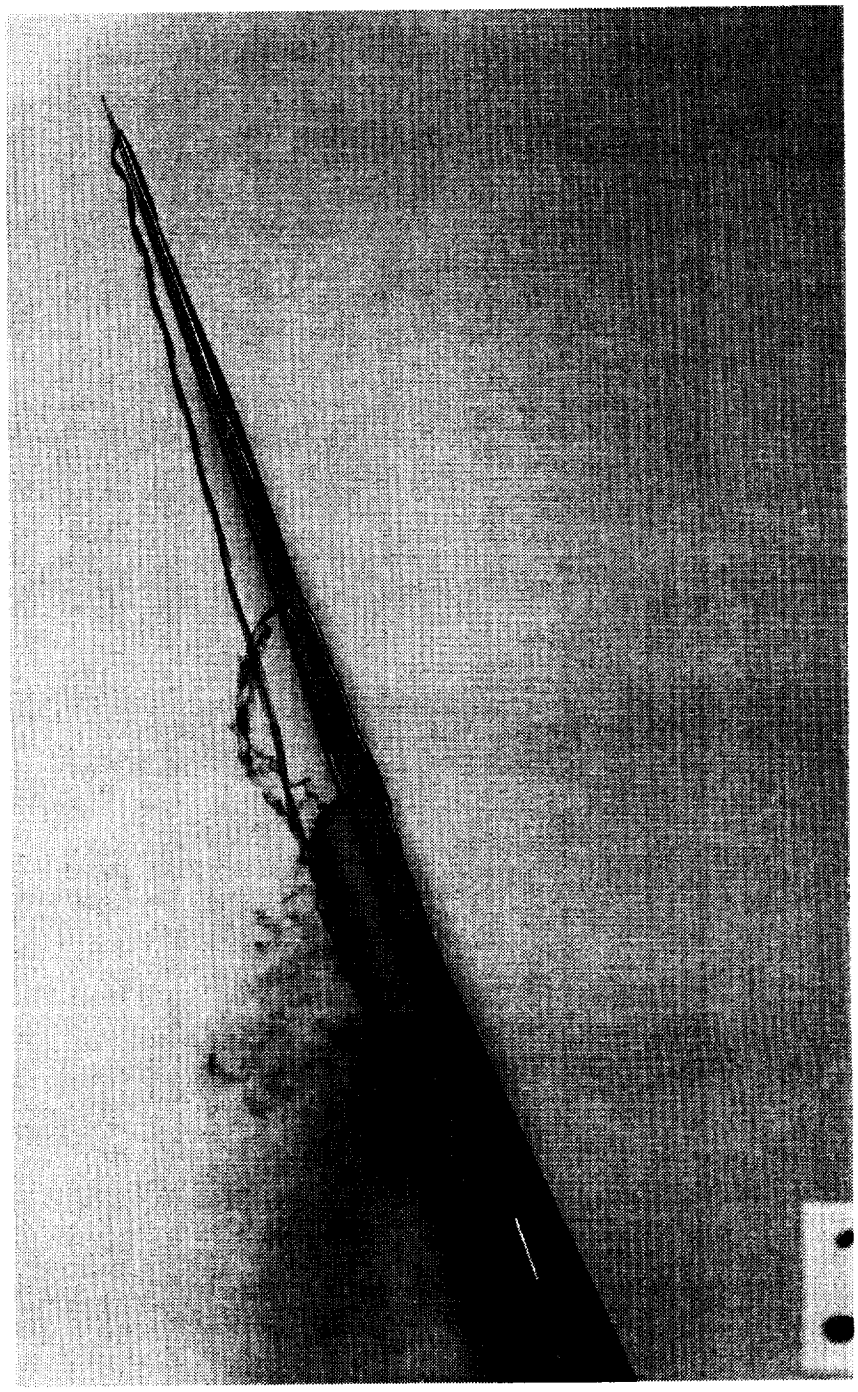

(e) Side view; $\alpha = 20°$.

Figure 13. Continued.

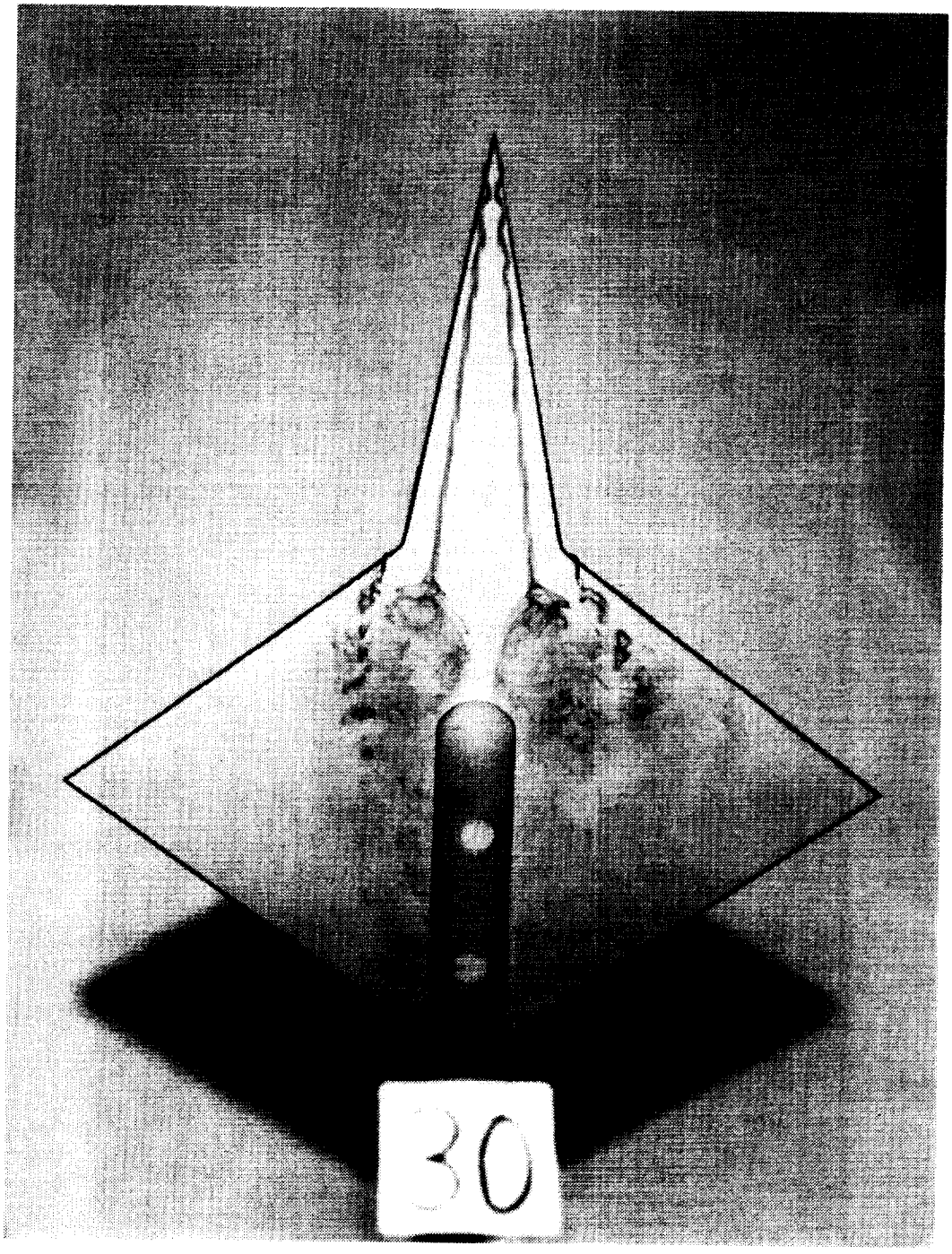

(f) Symmetric forebody vortex bursting; top view; $\alpha = 30°$.

Figure 13. Continued.

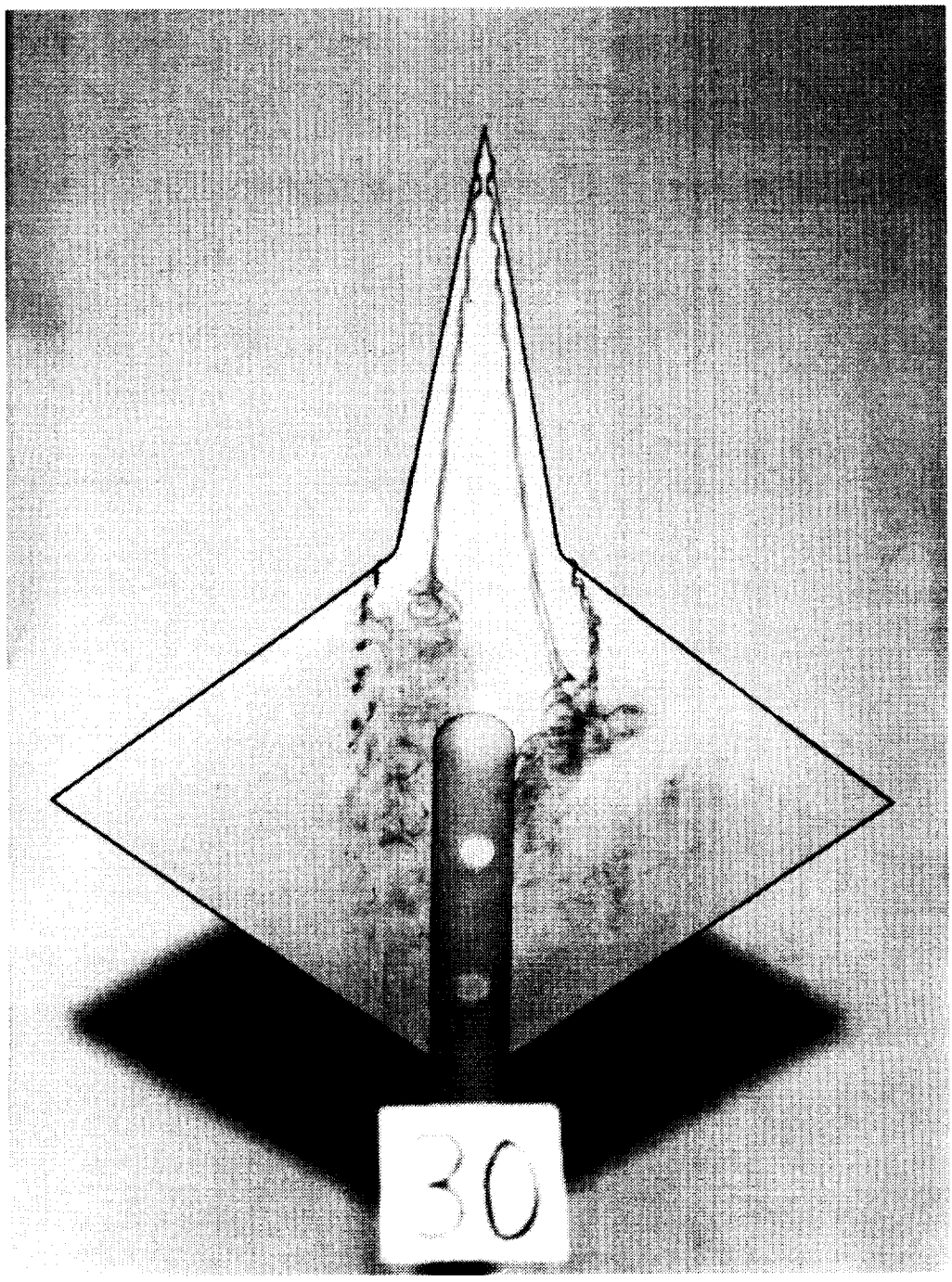

(g) Left-hand forebody vortex bursts first; top view; $\alpha = 30°$.

Figure 13. Continued.

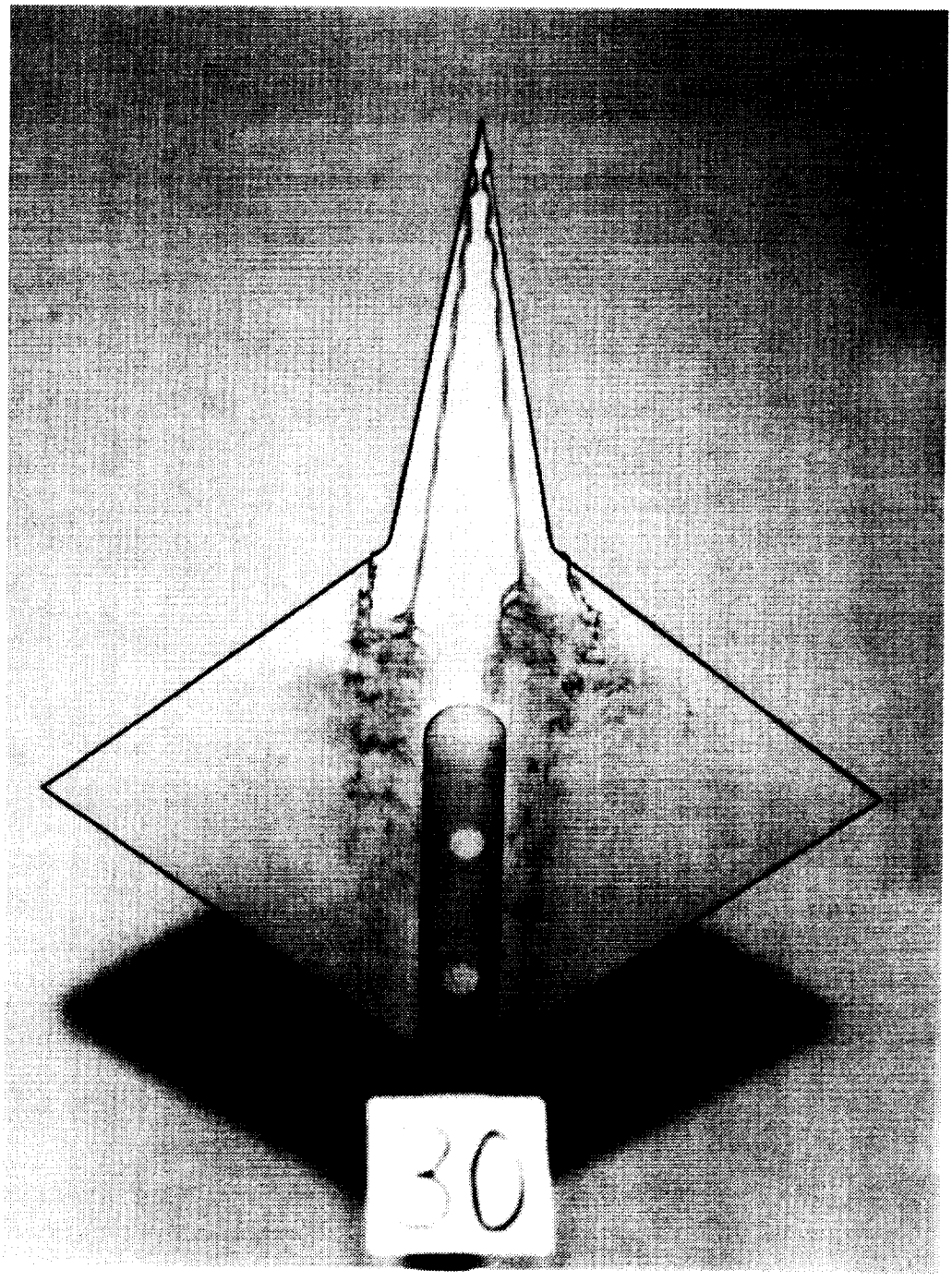

(h) Right-hand forebody vortex bursts first; top view; $\alpha = 30°$.

Figure 13. Continued.

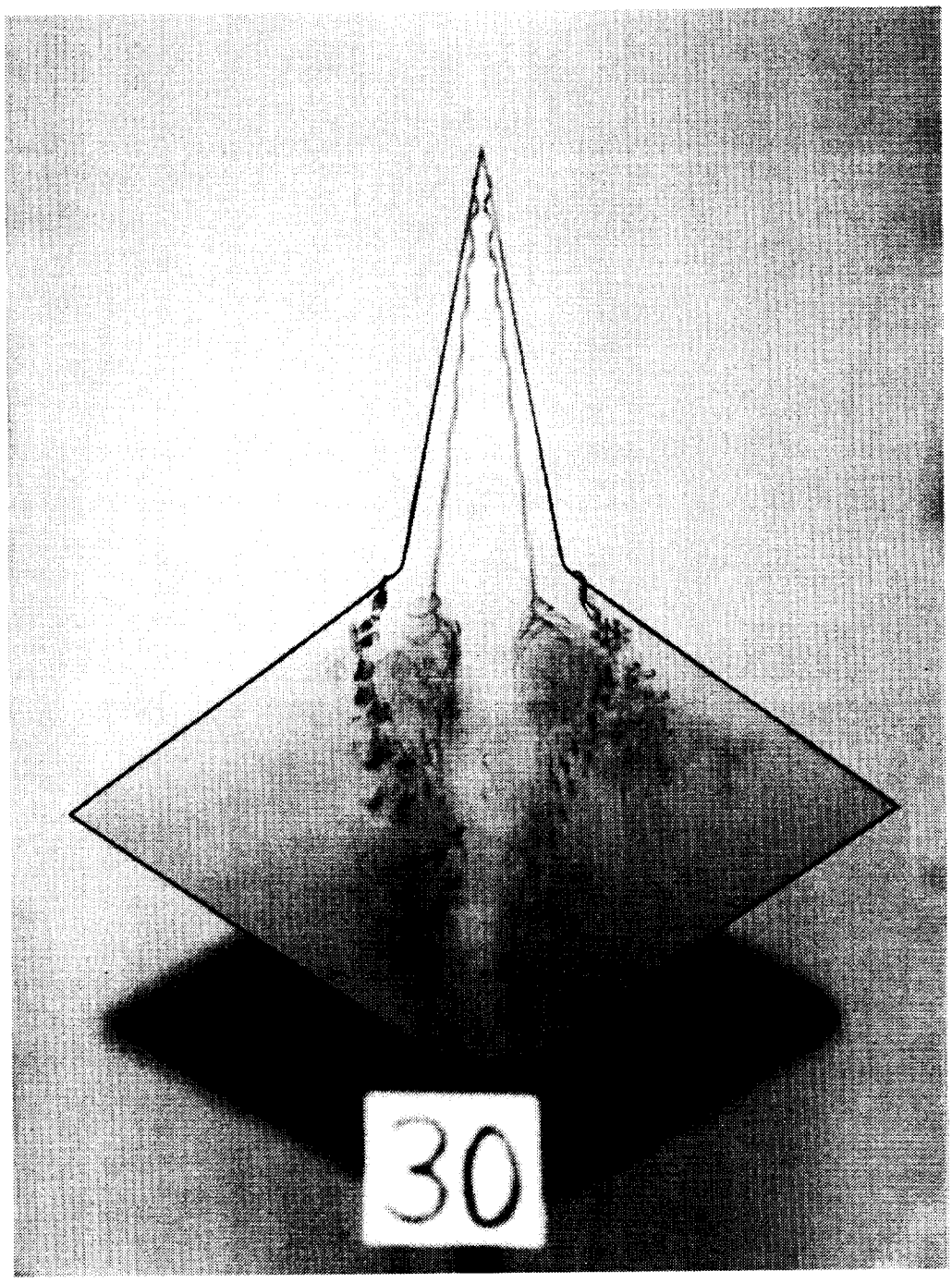

(i) Simulated balance housing removed; top view; $\alpha = 30°$.

Figure 13. Continued.

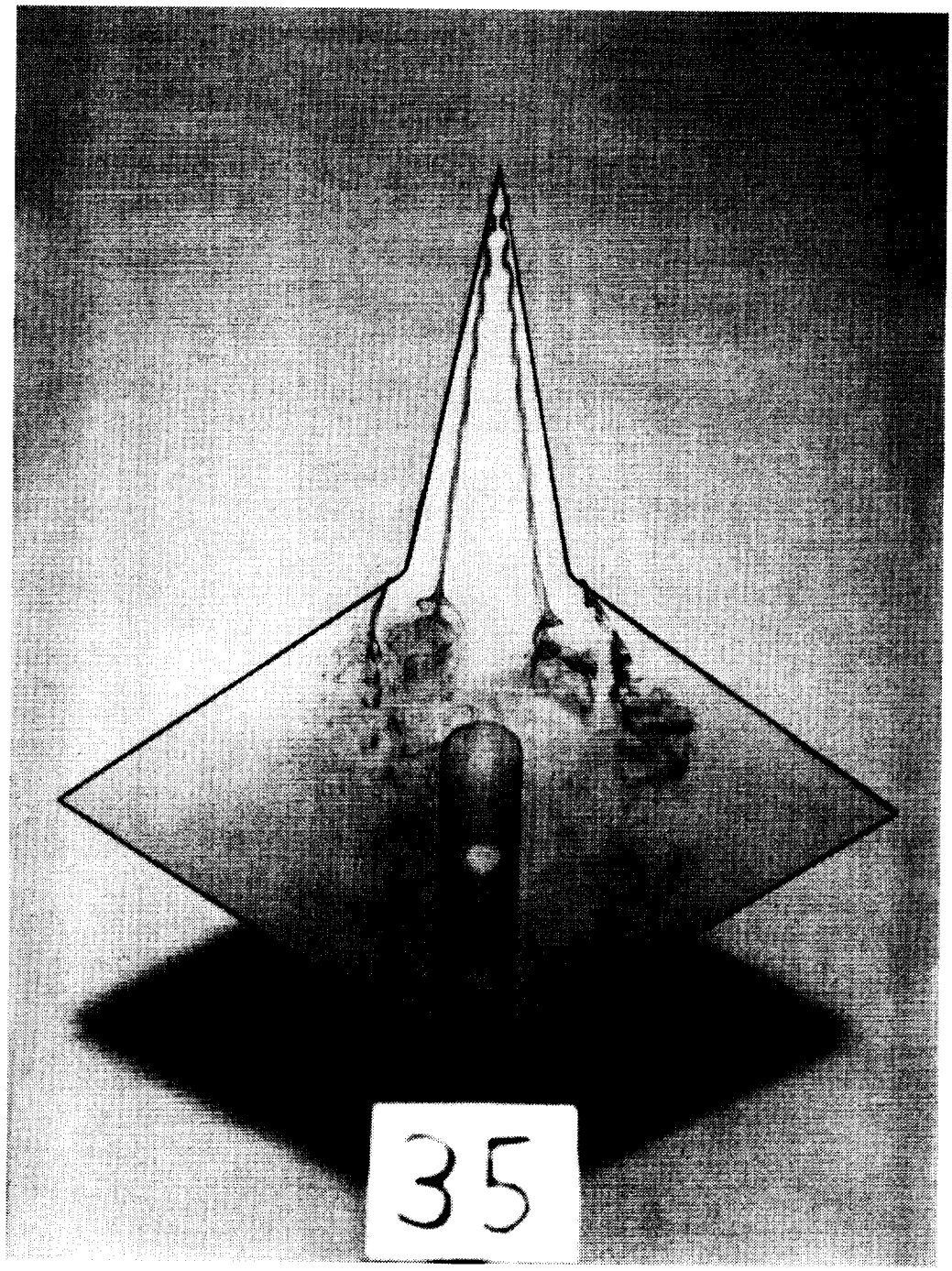

(j) Top view; $\alpha = 35°$.

Figure 13. Continued.

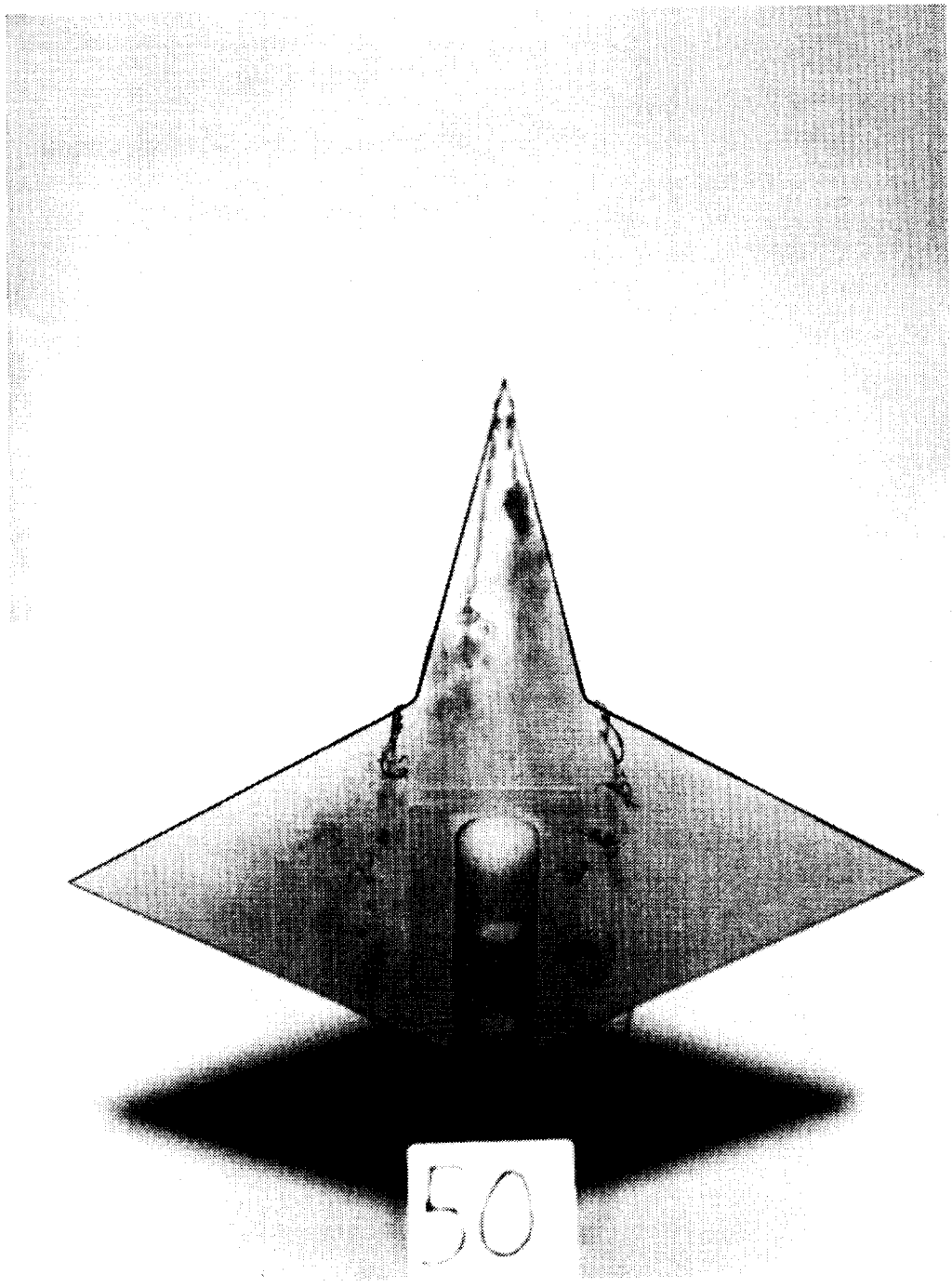

(k) Top view; $\alpha = 50°$.

Figure 13. Concluded.

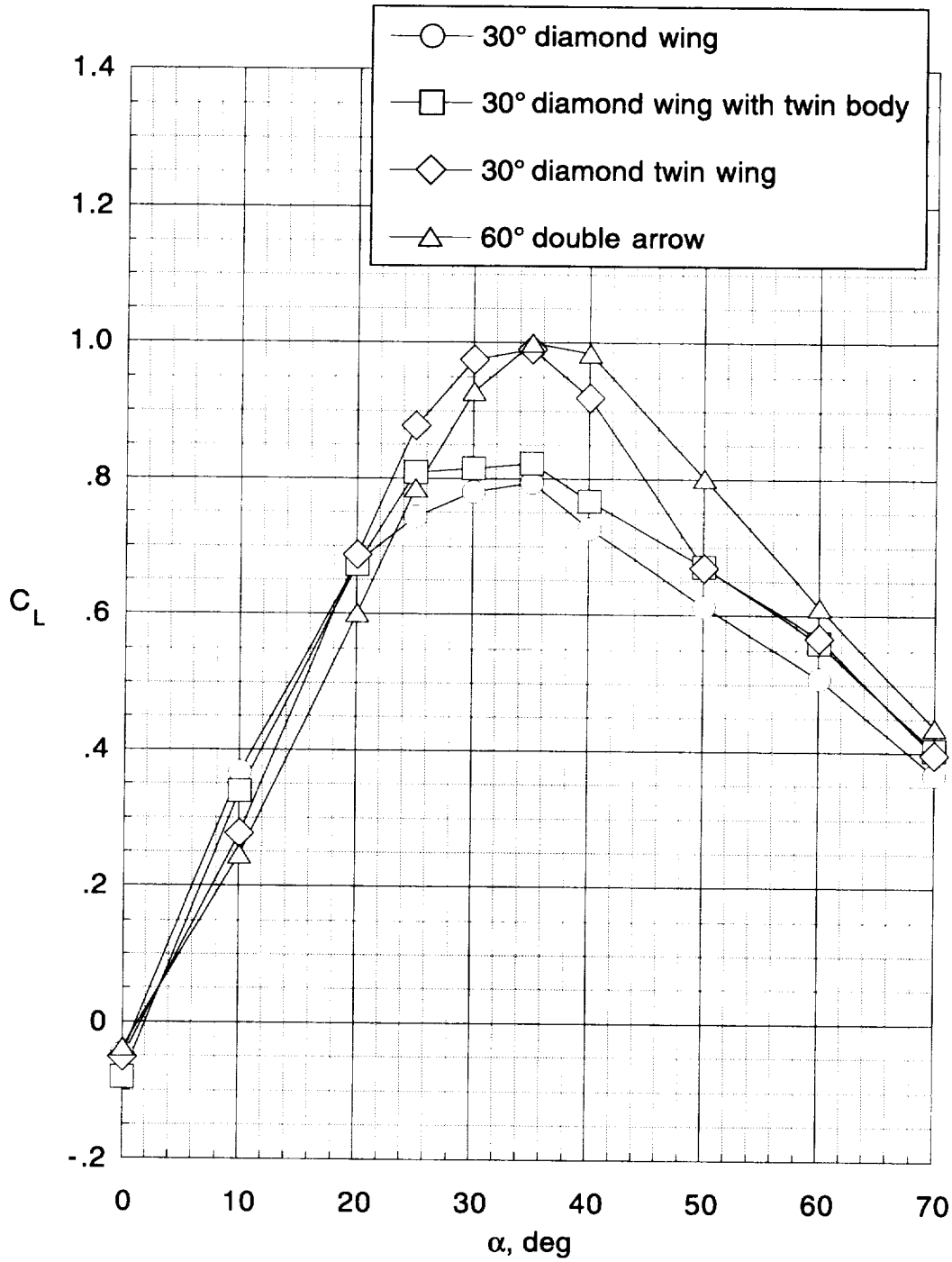

Figure 14. Lift coefficient versus angle of attack for twin-body and double-wing configurations (ref. 14).

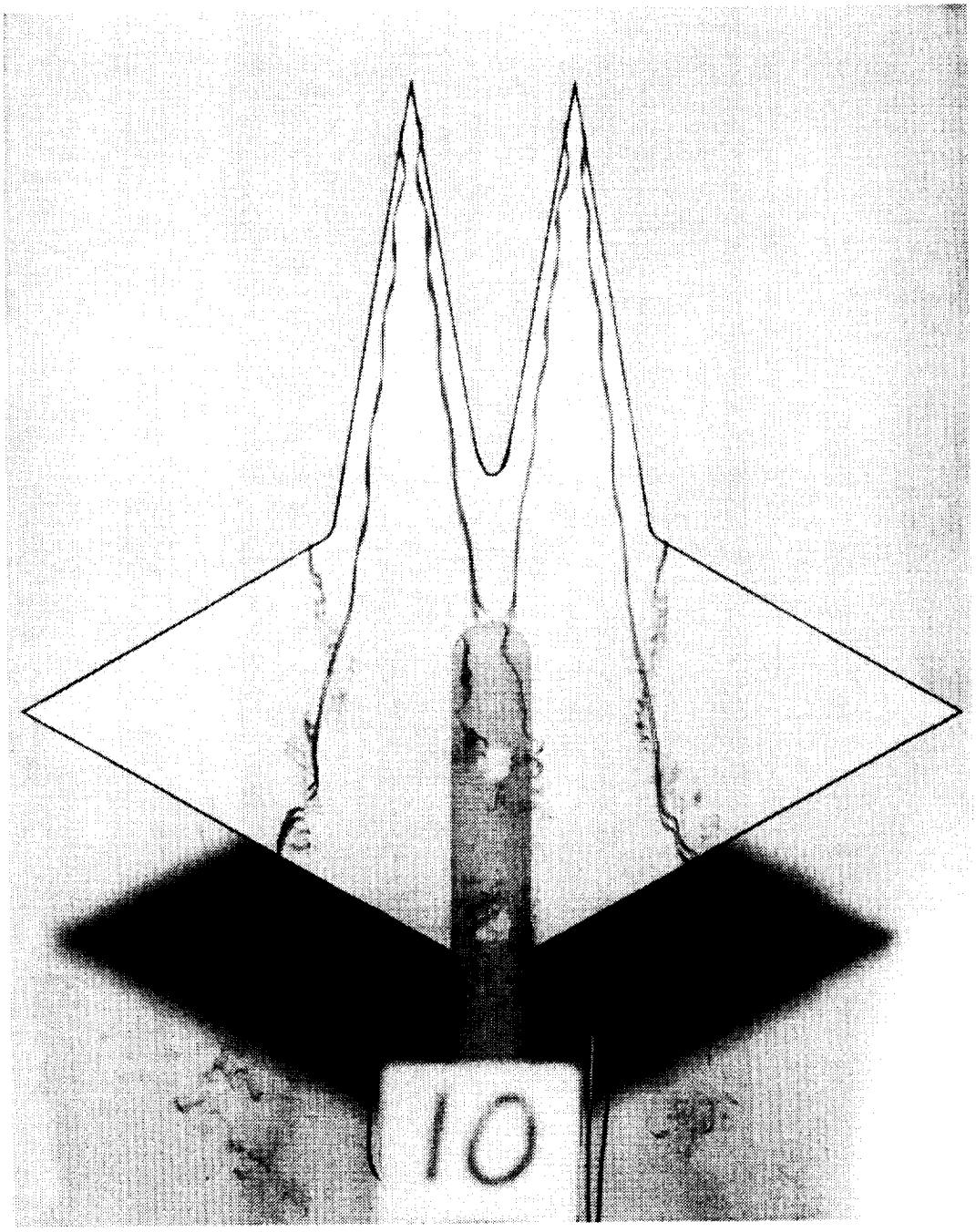

(a) Top view; $\alpha = 10°$.

Figure 15. Photographs of 30° diamond wing with twin body.

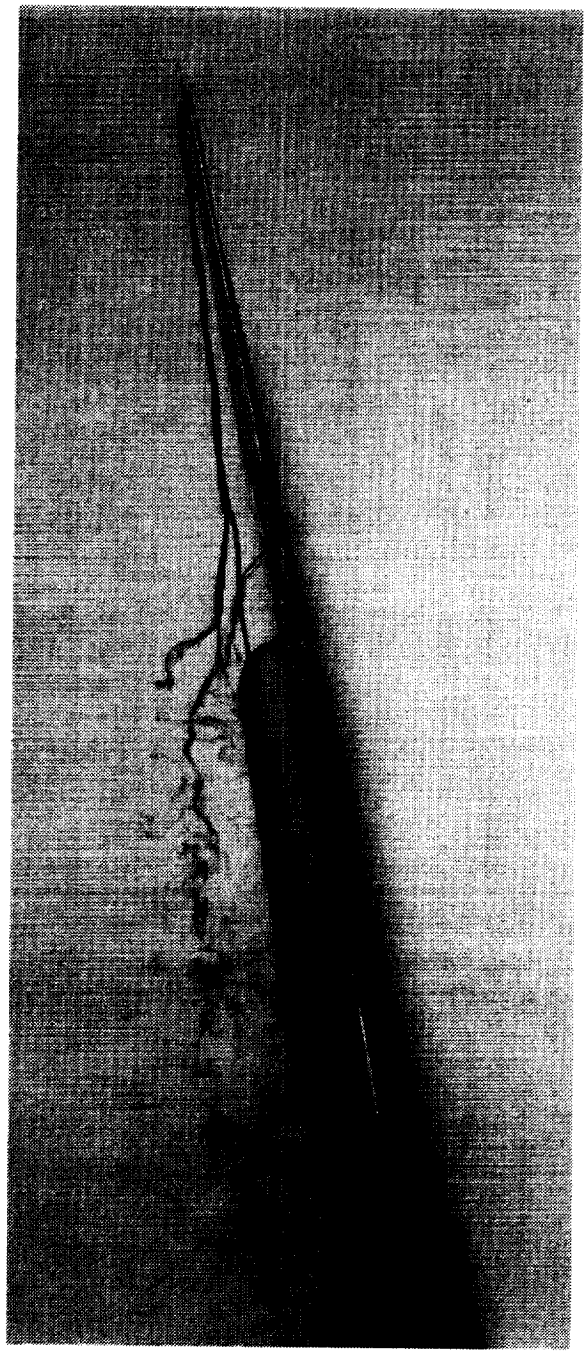

(b) Side view; $\alpha = 10°$.

Figure 15. Continued.

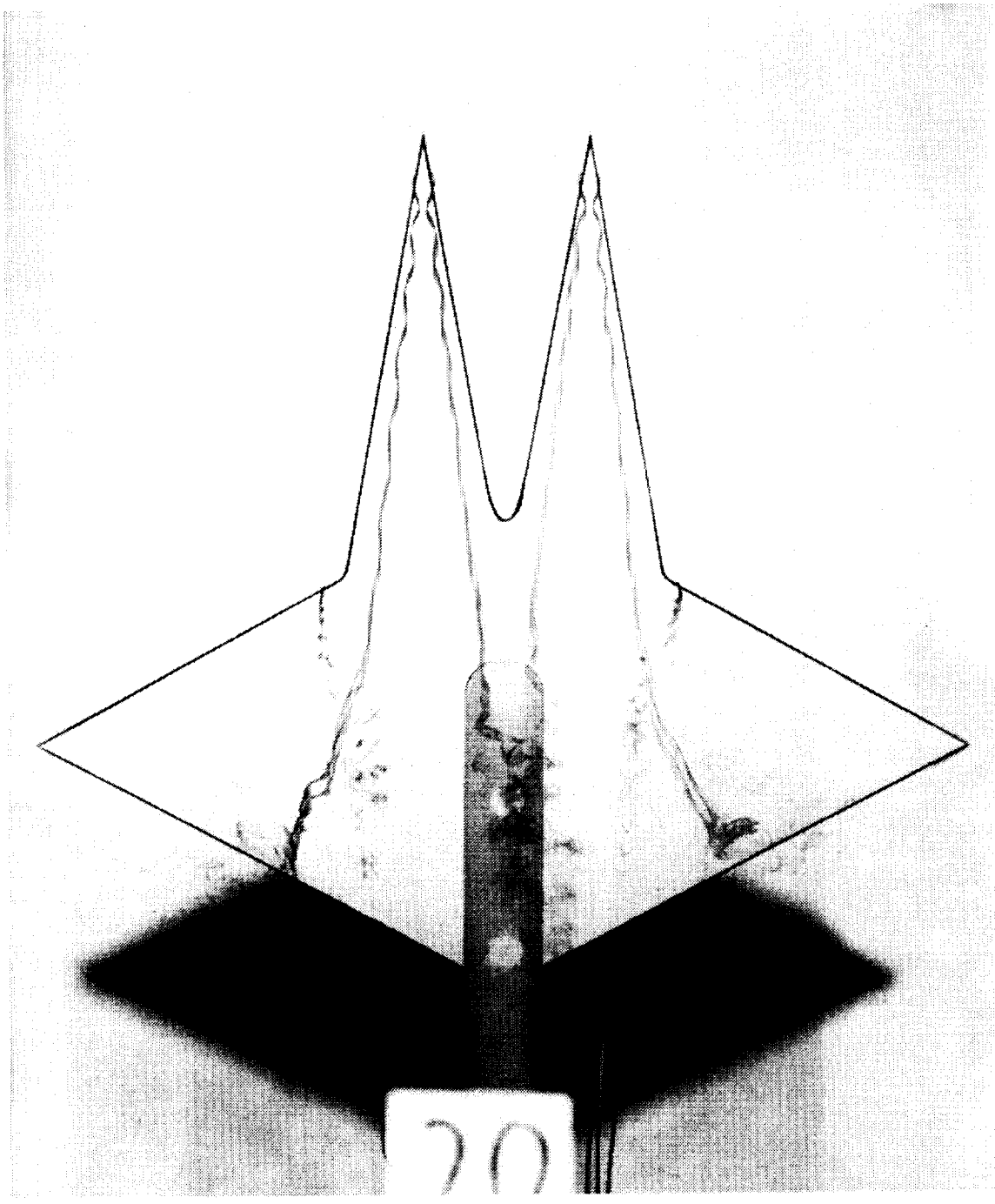

(c) Top view; $\alpha = 20°$.

Figure 15. Continued.

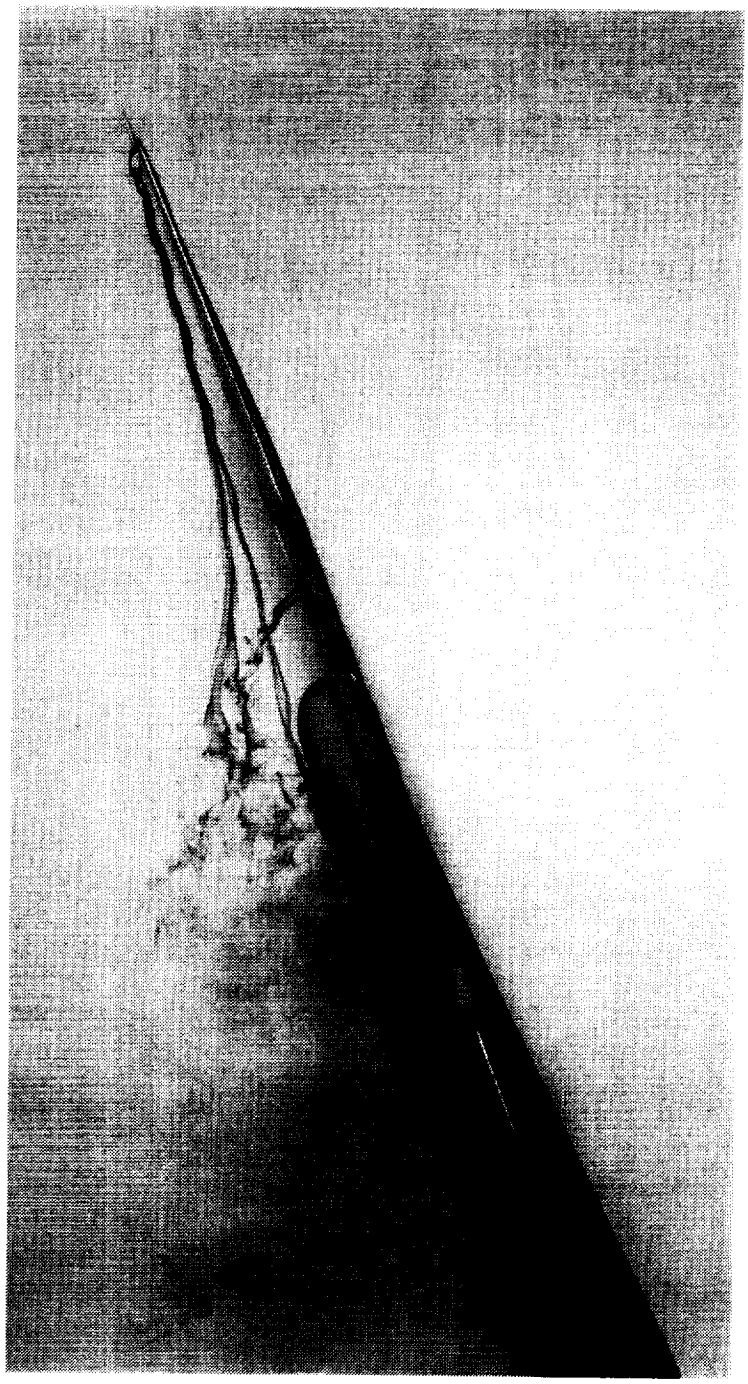

(d) Side view; $\alpha = 20°$.

Figure 15. Continued.

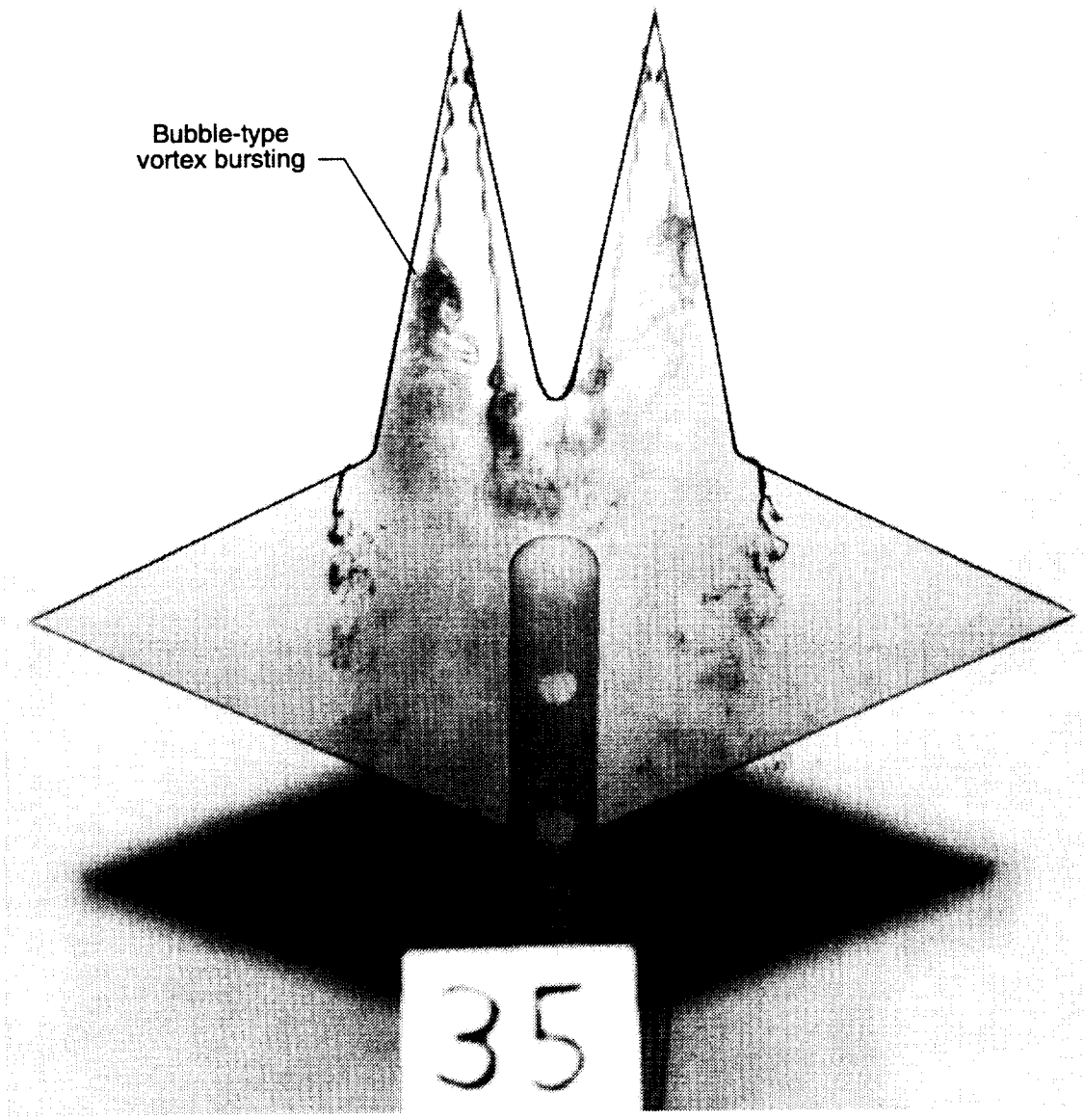

(e) Bubble-type vortex bursting; top view; $\alpha = 35°$.

Figure 15. Continued.

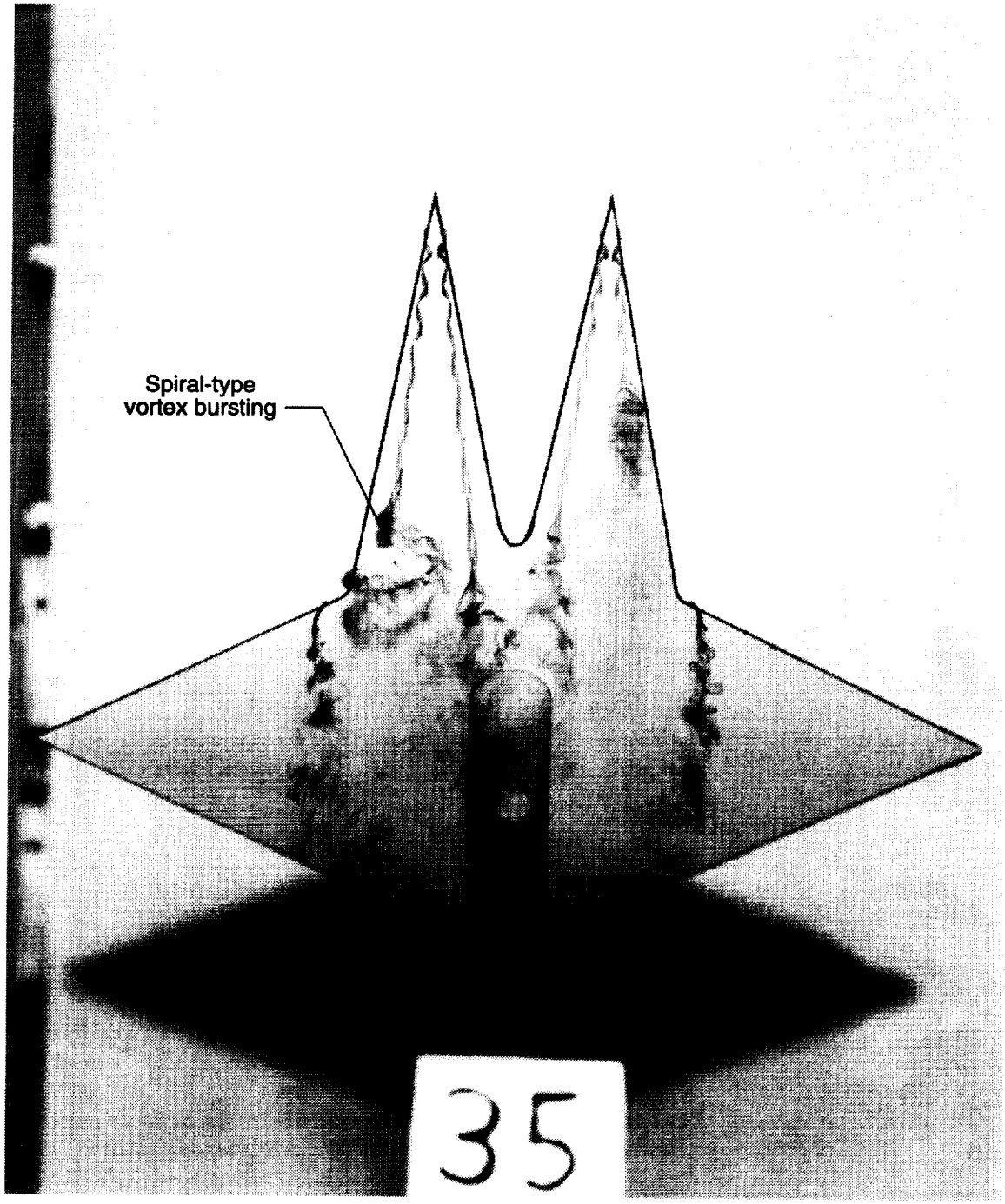

(f) Spiral-type vortex bursting; top view; $\alpha = 35°$.

Figure 15. Continued.

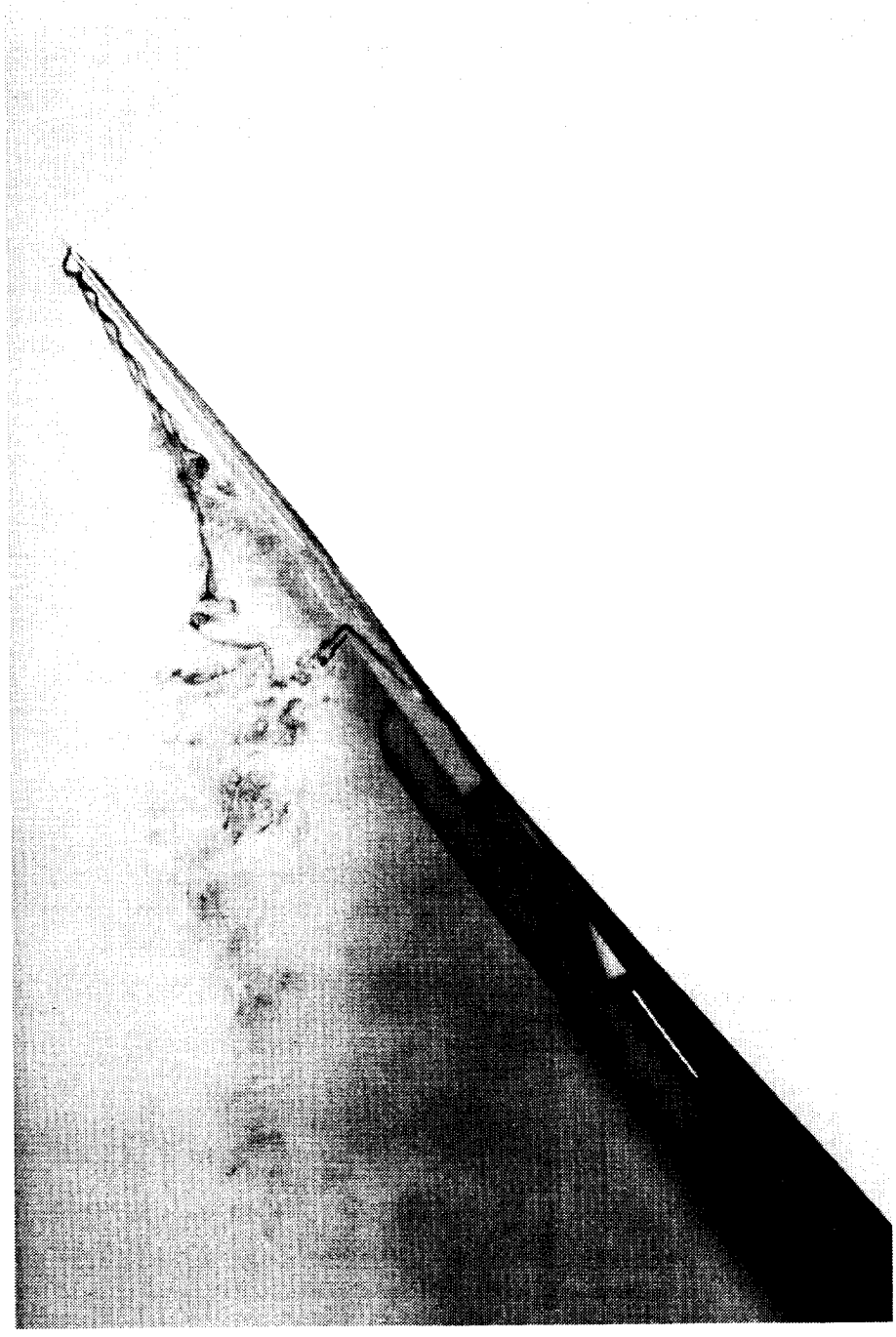

(g) Side view; $\alpha = 35°$.

Figure 15. Continued.

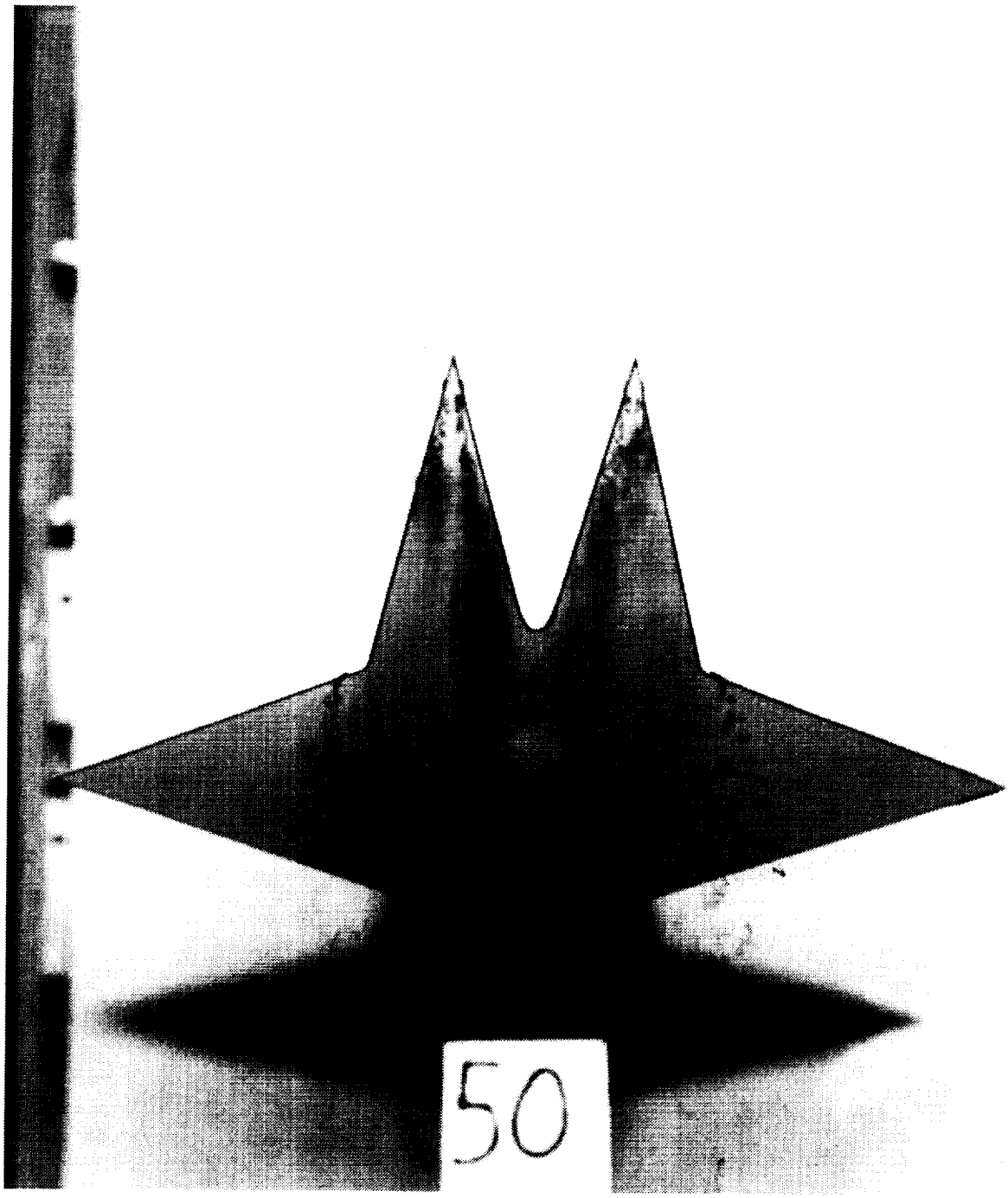

(h) Top view; $\alpha = 50°$.

Figure 15. Continued.

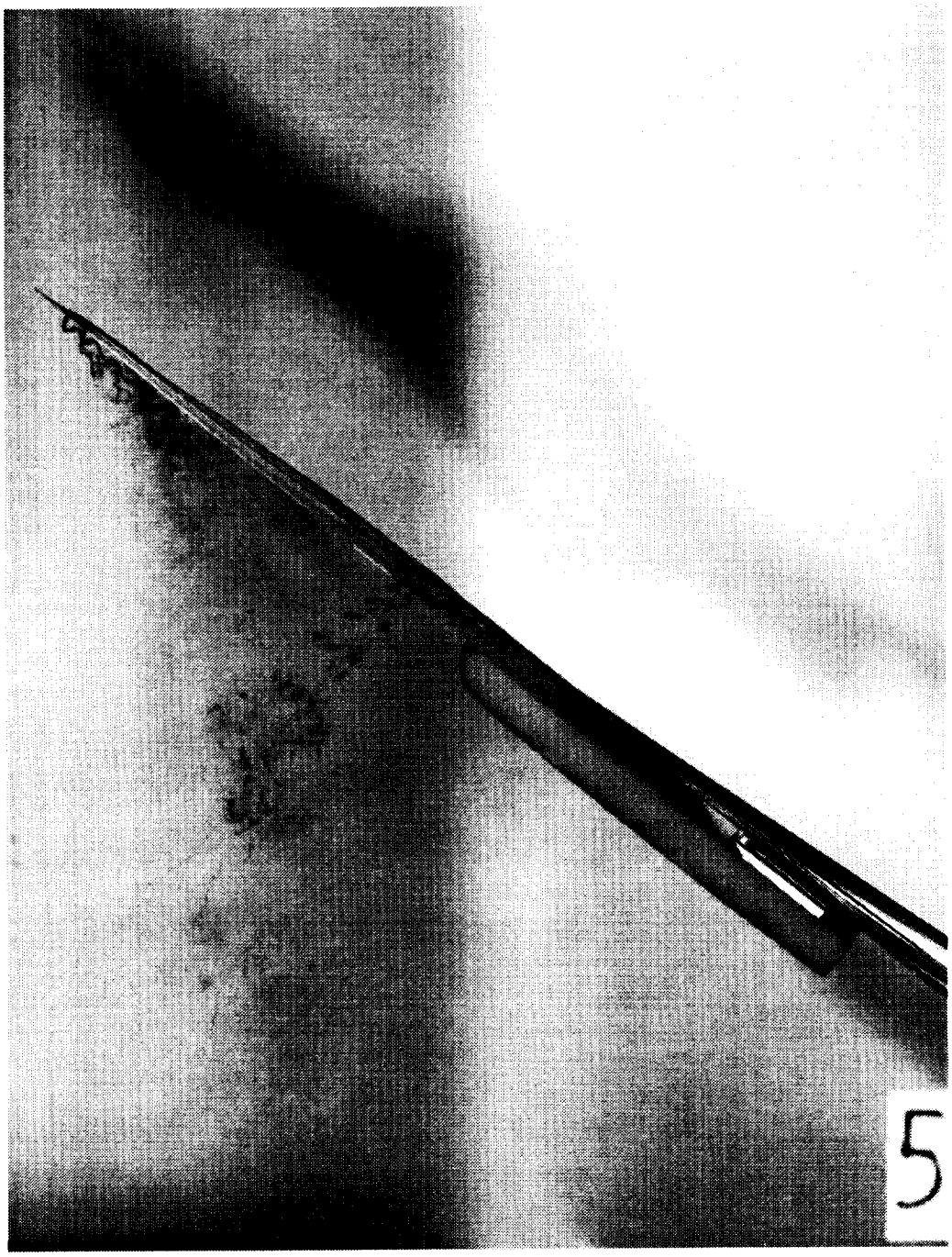

(i) Side view; $\alpha = 50°$.

Figure 15. Concluded.

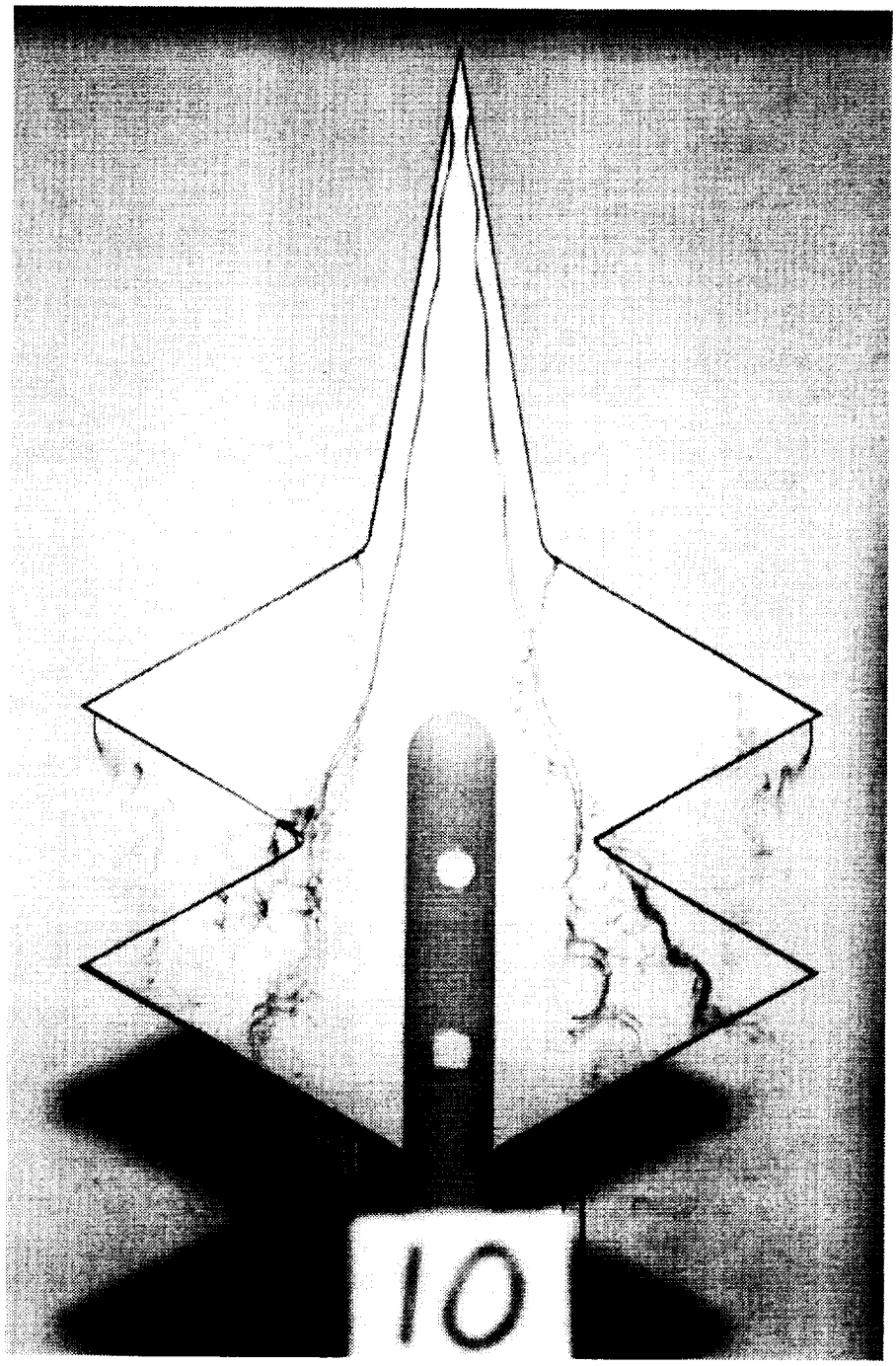

(a) $\alpha = 10°$.

Figure 16. Top-view photographs of 30° diamond twin wing.

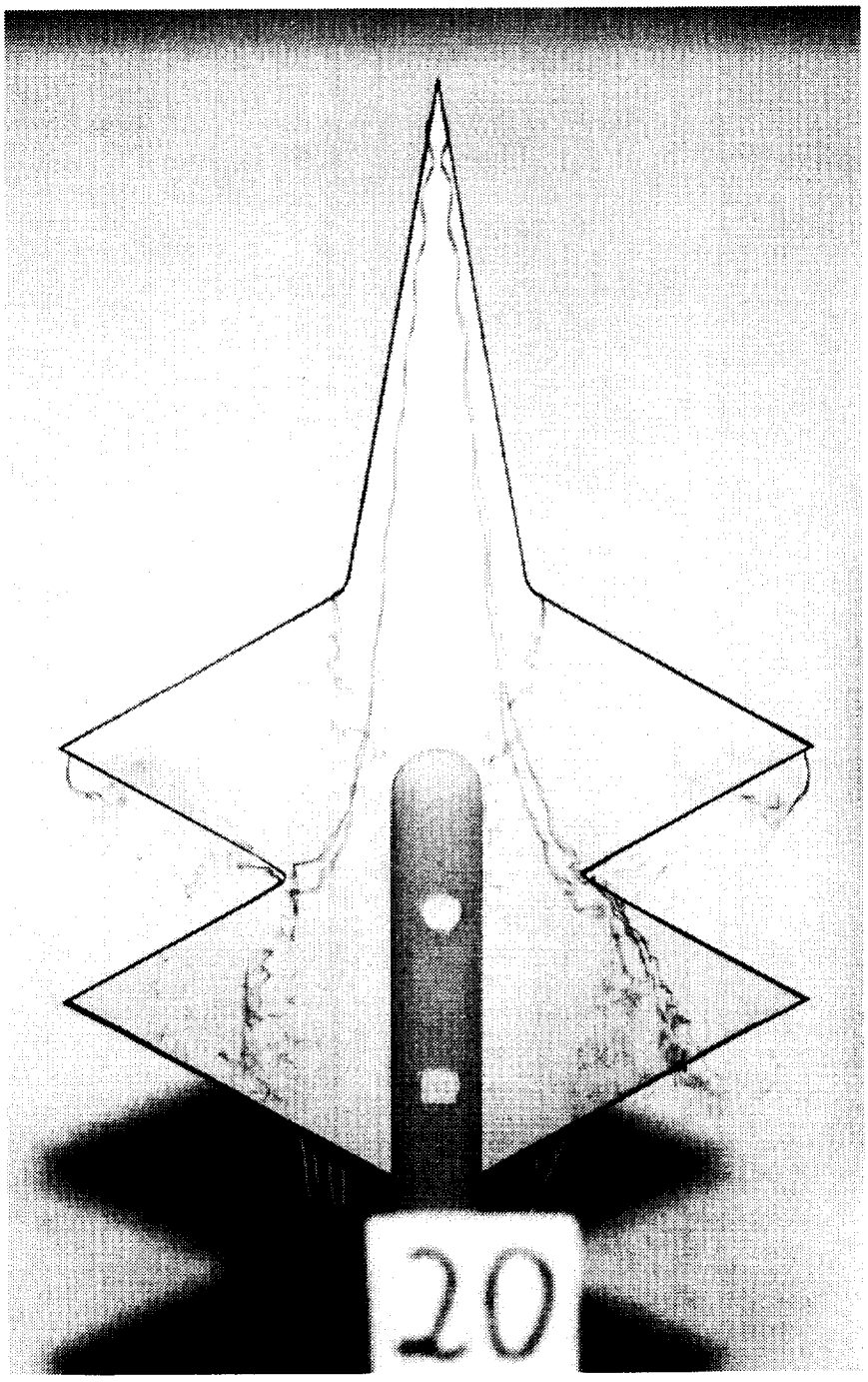

(b) $\alpha = 20°$.

Figure 16. Continued.

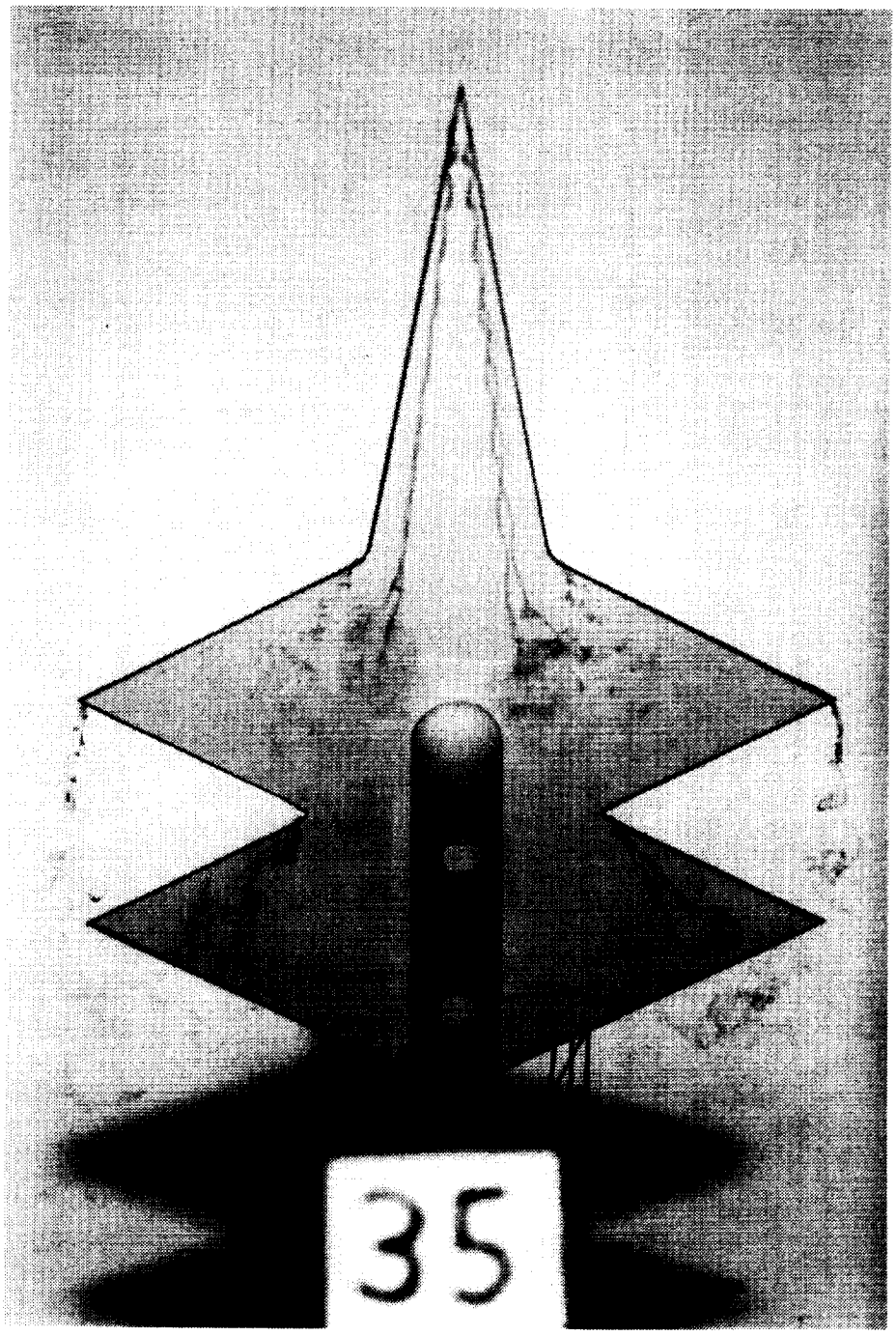

(c) $\alpha = 35°$.

Figure 16. Continued.

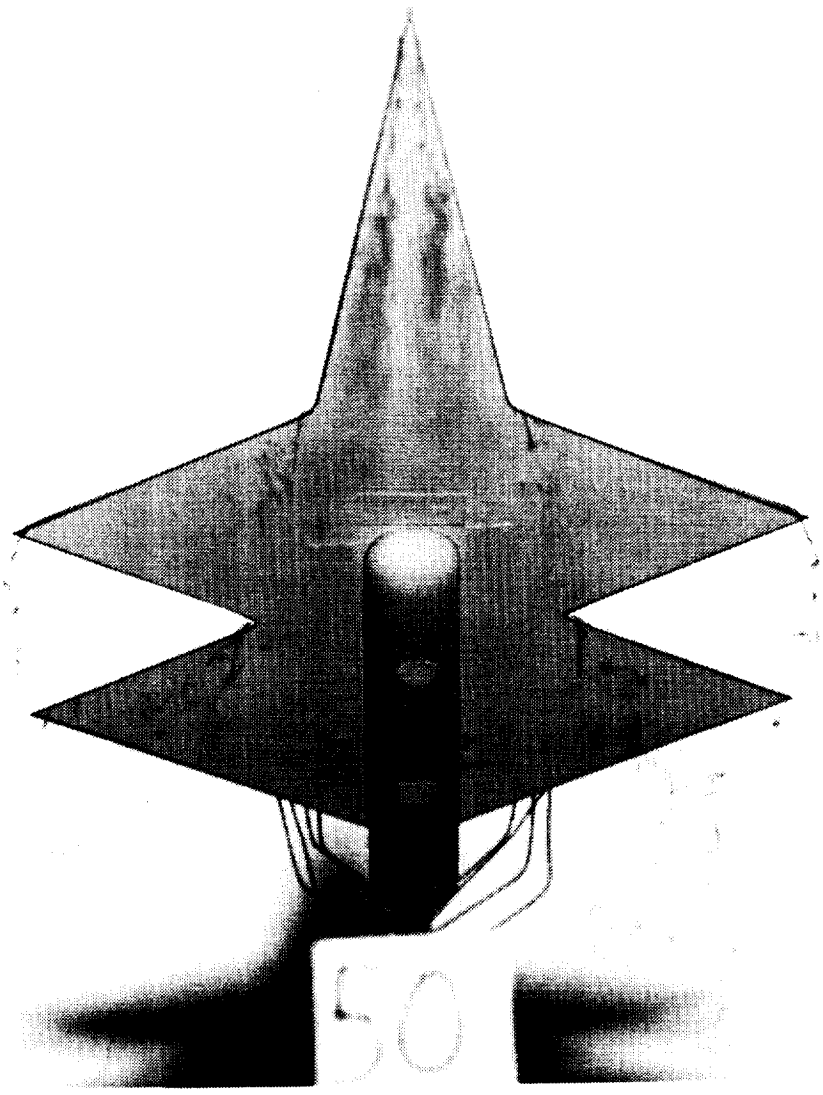

(d) $\alpha = 50°$.

Figure 16. Concluded.

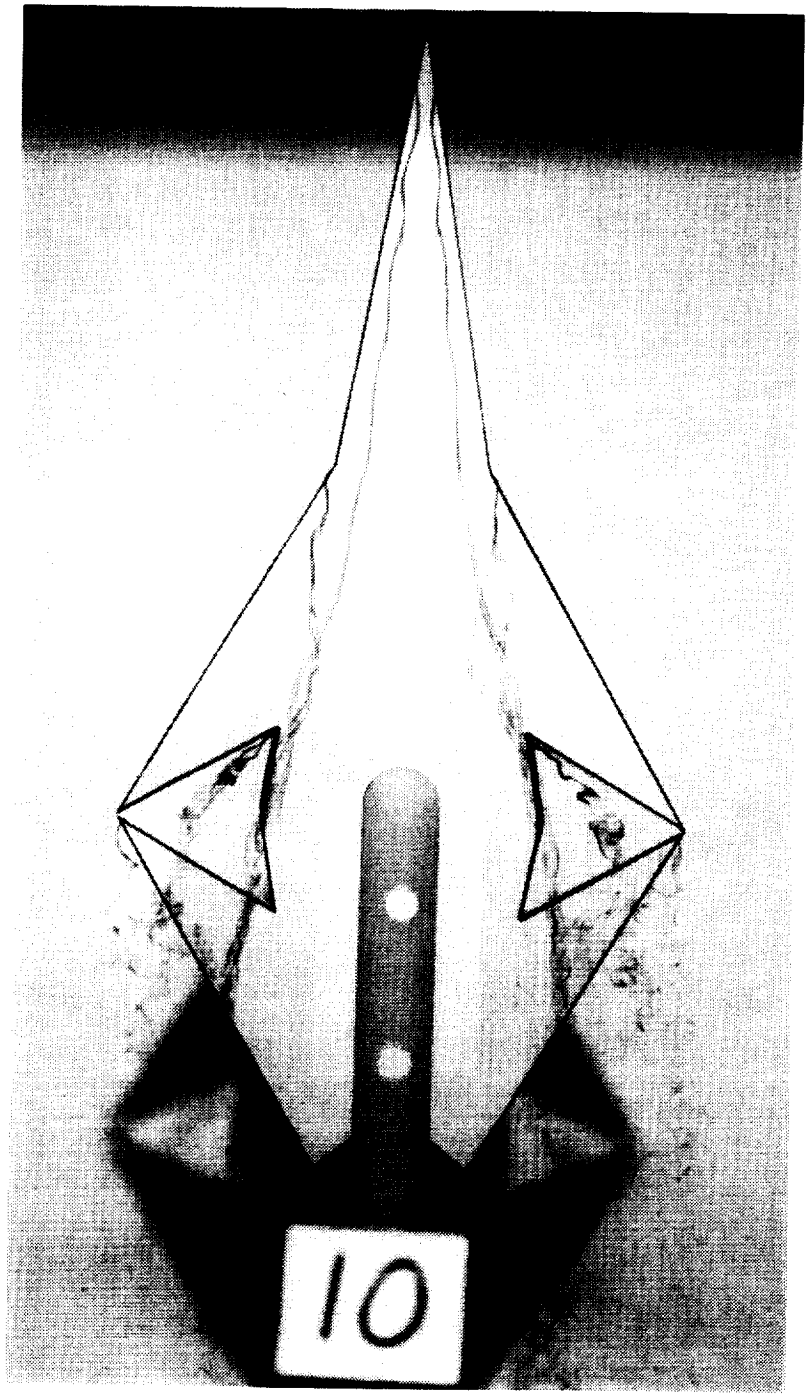

(a) Top view; $\alpha = 10°$.

Figure 17. Photographs of 60° double arrow.

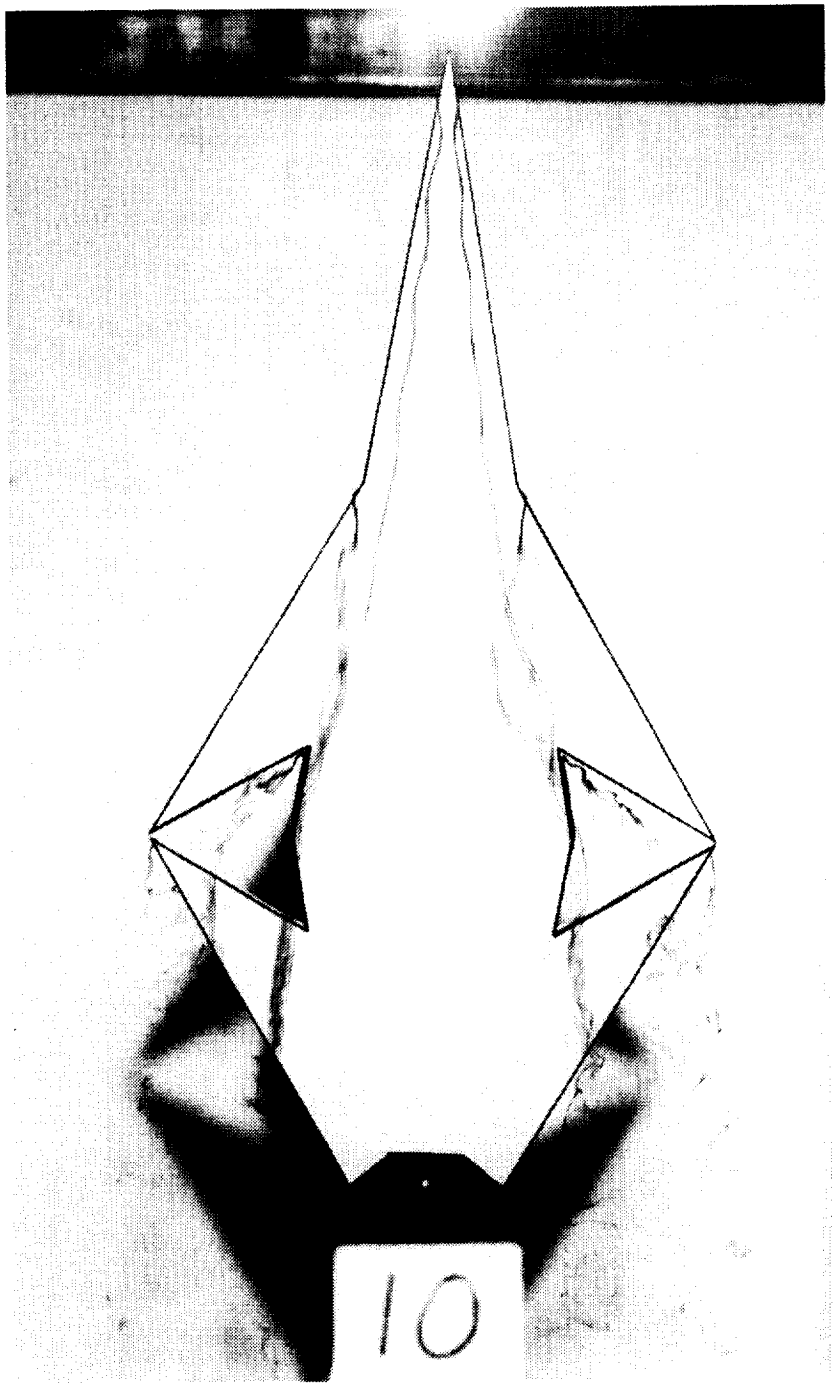

(b) Simulated balance housing removed; top view; $\alpha = 10°$.

Figure 17. Continued.

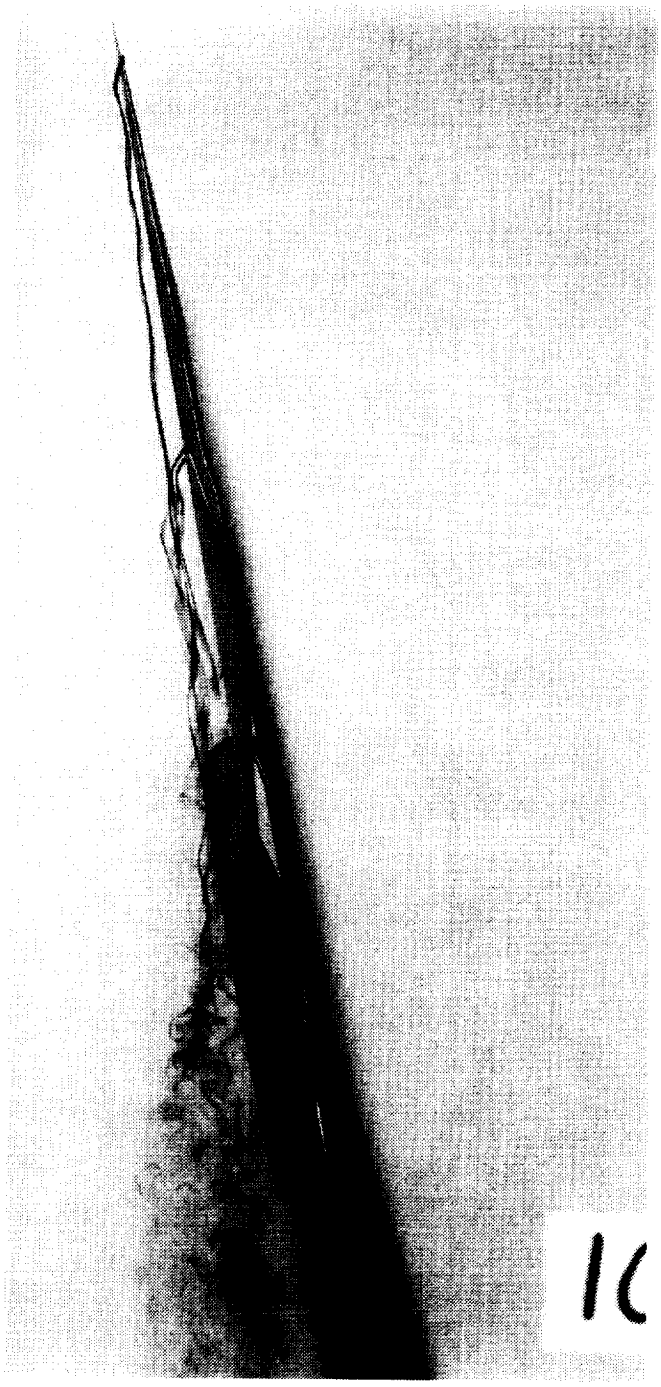

(c) Side view; $\alpha = 10°$.

Figure 17. Continued.

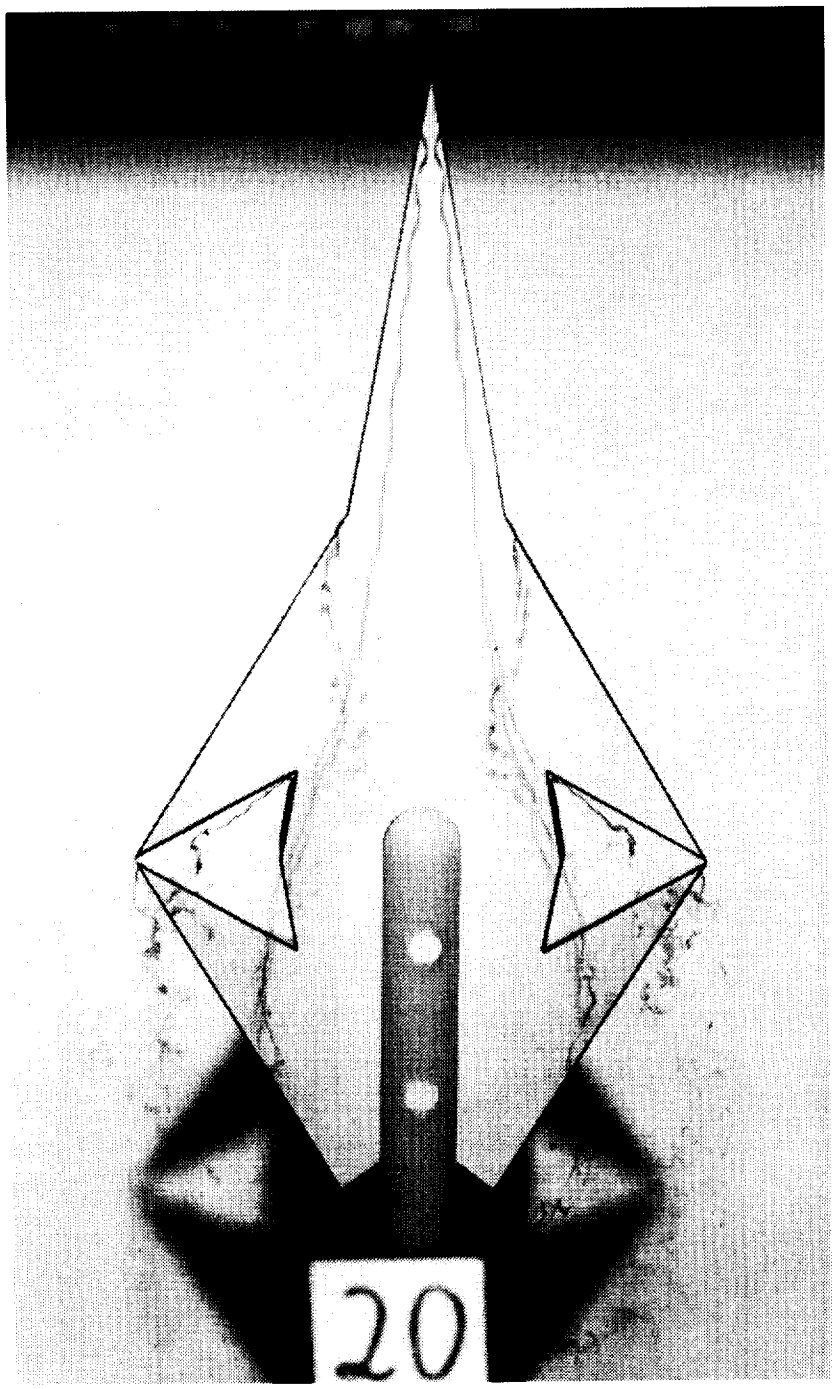

(d) Top view; $\alpha = 20°$.

Figure 17. Continued.

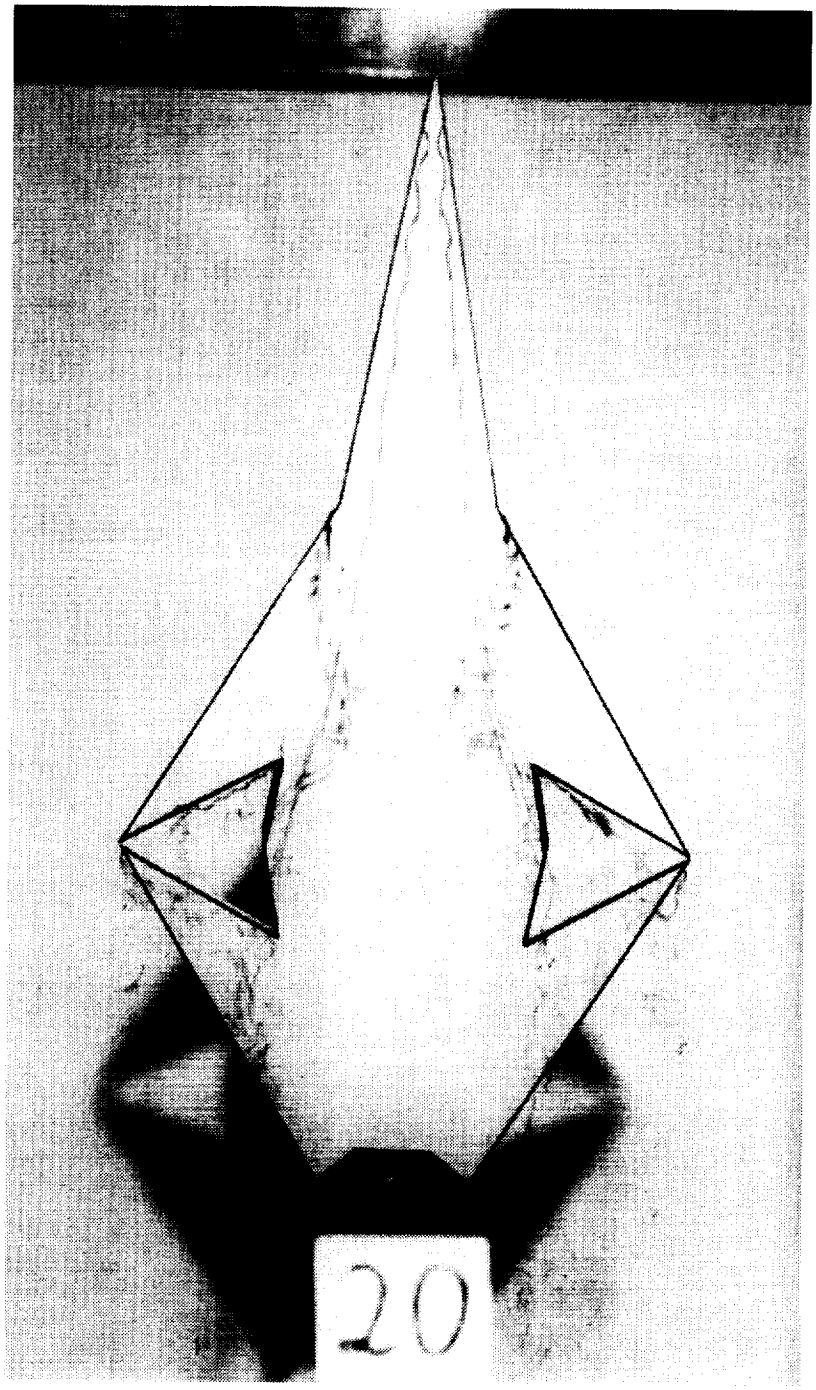

(e) Simulated balance housing removed; top view; $\alpha = 20°$.

Figure 17. Continued.

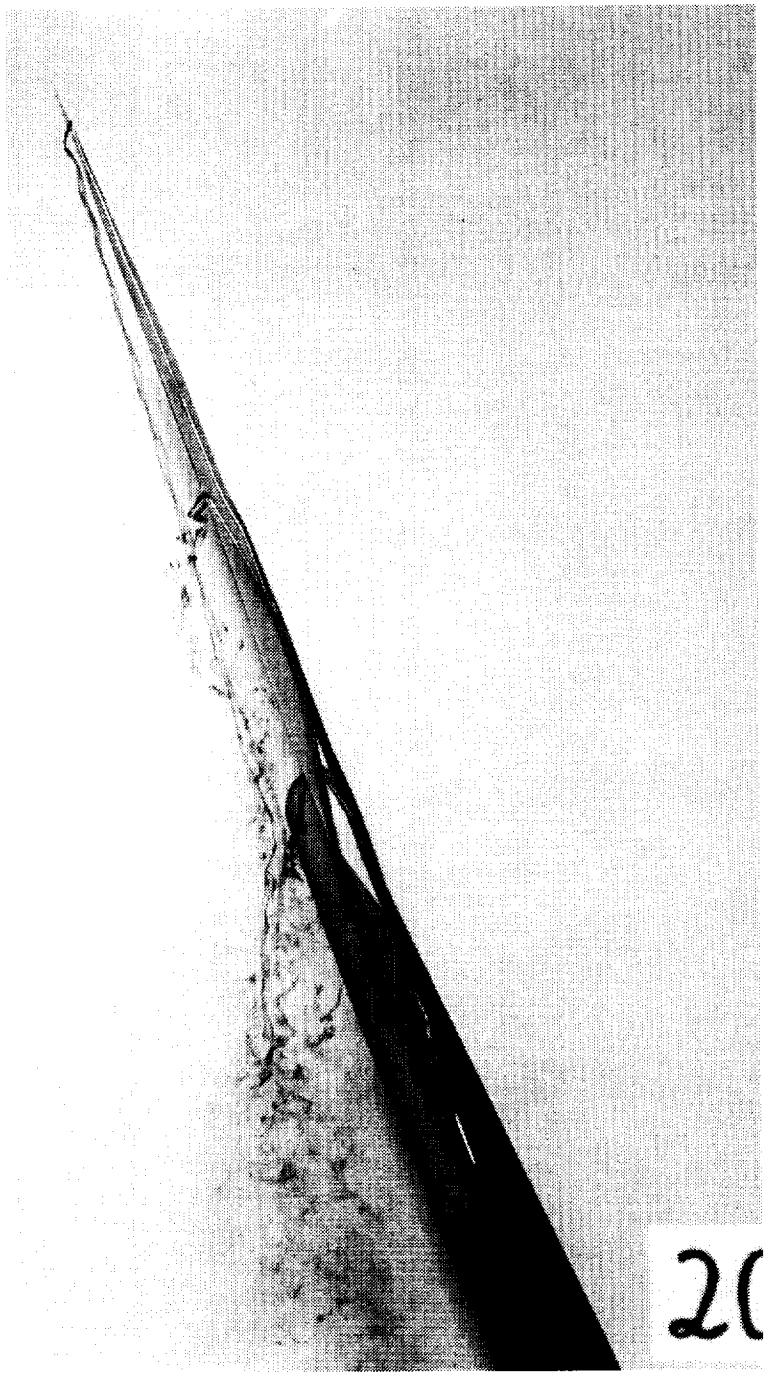

(f) Side view; $\alpha = 20°$.

Figure 17. Continued.

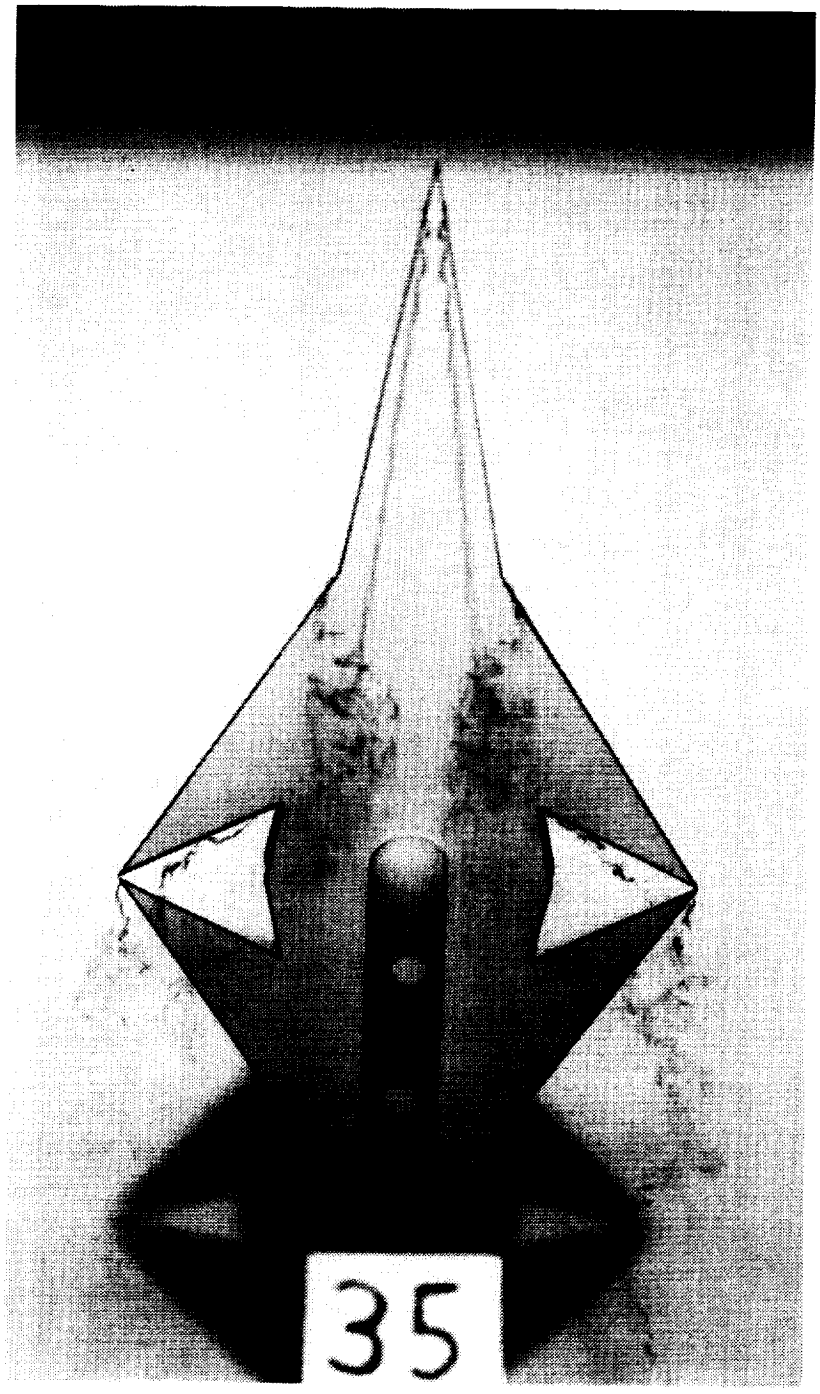

(g) Top view; $\alpha = 35°$.

Figure 17. Continued.

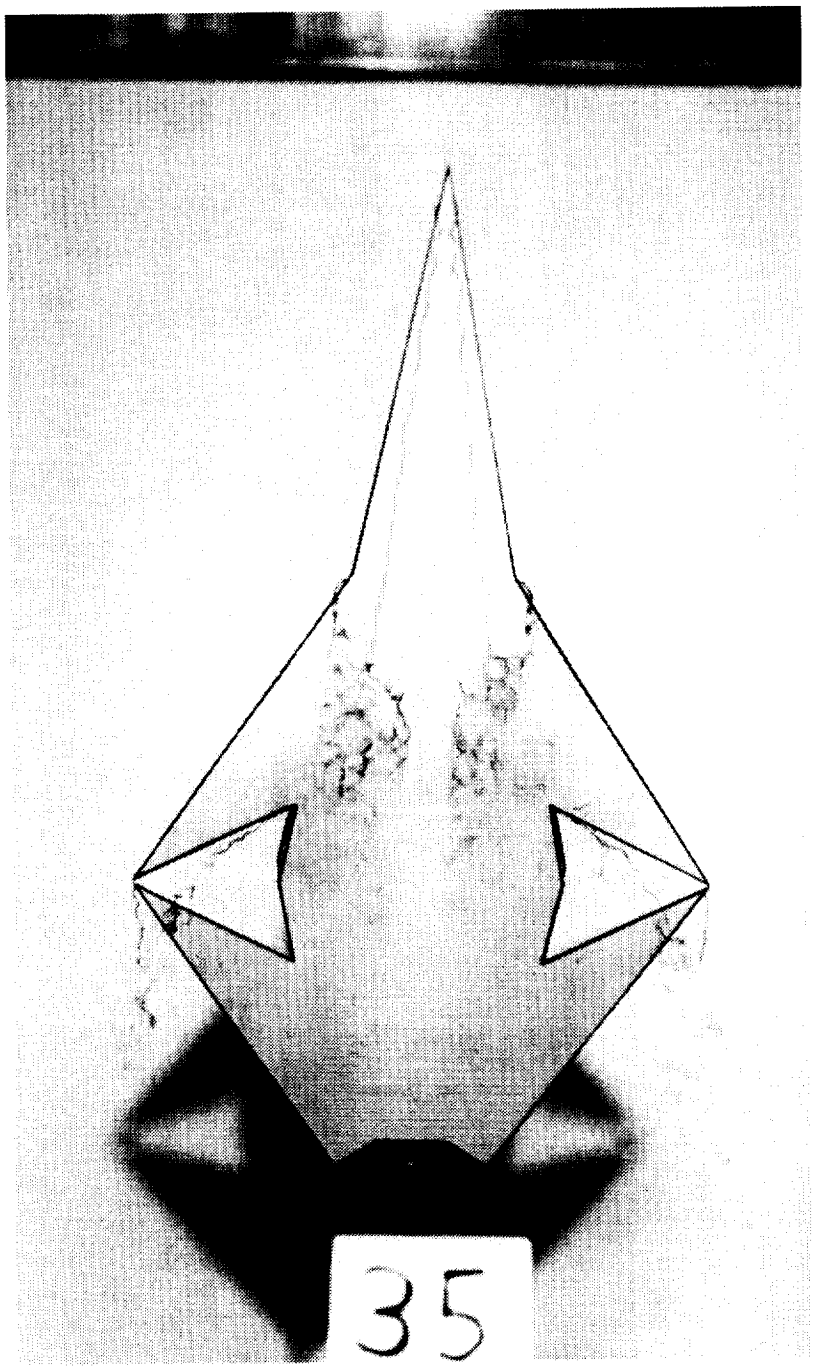

(h) Simulated balance housing removed; top view; $\alpha = 35°$.

Figure 17. Continued.

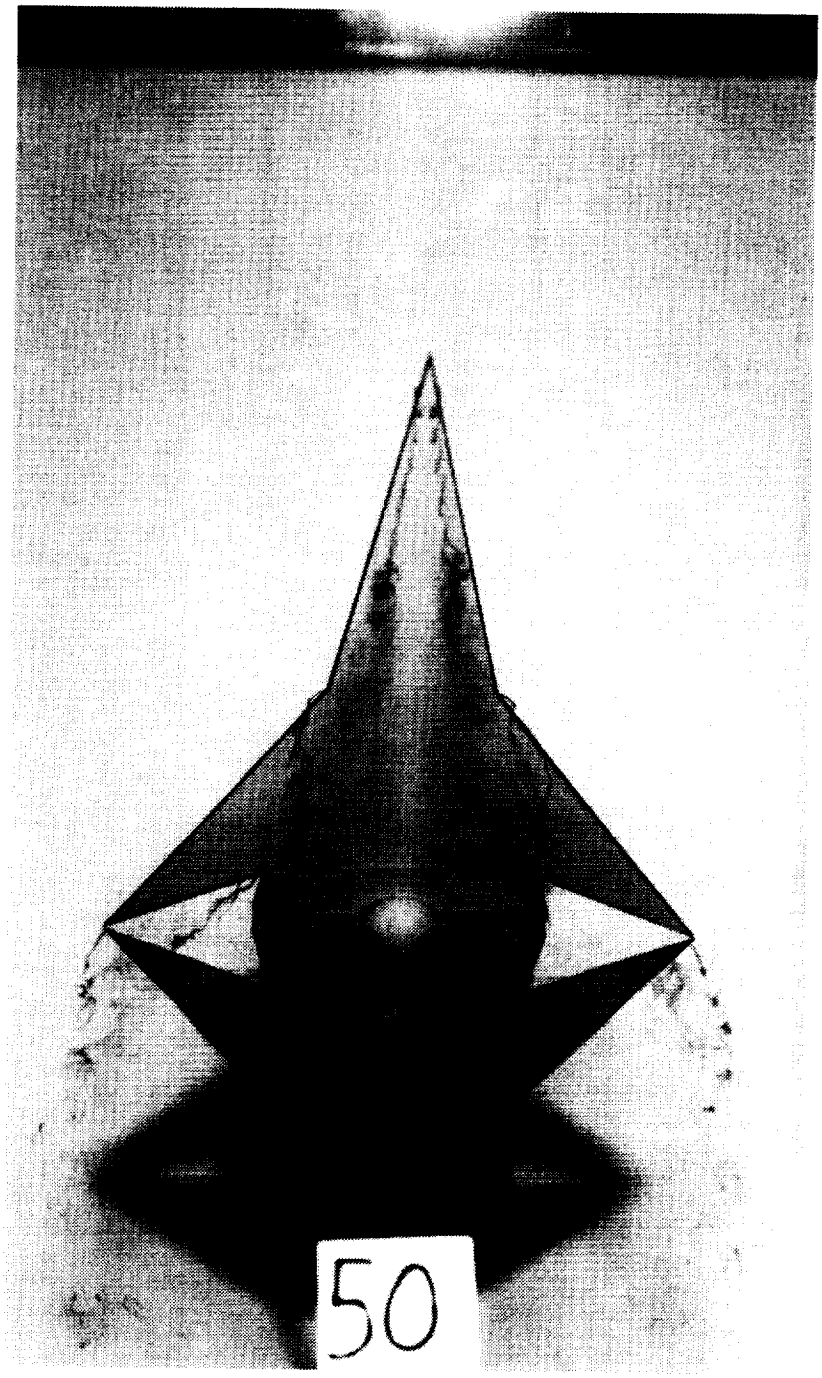

(i) Top view; $\alpha = 50°$.

Figure 17. Concluded.

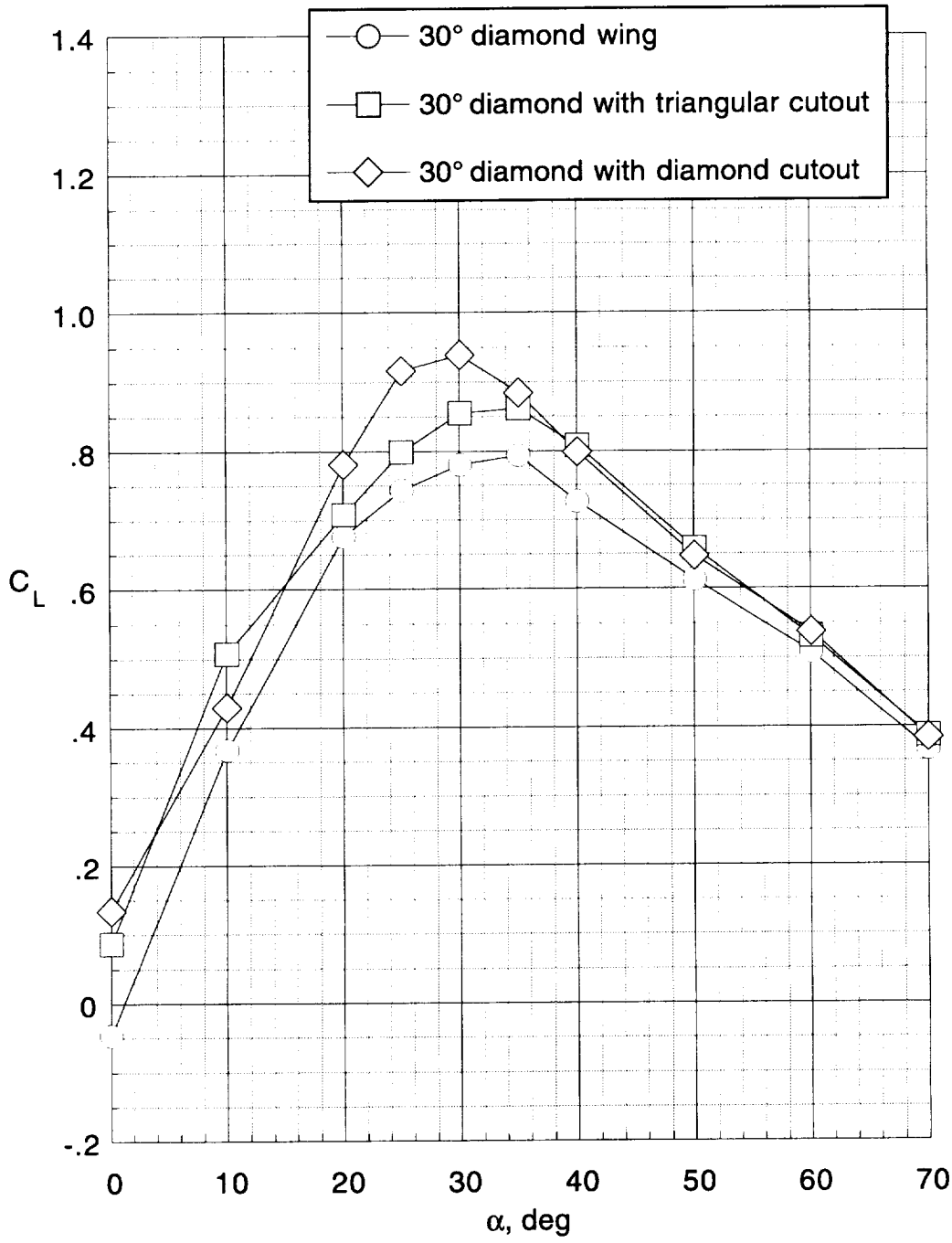

Figure 18. Lift coefficient versus angle of attack for cutout-wing configurations (ref. 14).

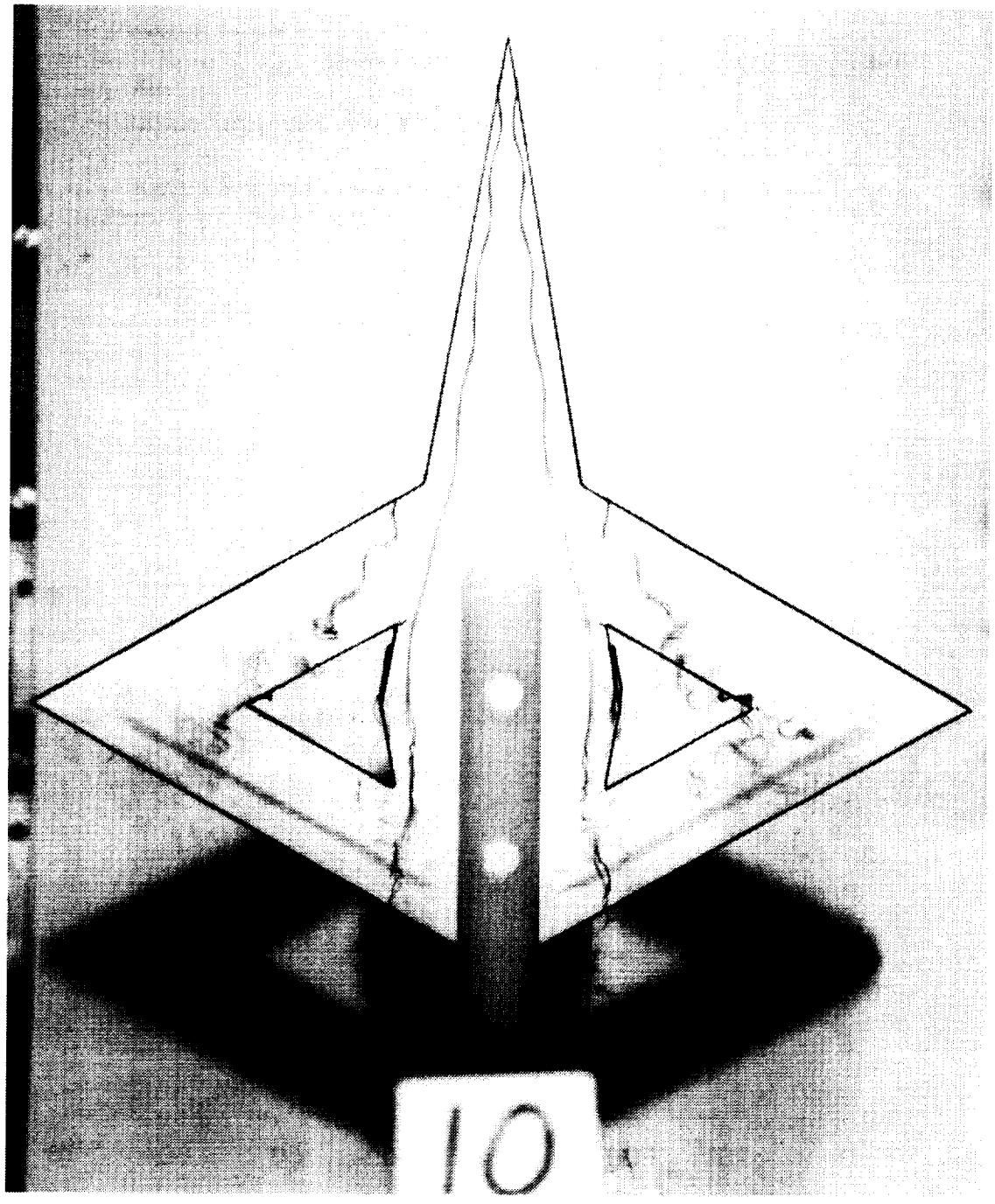

(a) $\alpha = 10°$.

Figure 19. Top-view photographs of 30° diamond with triangular cutout.

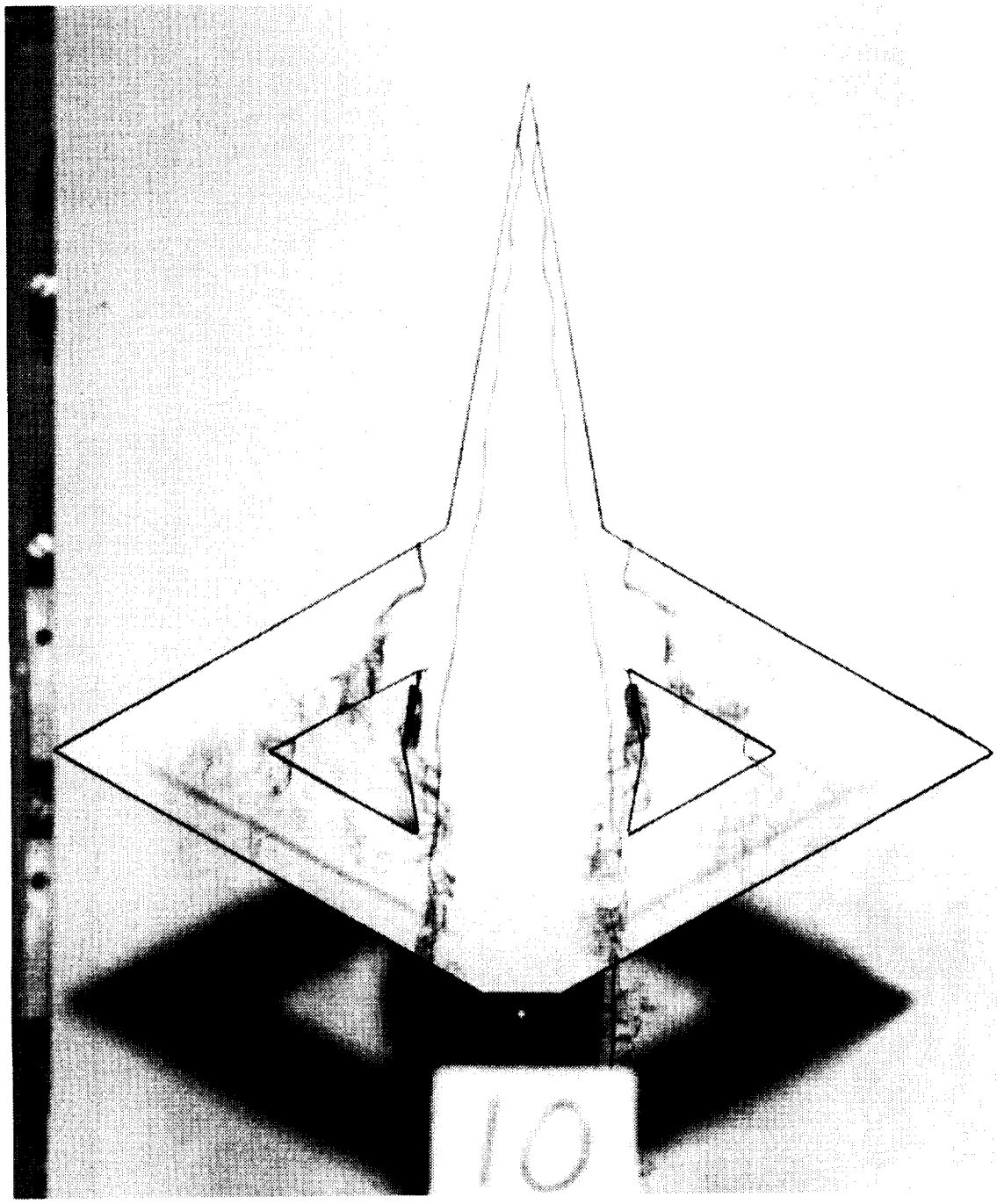

(b) Simulated balance housing removed; $\alpha = 10°$.

Figure 19. Continued.

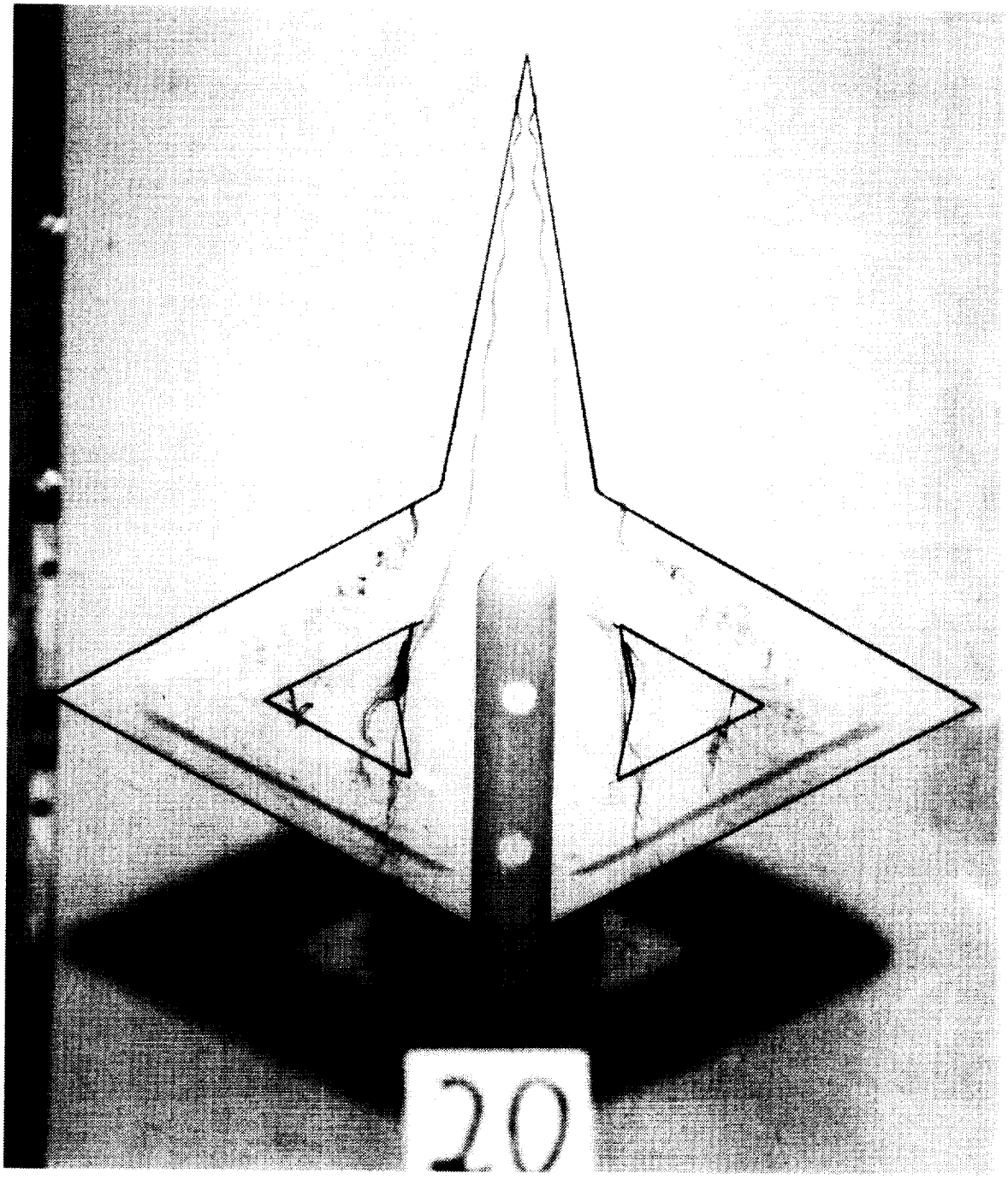

(c) $\alpha = 20°$.

Figure 19. Continued.

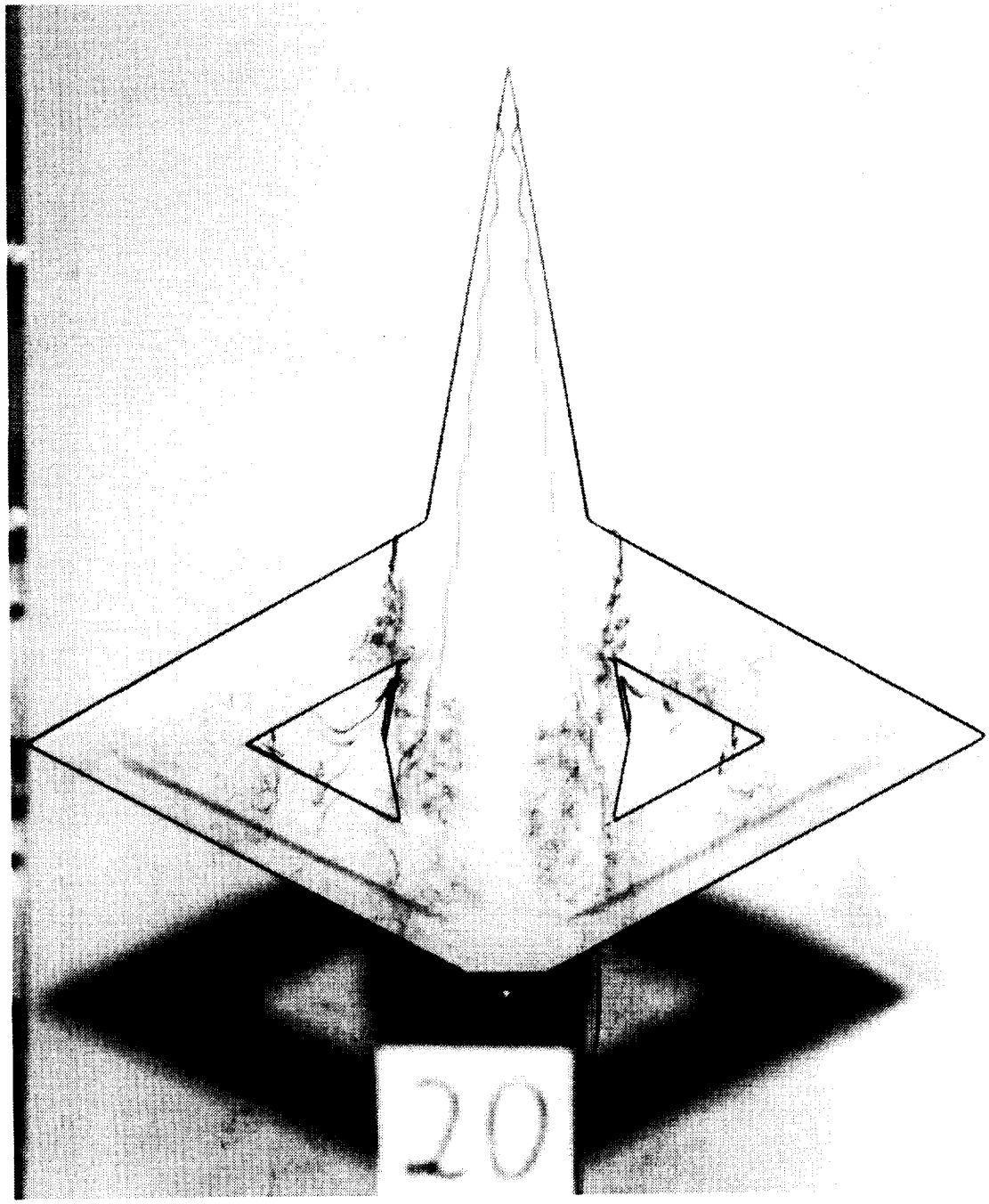

(d) Simulated balance housing removed; $\alpha = 20°$.

Figure 19. Continued.

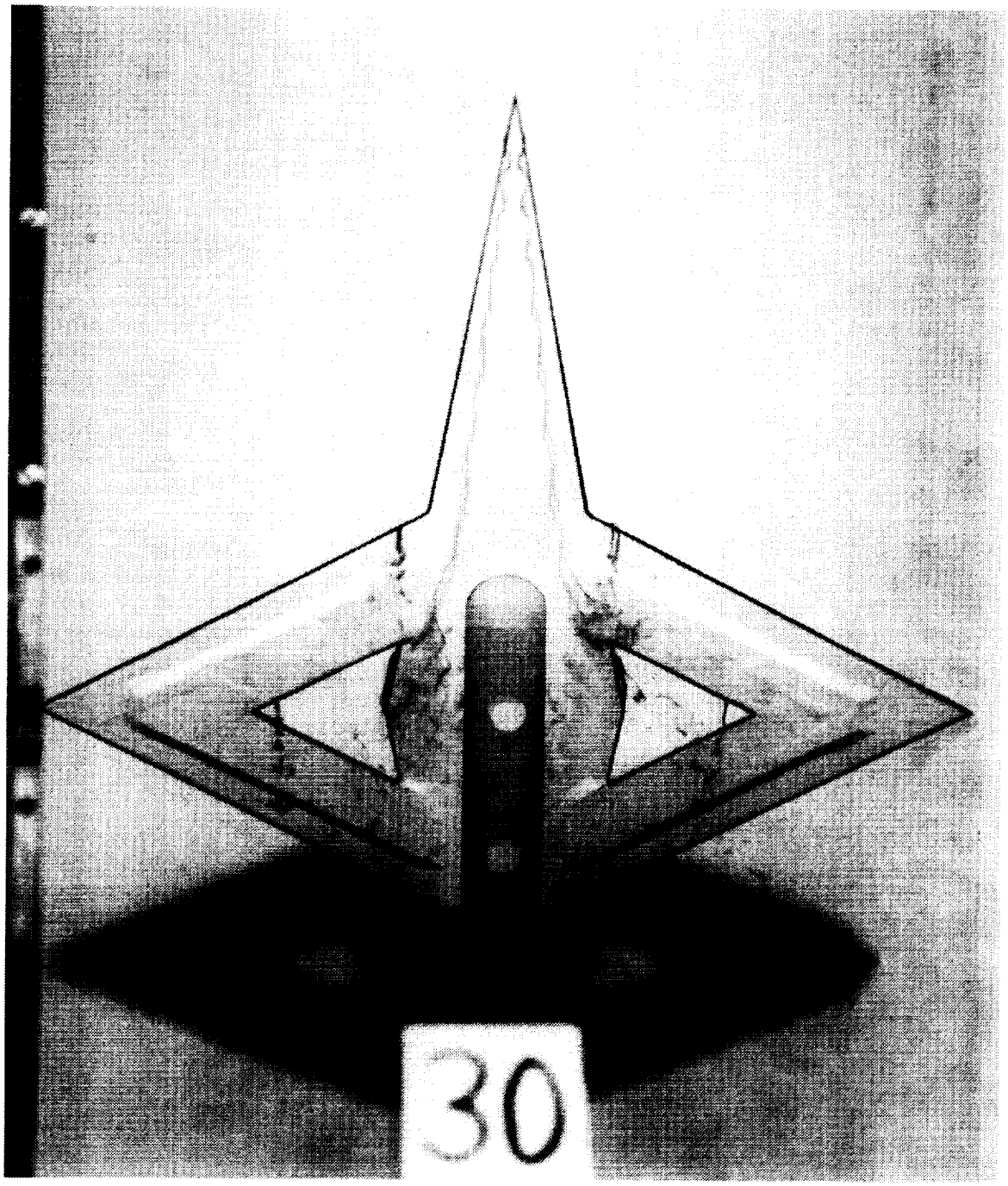

(e) $\alpha = 30°$.

Figure 19. Continued.

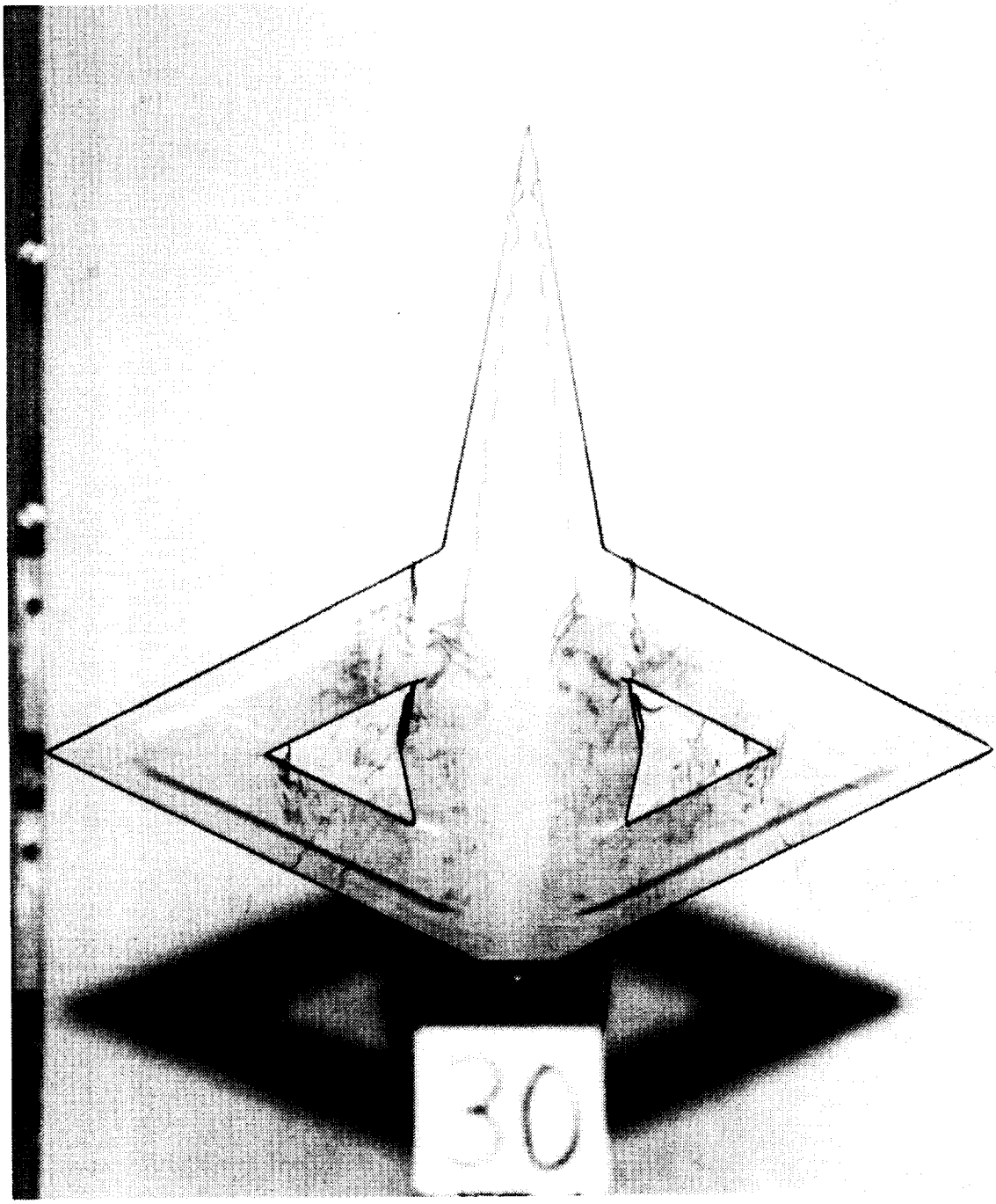

(f) Simulated balance housing removed; $\alpha = 30°$.

Figure 19. Continued.

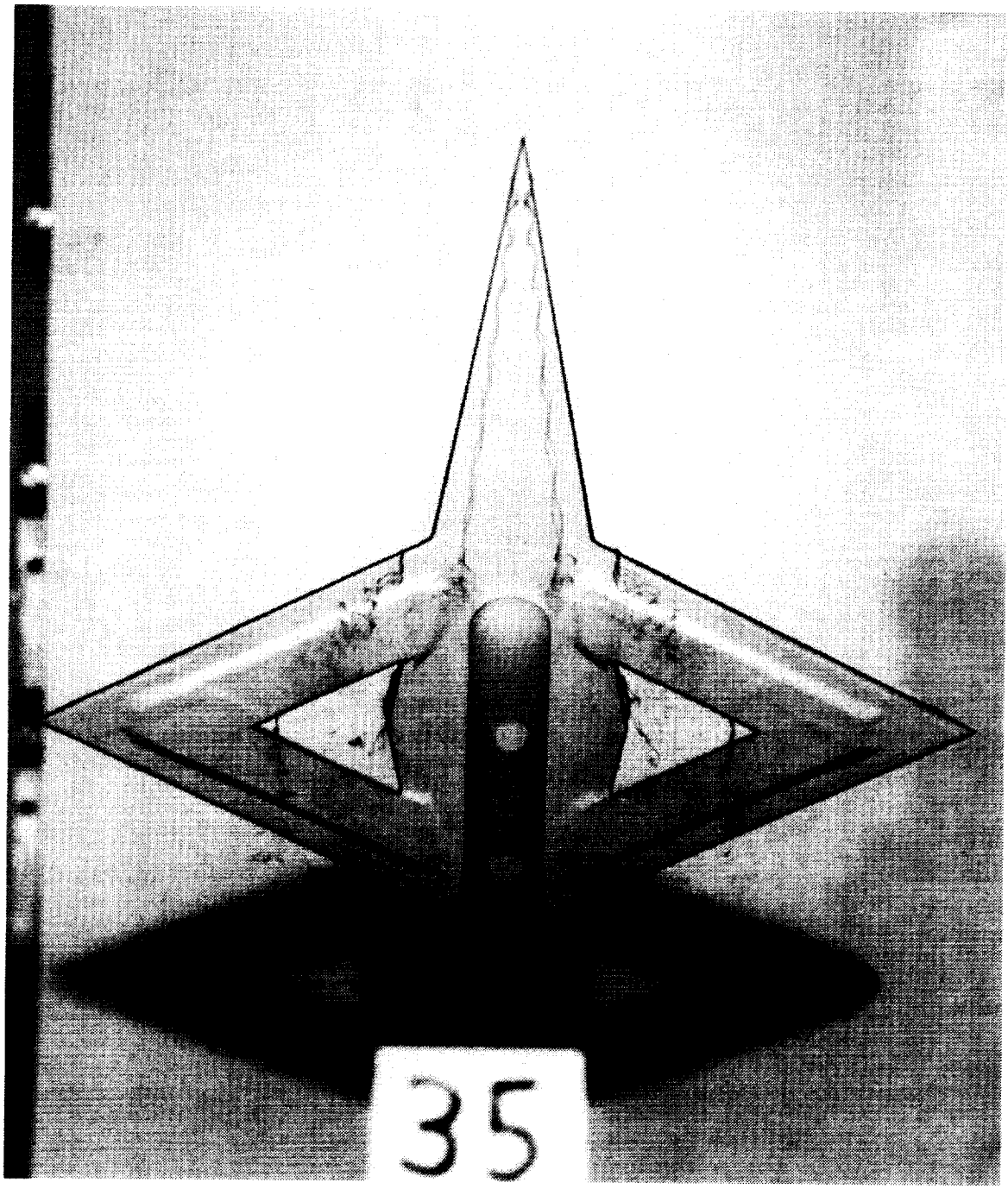

(g) $\alpha = 35°$.

Figure 19. Continued.

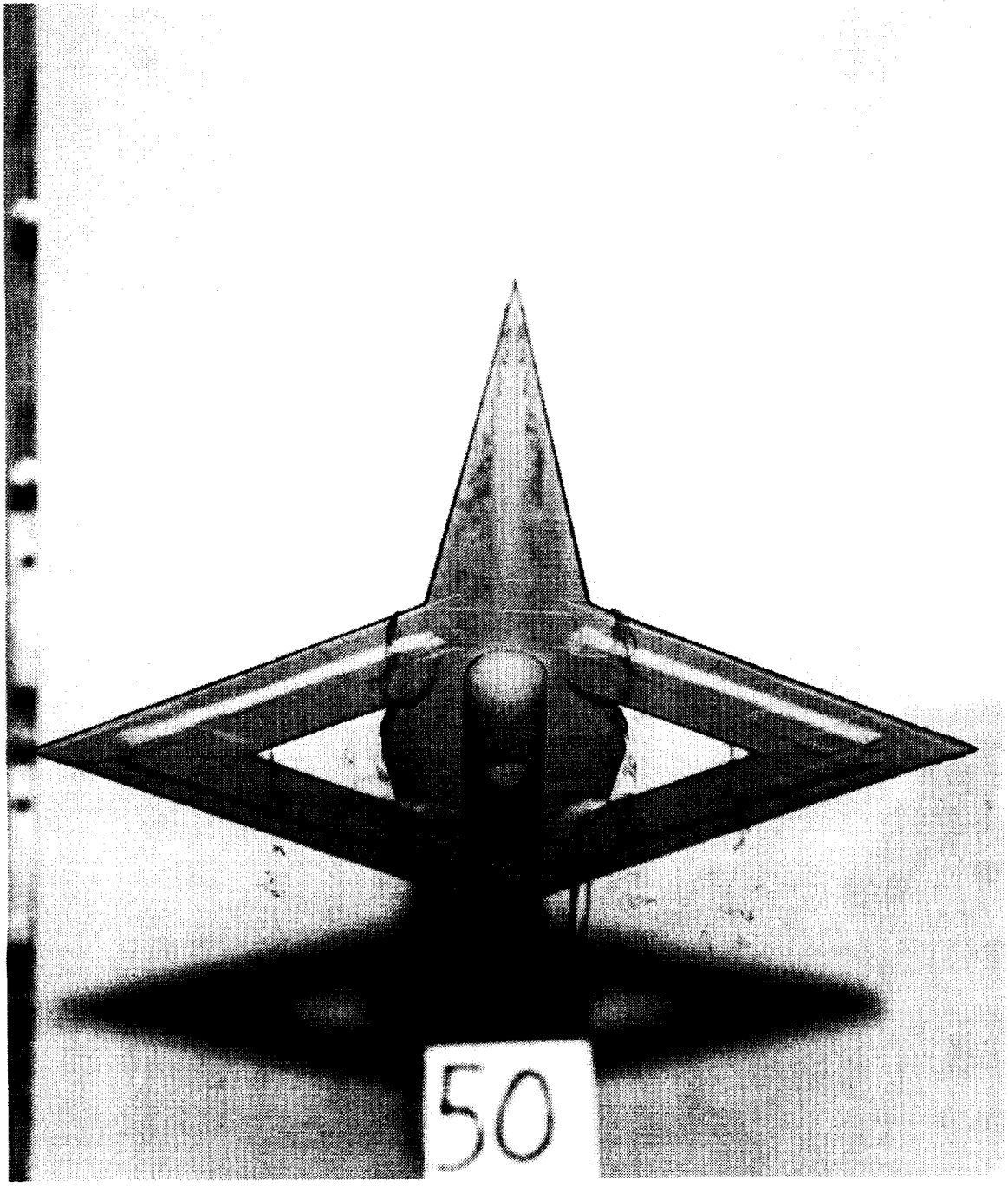

(h) $\alpha = 50°$.

Figure 19. Concluded.

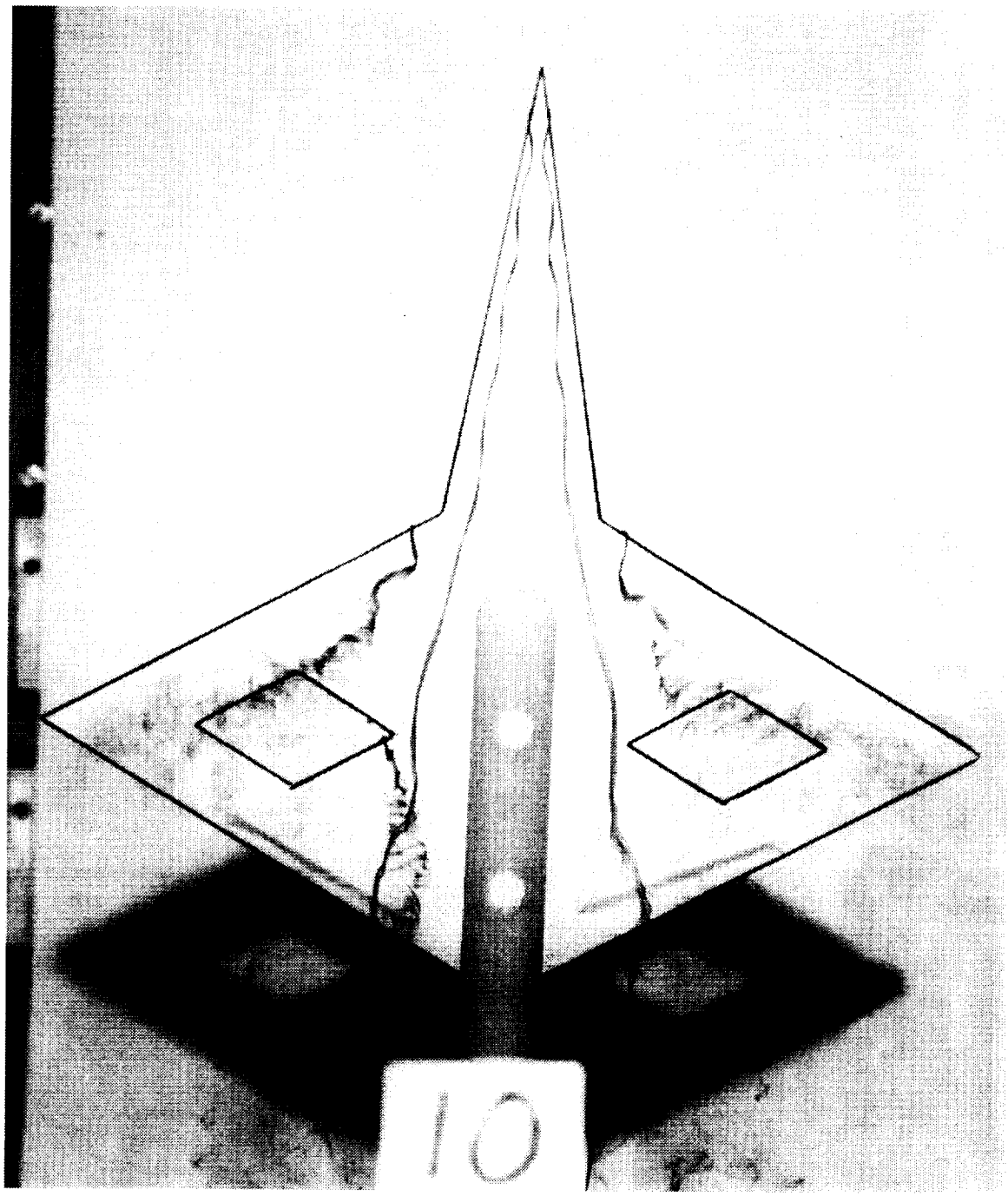

(a) $\alpha = 10°$.

Figure 20. Top-view photographs of 30° diamond with diamond cutout.

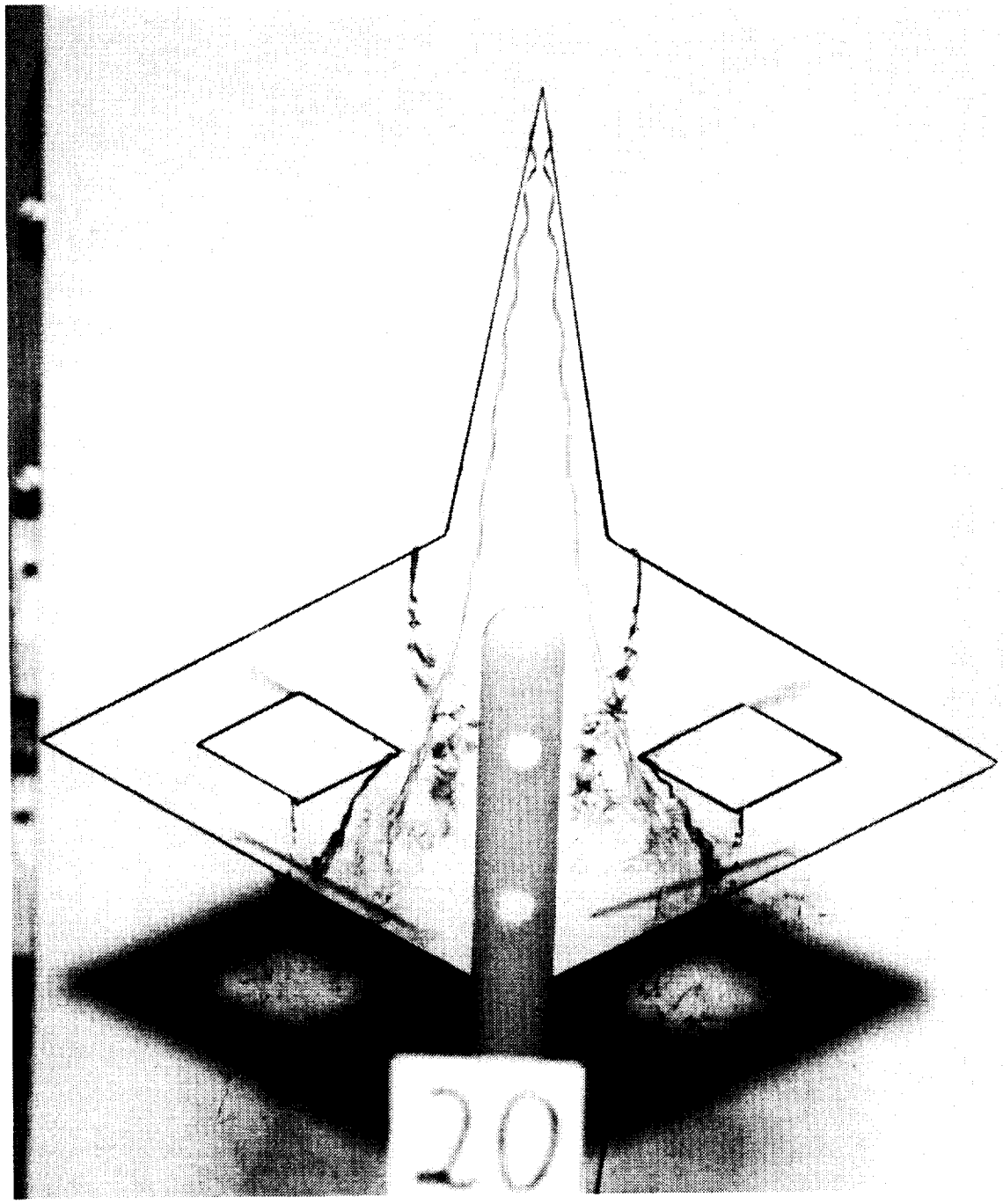

(b) $\alpha = 20°$.

Figure 20. Continued.

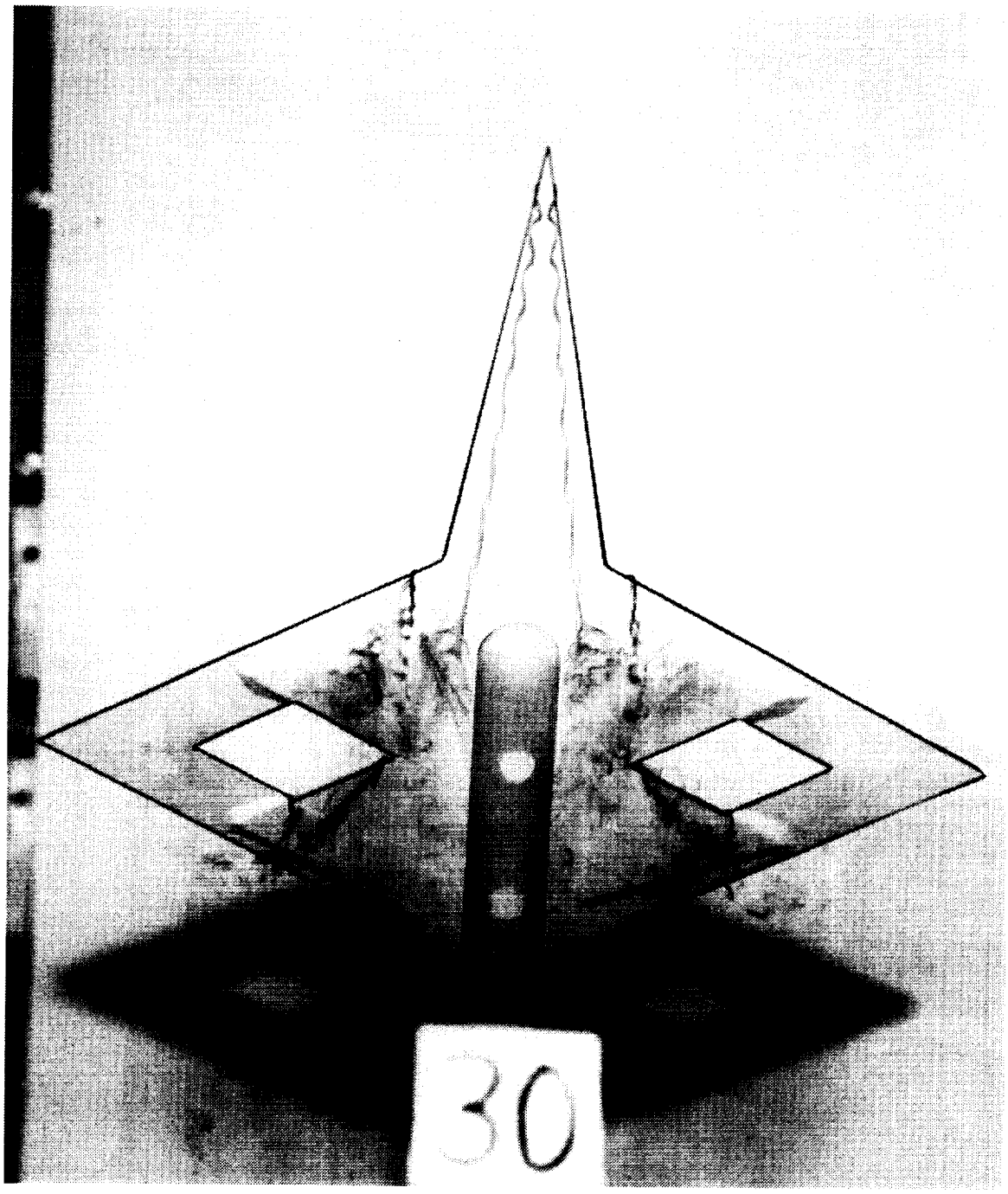

(c) $\alpha = 30°$.

Figure 20. Continued.

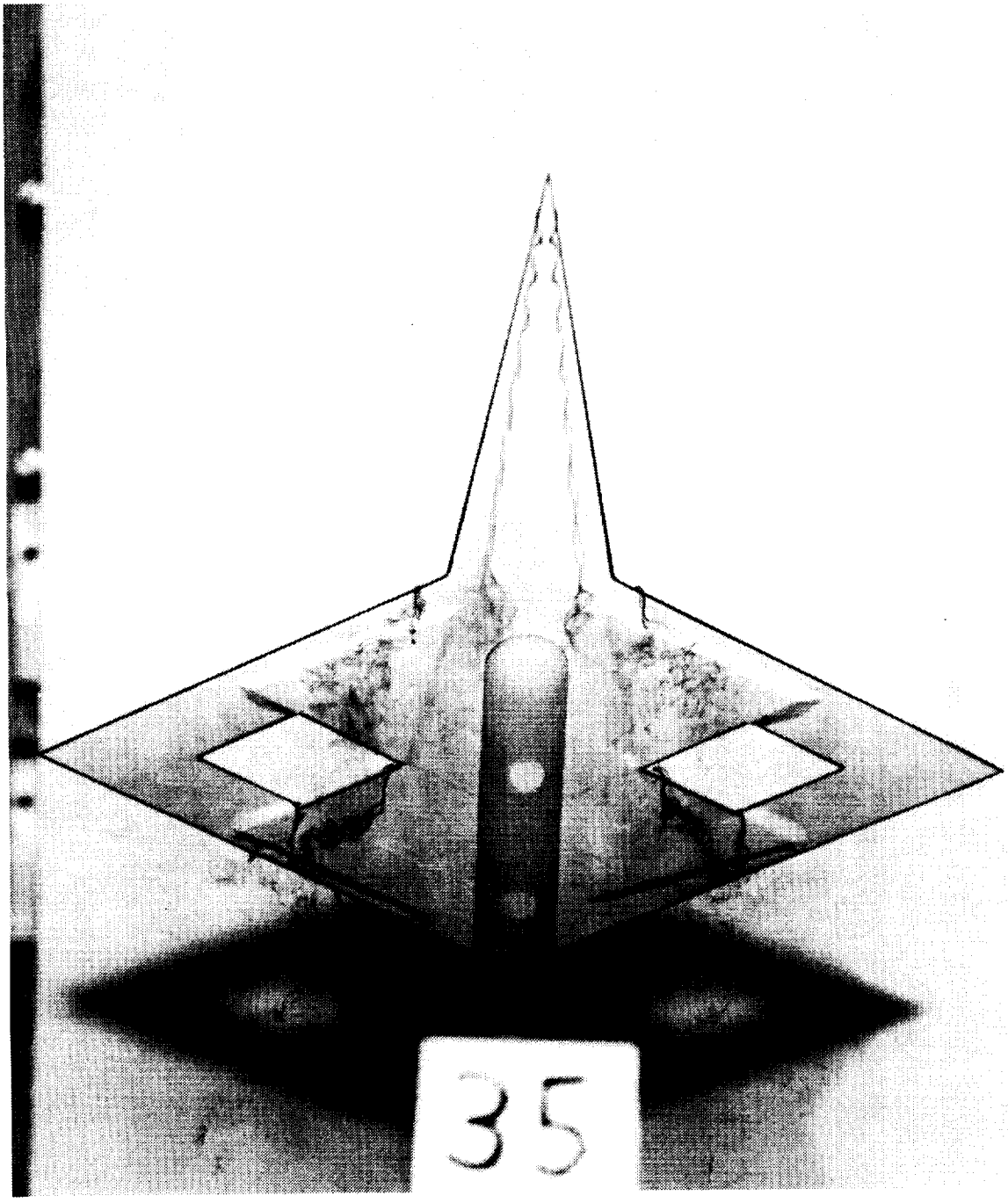

(d) $\alpha = 35°$.

Figure 20. Continued.

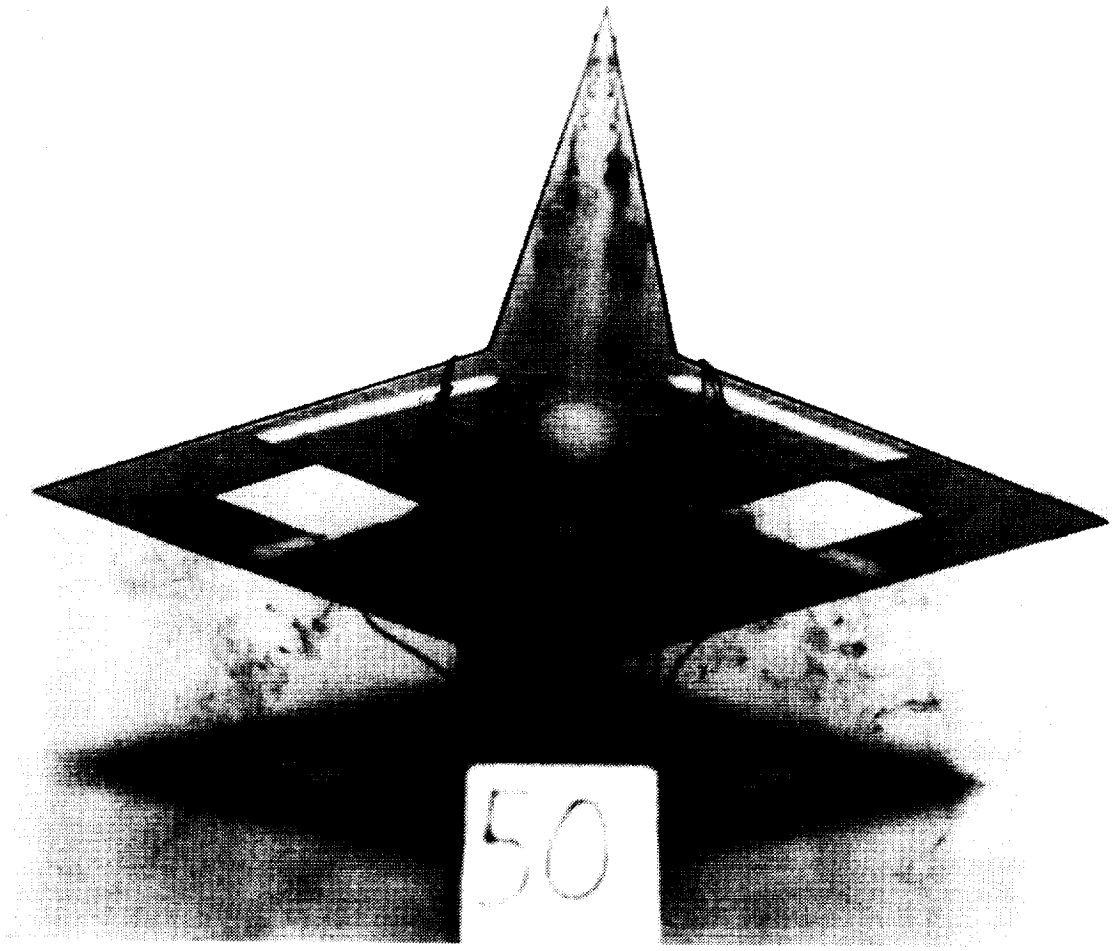

(e) $\alpha = 50°$.

Figure 20. Concluded.

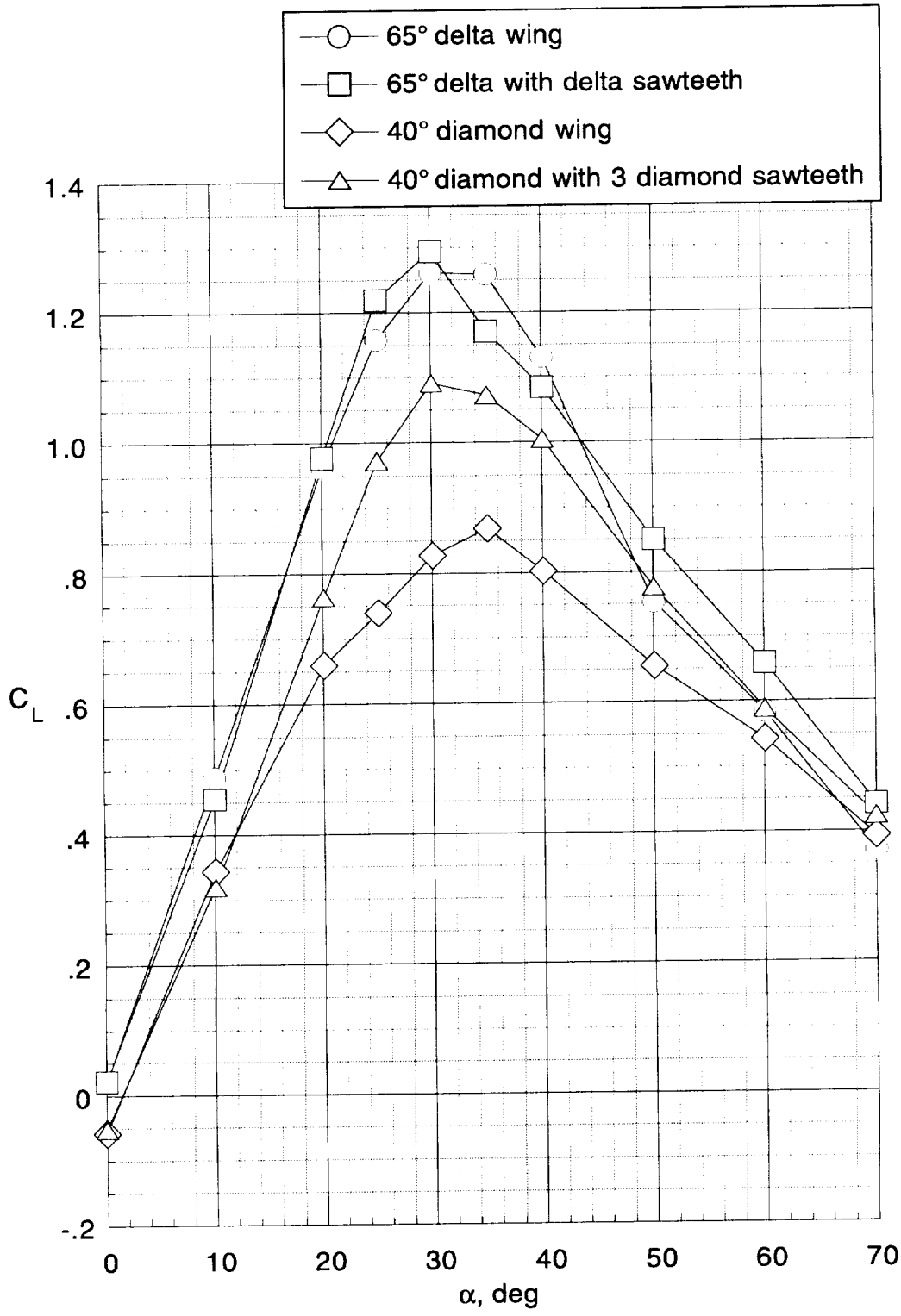

Figure 21. Lift coefficient versus angle of attack for serrated-forebody configurations (ref. 14).

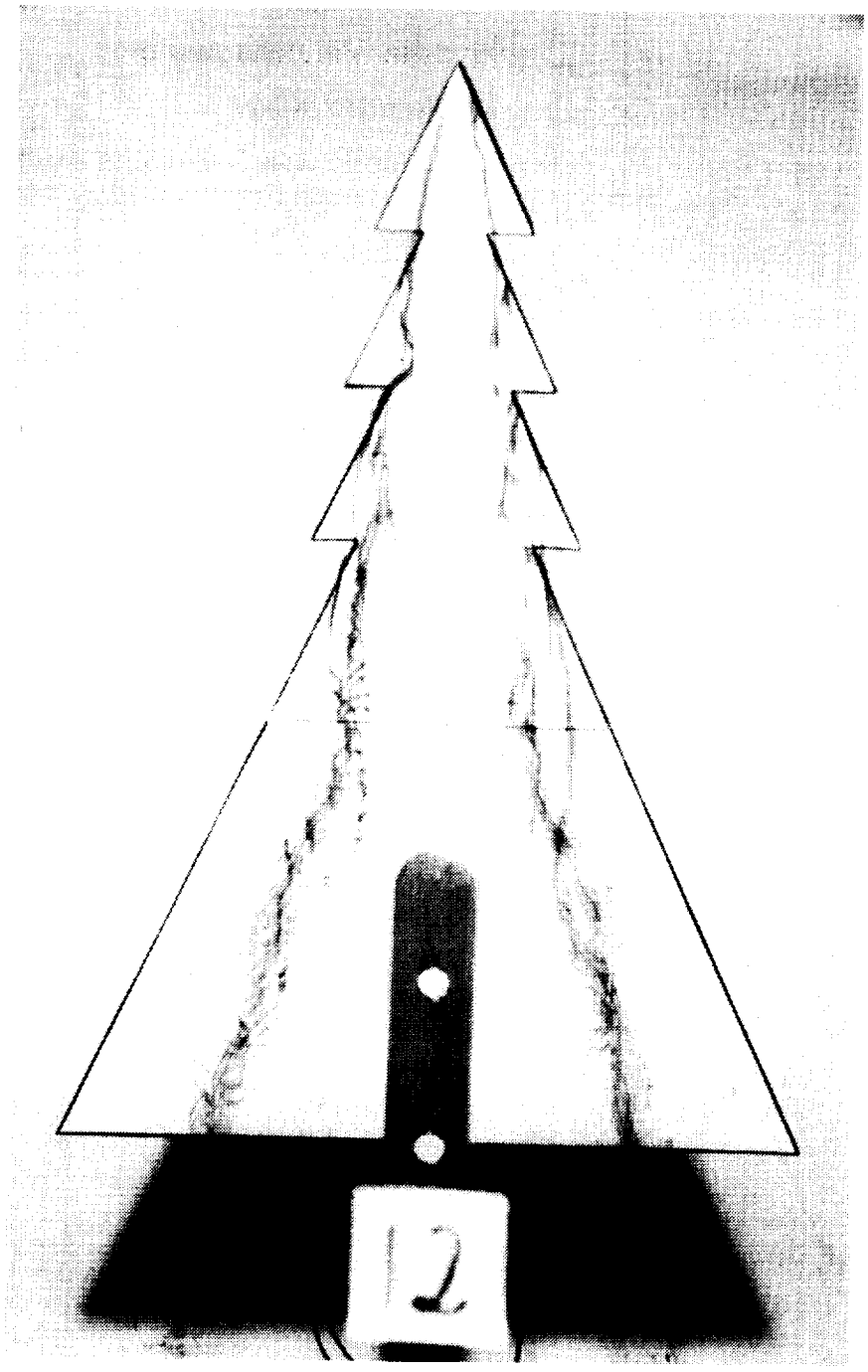

(a) Top view; $\alpha = 12°$.

Figure 22. Photographs of 65° delta with delta sawteeth.

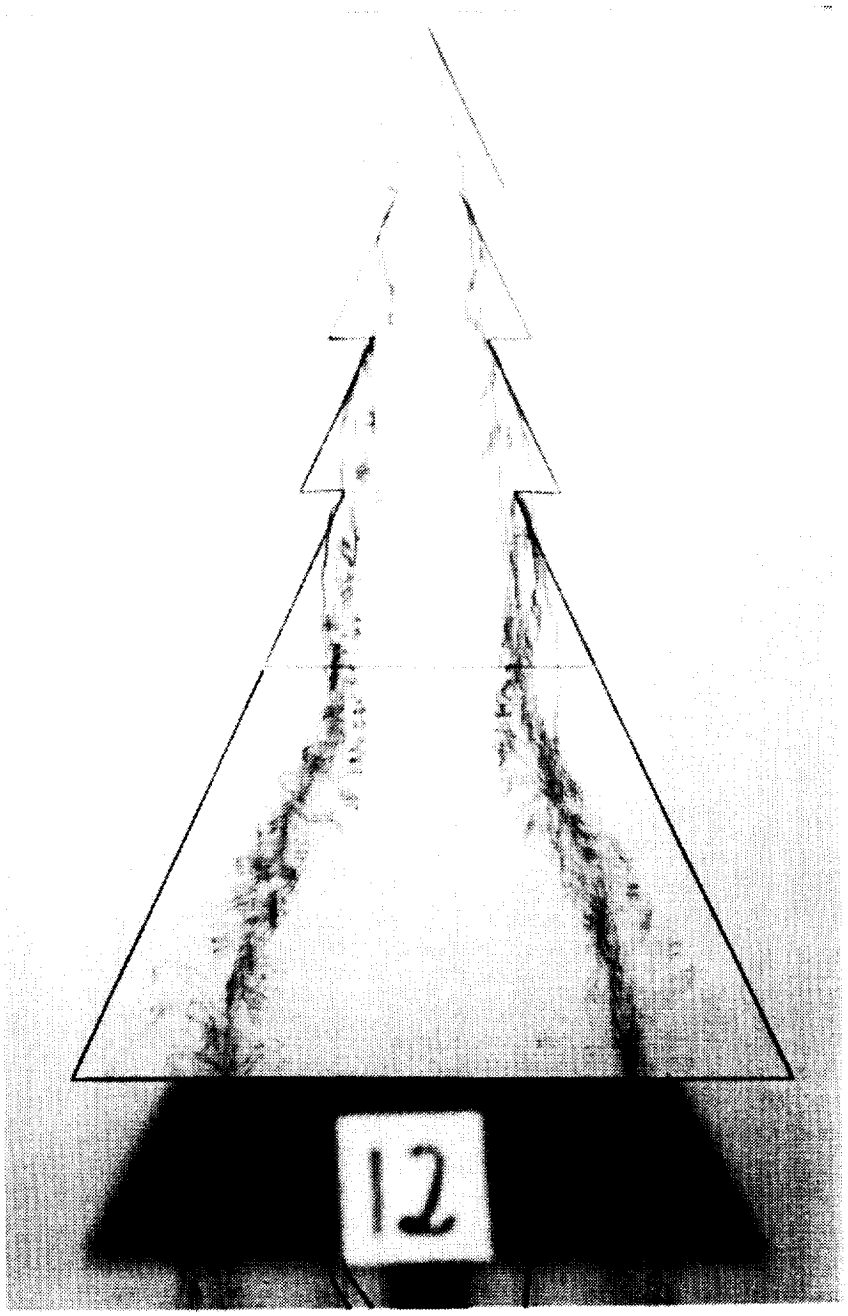

(b) Simulated balance housing removed; top view; $\alpha = 12°$.

Figure 22. Continued.

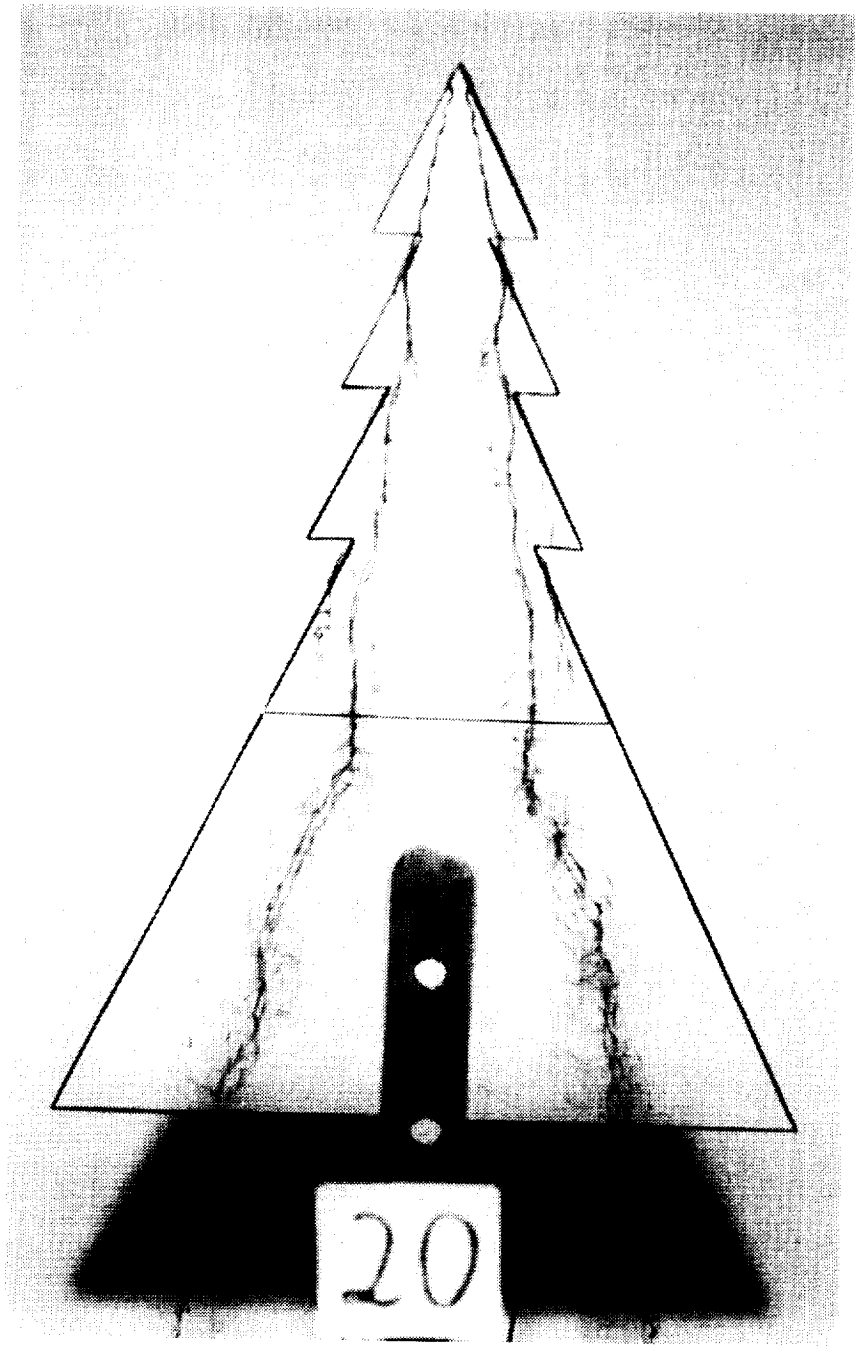

(c) Top view; $\alpha = 20°$.

Figure 22. Continued.

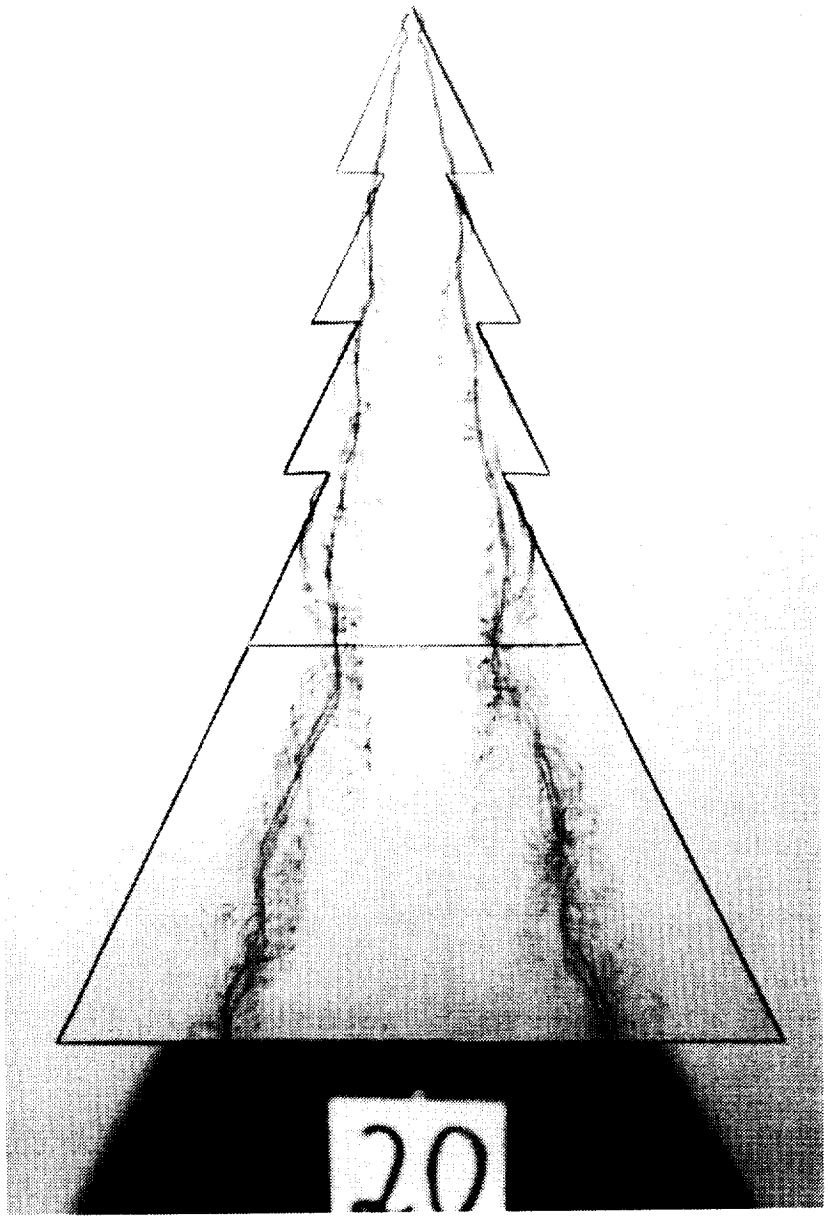

(d) Simulated balance housing removed; top view; $\alpha = 20°$.

Figure 22. Continued.

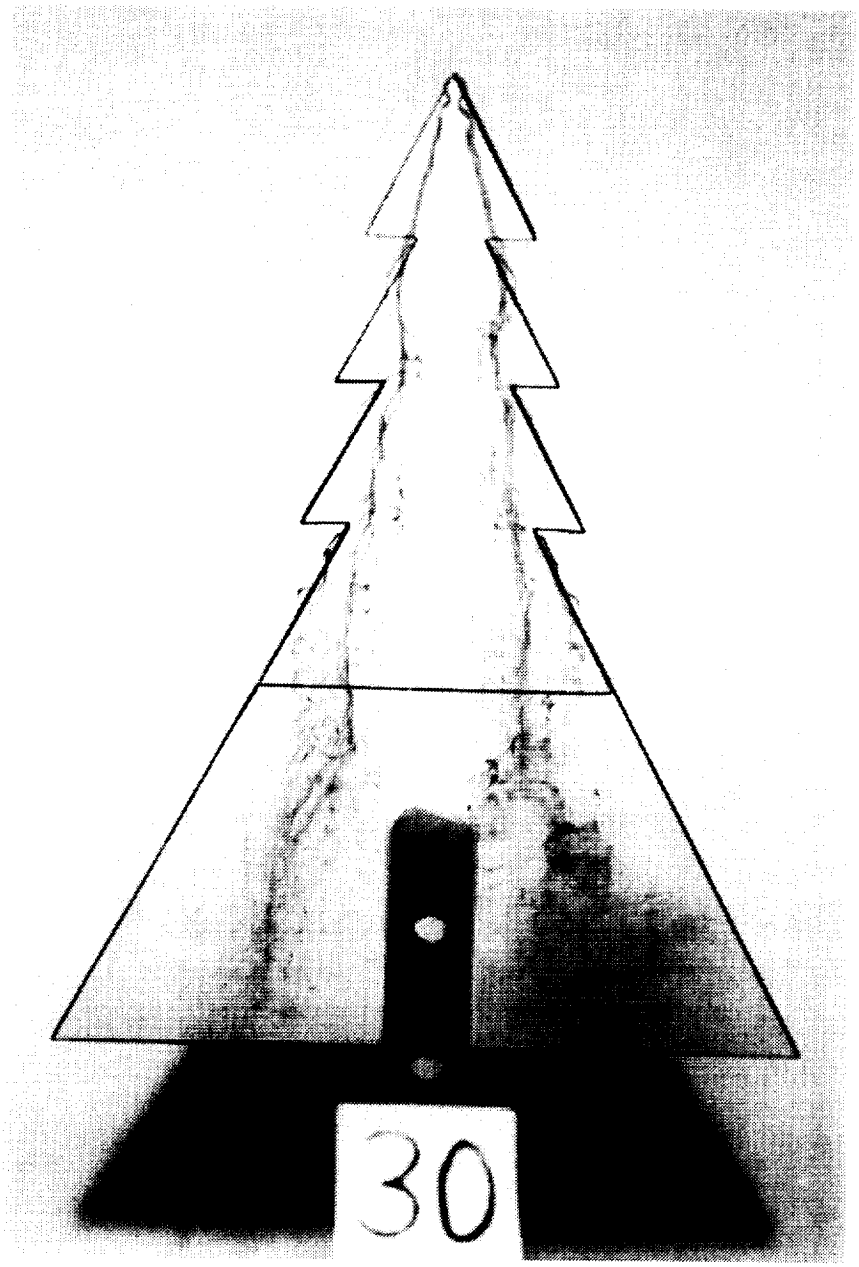

(e) Top view; $\alpha = 30°$.

Figure 22. Continued.

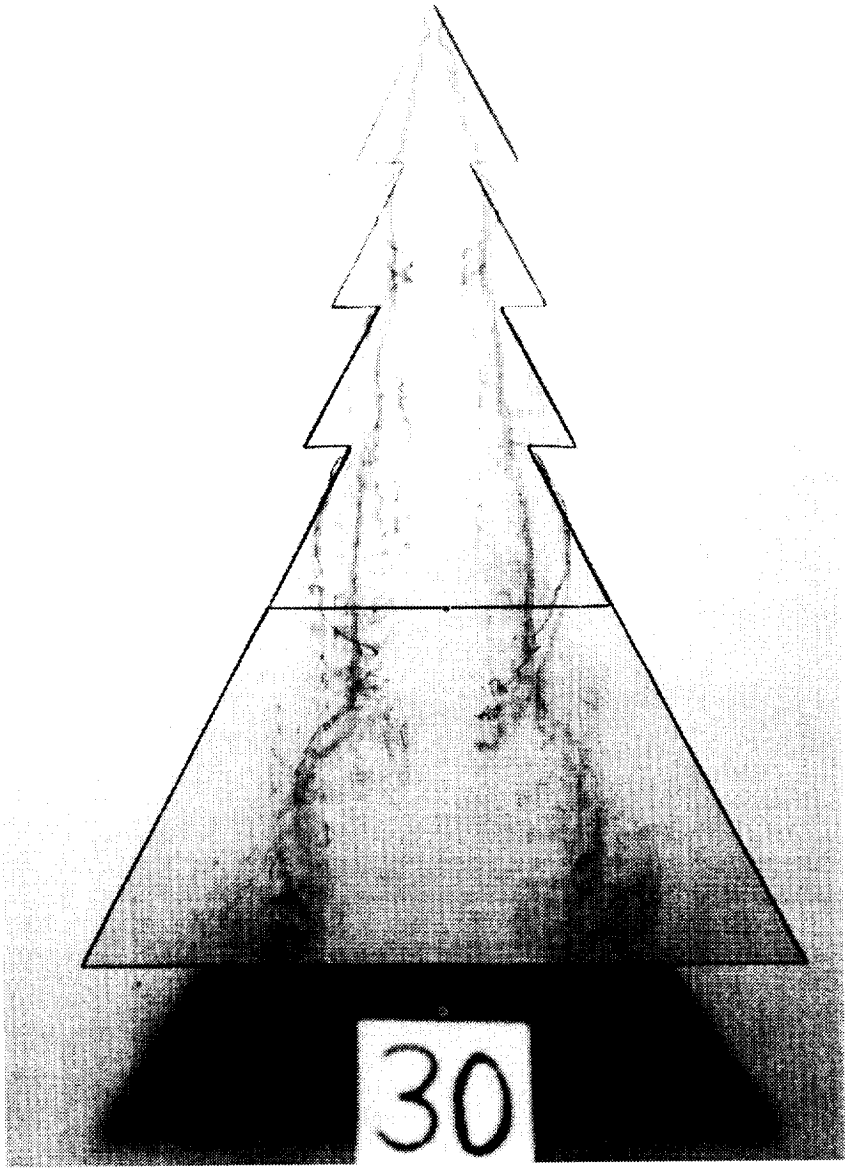

(f) Simulated balance housing removed; top view; $\alpha = 30°$.

Figure 22. Continued.

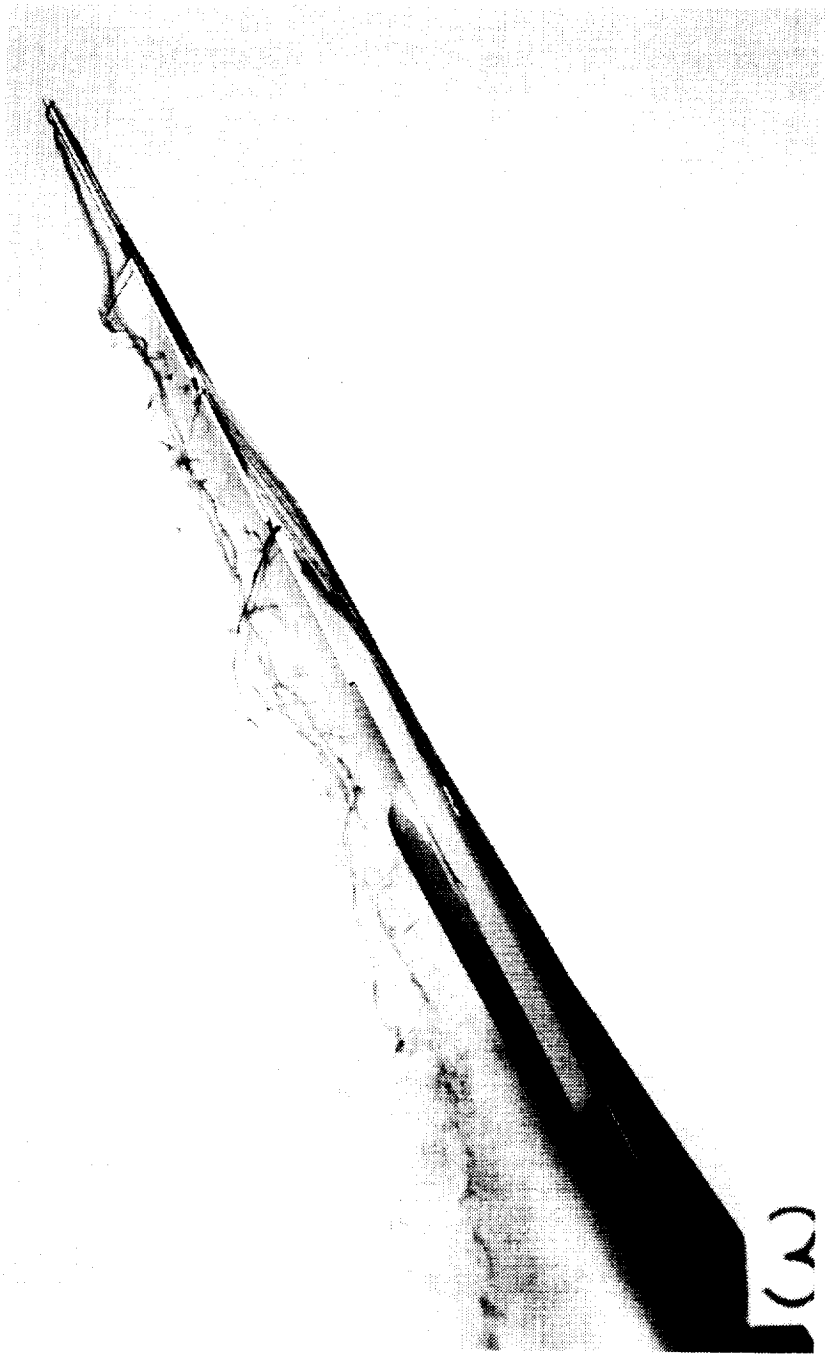

(g) Side view; $\alpha = 30°$.

Figure 22. Continued.

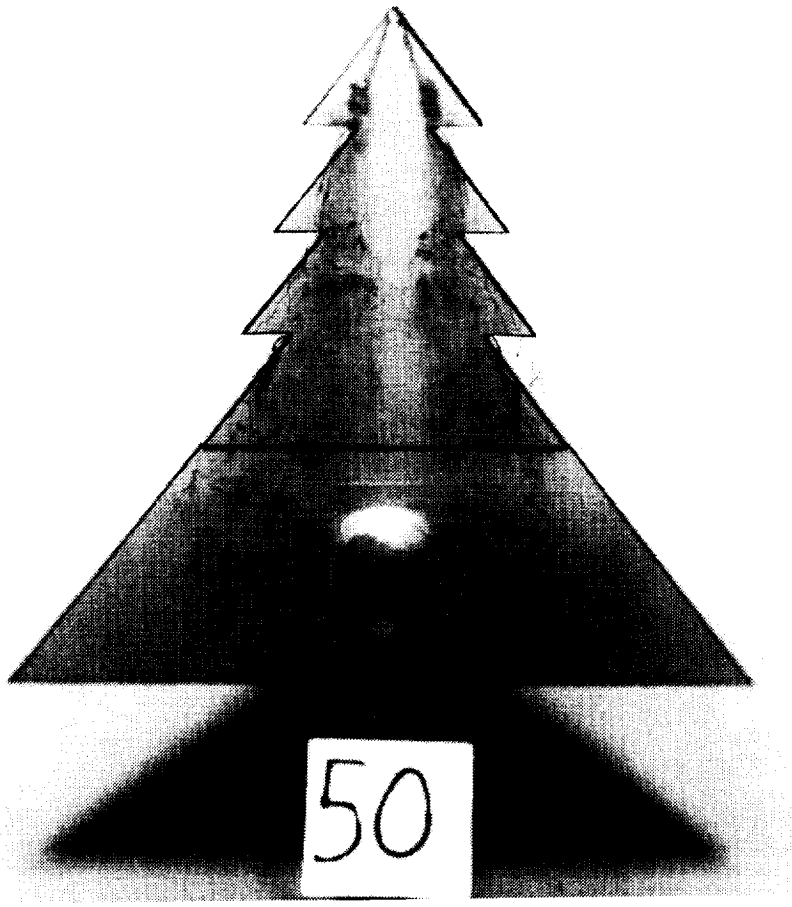

(h) Top view; $\alpha = 50°$.

Figure 22. Concluded.

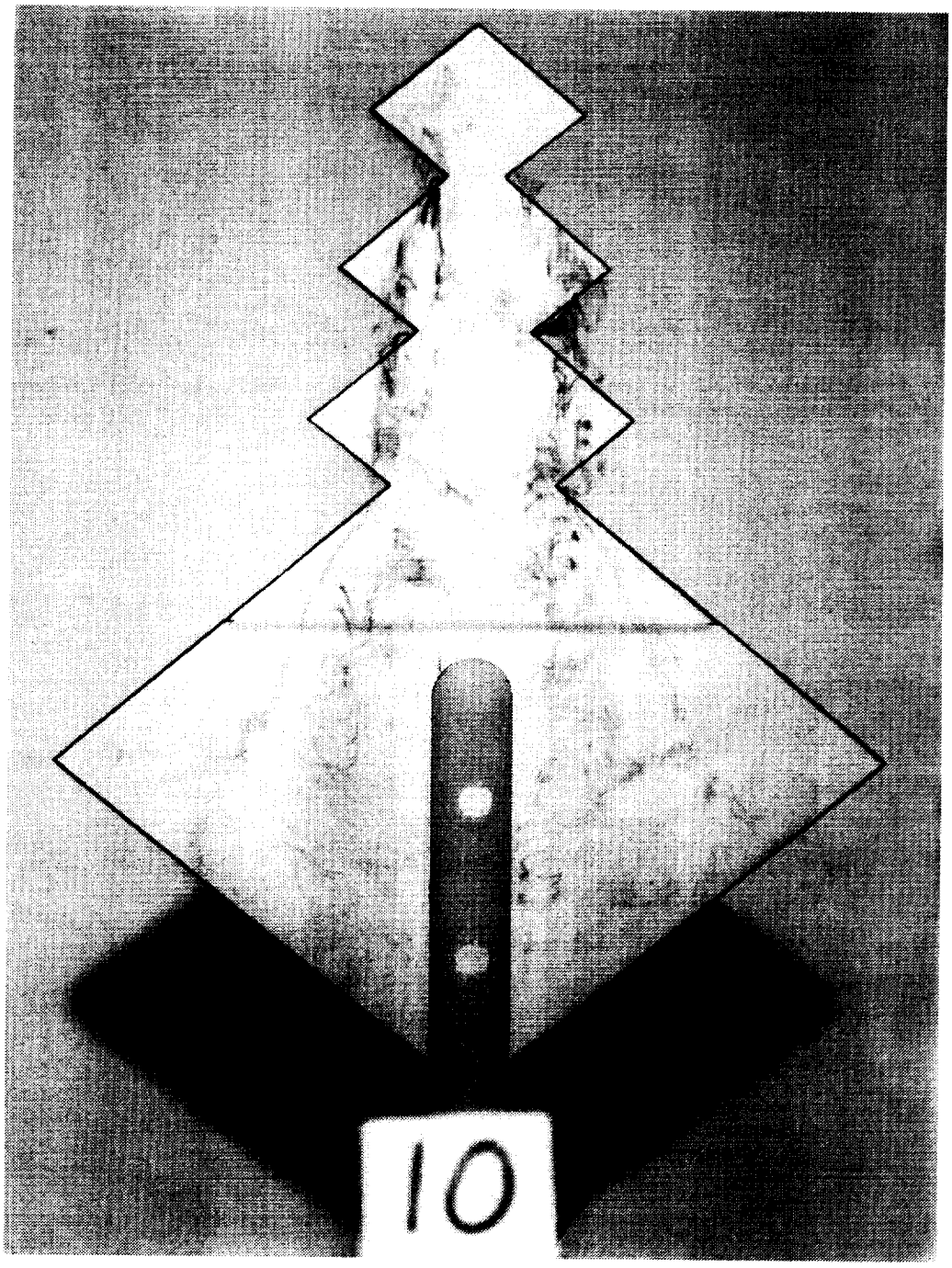

(a) Top view; $\alpha = 10°$.

Figure 23. Photographs of 40° diamond with 3 diamond sawteeth.

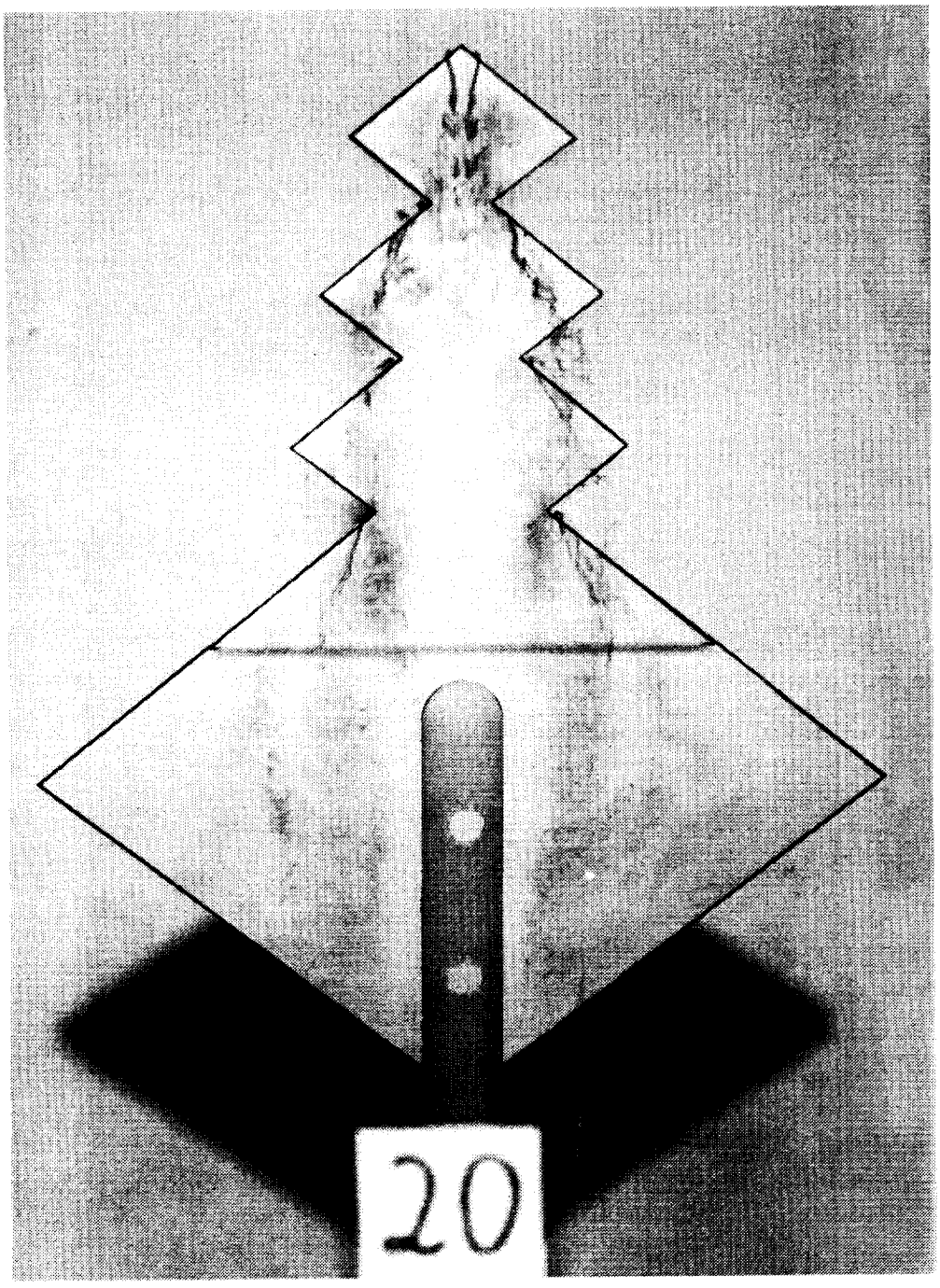

(b) Top view; $\alpha = 20°$.

Figure 23. Continued.

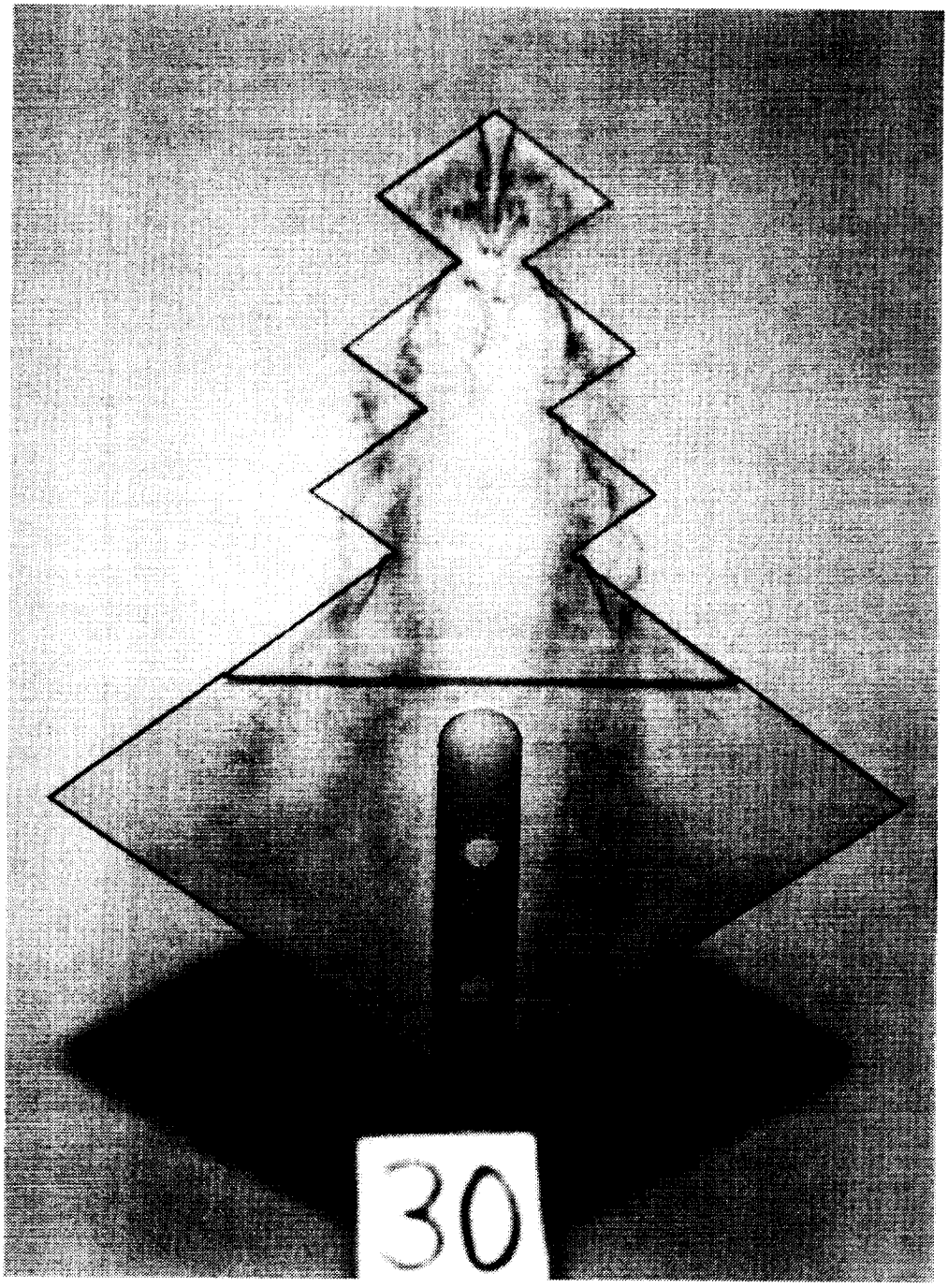

(c) Top view; $\alpha = 30°$.

Figure 23. Continued.

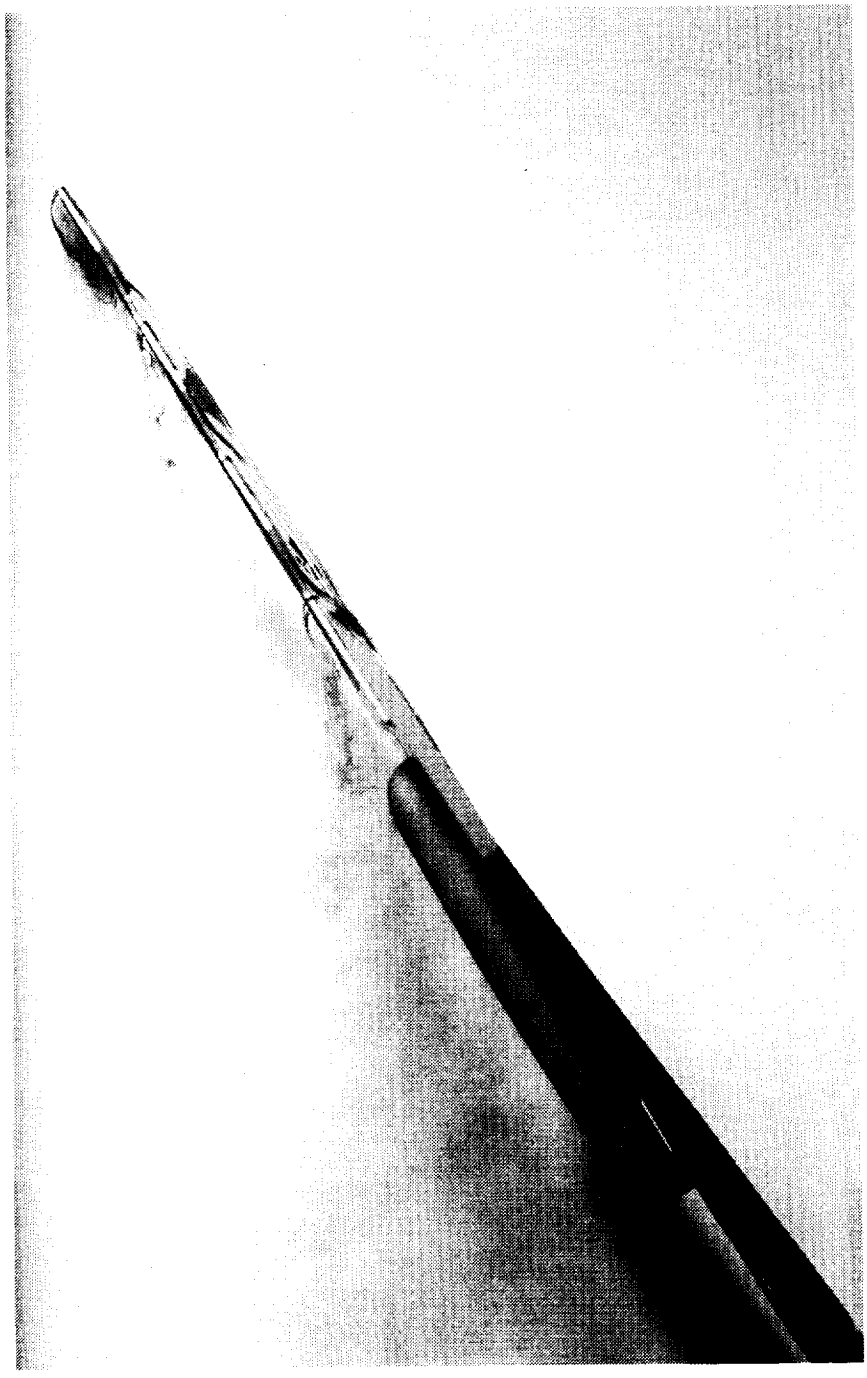

(d) Side view; $\alpha = 30°$.

Figure 23. Continued.

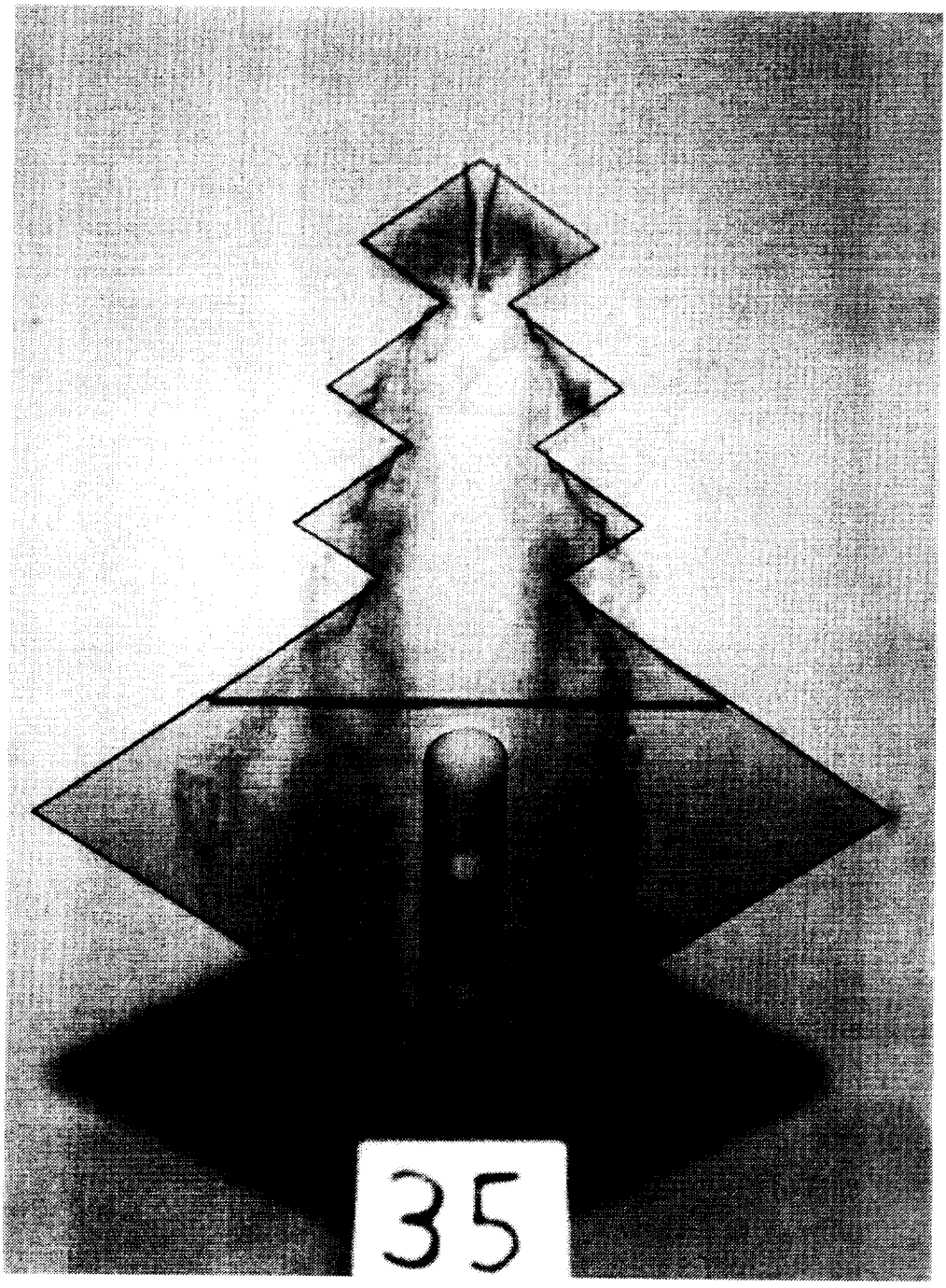

(e) Top view; $\alpha = 35°$.

Figure 23. Continued.

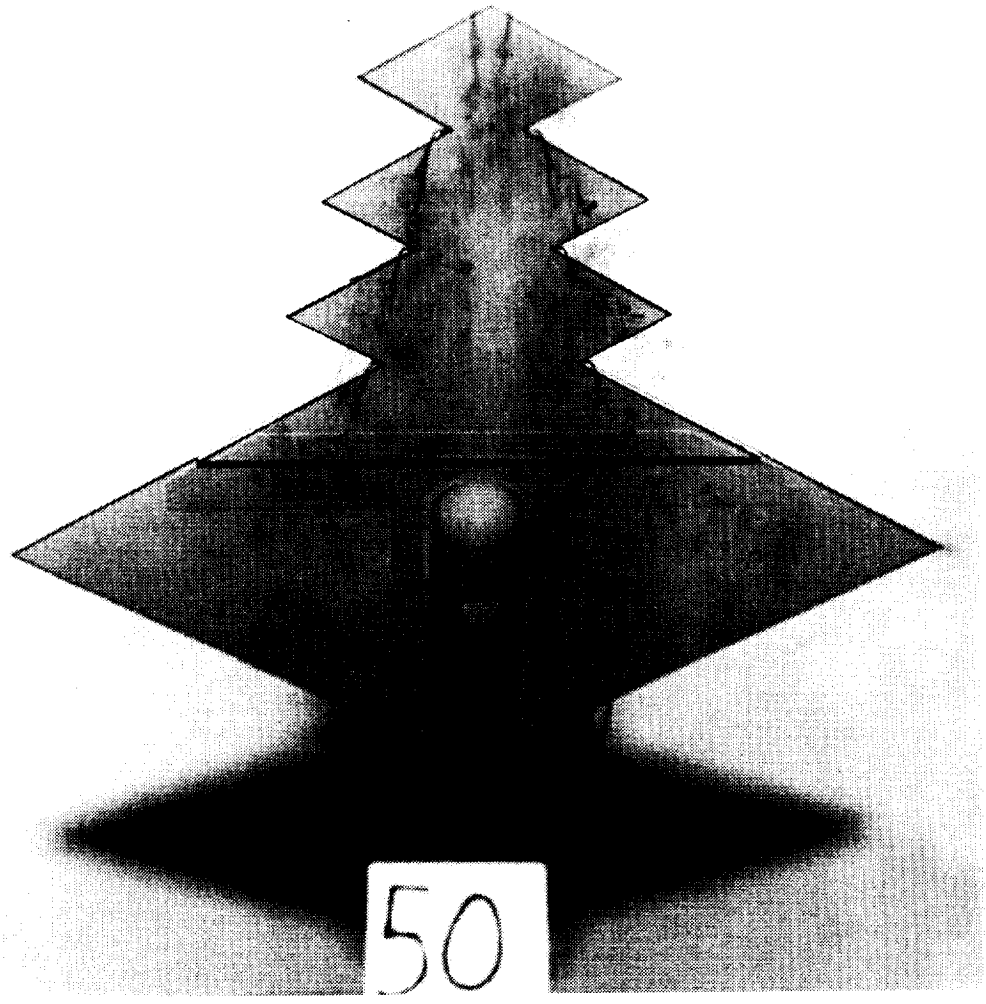

(f) Top view; $\alpha = 50°$.

Figure 23. Concluded.

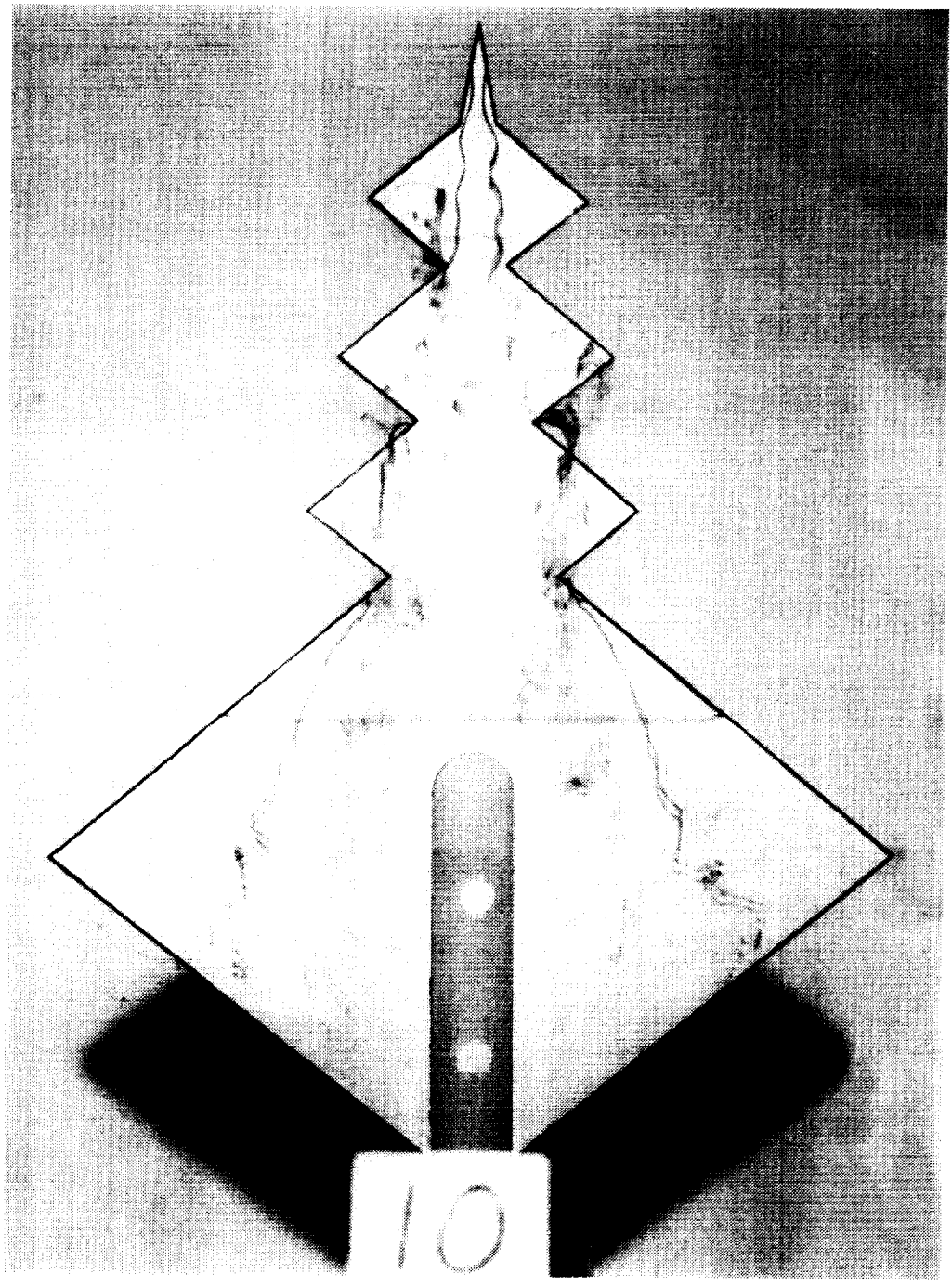

(a) Top view; $\alpha = 10°$.

Figure 24. Photographs of 40° diamond with 3 diamond sawteeth and nose tip.

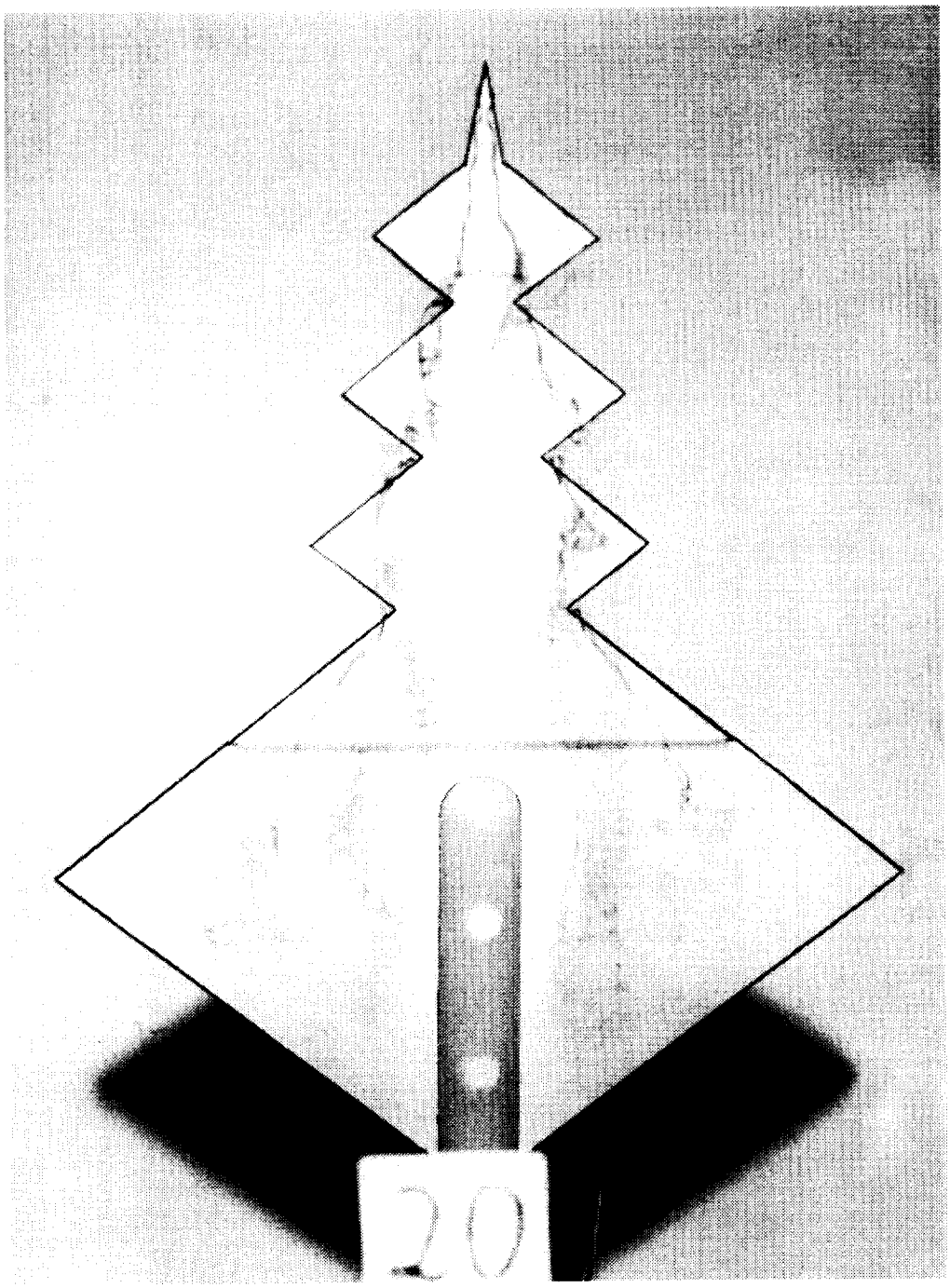

(b) Top view; $\alpha = 20°$.

Figure 24. Continued.

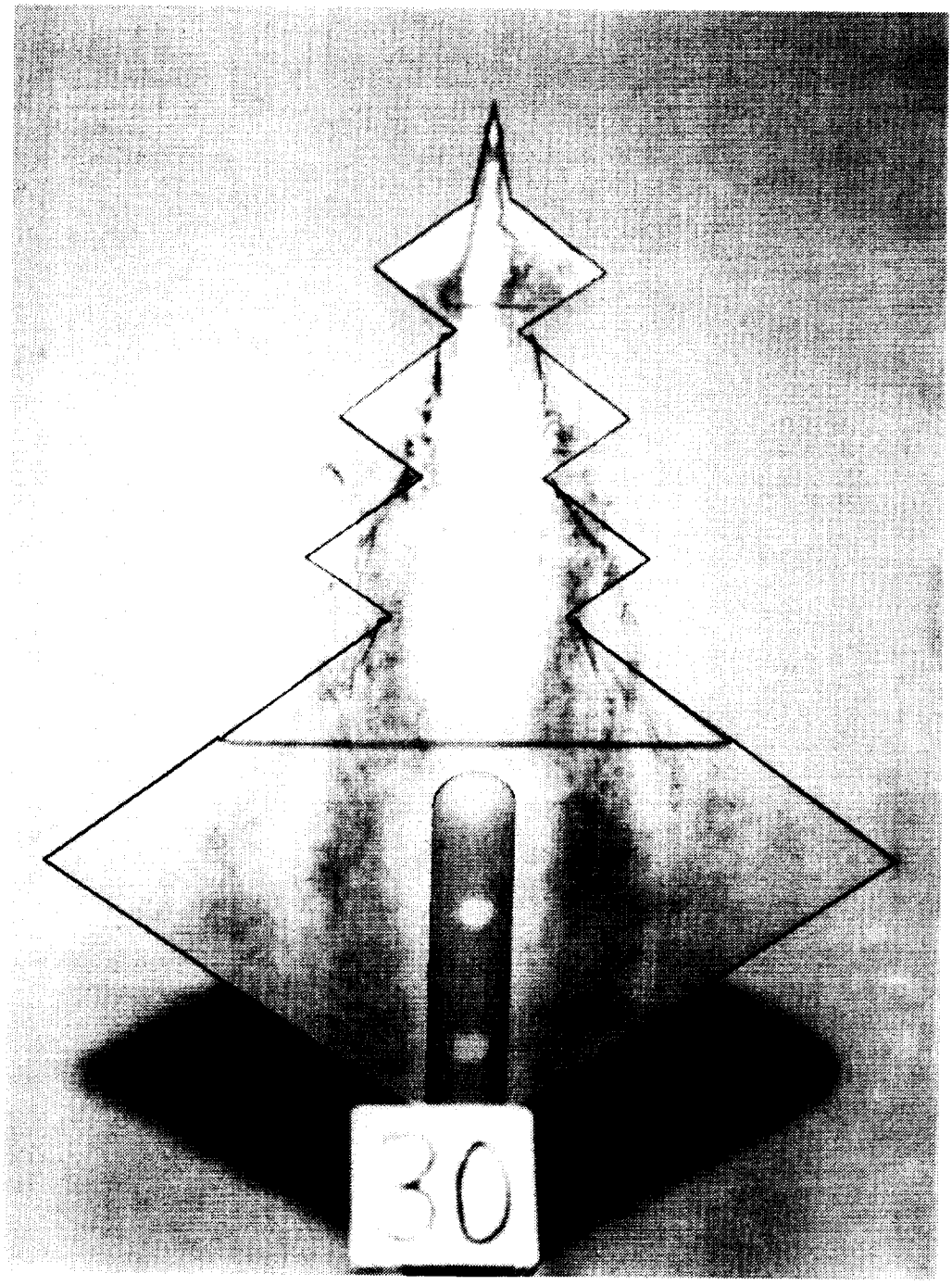

(c) Top view; $\alpha = 30°$.

Figure 24. Continued.

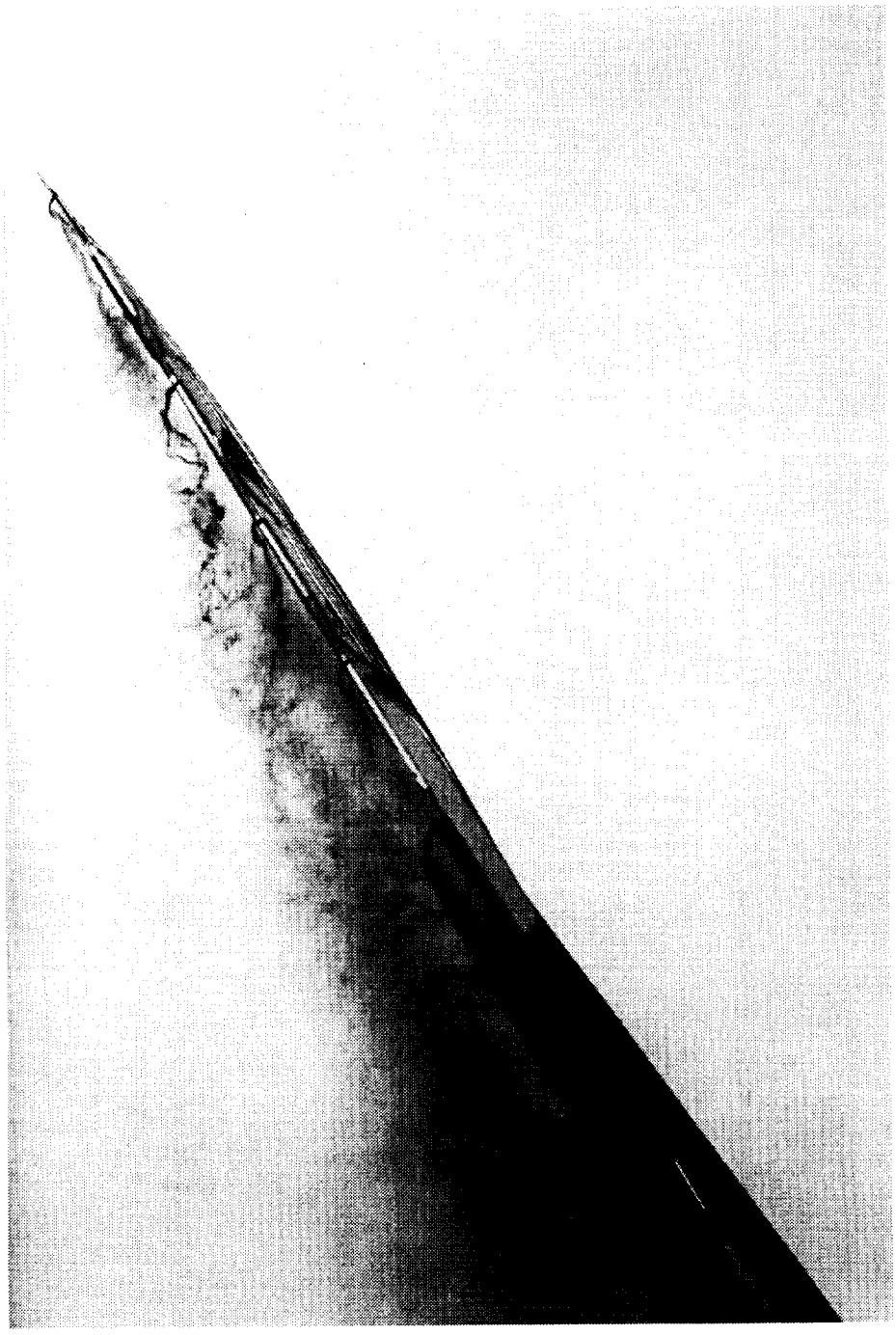

(d) Side view; $\alpha = 30°$.

Figure 24. Continued.

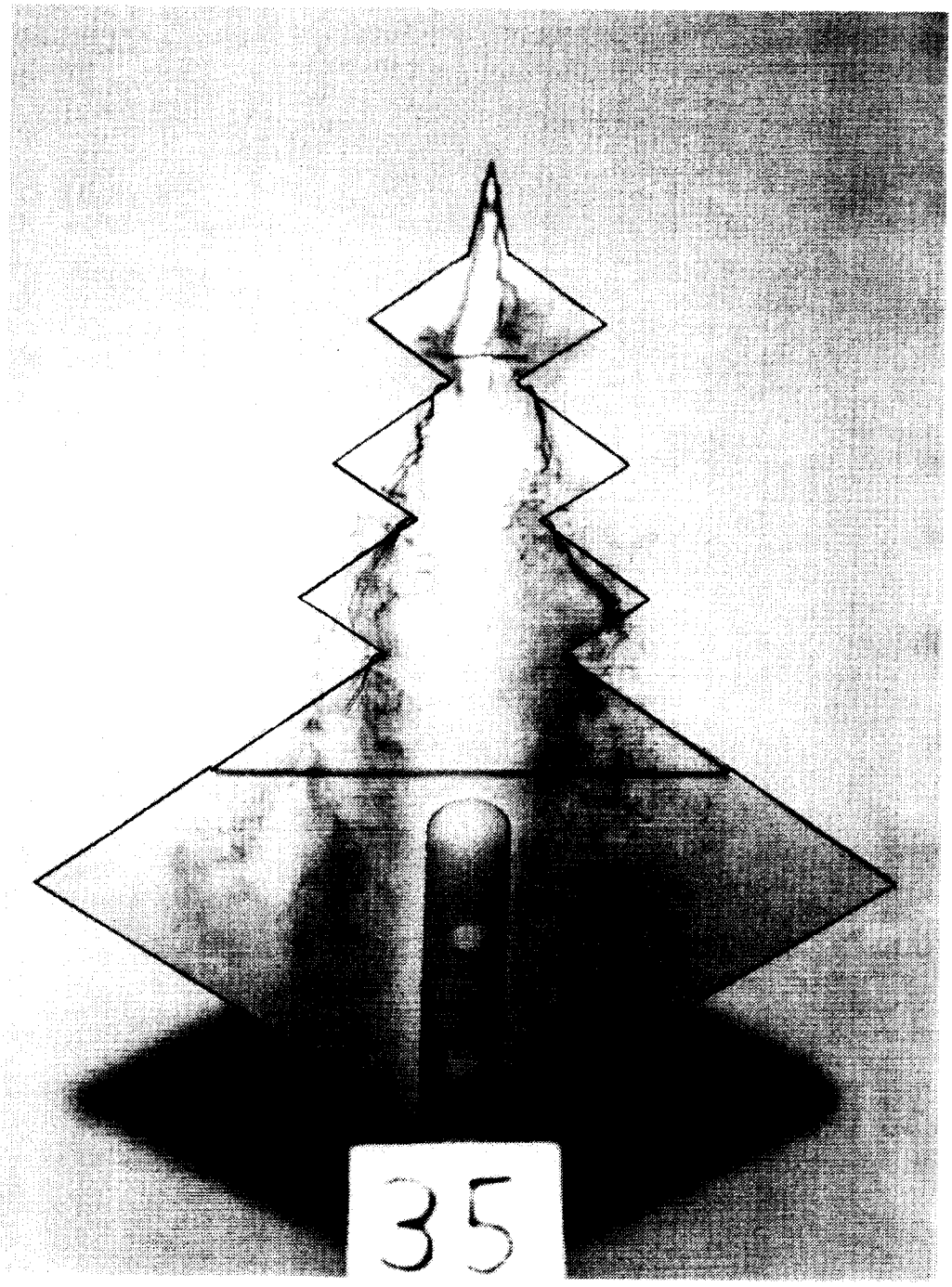

(e) Top view; $\alpha = 35°$.

Figure 24. Continued.

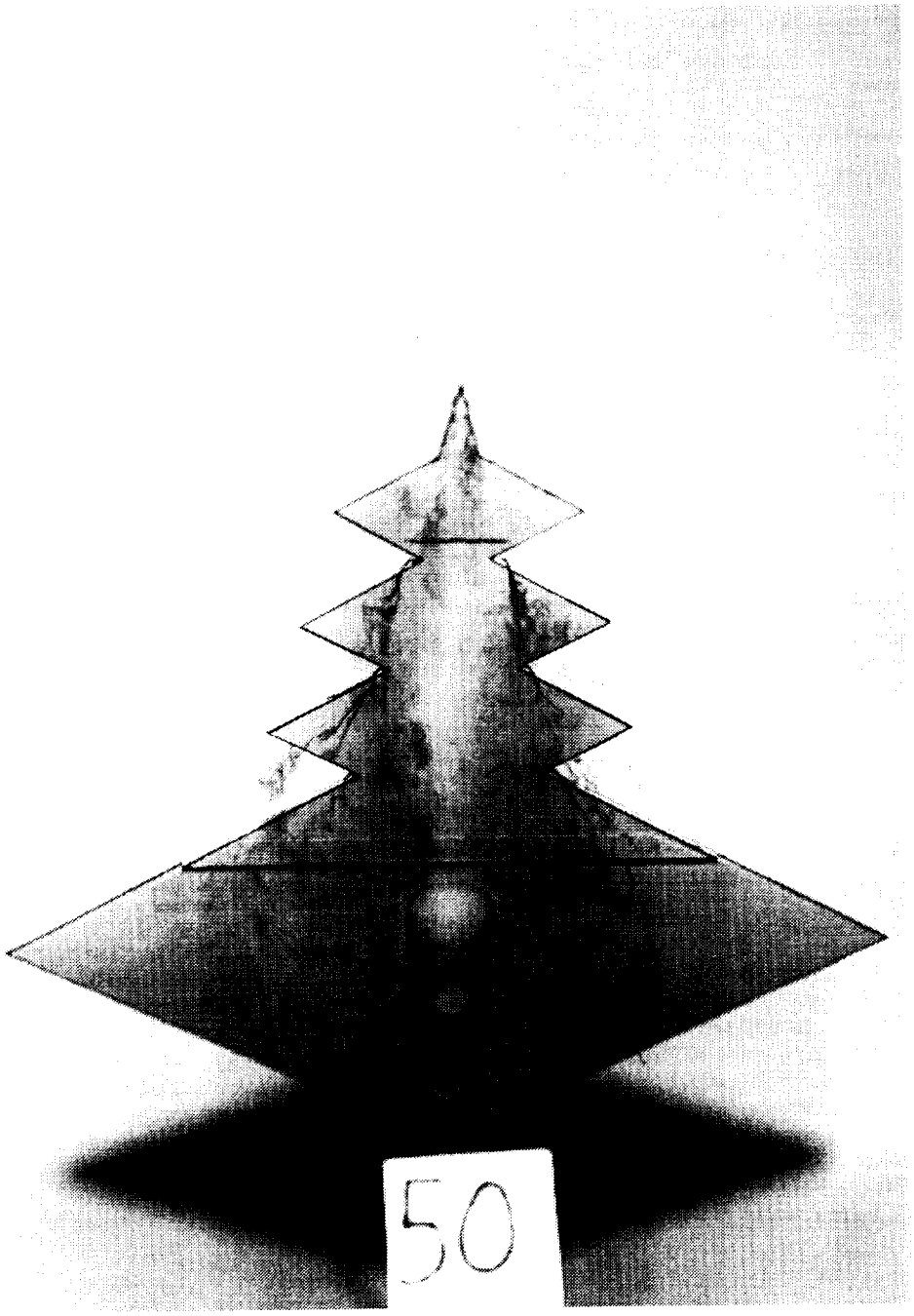

(f) Top view; $\alpha = 50°$.

Figure 24. Concluded.

REPORT DOCUMENTATION PAGE

Form Approved
OMB No. 0704-0188

1. AGENCY USE ONLY *(Leave blank)*	2. REPORT DATE	3. REPORT TYPE AND DATES COVERED
	March 1996	Technical Memorandum

4. TITLE AND SUBTITLE
Water Tunnel Flow Visualization Study Through Poststall of 12 Novel Planform Shapes

5. FUNDING NUMBERS
WU 505-68-70-04

6. AUTHOR(S)
Gregory M. Gatlin and Dan H. Neuhart

7. PERFORMING ORGANIZATION NAME(S) AND ADDRESS(ES)
NASA Langley Research Center
Hampton, VA 23681-0001

8. PERFORMING ORGANIZATION REPORT NUMBER
L-17418

9. SPONSORING/MONITORING AGENCY NAME(S) AND ADDRESS(ES)
National Aeronautics and Space Administration
Washington, DC 20546-0001

10. SPONSORING/MONITORING AGENCY REPORT NUMBER
NASA TM-4663

11. SUPPLEMENTARY NOTES
Gatlin: Langley Research Center, Hampton, VA; Neuhart: Lockheed Engineering & Sciences Company, Hampton, VA. Most copies of this report were printed in black and white; however, a limited number of color copies are available from the author. Color images are available in the electronic version at URL http://techreports.larc.nasa.gov/ltrs/ltrs.html.

12a. DISTRIBUTION/AVAILABILITY STATEMENT
Unclassified–Unlimited
Subject Category 02
Availability: NASA CASI (301) 621-0390

12b. DISTRIBUTION CODE

13. ABSTRACT *(Maximum 200 words)*

To determine the flow field characteristics of 12 planform geometries, a flow visualization investigation was conducted in the Langley 16- by 24-Inch Water Tunnel. Concepts studied included flat plate representations of diamond wings, twin bodies, double wings, cutout wing configurations, and serrated forebodies. The off-surface flow patterns were identified by injecting colored dyes from the model surface into the free-stream flow. These dyes generally were injected so that the localized vortical flow patterns were visualized. Photographs were obtained for angles of attack ranging from 10° to 50°, and all investigations were conducted at a test section speed of 0.25 ft per sec. Results from the investigation indicate that the formation of strong vortices on highly swept forebodies can improve poststall lift characteristics; however, the asymmetric bursting of these vortices could produce substantial control problems. A wing cutout was found to significantly alter the position of the forebody vortex on the wing by shifting the vortex inboard. Serrated forebodies were found to effectively generate multiple vortices over the configuration. Vortices from 65° swept forebody serrations tended to roll together, while vortices from 40° swept serrations were more effective in generating additional lift caused by their more independent nature.

14. SUBJECT TERMS	15. NUMBER OF PAGES
Planform shapes; Water tunnel; Flow visualization; Twin wing; Twin body; Cutout wing; Serrated forebody	126
	16. PRICE CODE A07

17. SECURITY CLASSIFICATION OF REPORT	18. SECURITY CLASSIFICATION OF THIS PAGE	19. SECURITY CLASSIFICATION OF ABSTRACT	20. LIMITATION OF ABSTRACT
Unclassified	Unclassified	Unclassified	